

Uniwersytet im. Adama Mickiewicza w Poznaniu  
Szkoła Doktorska Nauk Przyrodniczych  
Wydział Nauk Geograficznych i Geologicznych



**Szymon Śledź**

**Optymalizacja przetwarzania zdjęć z bezzałogowych statków powietrznych  
na potrzeby analizy dynamiki rzeźby terenu  
w badaniach z zakresu geomorfologii glacialnej**

*Optimization of the processing of images from unmanned aerial vehicles  
for the analysis of land surface dynamics in glacial geomorphology*

Rozprawa doktorska napisana pod kierunkiem:  
Prof. UAM dr hab. inż. Jana Piekarczyka  
Prof. UAM dr hab. Marka Ewertowskiego

Poznań 2024

## **Spis treści**

|  |    |
|--|----|
| <b>Podziękowania</b> .....                                     | 3  |
| <b>Streszczenie</b> .....                                      | 5  |
| <b>Publikacje wchodzące w skład rozprawy doktorskiej</b> ..... | 7  |
| <b>1. Wstęp</b> .....  | 8  |
| <b>2. Zarys treści publikacji</b> .....                        | 10 |
| 2.1. Publikacja nr I.....                                      | 10 |
| 2.2. Publikacja nr II .....                                    | 11 |
| 2.3. Publikacja nr III.....                                    | 13 |
| <b>3. Dyskusja</b> .....                                       | 16 |
| <b>4. Podsumowanie</b> .....                                   | 19 |
| <b>Bibliografia</b> .....                                      | 20 |
| <b>Publikacja nr I z załącznikiem</b> .....                    | 24 |
| <b>Publikacja nr II z załącznikami</b> .....                   | 41 |
| <b>Publikacja nr III</b> .....                                 | 71 |
| <b>Oświadczenia autorów</b> .....                              | 97 |

## **Podziękowania**

Przedłożona rozprawa doktorska została napisana dzięki wsparciu wielu osób, które podczas ostatnich czterech lat dzieliły się ze mną swoimi doświadczeniami i udzielały mi wartościowych rad – pozwoliły mi one poznać naukę na międzynarodowym poziomie, jak i stać się lepszym człowiekiem.

W pierwszej kolejności chciałbym podziękować Promotorom:

prof. UAM dr hab. inż. Janowi Piekarczykowi,

za wprowadzenie mnie w trakcie studiów licencjackich w świat teledetekcji, od czego zaczęła się moja przygoda z nauką;

prof. UAM dr hab. Markowi Ewertowskiemu,

za pasję, nieustępliwość i wysoko ustawioną poprzeczkę, co dziś pozwala mi mierzyć się z każdym wyzwaniem z łatwością i spokojem.

Szczególne podziękowania składam Adamowi Młynarczykowi za altruizm i zaraźliwy optymizm, Grzegorzowi Jankowiakowi za wsparcie nie tylko techniczne oraz Marlenie Kaźmierskiej za zaangażowanie mnie w działalność Samorządu Doktorantów UAM.

Dalej pragnę serdecznie podziękować pracownikom oraz obecnym i byłym doktorantom Zakładu Teledetekcji Środowiskowej i Gleboznawstwa za okazaną pomoc i liczne rozmowy poszerzające horyzonty naukowe i życiowe. Dziękuję Aleksandrze Tomczyk i Wojciechowi Ewertowskiemu za wspólną pracę podczas wyjazdu na badania terenowe na Islandii. Wysłałam podziękowania dla Pana dr Wesleya Farnswortha za przyjęcie mnie na staż w University of Iceland. Dziękuję Pani prof. UAM dr hab. Agnieszce Ludwików oraz Pani Małgorzacie Klimorowskiej za wspieranie doktorantów podczas ich kształcenia w Szkole Doktorskiej Nauk Przyrodniczych. Dziękuję koleżankom i kolegom z roku za wspólne pokonywanie trudności podczas pandemii COVID-19. Dziękuję pracownikom Uniwersytetu za ich pracę i życzliwość. Dziękuję wszystkim, którzy w jakikolwiek sposób przyczynili się do powstania tej rozprawy.

Na koniec chciałbym podziękować mojej małżonce Justynie, Rodzicom oraz siostrze Wiktorii za nieustanną pomoc w codzienności i okazanemu wsparciu w chwilach słabości. Dziękuję przyjaciółom i znajomym za motywację i wiarę w moją osobę.

Badania terenowe, publikacja artykułów w otwartym dostępie oraz zagraniczne wyjazdy konferencyjne zostały sfinansowane z poniższych źródeł:

- 1) projektu Narodowego Centrum Nauki OPUS nr 2019/35/B/ST10/03928: „Kartowanie i analiza ilościowa krótkookresowej dynamiki obszarów proglacjalnych” (kierownik: prof. UAM dr hab. Marek Ewertowski);
- 2) programu „Inicjatywa Doskonałości – Uczelnia Badawcza”;
- 3) programu „Uniwersytet Jutra II – zintegrowany program rozwoju Uniwersytetu im. Adama Mickiewicza w Poznaniu” nr POWR.03.05.00-00-Z303/18,

realizowanych na Uniwersytecie im. Adama Mickiewicza w Poznaniu.

Pozwolenia na badania naukowe w terenie zostały udzielone przez Park Narodowy Vatnajökull i Islandzką Radę ds. Badań Naukowych (RANNIS).

Rozprawę doktorską dedykuję zmarłym Panu Kazimierzowi Gmerkowi oraz Panu dr Andrzejowi Kijowskiemu.

## Streszczenie

Niniejsza rozprawa doktorska łączy tematykę wykorzystania bezzałogowych statków powietrznych w badaniach z zakresu geomorfologii glacialnej z problematyką efektywnego przetwarzania wysokorozdzielczych obrazów w oprogramowaniu fotogrametrycznym. Przeprowadzona kwerenda literatury wskazała istotne luki dotyczące opisu metodologii przetwarzania zdjęć w wielu publikacjach naukowych dotyczących zastosowania cyfrowych modeli wysokościowych i ortomozaik w geomorfologii glacialnej. Błędy bądź niewiedza na tym etapie mogą mieć duże znaczenie dla dokładności produktów fotogrametrycznych, a w konsekwencji dla wyników dalszych analiz i interpretacji geomorfologicznych. Aby uzupełnić wskazaną lukę, w ramach pracy doktorskiej, przeprowadzono eksperymenty z wykorzystaniem oprogramowania Agisoft Metashape, mające na celu opracowaniu optymalnych schematów postępowania i doboru ustawień zależnie od oczekiwanych efektów: skrócenia czasu obliczeń lub uzyskania możliwie najmniejszych błędów cyfrowych modeli wysokościowych. Efektem prac były trzy skrypty w języku Python, które w znaczący sposób ułatwiają pracę w oprogramowaniu, jak i wspomagają efektywne zarządzanie wieloma projektami jednocześnie, np. przy użyciu wielowątkowego klastra obliczeniowego. Ostatnią częścią rozprawy było wykorzystanie wiedzy z przeglądu literatury wraz z opracowanymi skryptami do analizy dynamiki rzeźby terenu przedpoła lodowca Kviár na Islandii. Kwantyfikacji zmian form terenu dokonano na podstawie zdjęć pozyskanych z bezzałogowych statków powietrznych w latach 2014–2022. Zrealizowane badania potwierdziły użyteczność opracowanych skryptów do pracy z rozbudowanym zbiorem danych, udokumentowały wysoką dynamikę form na przedpołu lodowca związaną przede wszystkim z wytapianiem trzonów lodowych oraz wskazały pewne ograniczenia metody Structure-from-Motion. Całość pracy stanowi ważny wkład w rozwój metodologii przetwarzania obrazów z bezzałogowych statków powietrznych w badaniach z zakresu geomorfologii glacialnej, a opracowane skrypty mogą być przydatne dla innych naukowców pracujących z podobnymi danymi.

**Słowa kluczowe:** Structure-from-Motion, bezzałogowy statek powietrzny, geomorfologia glacialna, detekcja zmian, fotogrametria, Agisoft Metashape

## **Abstract**

This doctoral dissertation integrates the application of unmanned aerial vehicles in glacial geomorphology with the challenges of efficient processing of high-resolution images in photogrammetric software. The literature review revealed significant gaps in describing image processing methodologies in numerous scientific publications related to the application of digital elevation models and orthomosaics in glacial geomorphology. Errors or lack of knowledge at this stage can have a considerable impact on the accuracy of photogrammetric products and, consequently, on the results of further geomorphological analyses and interpretations. As part of the doctoral research, to address this identified gap, experiments were conducted using Agisoft Metashape software. The aim was to develop optimal procedures and settings depending on the desired outcomes: either reducing computation time or achieving minimal errors in digital elevation models. The outcome of these efforts resulted in three Python scripts, significantly facilitating work within the software, and supporting effective management of multiple projects simultaneously, for example, through using of multi-threaded computing clusters. The final part of the dissertation involved applying the knowledge from the literature review along with the developed scripts to analyze the dynamics of the terrain in front of the Kvíár glacier in Iceland. Quantification of changes in landforms was carried out based on images acquired from unmanned aerial vehicles between 2014 and 2022. The conducted research confirmed the usefulness of the developed scripts for working with extensive datasets, documented high dynamics of landforms in front of the glacier primarily associated with the degradation of ice cores, and indicated certain limitations of the Structure-from-Motion method. The entire work constitutes a significant contribution to the development of image processing methodologies in glacial geomorphology research, and the developed scripts may be valuable for other researchers working with similar data.

**Keywords:** Structure-from-Motion, unmanned aerial vehicle, glacial geomorphology, change detection, photogrammetry, Agisoft Metashape

## Publikacje wchodzące w skład rozprawy doktorskiej

Rozprawa doktorska składa się z trzech artykułów naukowych stanowiących spójny tematycznie zbiór publikacji, które w tekście oznaczono cyframi rzymskimi. Wskaźniki bibliometryczne oraz liczba cytowań była aktualna na dzień 8 lutego 2024 r.

- I. Śledź, S., Ewertowski, M. W., & Piekarczyk, J. (2021). Applications of unmanned aerial vehicle (UAV) surveys and Structure from Motion photogrammetry in glacial and periglacial geomorphology. *Geomorphology*, 378.  
<https://doi.org/10.1016/j.geomorph.2021.107620>

Q2 Web of Science; 93 percentyl Scopus (2021); IF2021 = 4.139; MEiN<sub>2021</sub> = 100 pkt

Liczba cytowań: Google Scholar: 75; Scopus: 56; Web of Science: 50

- II. Śledź, S., & Ewertowski, M. W. (2022). Evaluation of the Influence of Processing Parameters in Structure-from-Motion Software on the Quality of Digital Elevation Models and Orthomosaics in the Context of Studies on Earth Surface Dynamics. *Remote Sensing*, 14(6). <https://doi.org/10.3390/rs14061312>

Q1 Web of Science; 90 percentyl Scopus (2022); IF2022 = 5.349; MEiN<sub>2022</sub> = 100 pkt

Liczba cytowań: Google Scholar: 10; Scopus: 9; Web of Science: 7

- III. Śledź, S., Ewertowski, M. W., & Evans, D. J. A. (2023). Quantification of short-term transformations of proglacial landforms in a temperate, debris-charged glacial landsystem, Kvíárjökull, Iceland. *Land Degradation & Development*, 34(17), 5566-5590.  
<https://doi.org/10.1002/ldr.4865>

Q2 Web of Science; 91 percentyl Scopus (2022); IF2022 = 4.377; MEiN<sub>2023</sub> = 200 pkt

Liczba cytowań: Google Scholar: 0; Scopus: 0; Web of Science: 0

## 1. Wstęp

Bezzałogowy statek powietrzy (BSP), w literaturze definiowany jako ang. *Unmanned Aerial Systems* (UAS), *Unmanned/Uncrewed/Unoccupied Aerial Vehicle* (UAV), *aerial robot* lub popularnie *drone* ([Colomina i Molina, 2014](#)), jest przykładem narzędzia, które jako platforma do montażu wybranego sensora, umożliwia operatorowi zdalne zbieranie danych o punktowych lub obszarowych obiektach badawczych bez bezpośredniego kontaktu z nimi. Dzięki możliwości konfiguracji i wysokiej mobilności, znajduje on obecnie szerokie zastosowanie w różnych dziedzinach badań środowiskowych, w tym w geomorfologii ([Westoby i in., 2012](#)), hydrologii ([Carrivick i Smith, 2019](#)), glaciologii ([Bhardwaj i in., 2016](#)) czy rolnictwie precyzyjnym ([Anderson i Gaston, 2013](#)). Zdjęcia wykonywane z pułapu BSP są konkurencyjną alternatywą, zarówno dla wysokorozdzielczych zobrazowań satelitarnych, jak i tradycyjnych lotniczych nalotów fotogrametrycznych ([Manfreda i in., 2018](#)). Zastosowanie BSP oferuje lepszą elastyczność czasową oraz wyższą rozdzielczość przestrzenną zdjęć (nawet rzędu kilku milimetrów) przy niskim koszcie nabycia (poniżej 10 000,00 PLN), do którego jednak należy doliczyć koszty szkolenia operatora oraz jego pobytu w terenie.

Zdjęcia pozyskane przy pomocy BSP przetwarzane są najczęściej w oprogramowaniu fotogrametrycznym, gdzie wykorzystuje się metodę Structure-from-Motion (SfM) do łączenia zdjęć wykonanych pod różnym kątem i z różnej odległości ([Westoby i in., 2012](#)). Algorytm SfM łączy je ze sobą na podstawie punktów charakterystycznych, wyznaczonych przynajmniej na dwóch zdjęciach. W efekcie otrzymuje się najpierw rzadką chmurę punktów (ang. *sparse point cloud*), a w kolejnym kroku gęstą chmurę punktów (ang. *dense point cloud*), która jest podstawą do wygenerowania końcowych opracowań fotogrametrycznych: ortomozaiki oraz cyfrowego modelu wysokościowego (DEM – ang. *Digital Elevation Model*), będącego trójwymiarowym odwzorowaniem powierzchni badanego obszaru ([Agisoft, 2022](#)). Wymienione opracowania są powszechnie stosowane do kartowania geomorfologicznego ([Allaart i in., 2018](#); [Dąbski i in., 2020](#); [Ewertowski i Tomczyk, 2020](#); [Storrar i in., 2019](#)), analizy zmian objętości form glacialnych ([Chandler i in., 2020a](#); [Fugazza i in., 2018](#); [Tomczyk i in., 2020](#); [Whitehead i in., 2013](#)), badania procesów morfogenetycznych ([Chandler i in., 2020b](#)) czy badań sedymentologicznych ([Kociuba, 2017](#); [Westoby i in., 2015](#)). Kosztowniejszą alternatywą dla metody SfM jest LIDAR (ang. *Light Detection and Ranging*), gdzie wynikiem pomiaru laserowego jest chmura punktów, którą również wykorzystuje się do opracowania cyfrowego modelu wysokościowego ([Mosbrucker i in., 2017](#)).



W badaniach z zakresu geomorfologii glacialnej cyfrowy model wysokościowy oraz ortomozaika stanowią bardzo dobre uzupełnienie tradycyjnych pomiarów terenowych ([Śledź i in., 2023](#)). BSP i metoda SfM są szczególnie użyteczne w badaniach dynamiki rzeźby terenu, w których kładzie się nacisk na regularne pomiary w celu ilościowego ujęcia zachodzących zmian ([Chandler i in., 2020a](#); [Westoby i in., 2020](#)). Od 2014 roku można zaobserwować zauważalny wzrost liczby publikacji z wykorzystaniem BSP i metody SfM w badaniach geomorfologicznych ([Bhardwaj i in., 2016](#); [Gaffey i Bhardwaj, 2020](#); [Śledź i in., 2021](#)), jednak wcześniej nie podjęto próby ich usystematyzowania pod kątem użytego sprzętu, technologii i techniki wykonywania zdjęć. Metodyka badań w terenie, jak i wytyczne dla prezentacji wyników są dobrze poznane i opisane w literaturze ([Carbonneau i Dietrich, 2017](#); [Ewertowski i in., 2019](#); [James i in., 2019](#)), jednak brakuje publikacji szczegółowo i krytycznie opisujących poszczególne etapy przetwarzania zdjęć w oprogramowaniu fotogrametrycznym wykorzystującym metodę SfM ([de Haas i in., 2021](#); [Hendrickx i in., 2018](#); [Nota i in., 2022](#); [Śledź i Ewertowski, 2022](#)). Brakuje ponadto artykułów prezentujących narzędzia usprawniające pracę z dużymi zbiorami danych (np. zdjęć pochodzących z cyklicznych pomiarów tego samego obiektu badań) i ułatwiających wybór optymalnych procedur ([Śledź i Ewertowski, 2022](#)), co w połączeniu z rosnącą szczegółowością i ilością danych obrazowych pozyskiwanych z BSP staje się coraz bardziej istotnym zagadnieniem metodycznym.

W niniejszej pracy skoncentrowano się na określeniu optymalnych warunków wykorzystania metody SfM do przetwarzania zdjęć pozyskiwanych z niskiego pułapu lotniczego na potrzeby analiz geomorfologicznych. Celem rozprawy doktorskiej było:

- 1) rozpoznanie luk w aktualnym stanie wiedzy dotyczących wykorzystania BSP w badaniach geomorfologicznych i przetwarzania zdjęć w oprogramowaniu fotogrametrycznym metodą SfM;
- 2) przetestowanie wpływu parametrów przetwarzania zdjęć metodą SfM na dokładność uzyskiwanych opracowań fotogrametrycznych;
- 3) zaproponowanie możliwości optymalizacji przetwarzania zdjęć z BSP metodą SfM dzięki automatyzacji opartej na skryptach;
- 4) przetestowanie zaproponowanych rozwiązań na przykładzie analizy dynamiki rzeźby terenu na przedpolu lodowca Kviár na Islandii.

W rozprawie doktorskiej autor prezentuje wyniki przeprowadzonej kwerendy literatury i wykonanych badań, które mają na celu uzupełnienie wymienionych luk w dotychczasowym stanie wiedzy. W kolejnych rozdziałach przedstawiono zarys treści publikacji wchodzących

w skład rozprawy, syntetycznie opisując ich problematykę, użyte metody badawcze oraz otrzymane wyniki. W podsumowaniu przedstawiono wkład rozprawy w aktualny stan wiedzy oraz wskazano nowe problemy naukowe wymagające dalszych badań. Na koniec, wraz z publikacjami i załącznikami, dołączono oświadczenia wszystkich autorów o swoim wkładzie w ich powstanie.

## **2. Zarys treści publikacji**

### **2.1. Publikacja nr I**

Celem artykułu nr I był przegląd dotychczasowych badań, w których BSP i metodę SfM wykorzystano w geomorfologii glacialnej. W pierwszym kroku, zebraną literaturę uporządkowano pod kątem zastosowania danych obrazowych z BSP, wyznaczając cztery typy badań: kartowanie geomorfologiczne (ang. *geomorphological mapping*), analiza dynamiki rzeźby terenu (ang. *change detection*), badania nad procesami morfogenetycznymi (ang. *process-form studies*) oraz badania osadów powierzchniowych (ang. *assessment of surficial geology*). Przeanalizowano również sposób pozyskiwania danych, wykorzystany sprzęt oraz obszary badawcze. Dodatkowo, wskazano potencjalne przyszłe kierunki badań, dzięki którym możliwe będzie np. jeszcze lepsze zrozumienie zmian zachodzących na przedpolach lodowców w reakcji na globalne ocieplenie.

Przeanalizowano łącznie 62 publikacje z lat 2013–2020, opublikowane w czasopismach indeksowanych w JRC (ang. *Journal Citations Reports*). Pierwszym wynikiem przeprowadzonej kwerendy literatury była informacja o lokalizacji badań – przeważały prace przedstawiające wyniki badań prowadzonych w Arktyce (30 artykułów), w szczególności na Spitsbergenie (13 artykułów), Grenlandii (7 artykułów) oraz Islandii (6 artykułów). Drugim często badanym regionem były Alpy (15 artykułów, z których 3 dotyczyły lodowca Forni). Szczegóły, w tym graficzna prezentacja regionów badań, zostały przedstawione na rycinie nr 1 oraz w tabeli nr 1 (publikacja nr I). Drugim zagadnieniem poruszonym w artykule był udział poszczególnych typów badań. Zestawienie zdominowały publikacje, w liczbie 60, dotyczące kartowania geomorfologicznego oraz analizy dynamiki rzeźby terenu. Uzupełnienie stanowiły pojedyncze artykuły z zakresu badań nad procesami morfogenetycznymi oraz badań osadów powierzchniowych (publikacja nr I, Fig. 2). Warto zwrócić uwagę na rosnącą liczbę publikacji w kolejnych latach, z wyjątkiem lat 2017 i 2019. Ze względu na fakt, iż większość prac dotyczyła kartowania pojedynczych form polodowcowych lub zmian ich powierzchni, obszar badań rzadko przekraczał 1 km<sup>2</sup>. Z metodycznego punktu widzenia istotne były informacje dotyczące wykorzystanego typu BSP: wielowirnikowca (ang. *multirotor*) lub płatowca

(ang. *wing*). Charakterystyczne dla ogólnych tendencji było częstsze użycie płatowców w początkowym okresie analizy (lata 2013–2015), co w kolejnych latach zmieniło się na rzecz wielowirnikowców. Odnotowano również zastosowanie w badaniach platform hybrydowych, konstrukcyjnie łączących oba wcześniej wspomniane typy BSP. W 51 publikacjach autorzy zadeklarowali wykorzystanie oprogramowania firmy Agisoft LLC. W kolejnych podpunktach artykułu opisano zastosowane sensory, otrzymaną rozdzielczość przestrzenną produktów fotogrametrycznych, charakterystykę i ustawienia dotyczące nalotów oraz napotymane problemy techniczne związane z odbywaniem misji. Szczegóły dotyczące badań opisanych we wszystkich analizowanych publikacjach zebrano w formie bazy danych jako suplement do artykułu (publikacja nr I, Appendix A.) w formacie Excel, oraz dodatkowo w formatach kml i shp w celu ułatwienia przetwarzania zbioru w oprogramowaniu GIS.

Dodatkowo, wskazano proponowane przez różnych badaczy schematy postępowania związanego z przetwarzaniem zdjęć metodą SfM oraz poruszono problematykę organizacji nalotów fotogrametrycznych, fotopunktów czy rekomendacji dot. publikowania wyników badań z użyciem BSP i metody SfM. Z kolei w ostatniej części publikacji zasygnalizowano potencjalną problematykę przyszłych badań: studia związane z procesami geomorfologicznymi, łączenie fotogrametrii lotniczej z naziemną czy użycie metody SfM do przetwarzania archiwalnych zdjęć lotniczych. Publikacja nr I to pierwszy tak kompleksowy artykuł przeglądowy dla zastosowań BSP w geomorfologii glacialnej.

## 2.2. Publikacja nr II

Wyniki przeprowadzonej kwerendy literatury zwróciły uwagę autorów na znikomą liczbę publikacji opisujących poszczególne etapy przetwarzania zdjęć w oprogramowaniu fotogrametrycznym. Wcześniejsze doświadczenia autorów sugerowały jednak, że ustawienia poszczególnych parametrów przetwarzania i właściwe zarządzanie pozyskanymi danymi mają istotne znaczenie dla dokładności modeli wysokościowych i ortomozaik, a co za tym idzie wiarygodności późniejszych pomiarów. W związku z tym, w kolejnym artykule opublikowanym w otwartym dostępie postawiono za cel poznanie wpływu poszczególnych parametrów obliczeniowych w oprogramowaniu Agisoft Metashape na dokładność dwóch produktów fotogrametrycznych: cyfrowego modelu wysokościowego oraz ortomozaiki. W pierwszej kolejności sformułowano 375 różnych schematów postępowania w oprogramowaniu, które następnie sprawdzono przy przetwarzaniu tego samego zbioru zdjęć przedstawiającego przykładowy obszar proglacialny. Dodatkowo, praktycznym celem badań było wytypowanie trzech schematów postępowania: (a) o najkrótszym czasie obliczeń;

(b) optymalnego, będącego kompromisem między dokładnością a czasem obliczeń;  
(c) możliwie najdokładniejszego, bez względu na czas obliczeń. Wybór oprogramowania Agisoft Metashape do przeprowadzenia analiz związany jest z jego wysoką popularnością, która została udokumentowana w wynikach publikacji nr I.

W eksperymencie przetwarzano zbiór 82 zdjęć przedstawiających zróżnicowaną rzeźbę terenu obszaru proglacialnego lodowca Breiðamerkur, Islandia (publikacja nr II, Fig. 1). Naloty przeprowadzono we wrześniu 2021 roku w trybie autonomicznym przy użyciu BSP marki DJI Phantom 4 Pro. Dla zapewnienia poprawnej georeferencji modelu, założono i wykorzystano w modelowaniu 40 fotopunktów (GCPs – ang. *Ground Control Points*), ustawionych w 4 rzędach po 10 punktów, oddalonych względem siebie o 15 metrów pod kątem 90°. Dodatkowo, w celu sprawdzenia dokładności cyfrowych modeli wysokościowych, założono losowo zlokalizowanych 30 punktów kontrolnych (CPs – ang. *Control Points*), których nie wykorzystano w georeferencji (publikacja nr II, Fig. 4). Pomiaru współrzędnych oraz tyczenia punktów dokonano przy pomocy odbiornika GNSS. Przetwarzanie fotogrametryczne zdjęć przeprowadzono przy użyciu stacji roboczej, której podczas obliczeń nie przydzielano innych zadań, by zachować jednakową moc obliczeniową dla wszystkich projektów.

Przyjęto, że ocenie wpływu na końcową dokładność produktów fotogrametrycznych i czas obliczeń zostaną poddane następujące etapy przetwarzania: (a) szczegółowość procesu łączenia zdjęć; (b) limit punktów charakterystycznych (*key points*) oraz punktów wiążących (*tie points*); (c) szczegółowość procesu generowania gęstej chmury punktów; (d) dobór parametrów optymalizacyjnych. Ostatnim etapem badań było sprawdzenie każdego cyfrowego modelu wysokościowego pod kątem dokładności wysokości, wykorzystując narzędzie Extract Values to Points i współrzędne punktów kontrolnych, by następnie obliczyć odchylenie standardowe (SD – ang. *Standard deviation*) i średnią kwadratową błędów (RMSE – ang. *Root Mean Square Error*). Wyniki eksperymentu dla każdego przyjętego schematu postępowania zamieszczono w suplemencie do artykułu w formie tabeli Excel (publikacja nr II, Appendix S1) i histogramów z rozkładem różnic wysokości między punktami kontrolnymi a cyfrowym modelem wysokościowym (publikacja nr II, Appendix S2).

Spośród 375 testowych schematów postępowania, w 195 nie udało się wygenerować produktów fotogrametrycznych. W 75 nieudanych przypadkach, przy niskiej dokładności generowania punktów wiążących, rzadka chmura punktów okazała się zbyt mało liczna do wygenerowania gęstej chmury punktów. To sugeruje, iż najniższy poziom dokładności generowania rzadkiej chmury punktów jest niewystarczający do obliczenia cyfrowych modeli wysokościowych oraz ortomozaik. Z kolei pozostałe 120 nieudane schematy nie zostały

zoptymalizowane przed wygenerowaniem gęstej chmury punktów parametrami optymalizacyjnymi k1 oraz k2, korygującymi dystorsję radialną zdjęć. Zdaniem autorów, taki stan rzeczy jest spowodowany wysoką dystorsją radialną obiektywu sensora DJI FC6310, z którego zdjęcia należy każdorazowo pod tym kątem korygować. Otrzymane wyniki użyto do krytycznej oceny każdego z badanych etapów przetwarzania w kontekście dokładności otrzymywanych cyfrowych modeli wysokościowych, jak i czasu obliczeń.

Wynikiem przeprowadzonych prac są trzy schematy postępowania: „najszybsze” (*The fastest*); „optymalne” (*Optimal*); „z najwyższą dokładnością” (*Best quality*). Ustawienia w wymienionych schematach wykorzystano do napisania trzech skryptów w języku Python do oprogramowania Agisoft Metashape, które w znaczący sposób ułatwiają pracę i automatyzują wiele procesów. „Najszybszy” skrypt (publikacja nr II, Appendix S3) może być użyty jeszcze w terenie, po odbyciu nalocie i eksporcie zdjęć z BSP do mobilnej stacji roboczej, np. w celu obliczenia rzadkiej chmury punktów i sprawdzenia jej jednorodności, rozkładu punktów i stopnia pokrycia badanego obszaru. Skrypty „optymalny” i „najwyższa jakość” (publikacja nr II, Appendix S4 i S5) mają za zadanie ułatwić przetwarzanie zdjęć po zakończonej pracy terenowej, zależnie od preferencji użytkownika: otrzymanie najniższych możliwych wartości RMSE i SD (skrypt „najwyższa jakość”) lub osiągnięcie kompromisu między dokładnością cyfrowego modelu wysokościowego a czasem obliczeń (skrypt „optymalny”).

### 2.3. Publikacja nr III

Do sprawdzenia użyteczności i powtarzalności opracowanych skryptów, wykorzystano jeden z nich do badań z zakresu analizy dynamiki rzeźby terenu (*change detection*). Celem tego artykułu opublikowanego w otwartym dostępie było zilustrowanie i kwantyfikacja krótkookresowej ewolucji form polodowcowych na przedpolu lodowca Kvíár, Islandia, w oparciu o zbiory zdjęć z BSP z lat 2014, 2016, 2021 i 2022 (publikacja nr III, Fig. 1, 3). Teren ten został wybrany do badań, ponieważ jest bardzo interesującym przykładem krajobrazu utworzonego na skutek kilkakrotnego nasuwania się i stagnacji jezora lodowcowego bogatego w materiał mineralny (ang. *incremental stagnation*) ([Bennett i Evans, 2012](#); [Bennett i in., 2010](#)). Badane przedpole składa się z kompleksów moren, teras kemowych i sandrów, zarówno stabilnych, jak i takich, które są intensywnie przekształcane przez degradację trzonów lodowych i działalność wód roztopowych. Ilościowy model rozwoju takiego krajobrazu nie został wcześniej przedstawiony w literaturze, a jest ważny w kontekście interpretacji paleoglacjologicznych.

Naloty wykonywano dwoma typami BSP: płatowcem (producent SmartPlane) oraz wielowirnikowcami kilku generacji z serii Phantom (producent DJI) (publikacja nr III, Tabela nr 1). Podczas nalogów w 2022 roku, realizowanych przy pomocy wielowirnikowca DJI Phantom 4 RTK, założono lokalną stację referencyjną GNSS w celu zwiększenia dokładności pomiaru współrzędnych środka rzutów zdjęć przy pomocy precyzyjnej techniki pomiaru RTK (ang. *Real Time Kinematic*). Do korekty współrzędnych i zastosowania poprawek PPP (ang. *Precise Point Positioning*) dla zdjęć i fotopunktów użyto oprogramowania Topcon Link oraz RTKLIB, wraz z oszacowaniem wpływu pływów morskich na pomiar. Cyfrowe modele wysokościowe i ortomozaiki opracowano w oprogramowaniu Agisoft Metashape. Ze względu na fakt, iż w 2022 roku dysponowano BSP z odbiornikiem RTK, skorzystano z jednego ze schematów przetwarzania zbiorów zdjęć zaproponowanych przez [Nota i in. \(2022\)](#) – dopasowano jednocześnie zbiory zdjęć z wszystkich lat (ang. *co-alignment*). Fotopunkty nałożono wyłącznie na zdjęcia z roku 2022. Nie korzystano ze współrzędnych środka rzutów zdjęć z pozostałych zbiorów (2014, 2016 i 2021) jako referencji. Wynikiem takiego postępowania była jedna, wspólna rzadka chmura punktów, która następnie została podzielona na cztery chmury w osobnych projektach według lat 2014, 2016, 2021 i 2022, w których pozostawiono jedynie zdjęcia właściwe dla danego roku. Przetwarzanie zbioru przeprowadzono według parametrów schematu postępowania ze skryptu „optymalnego” (publikacja nr II, Appendix S4). Jediną modyfikacją w skrypcie była wyższa dokładność generowania rzadkiej chmury punktów ze względu na częściowe wykorzystanie zdjęć w formacie JPG i niezadowolające wyniki na niskim poziomie. Efektem prac były cztery cyfrowe modele wysokościowe, których rozmiar komórki mieścił się w granicach od 0,05 do 0,08 m. Dodatkowo, wyeksportowano cztery wysokorozdzielcze ortomozaiki o rozmiarze komórki wynoszącej średnio 0,03 m.

Na podstawie opracowanych cyfrowych modeli wysokościowych oraz ortomozaik zdefiniowano cztery obszary zainteresowania na przedpolu lodowca (publikacja nr III, Fig. 2). Obszary te różnią się typem osadów, ukształtowaniem oraz dynamiką i skalą zmian powierzchni terenu. Na podstawie kartowania geomorfologicznego zidentyfikowano cztery zespoły form: terasy kemowej (ang. *kame terrace staircase; case study 1*), sandru (ang. *outwash plain; case study 2*), kompleks pagórków lodowo-morenowych (ang. *ice-cored hummocky moraine complex; case study 3*) oraz pokryty lodem, pagórkowaty teren z nieciągłymi, krętymi grzbietami (ang. *ice-cored hummocky terrain; case study 4*) (publikacja nr III, Fig. 3).

Do oszacowania zmian powierzchni badanych form konieczne było porównanie otrzymanych cyfrowych modeli wysokościowych z różnymi terminów. W tym celu,

do obliczenia plików wynikowych, tzn. cyfrowych modeli różnic wysokości (DoDs – ang. *DEMs of Difference*) oraz zmian objętości, wykorzystano oprogramowanie ArcMap i przeznaczoną dla tego oprogramowania wtyczkę do detekcji zmian Geomorphic Change Detection (GCD) (źródło: <http://gcd.riverscapes.xyz>) (Wheaton i in., 2010). Przed importem cyfrowych modeli wysokościowych do wtyczki dokonano ich przepróbkowania do rozmiaru komórki 0,06 m. Kartowanie badanego obszaru wykonano na podstawie ortomozaik, bezpośrednich badań terenowych i dokumentacji fotograficznej. Dodatkowo, aby sprawdzić, jaki był wpływ dynamiki lodowca na przekształcenia form, wyznaczono położenie czoła lodowca na podstawie serii czasowej (2011–2022) zobrażeń satelitarnych PlanetScope (rozmiar komórki 3,00 m) oraz opracowanych ortomozaik.

Wynikiem badań była dokumentacja zmian czoła lodowca: w latach 2011–2022 zaobserwowano zarówno nasunięcie jak i wycofanie krawędzi lodowca, a jednocześnie zachodziły duże różnice pomiędzy dynamiką północnej i południowej części jeziora lodowcowego (publikacja nr III, Fig. 5). Różnice te interpretowane są odmiennym tempem ablacji (ze względu na zróżnicowanie rozmieszczenia osadów supraglacialnych) oraz inne źródła zasilania obu części lodowca. Warto również odnotować znaczący rozwój jeziora proglacialnego od początku okresu obserwacji i jego powiększającą się powierzchnię. Jednak głównym wynikiem badań jest pomiar zmian powierzchniowych i objętościowych zespołów form (*case study 1–4*) przeprowadzony na podstawie DoDs. Ze względu na różnice w zasięgu przeprowadzanych nalotów BSP, pierwszym rokiem analizy był rok 2014 lub 2016. Do DoDs dołączono profile ilustrujące zmiany dla najbardziej charakterystycznych lokalizacji (publikacja nr III, Fig. 6, 7, 8, 10), a średnie zmiany powierzchniowe, objętościowe i pionowe przedstawiono w tabeli nr 2 (publikacja nr III, Tabela nr 2).

Terasy kemowe i sandr (*case study 1 i 2*) okazały się bardzo stabilne na większości swojej powierzchni. Obszarem o największych zmianach i najwyższej aktywności był kompleks pagórków lodowo-morenowych (*case study 3*). Porównując rok 2014 z 2022, różnice odnotowano na 87% powierzchni badanego obszaru (publikacja nr III, Tabela nr 2). Zmiany wysokości tej formy w ciągu niepełna 8 lat osiągnęły nawet 20 m, co można odczytać z profilu K–L (publikacja nr III, Fig. 8). Co istotne, dynamika była wysoka nawet w jednym roku (DoD 2021–2022), gdy wysokość zmieniła się punktowo aż o 5 m. Ostatni analizowany zespół form (*case study 4*) również okazał się aktywny w badanym okresie. Przekształcenia dotyczyły 76% jego powierzchni (DoD 2016–2022), a profile M–N i O–P wykonano w centralnej, najaktywniejszej części moreny, gdzie widać wyraźnie, że różnice w ukształtowaniu oraz

objętości koncentrują się w pobliżu jeziora (publikacja nr III, Fig. 10). W odległości powyżej 130 m od brzegu jeziora rzeźba terenu była stabilna.

W dalszej części artykułu nr III szerzej opisano uzyskane wyniki, wskazując na prawdopodobne procesy odpowiedzialne za ewolucję rzeźby terenu. Przedstawione zostały wyniki obliczeń średnich rocznych zmian objętości (ang. *average annual volume change*) oraz średnie roczne maksymalne miąższości zmian (ang. *average annual maximum thickness change*) (publikacja nr III, Tabela nr 3 i 5, Fig. 11). Ilościowe rezultaty zostały zestawione z danymi z literatury i przeprowadzonych wcześniej badań w celu porównania otrzymanych wyników z krótkookresową i długookresową dynamiką rzeźby terenu na przedpolach kilkunastu innych lodowców. Szczególną uwagę w dyskusji poświęcono kompleksowi pagórków lodowo-morenowych (*case study 3*) oraz przedstawiono historyczną rekonstrukcję zmian lodowca i przekształceń rzeźby terenu na jego przedpolu (publikacja nr III, Fig. 12). Na koniec odnotowano zauważone ograniczenia metody SfM, opisując komplikacje związane z modelowaniem terenu ze zbiornikami wodnymi (publikacja nr III, Fig. 14).

### **3. Dyskusja**

Z wyników badań wyłania się kilka kluczowych wniosków w kontekście wykorzystania BSP w geomorfologii glacialnej. Pierwszym z nich jest widoczny wzrost powszechności stosowania BSP. Przegląd literatury wykazał, że jest on mobilnym i elastycznym narzędziem, który stanowi realną, tanią alternatywę dla platform lotniczych i satelitarnych. W niskobudżetowych projektach, polegających na cyklicznych obserwacjach z powietrza stosunkowo niewielkich obszarów ( $<1 \text{ km}^2$ ), BSP są trudne do zastąpienia. Producenci BSP oferują coraz to bardziej specjalistyczne konstrukcje stworzone pod konkretne zadania, stąd należy uznać, że obecnie BSP stały się na tyle popularnym narzędziem, iż jego stosowanie w badaniach staje się normą. Ponadto, nowoczesne BSP zostają wyposażone w moduł GNSS RTK, który w połączeniu ze stacją referencyjną pozwala dostarczać zdjęcia z kilkucentymetrowym błędem położenia środka rzutów. Dzięki temu możliwe jest pominięcie procesu zakładania i pomiaru fotopunktów, co zdecydowanie obniża koszty misji i jej czasochłonność. Należy jednak podkreślić, że istotnym ograniczeniem BSP jest jego zasilanie (krótki efektywny czas lotu), jak i podatność na warunki atmosferyczne, co przy wielkoobszarowych obiektach badawczych czy trudnych warunkach meteorologicznych może dyskwalifikować go jako efektywne narzędzie do obrazowania. Dlatego, w niektórych przypadkach tanią alternatywą dla zdjęć z BSP mogą być nawet zdjęcia wykonane z telefonów komórkowych (smartfonów), wyposażonych w nowoczesne kamery, które pozwalają



na dostarczenie wysokorozdzielczych zdjęć wybranych obiektów badawczych (zwłaszcza stromo nachylonych, np. klifów czy wąwozów), zdalnych do szczegółowego modelowania ([Fugazza i in., 2018](#); [Tavani i in., 2020](#)). W ocenie autora, w przyszłych badaniach z wykorzystaniem BSP w geomorfologii glacialnej należy szukać możliwości łączenia danych pozyskanych z BSP z archiwalnymi zdjęciami lotniczymi lub satelitarnymi. Może to zdecydowanie wydłużyć okres obserwacji o kolejne lata wstecz, dzięki czemu w badaniach dotyczących np. procesów geomorfologicznych ([Chandler i in., 2020b](#)) będzie można przeprowadzić rekonstrukcje powstawania wybranej formy z większą pewnością.

Wraz ze wzrostem powszechności użycia BSP w badaniach geomorfologicznych rośnie liczba użytkowników oprogramowania fotogrametrycznego, którzy otrzymane zdjęcia przetwarzają w celu opracowania cyfrowego modelu wysokościowego oraz ortomozaiki. Odbywanie nalogu fotogrametrycznego najczęściej poprzedza szkolenie teoretyczne i praktyczne operatora, wraz z egzaminem weryfikacyjnym sprawdzającym jego wiedzę oraz umiejętności. To pozwala mieć pewność, że operator jest merytorycznie przygotowany do planowania i odbywania misji – dostępna literatura szczegółowo opisuje ten etap prac. Wspomniane we wstępie rozprawy braki w wiedzy związane z etapem przetwarzania zdjęć w oprogramowaniu fotogrametrycznym, zidentyfikowane w 2019 roku podczas planowania badań do niniejszej rozprawy, na przestrzeni ostatnich trzech lat są w ocenie autora sukcesywnie uzupełniane ([de Haas i in., 2021](#); [Nota i in., 2022](#); [Śledź i Ewertowski, 2022](#); [Wang i in., 2021](#)). Wkładem publikacji nr II w uzupełnienie wiedzy o przetwarzaniu są wyniki dotyczące parametrów optymalizacyjnych i zaproponowane skrypty do efektywniejszej pracy ze zbiorami zdjęć. Zastosowanie skryptów, zamiast ręcznego wybierania właściwych ustawień, będzie szczególnie pomocne podczas jednoczesnego przetwarzania wielu projektów w klastrze obliczeniowym, wpływając pozytywnie na efektywność jego wykorzystania. Ta użyteczność będzie kluczowa dla wieloletnich, cyklicznych analiz tych samych obszarów badawczych (np. przedpoli lodowców), gdyż zapewnia stały i porównywalny schemat postępowania, skróci czas przeznaczony na obliczenia i przygotowywania projektów oraz uwiarygodni porównywanie modeli między sobą, np. w badaniach geomorfologicznych z zakresu analizy zmian objętości. Warto w tym miejscu zwrócić uwagę na czas obliczeń w relacji do wielkości błędów, gdyż zmiana parametrów obliczeniowych w celu opracowania dokładniejszego cyfrowego modelu wysokościowego może okazać się niewspółmierna do czasu obliczeń, a co za tym idzie ponoszonych kosztów pracy stacji roboczej. Skrypty są dostępne za darmo dla każdego zainteresowanego na stronie czasopisma. Obserwując obecne trendy można wnioskować, że w przyszłości badania skoncentrują się na optymalizacji przetwarzania danych

z BSP z wykorzystaniem algorytmów sztucznej inteligencji. W najnowszej literaturze można znaleźć przykłady ich stosowania do generowania chmury punktów i cyfrowego modelu wysokościowego oraz klasyfikacji punktów ([Feng i in., 2023](#); [Maiwald i in., 2023](#)).

W publikacji nr III skorzystano z powodzeniem ze skryptu (publikacja II, Appendix S4) do przetwarzania zbioru zdjęć z czterech lat obserwacji (rok 2014, 2016, 2021 i 2022). Skrypt pozwolił na zautomatyzowanie prawie wszystkich etapów obliczeń, pozostawiając użytkownikowi jedynie manualny import zdjęć do oprogramowania i zaznaczenie fotopunktów na zdjęciach. Do tego zwiększył wykorzystanie klastra obliczeniowego, który przy manualnym zarządzaniu po każdym zakończonym etapie obliczeń pozostałby bezczynny do momentu ręcznego uruchomienia kolejnego etapu. Z użyciem skryptu obliczenia wykonują się automatycznie i zgodnie z harmonogramem, wraz z eksportem cyfrowego modelu wysokościowego i ortomozaiki do wybranego formatu, co pozwala użytkownikowi zaoszczędzić czas i daje możliwość przeznaczyć go na inne czynności badawcze. Propozycja [Nota i in. \(2022\)](#) dotycząca schematu przetwarzania danych ze zbiorem zdjęć pozyskanym przy pomocy odbiornika RTK okazała się skuteczna i dała zadowalające wyniki, w efekcie dostarczając właściwie obliczone DoDs. Realizując cele publikacji autorzy zwrócili uwagę na problemy związane z modelowaniem powierzchni wody – jest ona szczególnie ważna na dynamicznie zmieniających się przedpolach lodowców, zawierających znaczne ilości szybko wytapiającego się martwego lodu. W literaturze znane są przykłady udanego modelowania terenów podwodnych na podstawie wyznaczonych punktów znajdujących się pod wodą w płytkich, przezroczystych zbiornikach ([Carrivick i Smith, 2019](#)), jednak algorytm i metoda SfM jest nieskuteczna w przypadku zmętnionej wody bądź występowania w niej zawiesiny ([Tomczyk i Ewertowski, 2021](#)). Przypadek ten dotyczył jeziora proglacialnego na analizowanym obszarze, którego powierzchnia wody została początkowo błędnie zrekonstruowana w modelu. Aby ograniczyć wpływ tych artefaktów na dalsze obliczenia, zreklasyfikowano i usunięto mało wiarygodne punkty charakterystyczne występujące w granicach zbiornika. Dodatkowo, granice obszarów zainteresowania (*case study 1–4*) wytyczono w taki sposób, by nie zawierały terenów pokrytych przez wodę (publikacja nr III, Fig. 14a). Interesującym przykładem wskazującym na konieczność terenowej walidacji danych teledetekcyjnych i ciągłego weryfikowania wyników analiz jest modelowanie przez algorytm mniejszych, przezroczystych zbiorników, które nie w każdym przypadku zostały w odpowiedni sposób zrekonstruowane (publikacja nr III, Fig. 14b). Przykładowo, w *case study 2* (sandr) w latach 2021–2022 zanotowano wzrost objętości tej formy o 192 m<sup>3</sup>, jednak analiza

ortomozaiki wykazała, że wzrost wysokości nie był związany ze zmianą ukształtowania terenu, ale z wodą, która z biegiem czasu wypełniła zagłębienie (publikacja nr III, Fig. 14c).

#### **4. Podsumowanie**

Przeprowadzona kwerenda literatury pozwala stwierdzić, że wykorzystanie BSP w badaniach glacialnych stało się rzeczą powszechną, normą. Naukowcy wybierają różnego typu platformy do pozyskania wysokorozdzielczych zdjęć, które następnie są przetwarzane w oprogramowaniu fotogrametrycznym przy pomocy metody Structure-from-Motion do opracowania cyfrowego modelu wysokościowego oraz ortomozaiki. Wymienione produkty fotogrametryczne są szeroko stosowane w badaniach geomorfologicznych, szczególnie w badaniach dotyczących dynamiki wybranych form polodowcowych czy kartowania przedpola lodowców. Występująca luka badawcza w postaci niedostatecznej wiedzy o wpływie parametrów obliczeniowych w oprogramowaniu fotogrametrycznym na dokładność cyfrowych modeli wysokościowych i ortomozaik została przez autora uzupełniona w postaci wyników przeprowadzonego eksperymentu. Na ich podstawie wyznaczono trzy schematy postępowania w zależności od żądanych efektów, które opublikowano w formie skryptów w języku Python w otwartym dostępie. Użyteczność skryptów potwierdzono analizując serię czasową zdjęć dla przedpola jednego z lodowców na Islandii, znacząco przyspieszając cały proces obliczeń oraz zwiększając efektywność wykorzystania wielowątkowego klastra obliczeniowego.

Postępujący rozwój technologii związany z BSP już obecnie pozwala na rezygnację ze stosowania fotopunktów, co wraz ze spadkiem cen platform oferujących technikę RTK powinno stać się w kolejnych latach powszechnym schematem postępowania obniżającym koszty nalotów. W ocenie autora, przyszłym kierunkiem badań z zakresu optymalizacji przetwarzania zdjęć metodą SfM powinno być użycie algorytmów sztucznej inteligencji, które mogą jeszcze bardziej skrócić czas obliczeń, jak i zapewnić lepszą kontrolę nad coraz to dokładniejszymi i liczniejszymi zbiorami zdjęć z BSP. Najnowsze publikacje wskazują na użyteczność algorytmów sztucznej inteligencji w georeferencji archiwalnych zdjęć lotniczych na podstawie aktualnych danych z BSP, co wpisuje się w prognozę autorów publikacji nr I o tym kierunku badań jako przyszłościowym i wartym analiz.

## Bibliografia

- Agisoft. (2022). *Agisoft Metashape User Manual Professional Edition, Version 1.8*.  
[https://www.agisoft.com/pdf/metashape-pro\\_1\\_8\\_en.pdf](https://www.agisoft.com/pdf/metashape-pro_1_8_en.pdf)
- Allaart, L., Friis, N., Ingólfsson, Ó., Håkansson, L., Noormets, R., Farnsworth, W. R., Mertes, J., & Schomacker, A. (2018). Drumlins in the Nordenskiöldbreen forefield, Svalbard. *Gff*, 140(2), 170-188. <https://doi.org/10.1080/11035897.2018.1466832>
- Anderson, K., & Gaston, K. J. (2013). Lightweight unmanned aerial vehicles will revolutionize spatial ecology. *Frontiers in Ecology and the Environment*, 11(3), 138-146.  
<https://doi.org/10.1890/120150>
- Bennett, G. L., & Evans, D. J. A. (2012). Glacier retreat and landform production on an overdeepened glacier foreland: the debris-charged glacial landsystem at Kvíárjökull, Iceland. *Earth Surface Processes and Landforms*, 37(15), 1584-1602. <https://doi.org/10.1002/esp.3259>
- Bennett, G. L., Evans, D. J. A., Carbonneau, P., & Twigg, D. R. (2010). Evolution of a debris-charged glacier landsystem, Kvíárjökull, Iceland. *Journal of Maps*, 6(1), 40-67.  
<https://doi.org/10.4113/jom.2010.1114>
- Bhardwaj, A., Sam, L., Akanksha, Martín-Torres, F. J., & Kumar, R. (2016). UAVs as remote sensing platform in glaciology: Present applications and future prospects. *Remote Sensing of Environment*, 175, 196-204. <https://doi.org/10.1016/j.rse.2015.12.029>
- Carbonneau, P. E., & Dietrich, J. T. (2017). Cost-effective non-metric photogrammetry from consumer-grade sUAS: implications for direct georeferencing of structure from motion photogrammetry. *Earth Surface Processes and Landforms*, 42(3), 473-486.  
<https://doi.org/10.1002/esp.4012>
- Carrivick, J. L., & Smith, M. W. (2019). Fluvial and aquatic applications of Structure from Motion photogrammetry and unmanned aerial vehicle/drone technology. *WIREs Water*, 6(1), e1328.  
<https://doi.org/https://doi.org/10.1002/wat2.1328>
- Chandler, B. M. P., Evans, D. J. A., Chandler, S. J. P., Ewertowski, M. W., Lovell, H., Roberts, D. H., Schaefer, M., & Tomczyk, A. M. (2020a). The glacial landsystem of Fjallsjökull, Iceland: Spatial and temporal evolution of process-form regimes at an active temperate glacier. *Geomorphology*, 361. <https://doi.org/10.1016/j.geomorph.2020.107192>
- Chandler, B. M. P., Evans, D. J. A., Chandler, S. J. P., Ewertowski, M. W., Lovell, H., Roberts, D. H., Schaefer, M., & Tomczyk, A. M. (2020b). Sub-annual moraine formation at an active temperate Icelandic glacier. *Earth Surface Processes and Landforms*, 45(7), 1622-1643.  
<https://doi.org/10.1002/esp.4835>
- Colomina, I., & Molina, P. (2014). Unmanned aerial systems for photogrammetry and remote sensing: A review. *ISPRS Journal of Photogrammetry and Remote Sensing*, 92, 79-97.  
<https://doi.org/10.1016/j.isprsjprs.2014.02.013>

- Dąbski, M., Zmarz, A., Rodzewicz, M., Korczak-Abshire, M., Karsznia, I., Lach, K., Rachlewicz, G., & Chwedorzewska, K. (2020). Mapping Glacier Forelands Based on UAV BVLOS Operation in Antarctica. *Remote Sensing*, 12(4). <https://doi.org/10.3390/rs12040630>
- de Haas, T., Nijland, W., McArdeell, B. W., & Kalthof, M. W. M. L. (2021). Case Report: Optimization of Topographic Change Detection With UAV Structure-From-Motion Photogrammetry Through Survey Co-Alignment. *Frontiers in Remote Sensing*, 2. <https://doi.org/10.3389/frsen.2021.626810>
- Ewertowski, M. W., & Tomczyk, A. M. (2020). Reactivation of temporarily stabilized ice-cored moraines in front of polythermal glaciers: Gravitational mass movements as the most important geomorphological agents for the redistribution of sediments (a case study from Ebbabreen and Ragnarbreen, Svalbard). *Geomorphology*, 350. <https://doi.org/10.1016/j.geomorph.2019.106952>
- Ewertowski, M. W., Tomczyk, A. M., Evans, D. J. A., Roberts, D. H., & Ewertowski, W. (2019). Operational Framework for Rapid, Very-high Resolution Mapping of Glacial Geomorphology Using Low-cost Unmanned Aerial Vehicles and Structure-from-Motion Approach. *Remote Sensing*, 11(1). <https://doi.org/10.3390/rs11010065>
- Feng, Y., Leung, K. L., Li, Y., & Wong, K. L. (2023). An AI-Based Workflow for Fast Registration of UAV-Produced 3D Point Clouds. *Remote Sensing*, 15(21). <https://doi.org/10.3390/rs15215163>
- Fugazza, D., Scaioni, M., Corti, M., D'Agata, C., Azzoni, R. S., Cernuschi, M., Smiraglia, C., & Diolaiuti, G. A. (2018). Combination of UAV and terrestrial photogrammetry to assess rapid glacier evolution and map glacier hazards. *Natural Hazards and Earth System Sciences*, 18(4), 1055-1071. <https://doi.org/10.5194/nhess-18-1055-2018>
- Gaffey, C., & Bhardwaj, A. (2020). Applications of Unmanned Aerial Vehicles in Cryosphere: Latest Advances and Prospects. *Remote Sensing*, 12(6). <https://doi.org/10.3390/rs12060948>
- Hendrickx, H., Vivero, S., De Cock, L., De Wit, B., De Maeyer, P., Lambiel, C., Delaloye, R., Nyssen, J., & Frankl, A. (2018). The reproducibility of SfM algorithms to produce detailed Digital Surface Models: the example of PhotoScan applied to a high-alpine rock glacier. *Remote Sensing Letters*, 10(1), 11-20. <https://doi.org/10.1080/2150704x.2018.1519641>
- James, M. R., Chandler, J. H., Eltner, A., Fraser, C., Miller, P. E., Mills, J. P., Noble, T., Robson, S., & Lane, S. N. (2019). Guidelines on the use of structure-from-motion photogrammetry in geomorphic research. *Earth Surface Processes and Landforms*, 44(10), 2081-2084. <https://doi.org/10.1002/esp.4637>
- Kociuba, W. (2017). Assessment of sediment sources throughout the proglacial area of a small Arctic catchment based on high-resolution digital elevation models. *Geomorphology*, 287, 73-89. <https://doi.org/10.1016/j.geomorph.2016.09.011>

- Maiwald, F., Feurer, D., & Eltner, A. (2023). Solving photogrammetric cold cases using AI-based image matching: New potential for monitoring the past with historical aerial images. *ISPRS Journal of Photogrammetry and Remote Sensing*, 206, 184-200.  
<https://doi.org/10.1016/j.isprsjprs.2023.11.008>
- Manfreda, S., McCabe, M., Miller, P., Lucas, R., Pajuelo Madrigal, V., Mallinis, G., Ben Dor, E., Helman, D., Estes, L., Ciraolo, G., Müllerová, J., Tauro, F., de Lima, M., de Lima, J., Maltese, A., Frances, F., Caylor, K., Kohv, M., Perks, M., . . . Toth, B. (2018). On the Use of Unmanned Aerial Systems for Environmental Monitoring. *Remote Sensing*, 10(4).  
<https://doi.org/10.3390/rs10040641>
- Mosbrucker, A. R., Major, J. J., Spicer, K. R., & Pitlick, J. (2017). Camera system considerations for geomorphic applications of SfM photogrammetry. *Earth Surface Processes and Landforms*, 42(6), 969-986. <https://doi.org/10.1002/esp.4066>
- Nota, E. W., Nijland, W., & de Haas, T. (2022). Improving UAV-SfM time-series accuracy by co-alignment and contributions of ground control or RTK positioning. *International Journal of Applied Earth Observation and Geoinformation*, 109.  
<https://doi.org/10.1016/j.jag.2022.102772>
- Storrar, R. D., Ewertowski, M., Tomczyk, A. M., Barr, I. D., Livingstone, S. J., Ruffell, A., Stoker, B. J., & Evans, D. J. A. (2019). Equifinality and preservation potential of complex eskers. *Boreas*, 49(1), 211-231. <https://doi.org/10.1111/bor.12414>
- Śledź, S., & Ewertowski, M. W. (2022). Evaluation of the Influence of Processing Parameters in Structure-from-Motion Software on the Quality of Digital Elevation Models and Orthomosaics in the Context of Studies on Earth Surface Dynamics. *Remote Sensing*, 14(6).  
<https://doi.org/10.3390/rs14061312>
- Śledź, S., Ewertowski, M. W., & Evans, D. J. A. (2023). Quantification of short-term transformations of proglacial landforms in a temperate, debris-charged glacial landsystem, Kvíárjökull, Iceland. *Land Degradation & Development*, 34(17), 5566-5590.  
<https://doi.org/10.1002/ldr.4865>
- Śledź, S., Ewertowski, M. W., & Piekarczyk, J. (2021). Applications of unmanned aerial vehicle (UAV) surveys and Structure from Motion photogrammetry in glacial and periglacial geomorphology. *Geomorphology*, 378. <https://doi.org/10.1016/j.geomorph.2021.107620>
- Tavani, S., Granado, P., Riccardi, U., Seers, T., & Corradetti, A. (2020). Terrestrial SfM-MVS photogrammetry from smartphone sensors. *Geomorphology*, 367.  
<https://doi.org/10.1016/j.geomorph.2020.107318>
- Tomczyk, A. M., & Ewertowski, M. W. (2021). Baseline data for monitoring geomorphological effects of glacier lake outburst flood: a very-high-resolution image and GIS datasets of the distal part of the Zackenberg River, northeast Greenland. *Earth System Science Data*, 13(11), 5293-5309. <https://doi.org/10.5194/essd-13-5293-2021>

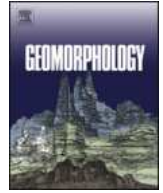
- Tomczyk, A. M., Ewertowski, M. W., & Carrivick, J. L. (2020). Geomorphological impacts of a glacier lake outburst flood in the high arctic Zackenberg River, NE Greenland. *Journal of Hydrology*, 591. <https://doi.org/10.1016/j.jhydrol.2020.125300>
- Wang, H., Duan, Y., Shi, Y., Kato, Y., Ninomiya, S., & Guo, W. (2021). EasyIDP: A Python Package for Intermediate Data Processing in UAV-Based Plant Phenotyping. *Remote Sensing*, 13(13). <https://doi.org/10.3390/rs13132622>
- Westoby, M. J., Brasington, J., Glasser, N. F., Hambrey, M. J., & Reynolds, J. M. (2012). 'Structure-from-Motion' photogrammetry: A low-cost, effective tool for geoscience applications. *Geomorphology*, 179, 300-314. <https://doi.org/10.1016/j.geomorph.2012.08.021>
- Westoby, M. J., Dunning, S. A., Woodward, J., Hein, A. S., Marrero, S. M., Winter, K., & Sugden, D. E. (2015). Sedimentological characterization of Antarctic moraines using UAVs and Structure-from-Motion photogrammetry. *Journal of Glaciology*, 61(230), 1088-1102. <https://doi.org/10.3189/2015JoG15J086>
- Westoby, M. J., Rounce, D. R., Shaw, T. E., Fyffe, C. L., Moore, P. L., Stewart, R. L., & Brock, B. W. (2020). Geomorphological evolution of a debris-covered glacier surface. *Earth Surface Processes and Landforms*, 45(14), 3431-3448. <https://doi.org/10.1002/esp.4973>
- Wheaton, J. M., Brasington, J., Darby, S. E., & Sear, D. A. (2010). Accounting for uncertainty in DEMs from repeat topographic surveys: improved sediment budgets. *Earth Surface Processes and Landforms*, 35(2), 136-156. <https://doi.org/10.1002/esp.1886>
- Whitehead, K., Moorman, B. J., & Hugenholtz, C. H. (2013). Brief Communication: Low-cost, on-demand aerial photogrammetry for glaciological measurement. *The Cryosphere*, 7(6), 1879-1884. <https://doi.org/10.5194/tc-7-1879-2013>

### **Publikacja nr I z załącznikiem**

Śledź, S., Ewertowski, M. W., & Piekarczyk, J. (2021). Applications of unmanned aerial vehicle (UAV) surveys and Structure from Motion photogrammetry in glacial and periglacial geomorphology. *Geomorphology*, 378. <https://doi.org/10.1016/j.geomorph.2021.107620>

Do publikacji dołączono załącznik (Appendix A.) – bazę danych dot. badań z zakresu geomorfologii glacialnej z wykorzystaniem bezzałogowych statków powietrznych.





## Applications of unmanned aerial vehicle (UAV) surveys and Structure from Motion photogrammetry in glacial and periglacial geomorphology

Szymon Śledź\*, Marek W. Ewertowski, Jan Piekarczyk

Faculty of Geographical and Geological Sciences, Adam Mickiewicz University, Krygowskiego 10, 61-680 Poznań, Poland

### ARTICLE INFO

#### Article history:

Received 10 December 2020  
 Received in revised form 13 January 2021  
 Accepted 14 January 2021  
 Available online 19 January 2021

#### Keywords:

Glacial geomorphology  
 Paraglacial geomorphology  
 Unmanned aerial vehicle  
 Mapping  
 Drone  
 Change detection

### ABSTRACT

Unmanned aerial vehicles (UAVs, UAS, drones) combined with Structure-from-Motion (SfM) photogrammetry have emerged over the last decade as the basis for a very efficient workflow in glacial and periglacial geomorphology by filling the spatial gap between traditional ground-based surveys and aerial or satellite remote sensing data. UAV-generated data offer flexible spatial and temporal resolution, thus enabling a shift from a pure description of geomorphological forms to a better understanding of process-form relationships, e.g., by quantification of short-term landscape changes in response to various drivers. In this contribution, we present an overview of current applications of UAV-SfM in studies of modern and past glacial environments that include mostly geomorphological mapping and change-detection analysis. We also indicate potential future applications, e.g., by combining UAV-data with historical archives, terrestrial SfM, and crowd-based image gathering to allow for a better understanding of landscape changes in response to present climate warming.

© 2021 Elsevier B.V. All rights reserved.

### Contents

|      |  |    |
|------|--|----|
| 1.   | Introduction . . . . .   | 2  |
| 2.   | Review of previous studies . . . . .   | 2  |
| 2.1. | Region of study . . . . .  | 4  |
| 2.2. | Types of study . . . . .   | 4  |
| 2.3. | Size of the studied area . . . . .   | 5  |
| 2.4. | Type of UAV used . . . . .   | 6  |
| 2.5. | Type of sensor . . . . .   | 6  |
| 2.6. | Spatial resolution . . . . .   | 7  |
| 2.7. | Mission design and performance . . . . .   | 7  |
| 2.8. | Problems encountered . . . . .   | 7  |
| 3.   | Overviews of current UAV applications in glacial and periglacial geomorphology . . . . . | 7  |
| 3.1. | Geomorphological mapping . . . . .   | 7  |
| 3.2. | Change detection . . . . .   | 8  |
| 3.3. | Process-form studies . . . . .   | 10 |
| 3.4. | Mapping of surficial geology . . . . .   | 10 |
| 3.5. | Existing workflows for UAV-SfM in glacial geomorphology . . . . .                        | 10 |
| 4.   | Potential future applications . . . . .  | 10 |
| 4.1. | Investigation of geomorphological processes . . . . .                                    | 11 |
| 4.2. | Combination of UAV and terrestrial photogrammetry . . . . .                              | 11 |
| 4.3. | SfM processing of archival images . . . . .  | 11 |
| 4.4. | Use of crowd-sourced images . . . . .  | 11 |
| 5.   | Conclusions . . . . .  | 11 |

\* Corresponding author at: Krygowskiego 10, 61-680 Poznań, Poland.  
 E-mail address: [szyszle@amu.edu.pl](mailto:szyszle@amu.edu.pl) (S. Śledź).

|   |    |
|---|----|
| Declaration of competing interest . . . . . | 12 |
| Acknowledgements . . . . .                  | 12 |
| Appendix A. Supplementary data . . . . .    | 12 |
| References . . . . .                        | 12 |

## 1. Introduction

Glacial geomorphology focuses on landforms developed as a result of processes related to glacier activity (Benn and Evans, 2010). Studying glacier-related landforms is important, as the areas affected by Quaternary glaciations encompass almost 1/3 of the Earth's surface, and various human activities (agriculture, construction, tourism) occur in terrains deglaciated after the end of the last glacial maximum, so a detailed knowledge of glacial sediments and landforms would be essential from an engineering standpoint (Evans, 2017). Moreover, sediments and landforms on deglaciated terrains can be used for reconstruction of the character of former glaciers and ice sheets, which is crucial to understanding their response to environmental changes. Studying glacial geomorphology concerning modern glaciers is also essential since proglacial landscapes are one of the most dynamic landscapes on Earth. Their transformations are important as they are a potential source of sediments and meltwater (from dead ice), which can affect sediment delivery to valleys and oceans and potentially be hazardous to life and infrastructure (e.g., by the initiation of such processes like debris flows or glacier lake outburst floods). Hazards are also associated with transformations of another element of the cryosphere – permafrost. High-dynamics of glacial and periglacial landscapes require the use of high-frequency monitoring tools. In the last decade, significant progress in mapping ability has been achieved, especially in the context of mapping and monitoring of relatively small areas characterized by high dynamics, due to the emergence of unmanned aerial vehicles (UAV) and Structure from Motion (SfM) technologies that make it possible to develop cm-scale orthomosaics and digital elevation models (DEMs), therefore offering an exceptional tool for detailed, on-demand mapping.

The unmanned aerial vehicle (UAV), also known as Unmanned Aerial System (UAS), Remotely Piloted Aerial System (RPAS), aerial robot or more popularly as “drone” (Colomina and Molina, 2014), is an example of a tool that, as a platform for mounting of a selected sensor (e.g. RGB, multispectral, or thermal imaging camera), enables the operator to execute the remote acquisition of data on a point or area without direct contact with it. The advent of UAV technology dates to the years of the Cold War when UAVs were designed for military purposes. In the late 1990s, the first UAVs were constructed for scientific purposes, where they were used to monitor, for instance, vegetation (Watts et al., 2012). The first publications describing the use of UAVs in scientific research highlighted their high efficiency in obtaining data, and Anderson and Gaston (2013) even heralded a revolution in environmental research thanks to the novel UAV technology. The great potential of UAVs in remote sensing research results from the flexible (and potentially very high) temporal resolution combined with a very high spatial resolution of the acquired imagery. An additional advantage of UAVs is the ability to choose surveys date and scope of research in accordance with the need of particular research group (e.g., allowing for on-demand surveys in case of occurrence of extreme events). Therefore, in the case of small study areas, UAV surveys are more economical and provide a more detailed alternative to high-resolution satellite imagery, which, despite the recent increase in spatial resolution and temporal coverage, is still not characterized by such high flexibility (Manfreda et al., 2018).

Glacial geomorphology has had a long tradition in the use of remote sensing data such as aerial photographs, satellite imagery and LIDAR (Light Detection And Ranging) surveys (cf., Benn and Evans, 2010; Mancini et al., 2013; Ely et al., 2017; Chandler et al., 2018), but these are much more expensive than UAV technology (Hackney and

Clayton, 2015; Wigmore and Mark, 2017). Aerial photographs, covering a larger area than those taken by UAVs, are useful for detailed analyses of large areas, but despite the possibility of being able to provide a high spatial resolution, they are not the optimal choice when a high temporal resolution is required (Hackney and Clayton, 2015). Satellite imagery offers high efficiency in imaging large territories and phenomena, but are characterized by a lower spatial resolution (down to 0.3 m) and susceptibility to weather conditions (cloud coverage) (Whitehead et al., 2013) which significantly affects the regularity and quality of the acquired data. Recently, PlanetScope satellite images (1-day revisit) started offering high time resolution data, providing images of the entire globe, but their spatial resolution (3 m) is still much worse than what could be achieved with UAVs. Before the emergence of small UAVs, an increase in the spatial and temporal resolution of remote surveys was attempted using small-format aerial photography obtained from cameras mounted on various platforms like kites, balloons, paragliders (see Aber and Gałazka, 2000; Boike and Yoshikawa, 2003; Aber et al., 2008, 2010).

UAV-generated images need to be processed to be useful for further analyses. The most common workflow utilizes Structure from Motion (SfM) photogrammetry with multi-view stereopsis (MVS) (Westoby et al., 2012; Smith et al., 2015). SfM-MVS combine images taken from different angles and distances to reconstruct the geometry of the scene based on characteristic points appearing in several images classified by the SIFT (Scale Invariant Feature Transform) algorithm (Westoby et al., 2012). As a result, the location of each image is solved, and a sparse point cloud is generated. Then, the dense point cloud is calculated. In the next step, Digital Elevation Model (DEM) and the orthomosaic are produced based on the dense point cloud. It is generally accepted that the SfM method is ideal for high-resolution collections of UAV images because, with its low financial expenditure, large datasets can be processed while the resulting high-resolution products (point cloud, DEM, orthomosaic) can easily be generated (Westoby et al., 2012), providing the basis for future geomorphological analysis.

In this study, we concentrated on the applications of UAVs in glacial and periglacial geomorphology, with particular focus on the description and recognition of landforms and landscapes resultant from the former activity of ice masses. Such studies provide knowledge on depositional and erosional processes and their interaction with ice and climate dynamics (Napieralski et al., 2007). So far, reviews of the use of UAVs in glaciology (Bhardwaj et al., 2016) and cryosphere studies in general (Gaffey and Bhardwaj, 2020) have been presented; however, no comprehensive evaluation of UAV applications in glacial geomorphology has been conducted. Such a review is crucial to providing a recap of current practices and ensuring meaningful compatibility of outputs from future works. The aim of this article is, therefore, to present recent applications of UAV and SfM in the field of glacial and periglacial geomorphology. In addition, potential directions of research development are also indicated (analysis of archival photo collections, integration of aerial and terrestrial photogrammetry, or the acquisition and analysis of image data from crowd-sourcing), by which it may be possible to understand better landscape changes taking place in response to global warming.

## 2. Review of previous studies

This paper reviewed the most relevant publications, which described UAVs' use in studies related to glacial, paraglacial or periglacial geomorphology. The publications were selected from the Web of

**Table 1**

List of selected publications in the field of glacial and periglacial geomorphology using UAV technology in the research. During the literature review, Internet bibliographical databases such as Google Scholar, Web of Science, and Scopus were used. The works included in the table were published before November 30, 2020.

| Region                         | Authors                       | Type of study                   | Key points of the research and/or encountered problems   |
|--------------------------------|-------------------------------|---------------------------------|--|
| <i>Antarctica</i>              |                               |                                 |  |
| Argentine Islands              | Lamsters et al. (2020a)       | Geomorphological mapping        | Mapping of multiple islands in high resolution by using UAV surveys and GNSS measurements  |
| Heritage Range                 | Westoby et al. (2015)         | Assessment of surficial geology | The remote UAV-SfM method used for particle size analysis reduces the workload compared to traditional methods   |
| Kings George Island            | Dąbski et al. (2017)          | Geomorphological mapping        | A comprehensive inventory of periglacial forms in the area of 0.5 km <sup>2</sup> ; 19 types of forms were detected (824 polygons in total)  |
| Kings George Island            | Dabski et al. (2020)          | Geomorphological mapping        | Flights over the forelands of 3 glaciers at the same time; high altitude (500 m above sea level), DEM resolution of only 25 cm   |
| Kings George Island            | Pereira et al. (2020)         | Geomorphological mapping        | Three different computational methods were tested to detect patterned grounds and describe their characteristics   |
| <i>Arctic</i>                  |                               |                                 |  |
| Alaska (USA)                   | Kienholz et al. (2020)        | Change detection                | Long-term observations of the glacier and the deglaciation process and the study of the impact of this process on floods   |
| Bylot Island (Canada)          | Bash and Moorman (2020)       | Change detection                | Observation of the rate of glacier melting   |
| Bylot Island (Canada)          | Whitehead et al. (2013)       | Change detection                | In addition to UAV images, images were also taken from a manned helicopter   |
| Greenland                      | Chudley et al. (2019)         | Geomorphological mapping        | Research without establishing GCP  |
| Greenland                      | Jouvet et al. (2016)          | Change detection                | Combination of UAV and Landsat satellite imagery to observe glacier melting and landscape transformation   |
| Greenland                      | Jouvet et al. (2018)          | Change detection                | Application of the hybrid UAV construction: Firefly6 UAV   |
| Greenland                      | Lamsters et al. (2020b)       | Geomorphological mapping        | Glacier foreground mapping with the use of GPR and UAV   |
| Greenland                      | Ryan et al. (2015)            | Change detection                | An attempt to use UAV-data in geomorphic change detection; due to the problem with GNSS measurements, the altitude of the DEM turned out to be inaccurate  |
| Greenland                      | Tomczyk and Ewertowski (2020) | Geomorphological mapping        | Mapping of the geomorphological effects of glacial lake outburst flood in permafrost terrain, Zackenberg River, NE Greenland   |
| Greenland                      | Tomczyk et al. (2020)         | Change detection                | Quantification of changes in response to glacial lake outburst flood, Zackenberg River. Observations were carried out the day before the flood, during the flood and after the water returned to the average level, and revealed the short-term response of permafrost in riverbanks |
| Iceland                        | Chandler et al. (2016)        | Geomorphological mapping        | Very accurate landform mapping based on UAV images – focus on small recessional moraines   |
| Iceland                        | Chandler et al. (2020a)       | Process-form studies            | The first use of time-series of UAV data to analyse the processes of formation of glacial forms  |
| Iceland                        | Chandler et al. (2020b)       | Change detection                | Comprehensive mapping of glacial landforms; time series of UAV data were used to detect recent changes in the proglacial landscape   |
| Iceland                        | Evans et al. (2016)           | Geomorphological mapping        | The research developed a conceptual model of the spatial and temporal development of glacial formations in the foreland of the Fláajökull  |
| Iceland                        | Hackney and Clayton (2015)    | Geomorphological mapping        | Mapping of glacial forelands using UAV wing construction in manual flight mode   |
| Northwest Territories (Canada) | Van der Sluijs et al. (2018)  | Change detection                | The use of UAVs for the observation of permafrost and its impact on infrastructure   |
| Svalbard                       | Allaart et al. (2018)         | Geomorphological mapping        | The first sedimentological studies of drumlins; apart from UAV images, aerial images were used   |
| Svalbard                       | Bernard et al. (2017)         | Change detection                | Research on the dynamics of moraine formation; problems with weather conditions during flights; ground collapse after heavy rainfall detected by the model of differences  |
| Svalbard                       | Bernard et al. (2018)         | Change detection                | The difference of DEMs between 2010 and 2016 showed noticeable morphological changes in the foreland, e.g., the appearance of new channels   |
| Svalbard                       | Berthling et al. (2020)       | Geomorphological mapping        | Detailed analysis of slopes in two different locations allowed to estimate the erosion rates of the slopes; TLS data, aerial imagery, DSMs, DTMs and UAV data were used  |
| Svalbard                       | Ewertowski and Tomczyk (2020) | Geomorphological mapping        | Investigation of geomorphological agents responsible for the transformation of temporarily stabilised ice-cored moraines in high-Arctic settings   |
| Svalbard                       | Ewertowski et al. (2016)      | Geomorphological mapping        | Mapping of two different parts of Nordenskiöldbreen foreland, UAV data used to map flutes in details   |
| Svalbard                       | Ewertowski et al. (2019)      | Geomorphological mapping        | A detailed description of the workflow for using the UAV-SfM in glacial geomorphology; presented with the example of mapping the Hørbye breen foreland   |
| Svalbard                       | Lousada et al. (2018)         | Geomorphological mapping        | Images taken by UAV revealed 180 polygons out of 268 measured in the field (ice-wedge research)  |
| Svalbard                       | Midgley et al. (2018)         | Change detection                | Quantification of deglaciation of the high-Arctic landscape (Midtre Lovénbreen) over eleven year period  |
| Svalbard                       | Rippin et al. (2015)          | Geomorphological mapping        | A significant correlation between the roughness of the terrain and its reflection when examining snowmelt channels were demonstrated using UAV-generated data  |
| Svalbard                       | Tomczyk et al. (2019)         | Geomorphological mapping        | The analysis of the morphology of the alluvial sediments shows that since 1960 the area of unstable (fresh) fluvial sediments has been systematically increasing   |
| Svalbard                       | Tonkin et al. (2016)          | Change detection                | A conceptual model of moraine evolution was developed based on a combination of different data sources   |
| Svalbard and Iceland           | Storror et al. (2020)         | Geomorphological mapping        | Details of the formation and evolution of two eskers complexes in Spitsbergen and Iceland  |
| <i>Other locations</i>         |                               |                                 |  |
| Alps (Austria)                 | Fey et al. (2017)             | Change detection                | Thanks to numerous data sources, the behaviour of a rockslide after the retreat of the glacier was reconstructed   |
| Alps (Austria)                 | Kaufmann et al. (2018)        | Change detection                | Images were acquired from 5 different UAVs and combined with other archival data sources; presenting changes in the area from 1954 to 2017   |
| Alps (Austria)                 | Seier et al. (2017)           | Change detection                | The ice block collapse was detected within two months, noting a height difference of 31 m between the models   |

(continued on next page)

Table 1 (continued)

| Region                      | Authors                     | Type of study            | Key points of the research and/or encountered problems   |
|-----------------------------|-----------------------------|--------------------------|--|
| Alps (Italy)                | Fey and Krainer (2020)      | Change detection         | Calculation of the velocities of the active rock glacier using UAV data and GNSS measurements  |
| Alps (Italy)                | Fugazza et al. (2015)       | Change detection         | Small-scale classification based on Landsat 8 satellite and UAV images showed a difference in area between the two sources by 1.5%   |
| Alps (Italy)                | Fugazza et al. (2018)       | Geomorphological mapping | Combination of UAV images, ground-based images and TLS data were also used to analyse geo-hazards related to the transformation of glacial landsystem  |
| Alps (Italy)                | Scaioni et al. (2018)       | Change detection         | Identification of large displacement of earth masses over one year period  |
| Alps (Italy)                | Westoby et al. (2020)       | Change detection         | Evolution of a debris-covered glacier surface based on three years of UAV observations   |
| Alps (Switzerland)          | Buhler et al. (2016)        | Change detection         | In addition to RGB images, infrared images were also taken by removing the built-in filter from the APS-CMOS sensor  |
| Alps (Switzerland)          | Eichel et al. (2020)        | Geomorphological mapping | Movements of small boulders by up to 16.5 cm were recorded Between 2014 and 2017   |
| Alps (Switzerland)          | Groos et al. (2019)         | Change detection         | Two last scheduled flights were unsuccessful due to technical problems; own UAV construction   |
| Alps (Switzerland)          | Hendrickx et al. (2020)     | Change detection         | Combination of UAV and TLS data demonstrated that debris flow, snow push phenomena, and rill erosion were the main geomorphological processes operating within high-alpine talus scope         |
| Alps (Switzerland)          | Rossini et al. (2018)       | Change detection         | The fastest melting of the glacier was recorded in the summer season   |
| Alps (Switzerland)          | Storni et al. (2020)        | Change detection         | Observation of rock glacier over a short period; visible displacement of the glacier due to landslide movement   |
| Alps (Switzerland)          | Vivero and Lambiel (2019)   | Change detection         | The destabilised part of the rock glacier mobilised around 27,000 m <sup>3</sup> of material   |
| Altai (Russia)              | Hedding et al. (2020)       | Geomorphological mapping | Investigation of the dynamic retreat of the Aktru glacier and the succession of vegetation onto the glacial foreland   |
| Andes (Chile)               | Wilson et al. (2019)        | Geomorphological mapping | Mapping of geomorphological effects of glacial lake outburst flood in Chileno Valley, Patagonia  |
| Andes (Peru)                | Wigmore and Mark (2017)     | Change detection         | Own UAV construction; due to the low air density, the power of the UAV was only enough for 12 min of flight at an altitude of 5000 m above sea level (25 min at sea level)                     |
| Dartmoor (SW England)       | Mather et al. (2019)        | Geomorphological mapping | Automated mapping of patterned ground using multiple types of data   |
| Făgăraş Mountains (Romania) | Tîrlă et al. (2020)         | Geomorphological mapping | Geomorphological mapping of glaciokarst  |
| Henan Province (China)      | Le Heron et al. (2019)      | Geomorphological mapping | Study of a subglacial landscape carved beneath ice masses in the Shimengou area (Henan Province, China)  |
| Himalaya (Nepal)            | Van Woerkom et al. (2019)   | Change detection         | The reduction of the moraine area (31 cm per year) increases the thickness of the sediment in the study area (max. 8 cm per year)  |
| Himalayas (India)           | Ramsankaran et al. (2020)   | Geomorphological mapping | Use of UAV-generated data to map glacial foreland in the Himalayas; lack of adequate satellite coverage, landing problems, and low air density were mentioned as the most significant problems |
| Himalayas (Nepal)           | Immerzeel et al. (2014)     | Change detection         | The first use of UAVs on a debris-covered glacier in the Himalayas   |
| Himalayas (Nepal)           | Kraaijenbrink et al. (2016) | Change detection         | The rate of rock mass movement turned out to be the highest in summer; the upper part of the glacial tongue shows the greatest movements, the lower part remains stable                        |
| Wales                       | Glasser et al. (2020)       | Geomorphological mapping | Use of UAV data and numerical ice-sheet modelling for the investigation of glacial abrasion in bedrock surfaces  |
| Wales                       | Tonkin et al. (2014)        | Geomorphological mapping | One of the first publications where UAV-SfM approach was used in glacial geomorphological research   |

Sciences, Scopus and Google Scholar databases based on a combination of keywords such as drone, unmanned/uncrewed aerial vehicle/system, UAV/UAS, remotely piloted aircraft system, RPAS, remotely operated aerial vehicle, ROAV, and glacial/periglacial/paraglacial geomorphology/geomorphological. Table 1 presents the list of key papers recorded in the Web of Sciences or Scopus before November 30, 2020, in which UAV component played a significant role and was used with a clear geomorphological context. Information about the research region and type of studies, together with a brief description of the most important findings or particular problems encountered while using UAV are also included (Table 1). In Section 2, we focus on a synthetic description of the analysed articles, while detailed information about each conducted study (including the type of research, coordinates, number of images, type of UAV and sensor, etc.) are presented in the supplementary material (Appendix A), together with a geodatabase to enable the reader to visualise the spatial distribution of the reviewed works.

### 2.1. Region of study

The literature review shows that in the years 2013–2020, there were a total of 62 publications in which the UAV-SfM method was instrumental in providing data related to glacial, paraglacial or periglacial geomorphology, of which 30 studies were carried out in the Arctic region (Fig. 1). Almost half of them were located on Svalbard (13 studies) (Fig. 1B), where the most popular sites were Nordenskiöldbreen, Austre and Midtre Lovénbreen, and Hørbye breen. Studies from Greenland (7 publications, 2 of which about Store and Bowdoin glaciers), Iceland (6 articles, two about Fjallsjökull), Canada (2 publications

about the Fountain glacier on the Bylot Island) and Alaska were also represented.

The second most frequented region for glacial and periglacial geomorphological research using UAVs was the European Alps (15 publications) (Fig. 1C), where the Forni glacier turned out to be the most popular object of study (3 publications). Antarctica was the research site in five studies, three of which concerned King George Island. The areas of the Lirung glacier in the Himalayas were mapped twice (a total of four studies from Himalayas region). The remaining 8 publications concerned individual sites in various regions of the world, e.g., mapping the foreground of the Maliy Aktru glacier in the Altai Mountains (Hedding et al., 2020) or observations of the dynamics of the Llaca glacier foreland in the Cordillera Blanca mountain range (Wigmore and Mark, 2017).

### 2.2. Types of study

A systematic increase in the use of the UAV-SfM method in glacial geomorphological studies can be seen (Fig. 2). The most popular topic was one-time geomorphological mapping (30 papers in total): 21 papers, most of which concerned single landforms or landform assemblages, were related to the mapping of a glacial foreland, and 9 studies were related to mapping periglacial and paraglacial elements of the landscape, such as rock glaciers, alluvial fans, or talus slopes. The same number of publications (30) were related to geomorphic change detection, which was also the subject of one of the first published articles utilizing UAV-SfM technology in the field of glacial geomorphology (2013 and 2014). The use of UAVs for sedimentological studies and research focusing on processes shaping glacial landforms was much less widespread (one

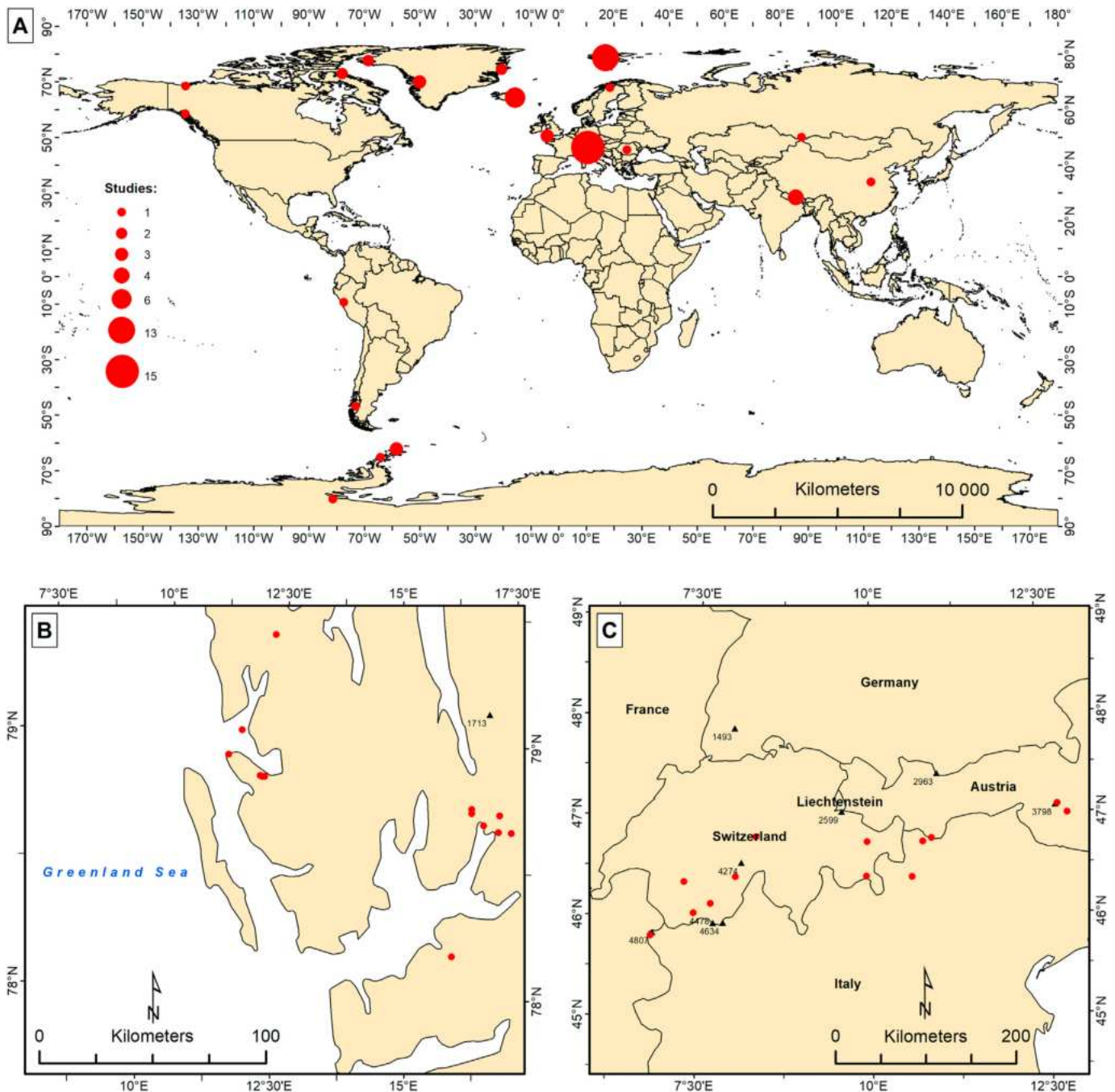


**Fig. 1.** The spatial distribution of publications in the field of glacial and periglacial geomorphology using UAV technology in the research. Part (A) contains a diagram of all research locations, while below are two maps with the location of the research carried out in Spitsbergen (B) and in the Alpine region (C). Locations are for works that were published before November 30, 2020, and listed in Web of Sciences or Scopus. Note, that in some cases, the concentration of publications in a particular region (e.g., Svalbard, Iceland) is associated with the same research group.

publication each). The high number of publications in 2020, which was 22 at the time the article was submitted, shows a significant increase in the popularity of UAVs in recent glacial geomorphological research. It might also reflect the global pandemic situation, which limited the opportunity to go into the field. Instead, many scientists focused on processing and publishing data collected in previous years.

### 2.3. Size of the studied area

The area surveyed by UAV in most publications did not exceed 1 km<sup>2</sup>, because most of the research concerned individual landforms or landform assemblages. The main factors limiting the size of the surveyed areas were the unfavourable meteorological conditions

(wind and precipitation), a limited number of available power packs, the desired spatial resolution and flight altitude necessary to achieve it, high image overlap necessary for proper reconstruction of landform details, and the UAV's weight which impacted the ability to transport the UAV within the study area. Severe restrictions were also related to the limited processing capacity of large datasets, which require high-performance computer hardware. The studied area can be effectively increased, especially using a fixed-wing UAV, as proven, for example, by Dabski et al. (2020), who performed surveys of a total area of 16.8 km<sup>2</sup>. Hence, small, lightweight multi-rotors represent a better solution to observe relatively small areas located far from roads where high mobility is essential, while for large areas, the wing-type construction will be a more effective solution.

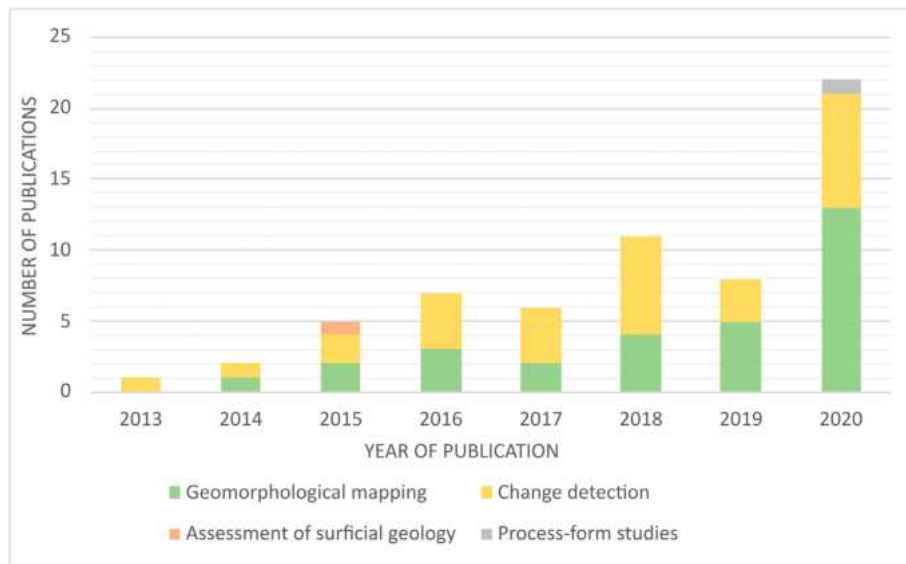


Fig. 2. Themes of works published in the years 2013–2020.

2.4. Type of UAV used

In the first publications from 2013 to 2015, UAVs with a wing design dominated, a multirotor was used only once (during the entire period under study, wing type was selected in 19 publications) (Fig. 3). This fact may be related to the lack of budget multi-rotors on the market, for it was only in 2013 that the Chinese company DJI presented its most popular family of vehicles, the “Phantom”. Its second version, available at the end of 2013, was first used for fieldworks in 2014 (e.g., Evans et al., 2016; Ewertowski et al., 2016; Tomczyk et al., 2019; Ewertowski and Tomczyk, 2020), and since then the use of DJI products in glacial geomorphological research has become dominant (out of 38 publications that used multi-rotors, 32 were produced by DJI). From 2016, the share of multi-rotors in publications began to increase - thanks to their small size, low cost, and easy transport. They become the preferred type of construction, as was evident in their sizable representation in studies published in 2020 (mainly DJI Phantom versions 3 and 4). Among the fixed-wing constructions, the most frequently

chosen UAVs were SenseFly (a subsidiary of the French company Parrot SA) eBee, and SwingletCAM models. In 2016, Jouvét et al. (2018) were the first to use BirdsEyeView’s Firefly6 hybrid construction, which despite the appearance of “wing” has four engines with double propellers, eliminating the disadvantages of the classic wing constructions such as the lack of vertical take-off and landing.

2.5. Type of sensor

RGB images from low altitude were used in all reviewed publications. Due to the type of gimbal used and the limited load capacity, budget multi-rotors limit sensor selection and modification. Therefore, in all publications that used the popular DJI Phantom models, images were taken with a built-in RGB sensor having a sensor of 12 to 20 MPx (depending on the specific UAV model). Larger constructions, such as the DJI S800 hexacopter or the Skywalker X8 wing, made it possible to mount a higher-class digital camera, which significantly improves the quality of images compared to built-in solutions. The most popular

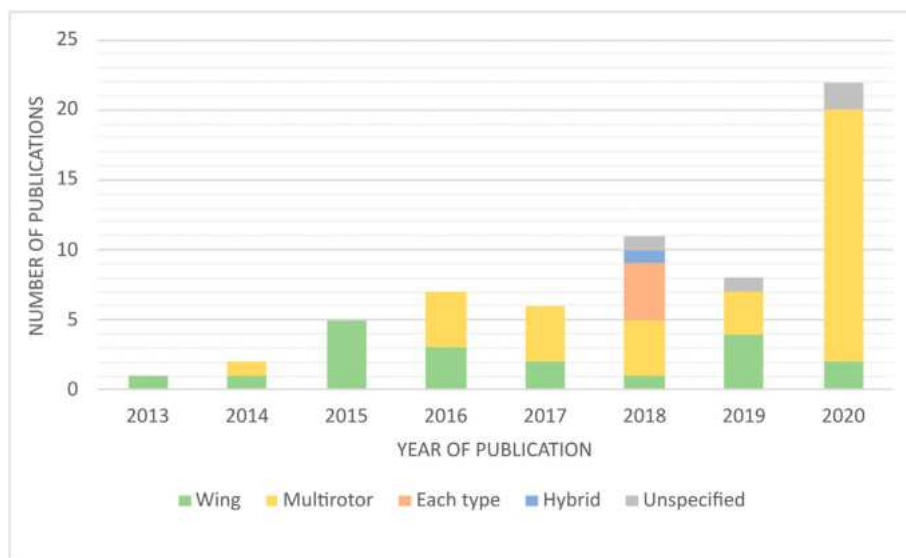


Fig. 3. Types of UAVs used in studies from the years 2013–2020.

cameras were Canon EOS-M, Sony α6000, and Panasonic Lumix. In some studies, UAV-generated RGB optical data were supplemented by multispectral data and point clouds from the terrestrial laser scanning (TLS), or from satellite or airborne altitude.

## 2.6. Spatial resolution

The most significant advantage of using UAV in glacial geomorphology studies is the ability to obtain very high resolution (cm-scale) orthomosaics and DEMs. In most studies (50), the ground sampling distance (GSD) varied from 0.02 m to 0.20 m (see Supplementary materials - Appendix A). Therefore, compared to satellite or aerial images, researchers were able to collect more accurate data with much less financial expenditure, which allowed them to conduct very detailed studies of small glacial landforms and processes (e.g., fluted moraines, small push moraines).

## 2.7. Mission design and performance

The advantage of the off-the-shelf UAVs, in addition to the relatively low purchase costs, is the optimized software for controlling the UAV and managing the mission, often available in the form of a mobile application (free or available to download for a small fee on Android or iOS devices). This software allowed operators to easily plan a flight directly in the application based on the selected research area. Autonomous flight programming was declared in 35 publications, in most cases based on linear flight and automatic taking of interval images from a pre-set altitude. To generate a more accurate model, in some publications, the image overlap was set to a value of even 90% (Ryan et al., 2015). In 14 other studies, UAVs were manually piloted, and all flight parameters were controlled directly by the UAV operator. In some works, in addition to vertical images, oblique images were also taken (e.g., Westoby et al., 2015; Chudley et al., 2019; Tomczyk et al., 2019; Tomczyk and Ewertowski, 2020), which during processing resulted in more accurate mapping of the vertical and near-vertical objects, e.g. large boulders, escarpments.

## 2.8. Problems encountered

The on-site meteorological conditions were the most common source of problems with UAV operations. Low cloud cover, fog, strong winds, and rainfall can effectively disrupt the work schedule and force operators to reschedule surveys. In addition, several other sources of problems were mentioned in the literature. Animals, especially birds, are a real threat to the success of a UAV flight; and in the Arctic, polar bears pose a potential danger to operators. Problems with GNSS cover and magnetometer readings can enforce a switch to manual flight instead of preplanned missions (Bernard et al., 2017). There were also problems with maintaining the desired image overlap during an autonomous flight (Fugazza et al., 2018), inaccurate GNSS measurements leading to low accuracy of the DEM (Ryan et al., 2015) or insufficient supply of power packets (which drains faster in a cold environment), causing the need to complete the surveys on another day (Lamsters et al., 2020b).

## 3. Overviews of current UAV applications in glacial and periglacial geomorphology

### 3.1. Geomorphological mapping

Detailed mapping is the primary application of UAV-generated data in studies related to glacial and periglacial geomorphology. Maps developed based on orthomosaics and DEMs, often combined with fieldwork ground-truthing, can be produced for regions of glacial forelands, usually focusing on a specific landform type or landform assemblage (Fig. 4), or, less often, for a whole glacial foreland. Such products provide

an inventory of various glacial landforms and constitute a basis for understanding the evolution and dynamics of glacial landsystems.

UAV data are often combined with other data sources, and a common practice involves a less detailed mapping of larger areas (e.g., whole glacial forelands) based on high-resolution satellite or aerial images, combined with a more detailed mapping of particular areas of glacial landsystems. Such an approach was used in the case of Fláajökull (Iceland) to produce a small scale map (1:6250 scale) of the whole glacial foreland complemented by a more detailed map (1:350 scale) of a sample area of a recently exposed landform assemblage that enabled a detailed analysis of this glacial landsystem (Evans et al., 2016). A similar approach was used in mapping Nordenskiöldbreen (Spitsbergen) by combining high-resolution satellite data (WorldView-2) with historical aerial photographs to produce small-scale maps of the whole glacial foreland, and UAV data for a very detailed mapping that focused on the fluted surface to provide morphometrical details of flute assemblage (Ewertowski et al., 2016). The same glacial foreland was also mapped based on aerial images combined with offshore data to produce geomorphological maps comprising onshore and offshore areas (Allaart et al., 2018). In this case, UAV-generated data were used to provide an inventory of drumlins present in the Nordenskiöldbreen foreland and to provide contexts for the results of sedimentological studies of these landforms (Allaart et al., 2018). Storrar et al. (2020) conducted a study of the esker complexes on the foreland of the Hørbyebreen (Spitsbergen) and Breiðamerkurjökull (Iceland). To analyse the formation and evolution of these forms, they used very detailed maps of both esker complexes, which were based on the UAV-generated data. Ely et al. (2017) produced an orthophotomap and a DEM of the Isfallsglaciären foreland in Sweden, aiming to assess the morphological properties of fluted moraines and to demonstrate the usefulness of UAV technology for registering minor details of glacial landforms.

Mapping the entire glacial foreland with the sole use of UAV-generated data is much less common, as achieving such extensive coverage is time-consuming and, in most cases, requires flights beyond visual line of sight (BVLOS), which is complicated from an organizational and law regulation standpoint. One example was demonstrated by Dabski et al. (2020), who surveyed the forelands of three glaciers (Ecology, Sphinx, and Baranowski on King George Island in West Antarctica) to determine the area and spatial distribution of individual glacial landforms. They used a large fixed-wing UAV construction, which allowed for effective acquisition of images (only three flights were performed) over a reasonably large territory (the total linear distance covered by the UAV was 720 km in 7 h). The achieved GSD of 0.06 m for orthomosaic and 0.25 m for DEM was, however, slightly lower than in most other applications of UAV in glacial geomorphology.

Apart from mapping with a strict focus on glacial landforms, UAV-generated data have also been used in paraglacial and periglacial geomorphology. For example, Lousada et al. (2018), based on UAV images, aerial images and satellite imagery, mapped a valley fragment at Adventdalen (Spitsbergen) to critically evaluate these three sources of remote sensing data for the detection of ice wedges. The authors emphasized that only UAV data and aerial images allowed for effective mapping of these structures, offering a resolution that was better than 0.2 m. The WorldView-1 satellite imagery (0.5 m GSD) only allowed for detecting 1/3 of the polygons inventoried within the study area. Tomczyk et al. (2019) surveyed the Dynamisk Creek alluvial fan (Spitsbergen) using a low-cost UAV and produced a very detailed (1:850 scale) geomorphological map confirming the usefulness of UAV-SfM technology for mapping the surface morphology of fans which developed as the landscape responded to the retreat of glaciers. They also indicate the UAV's susceptibility to weather conditions, limited power efficiency, or uselessness during polar nights. In other publications, UAV technology was used to (i) map the immediate reaction of the periglacial landscape to a glacial lake outburst flood (Tomczyk and Ewertowski, 2020), (ii) produce an inventory and describe

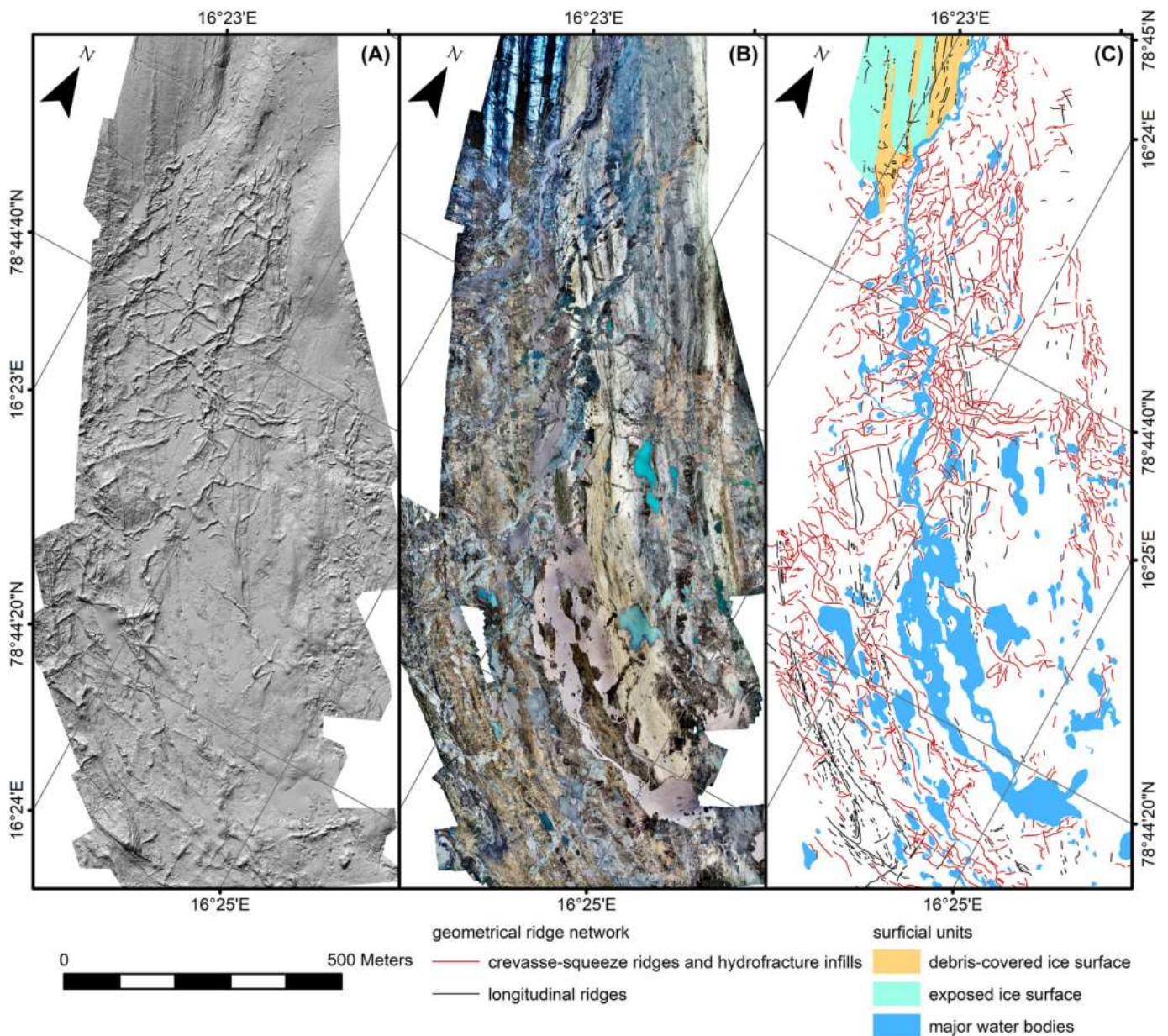


Fig. 4. An example of geomorphological mapping based on hillshade model and orthomosaic: a network of geometrical ridges in front of Hørbyebreen, Svalbard: (A) hillshade model; (B) orthomosaic; (C) geomorphological map showing complex pattern of cross-cutting ridges (Ewertowski et al., 2019).

the characteristics of stone circles (Pereira et al., 2020), (iii) observe the phenomenon of solifluction and its relationship with different factors, e.g., with the bedrock character (Eichel et al., 2020), or (iv) produce a general inventory of periglacial forms in the studied area (Dąbski et al., 2017).

### 3.2. Change detection

Change detection (volumetric and/or planimetric) is another popular application of UAV-generated data in geomorphological research. The UAV's high mobility and flexibility (e.g., in terms of sensor selection) allow for a much more flexible choice of the date of survey in comparison to regular aerial images or high-resolution satellite imagery. Multi-temporal surveys constitute a basis for the creation of time series of orthomosaics and DEMs. After subtracting the spatially overlapping cells of the two rasters, it is possible to obtain a DEM of Difference (DoD), illustrating the difference in height between the two models (e.g., Tonkin and Midgley, 2016; Chandler et al., 2020a)

(Fig. 5). The main motivations for conducting cyclical observations of landforms included understanding the evolution of the landscape (Tonkin et al., 2016; Seier et al., 2017; Kaufmann et al., 2018) or research into the influence of factors such as temperature and precipitation on landform transformation (Bernard et al., 2017).

Change detection can include one-period observations (e.g., month-to-month, year-to-year) to provide data on landscape change in this period, or can comprise a series of multiperiod observations to be able to judge not only the general direction of landscape transformation (i.e., erosion or deposition) but also trend in these changes (e.g., acceleration of erosion, seasonality). For example, Bernard et al. (2017) calculated a DoD of the Austre Lovénbreen (Spitsbergen) moraine during only a 7-day field visit (the first flight was made on 24 September 2015, and the second one on 1 October 2015). Even in such a short period, UAV-generated data enabled the detection of landform changes in the foreland caused by sudden flooding, which accounted for local terrain collapse to a depth of 3 m. Tonkin et al. (2016) also made a one-time change detection of the moraine relief



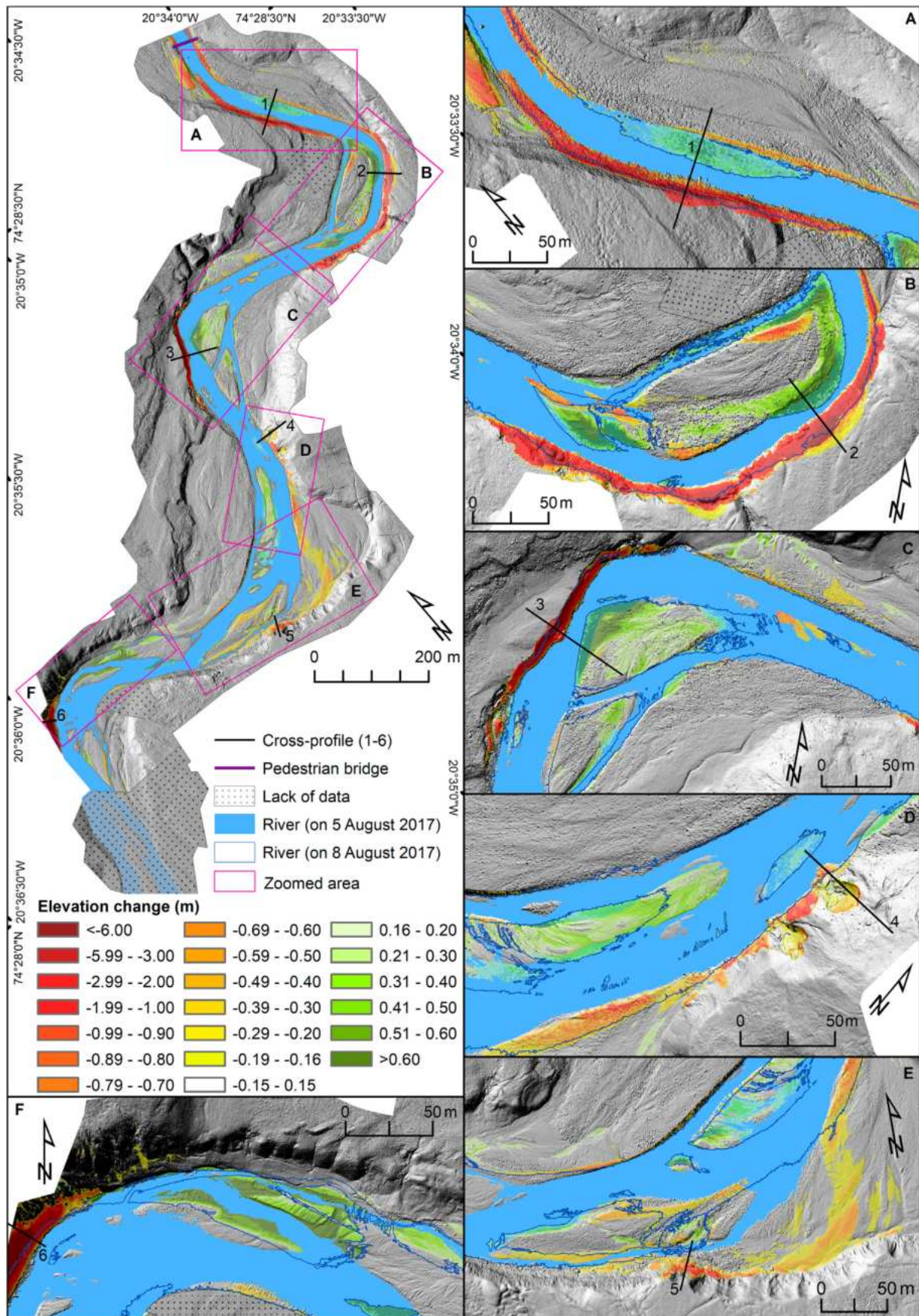


**Fig. 5.** An example of DEM of Differences used to study elevation changes in response to glacial lake outburst flood along the Zackenberg River, Greenland (Reprinted from Journal of Hydrology, Vol 591, Tomczyk et al., Geomorphological impacts of a glacier lake outburst flood in the high arctic Zackenberg River, NE Greenland, 125300, Copyright (2020), with permission from Elsevier.

on the same glacial foreland, but for a more extended period – they compared the images from 2003 (aerial photographs) and 2014 (UAV), quantifying the dynamics over this relatively long 11-year period. In publications that described a one-period change detection using UAV data, the most common interval between the two surveys varied from several dozen days to several years (e.g., Whitehead et al., 2013; Immerzeel et al., 2014; Ryan et al., 2015; Jouvét et al., 2016; Tonkin et al., 2016; Bernard et al., 2017; Seier et al., 2017; Wigmore and Mark, 2017; Jouvét et al., 2018; Rossini et al., 2018; Scaioni et al., 2018; Groos et al., 2019; Bash and Moorman, 2020).

Multiple-period analyses of surface changes are noticeably less common in the literature. This can be explained by the need to conduct regular observations of the same site, which is time-consuming and requires frequent field trips. In several studies that present the results of the multiperiod analysis, the difference between subsequent surveys was usually about one year (e.g., Kraaijenbrink et al., 2016; Fugazza et al., 2018; Kaufmann et al., 2018; Chandler et al., 2020b). In some cases, UAV-generated data were complemented with archival LIDAR data or aerial images (e.g., Fugazza et al., 2018; Chandler et al., 2020b). Repeated analyses of surface changes and regular observations of glacial and periglacial landscape transformation using UAVs can help to understand the dynamics of landforms better and enable the quantification of changes related to low-frequency and high-magnitude events such as intense melting, rainfall or glacier-lake outburst floods. For example, Tomczyk et al. (2020) provided an insight into the geomorphological response of high-arctic Zackenberg river to glacial lake outburst flood, by quantification and description of the spatial pattern of riverbank erosion and bars' modification (Fig. 5). Such results were possible thanks to UAV time-series' high temporal resolution - data were collected immediately before-, during-, and after- flood (5th, 6th, and 8th August 2017). It is probable that due to the growing popularity of UAVs in glacial studies, there will be an increase in studies that describe multiperiod observations.

### 3.3. Process-form studies

Another less popular application of UAV-generated data in glacial geomorphology is the study of processes forming and modifying glacial landforms. A time series of DEMs and orthomosaic enables monitoring changes in morphology and can therefore be used to observe or infer constructional and erosional processes and, as a consequence, to propose new models of landscape evolution. Chandler et al. (2020a) presented an example of such an approach, using a relatively long series of UAV observations (4 surveys between 2016 and 2019) of the foreland of Fjallsjökull (Iceland) to demonstrate the frequency of small push moraine formation. For the first time, UAV technology was able to provide clear evidence of the sub-annual moraine formation, which made it possible to develop a conceptual model of the formation of small recessional moraines in front of active temperate glaciers receding into overdeepenings.

### 3.4. Mapping of surficial geology

Sedimentological studies using UAV images and the SfM method in glacial and paraglacial areas are still rare. However, very-high-resolution images (better than 0.1 m) taken from a low altitude are a potentially excellent data source, e.g., to study grain size and distribution, thanks to the development of very accurate orthomosaics and DEMs which make it possible to identify sediment textures with high precision. Westoby et al. (2015) used UAV-SfM method, terrestrial SfM and terrestrial laser scanning (TLS) data to analyse the particle size distribution of the moraine complex at the Heritage Range (Antarctica) to determine if the SfM method could be used to interpret grain-size distribution in a site-scale, thereby replacing the traditional manual screening usually limited to patch-scale. Their research confirmed UAV-SfM workflow's usefulness, which enabled upscaling of

site-scale results to model median grain-size in a moraine-scale. Several other approaches which analysed orthomosaic texture, point cloud/DEM roughness or single image texture were used to quantify particle sizes from UAV data in fluvial geomorphology (cf., Carbonneau et al., 2018; Woodget et al., 2018), which can also be adapted to the glacial environment.

### 3.5. Existing workflows for UAV-SfM in glacial geomorphology

Several years of experience with the use of UAVs in geomorphological research mean that, in addition to publications presenting examples of applications of UAV technology, substantial methodological studies have also been published (e.g., Carbonneau and Dietrich, 2017; James et al., 2017, 2020). James et al. (2019) draw attention to the fact that due to reduction in the level of complexity with the use of computational methods (thanks mainly to the automated data processing software), many users are not sufficiently prepared in the theoretical aspects of numerical methods used in photogrammetric programs. This argument prompted them to provide a systematic guideline with details that should be presented in publications where UAV-SfM was used. The proposed guidelines include such aspects as the contribution of the publication to the progress of science, a detailed description of the sensors used, or the adopted calculation parameters in the software (James et al., 2019).

The methodology for using UAV-SfM in glacial and periglacial geomorphology is usually hierarchical, which is especially visible in publications where the authors first describe in detail the step-by-step workflows (e.g., Ely et al., 2017; Gindraux et al., 2017; Ewertowski et al., 2019), and later demonstrated its application on a real-world case study. The most common workflow is based on several key consecutive activities: (a) selection of the study area and appropriate equipment, (b) transport and preparatory field work (e.g., setting up Ground Control Points [GCPs]), (c) planning and execution of the UAV flight, (d) initial processing of the imagery in SfM software at a low level of details (i.e. on the lowest processing settings to enable rapid verification while still in the field) to ensure that the extent and quality of the data are satisfactory; (e) final processing and generation of orthomosaics and DEMs; and (f) geomorphological analysis (e.g., mapping, change detection). In the beginning, the set is pre-selected (blurred or overexposed images are rejected, etc.) and imported into a photogrammetric software (e.g., Agisoft Metashape) (e.g., Ewertowski et al., 2019). As the software processes the file using the SfM method, based on characteristic points appearing in several images, the number of characteristic points is crucial for the quality of the model. Hence, both the quality of the sensor and resolution of the images play a critical role (Westoby et al., 2012; Gindraux et al., 2017).

Depending on the field situation, available equipment, and the adopted research objectives, it is possible to omit the establishment of GCPs (Evans et al., 2016; Chudley et al., 2019) which will reduce the external accuracy of the model; however, data georeferenced based on an onboard GNSS will be of sufficient quality for a one-time mapping. If the external GCPs are surveyed, the most critical factor influencing the final accuracy is the optimal distribution, i.e. maintaining a maximum distance of 100 m between the GCPs (cf., Tonkin and Midgley, 2016). An alternative georeferencing solution, which can be used instead of surveying GCPs, is co-registration of the two surveys during the image alignment stage (Cook and Dietze, 2019).

## 4. Potential future applications

As presented in Section 2, the use of UAV-SfM technology in glacial and periglacial geomorphological research has increased recently, and more publications are expected to appear soon. The use of UAVs is quickly evolving as well, from the simple landform mapping in its earlier days to more advanced applications such as process-form studies. UAV-SfM technology has been successfully delivering high-resolution

spatial data over the past few years, which is ideal for change detection studies. In this section, we suggest some other potential future applications of UAV and SfM in glacial and periglacial geomorphology, which can be enhanced by combination with other data sources. The UAV optical imaging data can also be potentially combined with LIDAR laser measurements using a special scanner designed for UAVs (e.g., Livox Mid-40).

#### 4.1. Investigation of geomorphological processes

Thanks to a flexible temporal resolution, a time series of UAV observations can be used to analyse processes involved in the development and modification of landforms in the glacier foreland, e.g., moraine formation processes (Chandler et al., 2020a). Researching this subject requires a long time series of data, which will make it possible to recognize the impact of individual processes. Such an approach should lead to a significant increase in knowledge of the process-form-sediment relationship, e.g., by studies focused on: (1) eskers systems emerging from the ice cover and their further modifications by slope processes and dead ice melting; (2) disintegration of ice-cored moraines by mass movement processes; (3) evolution of kame-and-kettle topography due to dead-ice melt out; (4) evolution of debris-covered glacial tongues and their transformation until full de-icing stage; (5) modelling of sediment storage and transport as an effect of paraglacial landscape modifications; (6) assessment of preservation potential of subtle glacial landforms and their potential fingertip in the geomorphological record. Similarly, UAV-generated data can be used to observe and quantify geomorphic outcomes of processes in a periglacial environment, such as ice-wedge polygon development or their degradation by thermo-erosion.

#### 4.2. Combination of UAV and terrestrial photogrammetry

Another improvement in our understanding of glacial and periglacial landscapes may be related to the use of a combination of low-altitude (UAV-generated) and ground-based (terrestrial) images processed via the SfM workflow to obtain detailed models of steep surfaces like ice cliffs, gorges, and steep slopes. Such an approach was used by Fugazza et al. (2018), who, by comparing data from UAV, TLS and terrestrial photogrammetry, proved that the point density in the three obtained point clouds was the highest for images from terrestrial sensors. On this basis, it can be assumed that when examining vertical objects (e.g., steep gorges or cliffs), where there is a possibility of stable sensor positioning, ground photogrammetry will provide images of better quality than UAVs. Tavani et al. (2020) presented an effective modelling of the cliff using images taken by a budget smartphone, proving that even such a low-cost solution can be beneficial in geomorphological research. The advantage of terrestrial images of objects is undoubtedly the full freedom as to the choice of sensor, but with extensive, flat research objects, vertical and oblique images from UAVs would still be more favourable and more time-effective.

#### 4.3. SfM processing of archival images

UAV images offer exceptional spatial and temporal resolution, but their temporal coverage is mostly restricted to the last decade. However, as demonstrated by several studies (e.g., Mertes et al., 2017; Midgley and Tonkin, 2017; Kaufmann et al., 2018; Sziło and Bialik, 2018; Holmlund, 2020; Kavan, 2020), the SfM workflow can be successfully used to process archival aerial photographs, providing an excellent baseline that can be subsequently updated with UAV surveys to provide a better picture of the evolution of glacial landsystems. For example, Mertes et al. (2017) and Midgley and Tonkin (2017) demonstrated that even oblique aerial photographs from the beginning of the 20th century could deliver valuable data about landscape changes. Similarly, a combination of historical ground-based photographs with archival

aerial photographs (both sets processed using SfM) enabled quantification of glacier changes (e.g., Mertes et al., 2017; Holmlund, 2020; Kavan, 2020). However, the relatively large values of uncertainties (of the magnitude up to several m) would have to be considered, limiting their usefulness in quantifying the evolution of smaller geomorphological features.

#### 4.4. Use of crowd-sourced images

The spectacular increase in the popularity and ubiquity of social media in the last decade has significantly changed the way people share their data, e.g., images and videos, with others. Publishing images on a social network (e.g., Facebook, Twitter, and Instagram) with an added location and capture date may become valuable information for scientists, including geomorphologists. This source of data can be potentially useful in glacial and periglacial geomorphology, especially in areas commonly visited by tourists (e.g., Alps, SE Iceland). The growing number of high-resolution UAV-generated videos published on social media can be processed through SfM-MVS workflow, for example, frames from 4 K videos can be transformed into stills of about 12MP resolution and used to generate point clouds, DEMs and orthomosaics. Of course, such an approach would require the consent of the owners of images and/or videos. With a probable increase in the number of available movies, there is a potential to obtain high temporal coverage of data that can enormously enhance our ability to monitor and understand the processes of change and transformation concerning modern glacial and periglacial landscapes.

## 5. Conclusions

The UAV-collected images are the basis for the mapping of such forms as terminal moraines or alluvial cones, which are part of the current trend of developing thematic maps of selected landforms along with formulating detailed research questions for the studied phenomena (cf., Chandler et al., 2018). Recent works have focused on the mapping of individual landforms or their assemblages (e.g., Storrar et al., 2020), or mapping of the entire glacial foreground (e.g., Dabski et al., 2020). Repeated observations of landforms and regular acquisition of images make it possible to detect changes in their volume or area, which is necessary for understanding the dynamics, evolution, and response of glacial forelands to ongoing climate changes (e.g., Fugazza et al., 2015; Chandler et al., 2020b). The literature review revealed interesting information on the current use of the UAV-SfM method in glacial geomorphology:

- 1) Diverse research topics (mainly geomorphological mapping and geomorphological change detection analysis) and an increase in the number of publications in 2020 (22 papers, Fig. 2) prove the enormous usefulness of this method and its growing popularity.
- 2) Most of the studies were conducted in the Arctic and the Alps (Fig. 1), with a smaller number in Antarctica, Himalayas, Andes, and Alaska. The popularity of the Arctic (especially Svalbard and Iceland) and the Alps should come as no surprise. Climate changes, resulting in an increase in the average air temperature, tend to cause dynamic reactions in the glacial and periglacial landscape. The Arctic is also a natural “field-based laboratory” – the effects of climate change in the Arctic are much more intense than in other regions (see Moritz et al., 2002; Walsh et al., 2011; Duarte et al., 2012). Therefore, we can use Arctic-based observations to infer the future effects of climate warming in other areas, i.e. we may use the results of detailed quantification of processes in Arctic settings to speculate about the magnitude of future geomorphological changes in the lower latitudes.
- 3) In most cases, the study area did not exceed 1 km<sup>2</sup>, but some observations were also made of the entire glacial foreland. Multi-rotors were the most popular type of UAV used. In nearly all publications,

RGB images were used to develop orthomosaics and DEMs with a spatial resolution from 0.02 m to 0.20 m. Most of the operators used an autonomous flight mode. The most encountered problems were unfavourable weather conditions and insufficient energy reserve.

The presented overview highlights the utility of UAVs for obtaining images, which can be used to develop high-resolution orthomosaics and DEMs, thereby enabling a detailed geomorphological mapping as well as a precise identification of their morphological characteristics – that would not be possible using other remote data sources. As to the multi-temporal surveys, increased research interest on the process-form relationship is expected, and a significant contribution to this type of research could be made through the more widespread use of a combination of UAV-based images with ground-based photogrammetry and archival aerial images. Time series of observations may be supplemented with images and videos from private (i.e., crowd-based) collections available through social media. We speculate that in the 2021–2030 decade the following can be expected:

- 1) Use of small UAVs will become a standard in glacial and periglacial geomorphology – especially in mapping exercises;
- 2) Lowering of the costs for RTK-GNSS will enable direct referencing with the accuracy of several cm, therefore removing the necessity of GCP collection;
- 3) More widespread use of sensors different than RGB cameras (e.g., LiDAR or ground penetrating radar [GPR]) mounted on UAV will increase the accuracy of terrain modelling (LiDAR) and enable to interpret at least some of the subsurface features (e.g., dead ice presence) within glacial foreland (GPR);
- 4) Increase in the availability of multi-temporal datasets will enable detailed quantification of geomorphological effects of different processes (e.g., debris flows, dead-ice melting, meltwater erosion) and development of worldwide databases containing rates of the intensity of geomorphological processes in different climatic and environmental settings;
- 5) Multi-temporal datasets will also enable quantifying post-glacial transformations of glacial landforms and assessing their preservation potential – thus improving the interpretation of Pleistocene glacial record.

#### Declaration of competing interest

The authors declare that they have no known competing financial interests or personal relationships that could have appeared to influence the work reported in this paper.

#### Acknowledgements

This study was funded by Narodowe Centrum Nauki (National Science Centre, Poland), grant number 2019/35/B/ST10/03928. Both reviewers provided highly valuable comments and suggestions which greatly improved the quality and clarity of the manuscript.

#### Appendix A. Supplementary data

Supplementary data associated with this article can be found in the online version, at <https://doi.org/10.1016/j.geomorph.2021.107620>. These data include the Google map of the most important areas described in this article, and the full database (in Excel and shp formats), which can be used in GIS software.

#### References

Aber, J., Marzolf, I., Ries, J., 2010. Small-format aerial photography: principles, techniques and geoscience applications. *Photogramm. Rec.* [https://doi.org/10.1660/0022-8443\(2008\)111\[49:hkap\]2.0.co;2](https://doi.org/10.1660/0022-8443(2008)111[49:hkap]2.0.co;2).

Aber, J.S., Gałazka, D., 2000. Potential of kite aerial photography for Quaternary investigations in Poland. *Kwartalnik Geol.* 44, 33–38.

Aber, J.S., Aber, S.W., Janočko, J., Zabielski, R., Górska-Zabielska, M., 2008. High-altitude kite aerial photography. *Trans. Kans. Acad. Sci.* 111, 49–60.

Allaart, L., Friis, N., Ingólfsson, Ó., Håkansson, L., Noormets, R., Farnsworth, W.R., Mertes, J., Schomacker, A., 2018. Drumlins in the Nordenskiöldbreen forefield, Svalbard. *Gff* 140, 170–188. <https://doi.org/10.1080/11035897.2018.1466832>.

Anderson, K., Gaston, K.J., 2013. Lightweight unmanned aerial vehicles will revolutionize spatial ecology. *Front. Ecol. Environ.* 11, 138–146. <https://doi.org/10.1890/120150>.

Bash, E.A., Moorman, B.J., 2020. Surface melt and the importance of water flow—an analysis based on high-resolution unmanned aerial vehicle (UAV) data for an Arctic glacier. *Cryosphere* 14, 549–563. <https://doi.org/10.5194/tc-14-549-2020>.

Benn, D.I., Evans, D.J.A., 2010. *Glaciers and Glaciation*. Second Ed. Hodder Education, London and New York.

Bernard, E., Friedt, J.M., Tolle, F., Marlin, C., Griselin, M., 2017. Using a small COTS UAV to quantify moraine dynamics induced by climate shift in Arctic environments. *Int. J. Remote Sens.* 38, 2480–2494. <https://doi.org/10.1080/01431161.2016.1249310>.

Bernard, E., Friedt, J.M., Schiavone, S., Tolle, F., Griselin, M., 2018. Assessment of periglacial response to increased runoff: an Arctic hydrosystem bears witness. *Land Degrad. Dev.* 29, 3709–3720. <https://doi.org/10.1002/ldr.3099>.

Berthling, I., Berti, C., Mancinelli, V., Stendardi, L., Piacentini, T., Miccadei, E., 2020. Analysis of the paraglacial landscape in the Ny-Ålesund area and Blomstrandøya (Kongsfjorden, Svalbard, Norway). *J. Maps* 16, 818–833. <https://doi.org/10.1080/17445647.2020.1837684>.

Bhardwaj, A., Sam, L., Akanksha, Martín-Torres, F.J., Kumar, R., 2016. UAVs as remote sensing platform in glaciology: present applications and future prospects. *Remote Sens. Environ.* 175, 196–204. <https://doi.org/10.1016/j.rse.2015.12.029>.

Boike, J., Yoshikawa, K., 2003. Mapping of periglacial geomorphology using kite/balloon aerial photography. *Permafrost. Periglac. Process.* 14, 81–85. <https://doi.org/10.1002/ppp.437>.

Buhler, Y., Adams, M.S., Bosch, R., Stoffel, A., 2016. Mapping snow depth in alpine terrain with unmanned aerial systems (UASs): potential and limitations. *Cryosphere* 10, 1075–1088. <https://doi.org/10.5194/tc-10-1075-2016>.

Carbonneau, P.E., Dietrich, J.T., 2017. Cost-effective non-metric photogrammetry from consumer-grade sUAS: implications for direct georeferencing of structure from motion photogrammetry. *Earth Surf. Process. Landf.* <https://doi.org/10.1002/esp.4012>.

Carbonneau, P.E., Bizzi, S., Marchetti, G., 2018. Robotic photosieving from low-cost multirotor sUAS: a proof-of-concept. *Earth Surf. Process. Landf.* <https://doi.org/10.1002/esp.4298>.

Chandler, B.M.P., Evans, D.J.A., Roberts, D.H., Ewertowski, M., Clayton, A.I., 2016. Glacial geomorphology of the Skálafellsjökull foreland, Iceland: a case study of ‘annual’ moraines. *J. Maps* 12, 904–916. <https://doi.org/10.1080/17445647.2015.1096216>.

Chandler, B.M.P., Lovell, H., Boston, C.M., Lukas, S., Barr, I.D., Benediktsson, Í.Ó., Benn, D.I., Clark, C.D., Darvill, C.M., Evans, D.J.A., Ewertowski, M.W., Loibl, D., Margold, M., Otto, J.C., Roberts, D.H., Stokes, C.R., Storrar, R.D., Stroeven, A.P., 2018. Glacial geomorphological mapping: a review of approaches and frameworks for best practice. *Earth-Sci. Rev.* 185, 806–846. <https://doi.org/10.1016/j.earscirev.2018.07.015>.

Chandler, B.M.P., Chandler, S.J.P., Evans, D.J.A., Ewertowski, M.W., Lovell, H., Roberts, D.H., Schaefer, M., Tomczyk, A.M., 2020a. Sub-annual moraine formation at an active temperate Icelandic glacier. *Earth Surf. Process. Landf.* 45, 1622–1643. <https://doi.org/10.1002/esp.4835>.

Chandler, B.M.P., Evans, D.J.A., Chandler, S.J.P., Ewertowski, M.W., Lovell, H., Roberts, D.H., Schaefer, M., Tomczyk, A.M., 2020b. The glacial landsystem of Fjallsjökull, Iceland: spatial and temporal evolution of process-form regimes at an active temperate glacier. *Geomorphology* 361, 107192. <https://doi.org/10.1016/j.geomorph.2020.107192>.

Chudley, T.R., Christoffersen, P., Doyle, S.H., Abellan, A., Snooke, N., 2019. High-accuracy UAV photogrammetry of ice sheet dynamics with no ground control. *Cryosphere* 13, 955–968. <https://doi.org/10.5194/tc-13-955-2019>.

Colomina, I., Molina, P., 2014. Unmanned aerial systems for photogrammetry and remote sensing: a review. *ISPRS J. Photogramm. Remote Sens.* 92, 79–97. <https://doi.org/10.1016/j.isprsjprs.2014.02.013>.

Cook, K.L., Dietze, M., 2019. Short communication: a simple workflow for robust low-cost UAV-derived change detection without ground control points. *Earth Surf. Dyn.* 7, 1009–1017. <https://doi.org/10.5194/esurf-7-1009-2019>.

Dąbski, M., Zmarz, A., Pabjanek, P., Korczak-Abshire, M., Karsznia, I., Chwedorzewska, K.J., 2017. UAV-based detection and spatial analyses of periglacial landforms on Demay Point (King George Island, South Shetland Islands, Antarctica). *Geomorphology* 290, 29–38. <https://doi.org/10.1016/j.geomorph.2017.03.033>.

Dąbski, M., Zmarz, A., Rodzewicz, M., Korczak-Abshire, M., Karsznia, I., Lach, K., Rachlewicz, G., Chwedorzewska, K., 2020. Mapping glacier forelands based on UAV BVLOS operation in Antarctica. *Remote Sens.*, 12 <https://doi.org/10.3390/rs12040630>.

Duarte, C.M., Lenton, T.M., Wadhams, P., Wassmann, P., 2012. Abrupt climate change in the Arctic. *Nat. Clim. Change* <https://doi.org/10.1038/nclimate1386>.

Eichel, J., Draebing, D., Kattenborn, T., Senn, J.A., Klingbeil, L., Wieland, M., Heinz, E., 2020. Unmanned aerial vehicle-based mapping of turf-banked solifluction lobe movement and its relation to material, geomorphometric, thermal and vegetation properties. *Permafrost. Periglac. Process.* 31, 97–109. <https://doi.org/10.1002/ppp.2036>.

Ely, J.C., Graham, C., Barr, I.D., Rea, B.R., Spagnolo, M., Evans, J., 2017. Using UAV acquired photography and structure from motion techniques for studying glacier landforms: application to the glacial flutes at Isfjallsglaciären. *Earth Surf. Process. Landf.* 42, 877–888. <https://doi.org/10.1002/esp.4044>.

Evans, D.J.A., 2017. *Till: A Glacial Process Sedimentology*. John Wiley & Sons, Inc., Hoboken, NJ, USA <https://doi.org/10.1002/9781118652541>.

Evans, D.J.A., Ewertowski, M., Orton, C., 2016. Fláajökull (north lobe), Iceland: active temperate piedmont lobe glacial landsystem. *J. Maps* 12, 777–789. <https://doi.org/10.1080/17445647.2015.1073185>.

- Ewertowski, M.W., Tomczyk, A.M., 2020. Reactivation of temporarily stabilized ice-cored moraines in front of polythermal glaciers: gravitational mass movements as the most important geomorphological agents for the redistribution of sediments (a case study from Ebbabreen and Ragnarabreen, Svalbard). *Geomorphology* 350, 106952. <https://doi.org/10.1016/j.geomorph.2019.106952>.
- Ewertowski, M.W., Evans, D.J.A., Roberts, D.H., Tomczyk, A.M., 2016. Glacial geomorphology of the terrestrial margins of the tidewater glacier, Nordenskiöldbreen, Svalbard. *J. Maps* 12, 476–487. <https://doi.org/10.1080/17445647.2016.1192329>.
- Ewertowski, M.W., Tomczyk, A.M., Evans, D.J.A., Roberts, D.H., Ewertowski, W., 2019. Operational framework for rapid, very-high resolution mapping of glacial geomorphology using low-cost unmanned aerial vehicles and structure-from-motion approach. *Remote Sens.* 11. <https://doi.org/10.3390/rs11010065>.
- Fey, C., Krainer, K., 2020. Analyses of UAV and GNSS based flow velocity variations of the rock glacier Lazaun (Ötztal Alps, South Tyrol, Italy). *Geomorphology* 365, 107261. <https://doi.org/10.1016/j.geomorph.2020.107261>.
- Fey, C., Wichmann, V., Zangerl, C., 2017. Reconstructing the evolution of a deep seated rockslide (Marzell) and its response to glacial retreat based on historic and remote sensing data. *Geomorphology* 298, 72–85. <https://doi.org/10.1016/j.geomorph.2017.09.025>.
- Fugazza, D., Senese, A., Azzoni, R.S., Smiraglia, C., Cernuschi, M., Severi, D., Diolaiuti, G.A., 2015. High-resolution mapping of glacier surface features. the uav survey of the forni glacier (Stelvio National Park, Italy). *Geogr. Fis. Din. Quat.* 38, 25–33. <https://doi.org/10.4461/GFDQ.2015.38.03>.
- Fugazza, D., Scaioni, M., Corti, M., D'Agata, C., Azzoni, R.S., Cernuschi, M., Smiraglia, C., Adele Diolaiuti, G., 2018. Combination of UAV and terrestrial photogrammetry to assess rapid glacier evolution and map glacier hazards. *Nat. Hazards Earth Syst. Sci.* 18, 1055–1071. <https://doi.org/10.5194/nhess-18-1055-2018>.
- Gaffey, C., Bhardwaj, A., 2020. Applications of unmanned aerial vehicles in cryosphere: latest advances and prospects. *Remote Sens.*, 12 <https://doi.org/10.3390/rs12060948>.
- Gindraux, S., Boesch, R., Farinotti, D., 2017. Accuracy assessment of digital surface models from unmanned aerial vehicles' imagery on glaciers. *Remote Sens.* 9, 1–15. <https://doi.org/10.3390/rs9020186>.
- Glasser, N.F., Roman, M., Holt, T.O., Zebre, M., Patton, H., Hubbard, A.L., 2020. Modification of bedrock surfaces by glacial abrasion and quarrying: evidence from North Wales. *Geomorphology* 365. <https://doi.org/10.1016/j.geomorph.2020.107283>.
- Groos, A.R., Bertschinger, T.J., Kummer, C.M., Erlwein, S., Munz, L., Philipp, A., 2019. The potential of low-cost UAVs and open-source photogrammetry software for high-resolution monitoring of alpine glaciers: a case study from the kanderfirn (Swiss Alps). *Geosci.* 9. <https://doi.org/10.3390/geosciences9080356>.
- Hackney, C., Clayton, A.I., 2015. Unmanned Aerial Vehicles (UAVs) and their application in geomorphic mapping. *Geomorphol. Technol.* 7, 1–12.
- Hedding, D.W., Erofeev, A.A., Hansen, C.D., Khon, A.V., Abbasov, Z.R., 2020. Geomorphological processes and landforms of glacier forelands in the upper Aktru River basin (Gorniy Altai), Russia: evidence for rapid recent retreat and paraglacial adjustment. *J. Mt. Sci.* 17, 824–837. <https://doi.org/10.1007/s11629-019-5845-5>.
- Hendrickx, H., De Sloover, L., Stal, C., Delaloye, R., Nyssen, J., Frankl, A., 2020. Talus slope geomorphology investigated at multiple time scales from high-resolution topographic surveys and historical aerial photographs (Sanetsch Pass, Switzerland). *Earth Surf. Process. Landf.* 45, 3653–3669. <https://doi.org/10.1002/esp.4989>.
- Holmlund, E.S., 2020. Aldegondabreen glacier change since 1910 from structure-from-motion photogrammetry of archived terrestrial and aerial photographs: utility of a historic archive to obtain century-scale Svalbard glacier mass losses. *J. Glaciol.* <https://doi.org/10.1017/jog.2020.89>.
- Immerzeel, W.W., Kraaijenbrink, P.D.A., Shea, J.M., Shrestha, A.B., Pellicciotti, F., Bierkens, M.F.P., De Jong, S.M., 2014. High-resolution monitoring of Himalayan glacier dynamics using unmanned aerial vehicles. *Remote Sens. Environ.* 150, 93–103. <https://doi.org/10.1016/j.rse.2014.04.025>.
- James, M.R., Robson, S., d'Oleire-Oltmanns, S., Niethammer, U., 2017. Optimising UAV topographic surveys processed with structure-from-motion: ground control quality, quantity and bundle adjustment. *Geomorphology* 280, 51–66. <https://doi.org/10.1016/j.geomorph.2016.11.021>.
- James, M.R., Chandler, J.H., Eltner, A., Fraser, C., Miller, P.E., Mills, J.P., Noble, T., Robson, S., Lane, S.N., 2019. Guidelines on the use of structure-from-motion photogrammetry in geomorphic research. *Earth Surf. Process. Landf.* 44, 2081–2084. <https://doi.org/10.1002/esp.4637>.
- James, M.R., Antoniazza, G., Robson, S., Lane, S.N., 2020. Mitigating systematic error in topographic models for geomorphic change detection: accuracy, precision and considerations beyond off-nadir imagery. *Earth Surf. Process. Landf.* 45, 2251–2271. <https://doi.org/10.1002/esp.4878>.
- Jouvet, G., Weidmann, Y., Seguinot, J., Funk, M., Abe, T., Sakakibara, D., Seddik, H., Sugiyama, S., 2016. Initiation of a major calving event on Bowdoin Glacier captured by UAV photogrammetry. *Cryosphere Discuss.* 1–17. <https://doi.org/10.5194/tc-2016-246>.
- Jouvet, G., Weidmann, Y., Kneib, M., Detert, M., Seguinot, J., Sakakibara, D., Sugiyama, S., 2018. Short-lived ice speed-up and plume water flow captured by a VTOL UAV give insights into subglacial hydrological system of Bowdoin Glacier. *Remote Sens. Environ.* 217, 389–399. <https://doi.org/10.1016/j.rse.2018.08.027>.
- Kaufmann, V., Seier, G., Sulzer, W., Wecht, M., Liu, Q., Lauk, G., Maurer, M., 2018. Rock glacier monitoring using aerial photographs: conventional vs. UAV-based mapping - a comparative study. *Int. Arch. Photogramm. Remote Sens. Spat. Inf. Sci.* 42, 239–246. <https://doi.org/10.5194/isprs-archives-XLII-1-239-2018>.
- Kavan, J., 2020. Early twentieth century evolution of Ferdinand glacier, Svalbard, based on historic photographs and structure-from-motion technique. *Geogr. Ann. A Phys. Geogr.* <https://doi.org/10.1080/04353676.2020.1715124>.
- Kienholz, C., Pierce, J., Hood, E., Amundson, J.M., Wolken, G.J., Jacobs, A., Hart, S., Wikstrom Jones, K., Abdel-Fattah, D., Johnson, C., Conaway, J.S., 2020. Deglaciation of a Marginal Basin and Implications for Outburst Floods, Mendenhall Glacier, Alaska. *Front. Earth Sci.* 8, 1–21. <https://doi.org/10.3389/feart.2020.00137>.
- Kraaijenbrink, P., Meijer, S.W., Shea, J.M., Pellicciotti, F., De Jong, S.M., Immerzeel, W.W., 2016. Seasonal surface velocities of a Himalayan glacier derived by automated correlation of unmanned aerial vehicle imagery. *Ann. Glaciol.* 57, 103–113. <https://doi.org/10.3189/2016Aog71A072>.
- Lamsters, K., Karušs, J., Krievāns, M., Ješkins, J., 2020a. High-resolution orthophoto map and digital surface models of the largest Argentine Islands (the Antarctic) from unmanned aerial vehicle photogrammetry. *J. Maps* 16, 335–347. <https://doi.org/10.1080/17445647.2020.1748130>.
- Lamsters, K., Karušs, J., Krievāns, M., Ješkins, J., 2020b. High-resolution surface and bed topography mapping of Russell Glacier (SW Greenland) using UAV and GPR. *ISPRS Ann. Photogramm. Remote Sens. Spat. Inf. Sci.* V-2–2020, 757–763. <https://doi.org/10.5194/isprs-annals-v-2-2020-757-2020>.
- Le Heron, D.P., Vandyk, T.M., Kuang, H., Liu, Y., Chen, X., Wang, Y., Yang, Z., Scharfenberg, L., Davies, B., Shields, G., 2019. Bird's-eye view of an Ediacaran subglacial landscape. *Geology* 47, 705–709. <https://doi.org/10.1130/G46285.1>.
- Lousada, M., Pina, P., Vieira, G., Bandeira, L., Mora, C., 2018. Evaluation of the use of very high resolution aerial imagery for accurate ice-wedge polygon mapping (Adventdalen, Svalbard). *Sci. Total Environ.* 615, 1574–1583. <https://doi.org/10.1016/j.scitotenv.2017.09.153>.
- Mancini, F., Dubbini, M., Gattelli, M., Stecchi, F., Fabbri, S., Gabbianelli, G., 2013. Using unmanned aerial vehicles (UAV) for high-resolution reconstruction of topography: the structure from motion approach on coastal environments. *Remote Sens.* 5, 6880–6898. <https://doi.org/10.3390/rs5126880>.
- Manfreda, S., McCabe, M.F., Miller, P.E., Lucas, R., Madrigal, V.P., Mallinis, G., Dor, E. Ben, Helman, D., Estes, L., Ciraolo, G., Müllerová, J., Tauro, F., de Lima, M.I., de Lima, J.L.M.P., Maltese, A., Frances, F., Caylor, K., Kohv, M., Perks, M., Ruiz-Pérez, G., Su, Z., Vico, G., Toth, B., 2018. On the use of unmanned aerial systems for environmental monitoring. *Remote Sens.*, 10 <https://doi.org/10.3390/rs10040641>.
- Mather, A.E., Fyfe, R.M., Clason, C.C., Stokes, M., Mills, S., Barrows, T.T., 2019. Automated mapping of relict patterned ground: an approach to evaluate morphologically subdued landforms using unmanned-aerial-vehicle and structure-from-motion technologies. *Prog. Phys. Geogr.* 43, 174–192. <https://doi.org/10.1177/0309133318788966>.
- Mertes, J.R., Gullely, J.D., Benn, D.I., Thompson, S.S., Nicholson, L.I., 2017. Using structure-from-motion to create glacier DEMs and orthoimagery from historical terrestrial and oblique aerial imagery. *Earth Surf. Process. Landf.* <https://doi.org/10.1002/esp.4188>.
- Midgley, N.G., Tonkin, T.N., 2017. Reconstruction of former glacier surface topography from archive oblique aerial images. *Geomorphology* 282, 18–26. <https://doi.org/10.1016/j.geomorph.2017.01.008>.
- Midgley, N.G., Tonkin, T.N., Graham, D.J., Cook, S.J., 2018. Evolution of high-Arctic glacial landforms during deglaciation. *Geomorphology* 311, 63–75. <https://doi.org/10.1016/j.geomorph.2018.03.027>.
- Moritz, R.E., Bitz, C.M., Steig, E.J., 2002. Dynamics of recent climate change in the Arctic. *Science* (80- ) <https://doi.org/10.1126/science.1076522>.
- Napieralski, J., Harbor, J., Li, Y., 2007. Glacial geomorphology and geographic information systems. *Earth-Sci. Rev.* 85, 1–22. <https://doi.org/10.1016/j.earscirev.2007.06.003>.
- Pereira, F., Marques, J.S., Heleno, S., Pina, P., 2020. Detection and delineation of sorted stone circles in Antarctica. *Remote Sens.* 12, 1–15. <https://doi.org/10.3390/rs12010160>.
- Ramsankaran, R., Navinkumar, P.J., Dashora, A., Kulkarni, A., 2020. UAV-based Survey of Glaciers in Himalayas: Opportunities and Challenges. <https://doi.org/10.20944/PRINTER202002.0442.V1>.
- Rippin, D.M., Pomfret, A., King, N., 2015. High resolution mapping of supra-glacial drainage pathways reveals link between micro-channel drainage density, surface roughness and surface reflectance. *Earth Surf. Process. Landf.* 40, 1279–1290. <https://doi.org/10.1002/esp.3719>.
- Rossini, M., Di Mauro, B., Garzonio, R., Baccolo, G., Cavallini, G., Mattavelli, M., De Amicis, M., Colombo, R., 2018. Rapid melting dynamics of an alpine glacier with repeated UAV photogrammetry. *Geomorphology* 304, 159–172. <https://doi.org/10.1016/j.geomorph.2017.12.039>.
- Ryan, J.C., Hubbard, A.L., Box, J.E., Todd, J., Christoffersen, P., Carr, J.R., Holt, T.O., Snooke, N., 2015. UAV photogrammetry and structure from motion to assess calving dynamics at Store Glacier, a large outlet draining the Greenland ice sheet. *Cryosphere* 9, 1–11. <https://doi.org/10.5194/tc-9-1-2015>.
- Scaioni, M., Barazzetti, L., Corti, M., Crippa, J., Azzoni, R.S., Fugazza, D., Cernuschi, M., Diolaiuti, G.A., 2018. Integration of terrestrial and UAV photogrammetry for the assessment of collapse risk in Alpine glaciers. *Int. Arch. Photogramm. Remote Sens. Spat. Inf. Sci.* 42, 445–452. <https://doi.org/10.5194/isprs-archives-XLII-3-W4-445-2018>.
- Seier, G., Kellerer-Pirklbauer, A., Wecht, M., Hirschmann, S., Kaufmann, V., Lieb, G.K., Sulzer, W., 2017. UAS-based change detection of the glacial and proglacial transition zone at Pasterze Glacier, Austria. *Remote Sens.* 9, 1–19. <https://doi.org/10.3390/rs9060549>.
- Smith, M.W., Carrivick, J.L., Quincey, D.J., 2015. Structure from motion photogrammetry in physical geography. *Prog. Phys. Geogr.* <https://doi.org/10.1177/0309133315615805>.
- Storni, E., Hugentobler, M., Manconi, A., Loew, S., 2020. Monitoring and analysis of active rockslide-glacier interactions (Moosfluh, Switzerland). *Geomorphology* 371, 107414. <https://doi.org/10.1016/j.geomorph.2020.107414>.
- Storarr, R.D., Ewertowski, M., Tomczyk, A.M., Barr, I.D., Livingstone, S.J., Ruffell, A., Stoker, B.J., Evans, D.J.A., 2020. Equifinality and preservation potential of complex eskers. *Boreas* 49, 211–231. <https://doi.org/10.1111/bor.12414>.
- SziŃo, J., Bialik, R.J., 2018. Recession and ice surface elevation changes of baranowski glacier and its impact on proglacial relief (King George Island, West Antarctica). *Geosci.* 8. <https://doi.org/10.3390/geosciences8100355>.

- Tavani, S., Granado, P., Riccardi, U., Seers, T., Corradetti, A., 2020. Terrestrial SfM-MVS photogrammetry from smartphone sensors. *Geomorphology* 367, 107318. <https://doi.org/10.1016/j.geomorph.2020.107318>.
- Tirlă, L., Drăgușin, V., Bajo, P., Covaliov, S., Cruceru, N., Ersek, V., Hanganu, D., Hellstrom, J., Hoffmann, D., Mirea, I., Sava, T., Sava, G., Șandric, I., 2020. Quaternary environmental evolution in the South Carpathians reconstructed from glaciokarst geomorphology and sedimentary archives. *Geomorphology*, 354 <https://doi.org/10.1016/j.geomorph.2020.107038>.
- Tomczyk, A.M., Ewertowski, M.W., 2020. UAV-based remote sensing of immediate changes in geomorphology following a glacial lake outburst flood at the Zackenberg river, north-east Greenland. *J. Maps* 16, 86–100. <https://doi.org/10.1080/17445647.2020.1749146>.
- Tomczyk, A.M., Ewertowski, M.W., Stawska, M., Rachlewicz, G., 2019. Detailed alluvial fan geomorphology in a high-arctic periglacial environment, Svalbard: application of unmanned aerial vehicle (UAV) surveys. *J. Maps* 15, 460–473. <https://doi.org/10.1080/17445647.2019.1611498>.
- Tomczyk, A.M., Ewertowski, M.W., Carrivick, J.L., 2020. Geomorphological impacts of a glacier lake outburst flood in the high arctic Zackenberg River, NE Greenland. *J. Hydrol.* 591, 125300. <https://doi.org/10.1016/j.jhydrol.2020.125300>.
- Tonkin, T.N., Midgley, N.G., 2016. Ground-control networks for image based surface reconstruction: an investigation of optimum survey designs using UAV derived imagery and structure-from-motion photogrammetry. *Remote Sens.* 8, 16–19. <https://doi.org/10.3390/rs8090786>.
- Tonkin, T.N., Midgley, N.G., Graham, D.J., Labadz, J.C., 2014. The potential of small unmanned aircraft systems and structure-from-motion for topographic surveys: a test of emerging integrated approaches at Cwm Idwal, North Wales. *Geomorphology* 226, 35–43. <https://doi.org/10.1016/j.geomorph.2014.07.021>.
- Tonkin, T.N., Midgley, N.G., Cook, S.J., Graham, D.J., 2016. Ice-cored moraine degradation mapped and quantified using an unmanned aerial vehicle: a case study from a polythermal glacier in Svalbard. *Geomorphology* 258, 1–10. <https://doi.org/10.1016/j.geomorph.2015.12.019>.
- van der Sluijs, J., Kokelj, S.V., Fraser, R.H., Tunnicliffe, J., Lacelle, D., 2018. Permafrost terrain dynamics and infrastructure impacts revealed by UAV photogrammetry and thermal imaging. *Remote Sens.*, 10 <https://doi.org/10.3390/rs10111734>.
- Van Woerkom, T., Steiner, J.F., Kraaijenbrink, P.D.A., Miles, E.S., Immerzeel, W.W., 2019. Sediment supply from lateral moraines to a debris-covered glacier in the Himalaya. *Earth Surf. Dyn.* 7, 411–427. <https://doi.org/10.5194/esurf-7-411-2019>.
- Vivero, S., Lambiel, C., 2019. Monitoring the crisis of a rock glacier with repeated UAV surveys. *Geogr. Helv.* 74, 59–69. <https://doi.org/10.5194/gh-74-59-2019>.
- Walsh, J.E., Overland, J.E., Groisman, P.Y., Rudolf, B., 2011. Ongoing climate change in the arctic. *Ambio*. <https://doi.org/10.1007/s13280-011-0211-z>.
- Watts, A.C., Ambrosia, V.G., Hinkley, E.A., 2012. Unmanned aircraft systems in remote sensing and scientific research: classification and considerations of use. *Remote Sens.* 4, 1671–1692. <https://doi.org/10.3390/rs4061671>.
- Westoby, M.J., Brasington, J., Glasser, N.F., Hambrey, M.J., Reynolds, J.M., 2012. "Structure-from-Motion" photogrammetry: a low-cost, effective tool for geoscience applications. *Geomorphology* 179, 300–314. <https://doi.org/10.1016/j.geomorph.2012.08.021>.
- Westoby, M.J., Dunning, S.A., Woodward, J., Hein, A.S., Marrero, S.M., Winter, K., Sugden, D.E., 2015. Instruments and methods: sedimentological characterization of Antarctic moraines using UAVs and Structure-from-Motion photogrammetry. *J. Glaciol.* 61, 1088–1102. <https://doi.org/10.3189/2015jog15j086>.
- Westoby, M.J., Rounce, D.R., Shaw, T.E., Fyffe, C.L., Moore, P.L., Stewart, R.L., Brock, B.W., 2020. Geomorphological evolution of a debris-covered glacier surface. *Earth Surf. Process. Landf.* 45, 3431–3448. <https://doi.org/10.1002/esp.4973>.
- Whitehead, K., Moorman, B.J., Hugenholtz, C.H., 2013. Brief Communication: low-cost, on-demand aerial photogrammetry for glaciological measurement. *Cryosphere* 7, 1879–1884. <https://doi.org/10.5194/tc-7-1879-2013>.
- Wigmore, O., Mark, B., 2017. Monitoring tropical debris covered glacier dynamics from high resolution unmanned aerial vehicle photogrammetry, Cordillera Blanca, Peru. *Cryosphere Discuss.* 1–27. <https://doi.org/10.5194/tc-2017-31>.
- Wilson, R., Harrison, S., Reynolds, J., Hubbard, A., Glasser, N.F., Wünderlich, O., Iribarren Anaconda, P., Mao, L., Shannon, S., 2019. The 2015 Chileno Valley glacial lake outburst flood, Patagonia. *Geomorphology* 332, 51–65. <https://doi.org/10.1016/j.geomorph.2019.01.015>.
- Woodget, A.S., Fyffe, C., Carbonneau, P.E., 2018. From manned to unmanned aircraft: adapting airborne particle size mapping methodologies to the characteristics of sUAS and SfM. *Earth Surf. Process. Landf.* <https://doi.org/10.1002/esp.4285>.

Appendix A. Supplementary data.

| ID   | Author  | Year of publication | Region                           | Glacier/object                   | Latitude | Longitude | Date  | Type of study            | Forms           | Size of studied area [km <sup>2</sup> ] | Type of drone used | Name of drone used  | Type of sensor | Name of sensor                                       | Resolution of orthophotomap [cm] | Resolution of DEM [cm] | Total number of photos | Mission design and performance |
|------|---|---------------------|----------------------------------|----------------------------------|----------|-----------|---|--------------------------|-----------------|---|--------------------|---|----------------|--|----------------------------------|------------------------|------------------------|--------------------------------|
| 1    | <a href="#">Allaert et al. (2018)</a>         | 2018                | Svalbard                         | Nordenskiöldbreen                | 78.6719  | 16.9108   | 07.2017                                     | Geomorphological mapping | drumlins        | 0.375                                   | multirotor         | DJI Phantom 4 Pro   | RGB            | build-in   | N/A                              | 11                     | 671                    | Manually                       |
| 2    | <a href="#">Bash and Moorman (2020)</a>       | 2020                | Bylot Island (Canada)            | Fountain glacier                 | 72.9167  | -78.6667  | 07.2016                                     | Change detection         | N/A             | 0.185                                   | unknown            | N/A   | RGB            | N/A  | 10                               | 10                     | N/A                    | N/A                            |
| 3    | <a href="#">Bernard et al. (2017)</a>         | 2017                | Svalbard                         | Austre Lovénbreen                | 78.8867  | 12.1472   | 09.2015; 10.2015                            | Change detection         | moraine         | 0.040                                   | multirotor         | DJI Phantom 3 Professional  | RGB            | build-in   | N/A                              | N/A                    | N/A                    | Manually                       |
| 4    | <a href="#">Bernard et al. (2018)</a>         | 2018                | Svalbard                         | Austre Lovénbreen                | 79.4500  | 12.2500   | 2016  | Change detection         | N/A             | N/A                                     | multirotor         | DJI Phantom 3 Advanced  | RGB            | build-in   | 10                               | 10                     | 1758                   | Autonomous                     |
| 5_1  | <a href="#">Berthling et al. (2020)</a>       | 2020                | Svalbard                         | Ny-Ålesund area                  | 78.9667  | 11.3833   | 2016  | Geomorphological mapping | various         | N/A                                     | unknown            | N/A   | RGB            | N/A  | 20                               | 20                     | N/A                    | N/A                            |
| 5_2  | <a href="#">Berthling et al. (2020)</a>       | 2020                | Svalbard                         | Blomstrandøya                    | 79.0667  | 11.6333   | 2016  | Geomorphological mapping | various         | N/A                                     | unknown            | N/A   | RGB            | N/A  | 20                               | 20                     | N/A                    | N/A                            |
| 6    | <a href="#">Buhler et al. (2016)</a>          | 2016                | Alps (Switzerland)               | Flüela Valley                    | 46.7503  | 9.9475    | 08.2015; 09.2015                            | Change detection         | N/A             | 0,128; 0,363                            | multirotor         | Falcon 8  | RGB; NIR       | Sony Nex-7   | 2.5                              | 10                     | 252; 359               | Autonomous                     |
| 7    | <a href="#">Chandler et al. (2016)</a>        | 2016                | Iceland                          | Skálafellsjökull                 | 64.3019  | -15.7922  | 2013  | Geomorphological mapping | moraine         | 2.000                                   | multirotor         | Quest UAV 200   | RGB            | Panasonic LUMIX DMC-LX5                              | N/A                              | 9                      | 1980                   | N/A                            |
| 8    | <a href="#">Chandler et al. (2020a)</a>       | 2020                | Iceland                          | Fjallsjökull                     | 64.0167  | -16.4167  | 2016; 2017; 2018; 2019                      | Process-form studies     | moraine         | ~0,500                                  | multirotor         | DJI Phantom 3 Advanced; DJI Phantom 3 Professional; DJI Phantom 4 Pro | RGB            | build-in   | ~3                               | ~6                     | 515; 642; 706; 449     | Autonomous; manually           |
| 9    | <a href="#">Chandler et al. (2020b)</a>       | 2020                | Iceland                          | Fjallsjökull                     | 64.0167  | -16.4167  | 2016; 2017; 2018; 2019                      | Change detection         | foreland        | ~0,500                                  | multirotor         | DJI Phantom 3 Advanced; DJI Phantom 3 Professional; DJI Phantom 4 Pro | RGB            | build-in   | ~5                               | ~5                     | 515; 642; 706; 449     | Autonomous; manually           |
| 10   | <a href="#">Chudley et al. (2019)</a>         | 2019                | Greenland                        | Store glacier                    | 70.0667  | -50.0833  | 08.2017                                     | Geomorphological mapping | N/A             | ~5,000                                  | wing               | Skywalker X8  | RGB            | Sony α6000   | 15                               | 20                     | ~3000                  | Autonomous                     |
| 11   | <a href="#">Dabbski et al. (2017)</a>         | 2017                | Kings George Island (Antarctica) | Demay Point Peninsula            | -62.2125 | -58.4306  | 10.2015                                     | Geomorphological mapping | various         | 0.500                                   | wing               | PW-ZOOM UAV   | RGB            | Canon 700D   | 5                                | 20                     | 766                    | Autonomous                     |
| 12_1 | <a href="#">Dabbski et al. (2020)</a>         | 2020                | Kings George Island (Antarctica) | Ecology glacier                  | -62.1833 | -58.4667  | 11.2016                                     | Geomorphological mapping | various         | 16.800                                  | wing               | PW-ZOOM UAV   | RGB            | Canon 700D   | 6                                | 25                     | 7678                   | Autonomous                     |
| 12_2 | <a href="#">Dabbski et al. (2020)</a>         | 2020                | Kings George Island (Antarctica) | Sfinks glacier                   | -62.1889 | -58.4583  | 11.2016                                     | Geomorphological mapping | various         | 16.800                                  | wing               | PW-ZOOM UAV   | RGB            | Canon 700D   | 6                                | 25                     | 7678                   | Autonomous                     |
| 12_3 | <a href="#">Dabbski et al. (2020)</a>         | 2020                | Kings George Island (Antarctica) | Baranowski glacier               | -62.2000 | -58.4500  | 11.2016                                     | Geomorphological mapping | various         | 16.800                                  | wing               | PW-ZOOM UAV   | RGB            | Canon 700D   | 6                                | 25                     | 7678                   | Autonomous                     |
| 13   | <a href="#">Eichel et al. (2020)</a>          | 2020                | Alps (Switzerland)               | Turtmann Valley                  | 46.1333  | 7.6872    | 08.2014; 08.2017                            | Geomorphological mapping | moraine         | 0.0004                                  | multirotor         | OktoXL; DJI Phantom 4 Pro+  | RGB            | Panasonic Lumix GX1; build-in                        | 0.2                              | 0.2                    | 416; 564               | Manually                       |
| 14   | <a href="#">Ely et al. (2017)</a>             | 2017                | Lapland (Sweden)                 | Isfallsglaciären                 | 67.9140  | 18.5720   | 08.2014                                     | Geomorphological mapping | flutes          | 0.600                                   | multirotor         | DroidWorx Gexacopter  | RGB            | Nikon D5300  | 2                                | 2                      | 836                    | Autonomous                     |
| 15   | <a href="#">Evans et al. (2016)</a>           | 2016                | Iceland                          | Fláajökull                       | 64.3653  | -15.6522  | 09.2014                                     | Geomorphological mapping | various         | 0.100                                   | multirotor         | N/A   | RGB            | N/A  | 2                                | 3                      | 175                    | Manually                       |
| 16   | <a href="#">Ewertowski et al. (2016)</a>      | 2016                | Svalbard                         | Nordenskiöldbreen                | 78.6667  | 17.1667   | 07.2014                                     | Geomorphological mapping | various         | 0.500                                   | multirotor         | N/A   | RGB            | N/A  | 2                                | 4                      | 400                    | N/A                            |
| 17   | <a href="#">Ewertowski et al. (2019)</a>      | 2019                | Svalbard                         | Hörbyebreen                      | 78.7667  | 16.3833   | 07.2016                                     | Geomorphological mapping | various         | ~1,000                                  | multirotor         | DJI Phantom 3 Advanced  | RGB            | build-in   | 2                                | 8                      | 2614                   | Manually                       |
| 18   | <a href="#">Ewertowski and Tomczyk (2020)</a> | 2020                | Svalbard                         | Ebbabreen, Ragnarbreen           | 78.7375  | 16.9496   | 2014  | Geomorphological mapping | moraine         | 3.330                                   | multirotor         | DJI Phantom 3 Advanced  | RGB            | build-in   | N/A                              | N/A                    | N/A                    | N/A                            |
| 19   | <a href="#">Fey and Krainer (2020)</a>        | 2020                | Alps (Italy)                     | rockglacier Lazaun               | 46.7469  | 10.7556   | 09.2016; 06.2017; 08.2017; 10.2017; 06.2018 | Change detection         | rock glacier    | 0.110                                   | multirotor         | Surveying Robot Mk.AD   | RGB            | Sony A6000   | 3                                | 10                     | N/A                    | Autonomous                     |
| 20   | <a href="#">Fey et al. (2017)</a>             | 2017                | Alps (Austria)                   | Marzell rockslide                | 46.7800  | 10.8800   | 10.2012                                     | Change detection         | rockslide       | N/A                                     | multirotor         | TWINS NRN   | RGB            | Ricoh GXR A12  | 5                                | N/A                    | N/A                    | N/A                            |
| 21   | <a href="#">Fugazza et al. (2015)</a>         | 2015                | Alps (Italy)                     | Forni glacier                    | 46.3989  | 10.5903   | 08.2014                                     | Change detection         | various         | 0.960                                   | wing               | SwingletCam   | RGB            | Canon Ixus 127 HS                                    | 12                               | 60                     | N/A                    | Autonomous                     |
| 22   | <a href="#">Fugazza et al. (2018)</a>         | 2018                | Alps (Italy)                     | Forni glacier                    | 46.3989  | 10.5903   | 2014; 2016                                  | Geomorphological mapping | N/A             | 2.210                                   | wing               | SwingletCam   | RGB            | Canon Ixus 127 HS; Canon Powershot                   | 15                               | 60                     | N/A                    | Autonomous                     |
| 23   | <a href="#">Glasser et al. (2020)</a>         | 2020                | Wales                            | Moel Ysgyfarnogod                | 52.8872  | -3.9961   | N/A   | Geomorphological mapping | bedrock surface | 0.0004                                  | multirotor         | DJI Phantom 4   | RGB            | build-in   | 2.33                             | 4.67                   | 872                    | N/A                            |
| 24   | <a href="#">Groos et al. (2019)</a>           | 2019                | Alps (Switzerland)               | Kanderfirn                       | 46.8000  | 8.3333    | 09.2017; 06.2018; 08.2018; 09.2018          | Change detection         | N/A             | 3.400                                   | wing               | Own construction (Paparazzi UAV project)                              | RGB            | GoPro Gero 5 Black                                   | 5                                | 25                     | 314; 824; 850; 215     | Autonomous                     |
| 25   | <a href="#">Hackney and Clayton (2015)</a>    | 2015                | Iceland                          | Skálafellsjökull; Heinbergjökull | 64.3019  | -15.7922  | 2013  | Geomorphological mapping | foreland        | 15.000                                  | wing               | Quest UAV 200   | RGB            | Panasonic LUMIX DMC-LX5                              | 5                                | 10                     | 1980                   | Manually                       |
| 26   | <a href="#">Hedding et al. (2020)</a>         | 2020                | Altai (Russia)                   | Malyi Aktru glacier              | 50.1008  | 87.6706   | 08.2018; 08.2019                            | Geomorphological mapping | moraine         | 1.700                                   | multirotor         | DJI Mavic Pro   | RGB            | build-in   | 5; 10; 5                         | 17; 30; 10             | 787                    | N/A                            |
| 27   | <a href="#">Hendrickx et al. (2020)</a>       | 2020                | Alps (Switzerland)               | Sanetsch Pass                    | 46.3458  | 7.3042    | 2017; 2018; 2019                            | Change detection         | talus slope     | 1,2; 1,3; 2,0                           | multirotor         | DJI F550; DJI Phantom 4 Pro   | RGB            | Panasonic Lumix DMX-GM5; build in                    | 10                               | 10                     | 1088; 2493; 3053       | Autonomous                     |
| 28   | <a href="#">Immerzeel et al. (2014)</a>       | 2014                | Himalaya (Nepal)                 | Lirung glacier                   | 28.4220  | 85.5170   | 05.2013; 10.2013                            | Change detection         | N/A             | 1.600                                   | wing               | SwingletCam   | RGB            | Canon Ixus 125 HS                                    | 10                               | 20                     | 776; 456               | Autonomous                     |
| 29   | <a href="#">Jouvet et al. (2016)</a>          | 2016                | Greenland                        | Bowdoin glacier                  | 77.6833  | -68.5833  | 05.2015; 06.2015; 07.2015; 08.2015          | Change detection         | N/A             | 2.000                                   | wing               | Skywalker X8  | RGB            | Sony α6000   | 10                               | 100                    | 1000                   | Autonomous                     |
| 30   | <a href="#">Jouvet et al. (2018)</a>          | 2018                | Greenland                        | Bowdoin glacier                  | 77.6833  | -68.5833  | 07.07.2016 - 19.07.2016                     | Change detection         | N/A             | 3.000                                   | hybrid             | Firefly6  | RGB            | Sony α6000   | 10                               | 10                     | 3900                   | Autonomous                     |
| 31   | <a href="#">Kaufmann et al. (2018)</a>        | 2018                | Alps (Austria)                   | Tschadinhorn rock glacier        | 46.9939  | 12.8631   | 07.2016; 08.2017                            | Change detection         | rock glacier    | 0.053                                   | each type          | Hexacopter twinHex; QuestUAV; DJI Mavic Pro; Falcon 8; DJI Phantom 4  | RGB            | Ricoh GXR A12; Sony ILCE-6000; Sony NEX-5N; build-in | 10; 5                            | 2; 10                  | 1636                   | N/A                            |
| 32   | <a href="#">Kienholz et al. (2020)</a>        | 2020                | Alaska (USA)                     | Mendenhall glacier               | 58.4958  | -134.5322 | 2018; 2019                                  | Change detection         | N/A             | N/A                                     | multirotor         | DJI Phantom 4 Pro   | RGB            | build-in   | N/A                              | N/A                    | 28900                  | N/A                            |
| 33   | <a href="#">Kraaijenbrink et al. (2016)</a>   | 2016                | Himalaya (Nepal)                 | Lirung glacier                   | 28.1311  | 85.5242   | 05.2013; 10.2013; 05.2014                   | Change detection         | N/A             | ~1,600                                  | wing               | SwingletCam   | RGB            | N/A  | 20                               | 20                     | 284; 307; 314          | Autonomous                     |
| 34   | <a href="#">Lamsters et al. (2020)</a>        | 2020                | Greenland                        | Russell glacier                  | 67.0958  | -50.2167  | 07.2016                                     | Geomorphological mapping | N/A             | 0.450                                   | multirotor         | DJI Phantom 3 Advanced  | RGB            | build-in   | 4                                | 8                      | 453                    | Autonomous                     |
| 35   | <a href="#">Lamsters et al. (2020)</a>        | 2020                | Antarctica                       | Argentine Islands                | -65.2500 | -64.2667  | 02.2018; 03.2018                            | Geomorphological mapping | N/A             | 4.480                                   | multirotor         | DJI Phantom 3 Advanced  | RGB            | build-in   | 3.4                              | 6.8                    | 9546                   | Autonomous                     |

|      |   |      |                                  |                                 |          |           |   |                                 |                       |                     |            |  |     |  |          |            |                       |                      |
|------|---|------|----------------------------------|---------------------------------|----------|-----------|---|---------------------------------|-----------------------|---------------------|------------|--|-----|--|----------|------------|-----------------------|----------------------|
| 36   | <a href="#">Le Heron et al. (2019)</a>        | 2019 | Henan Province (China)           | Shimengou                       | 33.9361  | 112.7139  | N/A   | Geomorphological mapping        | various               | N/A                 | multirotor | DJI Mavic Pro  | RGB | build-in   | N/A      | N/A        | ~1000                 | N/A                  |
| 37   | <a href="#">Lousada et al. (2018)</a>         | 2018 | Svalbard                         | Advent Valley                   | 78.1858  | 15.9239   | 07.2009   | Geomorphological mapping        | ice wedge             | 0.080               | unknown    | N/A  | RGB | N/A  | 6        | N/A        | N/A                   | N/A                  |
| 38   | <a href="#">Mather et al. (2018)</a>          | 2018 | Dartmoor (SW England)            | Leeden Tor                      | 50.5273  | -4.0292   | 08.2016; 09.2016  | Geomorphological mapping        | N/A                   | 0.42; 0.12          | each type  | Sensefly eBee; DJI Phantom 3 Professional                                    | RGB | build-in   | 3,6; 2,3 | 3,5; 2,6   | 219; 200              | Autonomous           |
| 39   | <a href="#">Midgley et al. (2018)</a>         | 2018 | Svalbard                         | Midtre Lovénbreen               | 78.8898  | 12.0563   | 07.2014   | Change detection                | moraine               | N/A                 | multirotor | DJI S800   | RGB | Canon EOS M                                      | 2        | 2          | 1042                  | N/A                  |
| 40   | <a href="#">Pereira et al. (2020)</a>         | 2020 | Kings George Island (Antarctica) | Barton Peninsula                | -62.2333 | -58.7667  | 02.2018   | Geomorphological mapping        | stone circles         | 0.013               | multirotor | DJI Phantom 3  | RGB | build-in   | 0.3      | 0.2        | 500                   | Manually             |
| 41_1 | <a href="#">Ramsankaran et al. (2020)</a>     | 2020 | Himalaya (India)                 | East Rathong glacier            | 27.5667  | 88.1083   | 10.2017   | Geomorphological mapping        | N/A                   | 1.070               | wing       | Sensefly eBee plus   | RGB | Sony DSC-WX220; build in                         | 10       | 10         | 135                   | Autonomous           |
| 41_2 | <a href="#">Ramsankaran et al. (2020)</a>     | 2020 | Himalaya (India)                 | Hamath glacier                  | 32.2667  | 77.3583   | 09.2018   | Geomorphological mapping        | N/A                   | 0.750               | wing       | Sensefly eBee plus   | RGB | Sony DSC-WX220; build in                         | 10       | 10         | 107                   | Autonomous           |
| 41_3 | <a href="#">Ramsankaran et al. (2020)</a>     | 2020 | Himalaya (India)                 | Panchinala-A glacier            | 32.7211  | 77.3044   | 06.2019   | Geomorphological mapping        | N/A                   | 1.380               | wing       | Sensefly eBee plus   | RGB | Sony DSC-WX220; build in                         | 10       | 10         | 360                   | Autonomous           |
| 42   | <a href="#">Rippin et al. (2015)</a>          | 2015 | Svalbard                         | Midtre Lovénbreen               | 78.8898  | 12.0563   | 08.2013; 09.2013  | Geomorphological mapping        | drainage pathways     | ~1,000              | wing       | Quest UAV 200  | RGB | Panasonic LUMIX DMC-LX5                          | 5        | 10         | 423                   | Autonomous           |
| 43   | <a href="#">Rossini et al. (2018)</a>         | 2018 | Alps (Switzerland)               | Morteratsch glacier             | 46.4094  | 9.9317    | 08.2016; 09.2016  | Change detection                | N/A                   | 0.382; 0.634        | multirotor | DJI Phantom 4  | RGB | build-in   | 5        | 2          | 172; 368              | Autonomous           |
| 44   | <a href="#">Ryan et al. (2015)</a>            | 2015 | Greenland                        | Store glacier                   | 70.4000  | -50.6000  | 08.2013; 09.2013  | Change detection                | N/A                   | 3,170; 4,950; 5,020 | wing       | Skywalker X8   | RGB | Panasonic LUMIX DMC-LX5                          | N/A      | 40; 38; 39 | 611; 1051; 567        | Autonomous           |
| 45   | <a href="#">Scaioni et al. (2018)</a>         | 2018 | Alps (Italy)                     | Forni glacier                   | 46.3989  | 10.5903   | 08.2014; 09.2016  | Change detection                | N/A                   | N/A                 | each type  | SwingletCam; Tarot quadcopter  | RGB | Canon Ixus 127 HS; Canon Powershot ELPH 320 HS   | N/A      | N/A        | N/A                   | Autonomous           |
| 46   | <a href="#">Seier et al. (2017)</a>           | 2017 | Alps (Austria)                   | Pasterze Glacier                | 47.0856  | 12.7233   | 09.2016; 11.2016  | Change detection                | glacier tongue        | 0.340               | wing       | Quest UAV  | RGB | Sony a6000                                       | 15       | 15         | 100; 354              | N/A                  |
| 47   | <a href="#">Storni et al. (2020)</a>          | 2020 | Alps (Switzerland)               | Moosfluh landslide              | 46.4000  | 8.0417    | 08.2018   | Change detection                | rockslide             | N/A                 | multirotor | DJI Phantom 4 Pro+   | RGB | build-in   | 3        | N/A        | ~3000                 | Autonomous           |
| 48_1 | <a href="#">Storror et al. (2020)</a>         | 2020 | Svalbard                         | Hørbyebreen                     | 78.7500  | 16.3833   | 08.2017   | Geomorphological mapping        | eskers                | N/A                 | multirotor | DJI Phantom 3 Advanced; DJI Mavic Pro  | RGB | build-in   | 5        | 16         | N/A                   | N/A                  |
| 48_2 | <a href="#">Storror et al. (2020)</a>         | 2020 | Iceland                          | Breiðamerkurjökull              | 64.0583  | -16.3000  | 05.2017   | Geomorphological mapping        | eskers                | N/A                 | multirotor | DJI Phantom 3 Advanced; DJI Mavic Pro  | RGB | build-in   | 3        | 60         | N/A                   | N/A                  |
| 49   | <a href="#">Tirila et al. (2020)</a>          | 2020 | Făgăraș Mountains (Romania)      | Muşeteica glacial cirque        | 45.5754  | 24.6494   | N/A   | Geomorphological mapping        | marble karst; caves   | 1.000               | multirotor | DJI Phantom 4  | RGB | build-in   | 10       | 50         | 1314                  | Autonomous           |
| 50   | <a href="#">Tomczyk et al. (2019)</a>         | 2019 | Svalbard                         | Dynamisk creek fan              | 78.7000  | 16.6167   | 08.2014   | Geomorphological mapping        | alluvial fans         | 0.800               | multirotor | DJI Phantom 2 Vision   | RGB | build-in   | 2        | 4          | 880                   | Manually             |
| 51   | <a href="#">Tomczyk and Ewertowski (2020)</a> | 2020 | Greenland                        | Zackenberk river                | 74.5000  | -20.5000  | 08.2017   | Geomorphological mapping        | river                 | N/A                 | multirotor | DJI Phantom 4 Pro  | RGB | build-in   | N/A      | N/A        | ~5000                 | Manually             |
| 52   | <a href="#">Tomczyk et al. (2020)</a>         | 2020 | Greenland                        | Zackenberk river                | 74.5000  | -20.5000  | 08.2017   | Change detection                | river                 | 0.150               | multirotor | DJI Phantom 4 Pro  | RGB | build-in   | 1.8-2.8  | 3.6-5.6    | ~5000                 | Manually             |
| 53   | <a href="#">Tonkin et al. (2014)</a>          | 2014 | Wales                            | Cwm Idwal moraine—mound complex | 53.1139  | -4.0272   | N/A   | Geomorphological mapping        | moraine               | 0.211               | multirotor | DJI S800   | RGB | Canon EOS-M                                      | 2.2      | 8.8        | 543                   | Autonomous           |
| 54   | <a href="#">Tonkin et al. (2016)</a>          | 2016 | Svalbard                         | Austre Lovénbreen               | 78.8867  | 12.0972   | 08.2014   | Change detection                | moraine               | 0.676               | multirotor | DJI S800   | RGB | Canon EOS-M                                      | N/A      | 50         | 1856                  | Autonomous           |
| 55   | <a href="#">Van der Sluijs et al. (2018)</a>  | 2018 | Northwest Territories (Canada)   | Mackenzie River                 | 68.5000  | -134.5000 | 2015; 2016; 2017  | Change detection                | permafrost terrain    | 14.270              | each type  | Spyder PX8 Plus; RX4-S Surveyor; DJI Inspire 1 Pro; eBee Plus; Phantom 4 Pro | RGB | Sony a6000; Sony RX100 III; Zenmuse X5; build in | 2.8      | 50         | 20461                 | Autonomous           |
| 56   | <a href="#">Van Woerkom et al. (2019)</a>     | 2019 | Himalaya (Nepal)                 | Lirung Glacier                  | 28.3833  | 85.9333   | 05.2013; 10.2013; 10.2015; 04.2016; 04.2017; 10.2017; 04.2018 | Change detection                | rock glacier; moraine | 1.500               | unknown    | N/A  | RGB | N/A  | 10       | 20         | N/A                   | N/A                  |
| 57   | <a href="#">Vivero and Lambiel (2019)</a>     | 2019 | Alps (Switzerland)               | La Roussette rock glacier       | 46.0368  | 7.4468    | 2016; 2017  | Change detection                | rock glacier          | 0.020               | wing       | eBee RTK   | RGB | SONY WX; S.O.D.A.                                | ~7       | ~7         | 63; 61; 57; 142; 150  | Autonomous           |
| 58   | <a href="#">Westoby et al. (2015)</a>         | 2015 | Antarctica                       | Heritage Range                  | -80.3000 | -81.3442  | N/A   | Assessment of surficial geology | moraine               | 0.300               | wing       | N/A  | RGB | Nikon D7000; Panasonic Lumix DMC-LX5             | N/A      | N/A        | 153                   | Autonomous; manually |
| 59   | <a href="#">Westoby et al. (2020)</a>         | 2020 | Alps (Italy)                     | Miage glacier                   | 45.8042  | 6.8406    | 06.2015; 07.2016; 07.2017; 07.2018                            | Change detection                | rock glacier          | 0.150               | multirotor | DJI Phantom 3 Professional   | RGB | build-in   | N/A      | 100        | 1052; 718; 1623; 1569 | Manually             |
| 60   | <a href="#">Whitehead et al. (2013)</a>       | 2013 | Bylot Island (Canada)            | Fountain glacier                | 73.0000  | -78.5000  | 2010; 2011  | Change detection                | N/A                   | N/A                 | wing       | Outlander UAV  | RGB | Panasonic Lumix DMC-LX3                          | 10       | 50         | 148                   | Autonomous           |
| 61   | <a href="#">Wjgmore and Mark (2017)</a>       | 2017 | Ands (Peru)                      | Llaca glacier                   | -9.4375  | -77.4417  | 07.2014; 07.2015  | Change detection                | N/A                   | ~0,500              | multirotor | Own construction   | RGB | Canon S110 Powershot                             | 5        | 10         | 323; 826              | Autonomous           |
| 62   | <a href="#">Wilson et al. (2019)</a>          | 2019 | Ands (Chile)                     | Chileno Valley                  | -46.8667 | -73.2000  | 02.2017   | Geomorphological mapping        | glacial lake          | 0.750               | wing       | Skywalker X8   | RGB | Sony NEX-5 N                                     | 50       | 50         | N/A                   | Autonomous           |



## Publikacja nr II z załącznikami

Śledź, S., & Ewertowski, M. W. (2022). Evaluation of the Influence of Processing Parameters in Structure-from-Motion Software on the Quality of Digital Elevation Models and Orthomosaics in the Context of Studies on Earth Surface Dynamics. *Remote Sensing*, 14(6). <https://doi.org/10.3390/rs14061312>

Do publikacji dołączono poniższe załączniki:

- 1) Appendix S1: Tabelę z wynikami eksperymentu dla każdego schematu postępowania w oprogramowaniu Agisoft Metashape;
- 2) Appendix S2: Histogramy rozkładu różnic wysokości, obliczonych na podstawie CPs dla każdego modelu otrzymanego w eksperymencie;
- 3) Appendix S3: Skrypt w języku Python do oprogramowania Agisoft Metashape. Wersja „The fastest”;
- 4) Appendix S4: Skrypt w języku Python do oprogramowania Agisoft Metashape. Wersja „Optimal”;
- 5) Appendix S5: Skrypt w języku Python do oprogramowania Agisoft Metashape. Wersja „Best quality”.



## Article

# Evaluation of the Influence of Processing Parameters in Structure-from-Motion Software on the Quality of Digital Elevation Models and Orthomosaics in the Context of Studies on Earth Surface Dynamics

Szymon Śledź \* and Marek W. Ewertowski

Faculty of Geographical and Geological Sciences, Adam Mickiewicz University, Krygowskiego 10, 61-680 Poznań, Poland; marek.ewertowski@gmail.com

\* Correspondence: szysle@amu.edu.pl; Tel.: +48-61-829-62-03

**Abstract:** The fully automated Structure-from-Motion approach for developing digital elevation models and orthomosaics has been known and used in photogrammetry for at least 15 years. Years of practice and experience have allowed researchers to provide a solid description of the applicability and limitations of this method. That being said, the impact of input processing parameters in software on the quality of photogrammetric products has yet to be fully ascertained empirically. This study is aimed at identifying the most advantageous processing workflow to fill this research gap by testing 375 different setup variations in the Agisoft Metashape software for the same set of images acquired using an unmanned aerial vehicle in a proglacial area. The purpose of the experiment was to determine three workflows: (1) the fastest, which has the shortest calculation time; (2) the best quality, which is as accurate as possible, regardless of the time taken for the calculations; and (3) the optimal, which is a compromise between accuracy and calculation time. Each of the 375 processing setup variations was assessed based on final product accuracy, i.e., orthomosaics and digital elevation models. The three workflows were selected based on calculating the height differences between the digital elevation models and the control points that did not participate in their georeferencing. The analyses of the root mean square errors (RMSE) and standard deviations indicate that excluding some of the optimization parameters during the camera optimization stage results in high RMSE and an increase in the values of standard deviation errors. Furthermore, it was shown that increasing the detail of individual processing steps in software does not always positively affect the accuracy of the resulting models. The experiment resulted in the development of three different workflows in the form of Python scripts for Agisoft Metashape software, which will help users to process image sets efficiently in the context of earth surface dynamics studies.



**Citation:** Śledź, S.; Ewertowski, M.W. Evaluation of the Influence of Processing Parameters in Structure-from-Motion Software on the Quality of Digital Elevation Models and Orthomosaics in the Context of Studies on Earth Surface Dynamics. *Remote Sens.* **2022**, *14*, 1312. <https://doi.org/10.3390/rs14061312>

Academic Editor: Waldemar Kociuba

Received: 26 January 2022

Accepted: 7 March 2022

Published: 9 March 2022

**Publisher's Note:** MDPI stays neutral with regard to jurisdictional claims in published maps and institutional affiliations.



**Copyright:** © 2022 by the authors. Licensee MDPI, Basel, Switzerland. This article is an open access article distributed under the terms and conditions of the Creative Commons Attribution (CC BY) license (<https://creativecommons.org/licenses/by/4.0/>).

**Keywords:** unmanned aerial vehicle; Structure-from-Motion; photogrammetry; Agisoft Metashape

## 1. Introduction

The relief of the Earth's surface is constantly modified by natural processes (e.g., erosion, weathering) and direct human activity. These dynamics are important to studies of the landscape evolution as well as studies of processes which may pose threats to human life and infrastructure. Therefore, landscape dynamics have been studied in a number of contexts that include the following: (a) the possibility of the occurrence of landslides and areas susceptible to their formation [1–3]; (b) to observe areas at risk of snow avalanches [4]; (c) to monitor land surface changes due to mining activities [5,6]; and (d) to assess the dynamics of aeolian processes [7] or changes to riverscapes [8–12]. One example of areas characterized by particularly high dynamics of the surface is proglacial areas [13–17]. Ongoing climate warming [18–20], characterized by an increase in mean annual air temperatures

and changes in precipitation, causes the melting of glaciers [21] and reveals numerous geomorphological forms in their forelands, previously hidden under the glacier ice [20,22–24]. Moreover, proglacial areas are an important storage of water (in the form of dead-ice) and sediments, which can be relatively easy to mobilize [20,25,26]. For example, meltwaters often have a significant erosive potential and can cause large transformations both in the immediate foreland of the glaciers and in the areas further away, through glacier lake outburst floods or debris flows [11,27–31]. For this reason, proglacial areas are currently the subject of research by many scientists who use modern research techniques to monitor and collect data on land surface characteristics and landform dynamics in front of retreating glaciers worldwide [17].

Unmanned aerial vehicles (UAV, drone), equipped with a sensor in the form of an RGB camera, have recently become a popular platform for observing various objects or areas from above [32–34]. The undoubted advantage of UAVs in environmental research is low price, mobility and high configuration options, depending on the model and manufacturer. Anderson and Gaston rightly noticed in 2013 [35] that UAVs will revolutionize spatial ecology—UAVs can now be found in more and more applications related to scientific and commercial activities. Thanks to the UAV, the operator can take images of the selected research objects from a low altitude while performing a manual or autonomous flight. A dedicated UAV application allows for setting up parameters such as flight altitude, flight speed, forward and side overlap of images, or marking the area of interest and designing the mission path. The current mobile applications significantly support the operator during a mission, e.g., automatically interrupting it when the battery is low and warning against bad weather conditions such as strong gusts of wind. In glacial geomorphology, UAVs have been widely used since 2010, and different studies utilized various UAV construction types, sensors, and flight parameters, depending on the shape of the studied area, meteorological conditions, research objectives and the expected accuracy of photogrammetric products [12,36,37]. It should be emphasized that in addition to aerial images obtained from UAVs, images collected from terrestrial photogrammetry (robotic or stationary) are becoming more and more popular (e.g., [38]).

The end result of the survey mission is a collection of images, which is a record of the current state of the studied area. The images can be used as photographic documentation, but primarily as data for the development of a digital elevation model (DEM) and orthomosaic as the end products of processing in Structure-from-Motion (SfM) software [39]. Thanks to the external Ground Control Points (GCPs), measured with the differential Global Navigation Satellite Systems (dGNSS) receiver (external georeferencing) or the locations embedded in the images from the on-board GNSS receiver (direct georeferencing, which can also be replaced by corrected camera positions as a text file imported to the software), the SfM software combines the images with each other based on characteristic points, marked on at least two images. As a result, first a sparse, and then a dense point cloud is obtained, which is the basis for generating the final photogrammetric products. A DEM, which is a three-dimensional model of the studied area's surface and orthomosaic, is commonly used for analyses related to geomorphological mapping (e.g., [22,28,40–42]), change detection (e.g., [38,43–45]), process-form studies [46] or mapping of surficial geology [47]. Evidence of the common use of UAV and the SfM method in geomorphology consists of publications in which the authors present the appropriate workflow of conduct during field research and in the further preparation of publications and presentation of results (e.g., [48–50]). Thus far, however, it has not been tested in detail how individual processing parameters in the SfM software affect the accuracy of the final result. Selection of the appropriate parameters is important because this stage has a crucial impact on the accuracy of the models obtained, which, if performed incorrectly, may lead to wrong results and thus incorrect conclusions from the conducted research.

Thus far, only limited publications have attempted to explain the influence of different calculation methods on the accuracy of photogrammetric products and possible ways to accelerate the processing of UAV-generated images into DEMs and orthomosaics.

For example, some attention was directed to the impact of mission design (e.g., [51–53]) or number and location of GCPs (e.g., [54–57]) on the accuracy of photogrammetric products. Another example is a work illustrating the processing of photo sets with no GCPs, but using co-registrations of the models (e.g., [58]). The authors proved that in this type of research, such as change detection, satisfactory results can be achieved even without GCPs, which is particularly important in the case of objects that are difficult to access. Similar conclusions were suggested by de Haas et al. [59], who presented evidence for the limited impact of GCPs on the increase in accuracy of models compared to projects where the co-alignment of multiple surveys is used. In addition, researchers also checked if the choice of software matters for the quality of DSM (e.g., [60]) and application of oblique photos (e.g., [61]), and critically assessed the use of RTK technology in UAVs compared to the traditional GCP scheme with UAVs without this technology [62]. The aim of this study was to investigate the influence of particular calculation parameters in the Agisoft Metashape software on the accuracy of photogrammetric products: DEMs and orthomosaics. Another objective was to find the most efficient workflows that can be used in the processing of large images sets of different research objects. For this purpose, 375 different workflows were formulated in the software, which were then checked while processing the same set of images representative of the proglacial area. Additionally, we aimed to select three workflows: (1) the fastest, which has the shortest calculation time; (2) the best quality, which is as accurate as possible, regardless of the time taken for calculations; and (3) the optimal, which is a compromise between accuracy and calculation time. These workflows are included in this article as Supplementary Materials in the form of Python scripts for processing a set of images in Agisoft Metashape. Thus far, there is no publication of such multi-threaded research in that form that can be easily implemented by other researchers in their work. The correct selection of the script and processing efficiency depend on the size of the image set, the expected accuracy, or the available computing power.

## 2. Materials and Methods

### 2.1. Study Area and Technical Information

The experiment used a set of UAV-collected images showing a sample area (~50,000 m<sup>2</sup>) of diverse terrain within the foreland of the Breiðamerkurjökull, Iceland (Figure 1). The flight took place on 5 September 2021 using the Map Pilot Pro mobile application in autonomous mode. To acquire the images, we used a multirotor DJI Phantom 4 Pro UAV equipped with a DJI FC6310 camera at a resolution of 20 MP and a focal length of 8.8 mm (24 mm equivalent for 35 mm format). In total, 82 vertical RAW images with a resolution of 5464 × 3640 pixels were taken and saved in the DNG format. The forward and side overlap were programmed at 80%, while the flight altitude was set at 70 m, rate of the image capture: ~5 s. The photographic exposure was set at 1/160 s (19 images) and 1/120 s (63 images). The GSD (Ground Sample Distance) of the images was ~1.92 cm/pix. The intention of the authors was to carefully reproduce the typical settings for missions performed for similar purposes [37]. During the flight, no strong gusts of wind or rainfall were noticed, even though the sky was fully cloudy. The quality of the images was checked in the Agisoft Metashape software before processing using a dedicated tool “Estimate image quality”—each image taken for calculations had a value above 0.80. DNG images were directly imported into Agisoft Metashape and were not subjected to exposure nor color modifications.

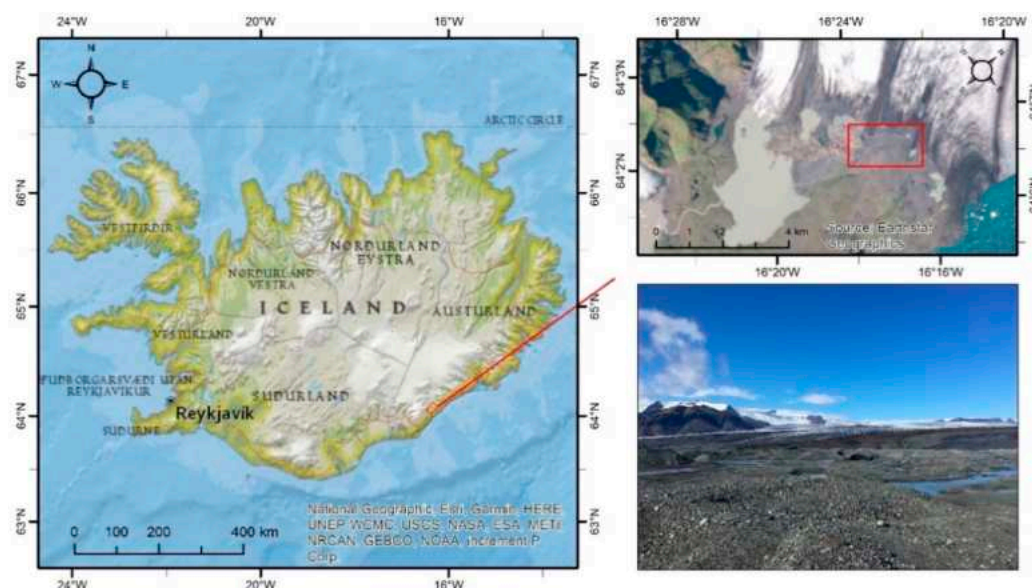


**Figure 1.** Location of the study area and a photo from the study area where the flight took place. The study areas represent a typical proglacial landscape, built from sands and gravel.

We used 40 GCPs, arranged in 4 rows of 10 points and 15 m apart at an angle of  $90^\circ$ , to georeference the model. Additionally, in order to check the accuracy of DEMs, 31 control points (CPs) not involved in georeferencing during SfM processing were randomly located in the study area. Each of the GCPs and CPs were constructed in the form of a circle of stones, in which the location of the middle stone was measured by the differential GNSS Topcon Hiper II receiver (Figure 2), using RTK survey technique and local base station (vector < 200 m). Survey uncertainties were between 0.008 and 0.015 m. The Agisoft Metashape Professional software (version 1.7.1 build 11,797) was used to process the set of images, model and generate DEMs and orthomosaics. The computing platform was a desktop computer with Windows 10 64 bit, a 6-core (12 thread) Intel Xeon E5-2440 processor with a base frequency of 2.40 GHz (2.90 GHz in Turbo mode), a GeForce GTX 1060 6 GB graphics card, and 79.97 GB DDR3 RAM. The computer was not used for other purposes during calculations to ensure the same computing power for all models.

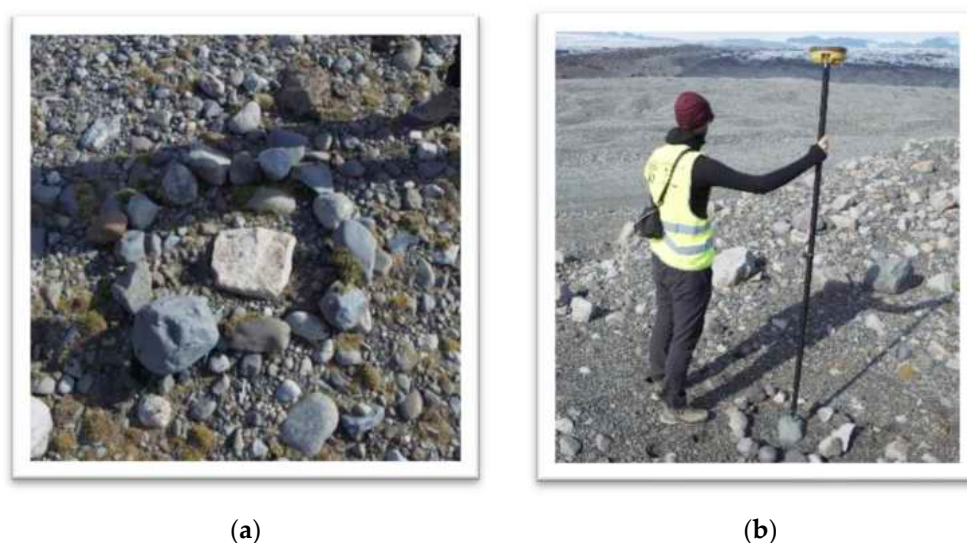


**Figure 2.** (a) Example of an established GCP; (b) method of measuring points with the GNSS receiver. GNSS measurement was carried out on the middle stone in the circle, which differed from the others by its size and shape.

## 2.2. Guidelines of the Experiment

Before starting the calculations, the planned variants of input processing parameters were formulated in the software, while naming of the projects followed a logical, structured and individual code (Figure 3). We investigated how the following parameters and their values would impact the final accuracy of the photogrammetric products (measured by errors on CPs) and calculation time:

- Alignment accuracy—five levels of accuracy: lowest, low, medium, high, and highest.
- The number of key points and tie—three sets were adopted:
  1. Set "A"—limit 10,000 key points and 1000 tie points.
  2. Set "B"—limit 100,000 key points and 10,000 tie points.
  3. Set "C"—no limit.
- Dense point cloud generation quality—five levels of quality: lowest, low, medium, high, and ultra-high.
- Optimization parameters—five sets were adopted:
  1. Set "A"—parameters: f.
  2. Set "B"—parameters: f, cx, cy.
  3. Set "C"—parameters: f, cx, cy, k1, k2.
  4. Set "D"—parameters: f, cx, cy, k1, k2, b1, b2.
  5. Set "E"—parameters: f, cx, cy, k1, k2, k3, k4, p1, p2, b1, b2.

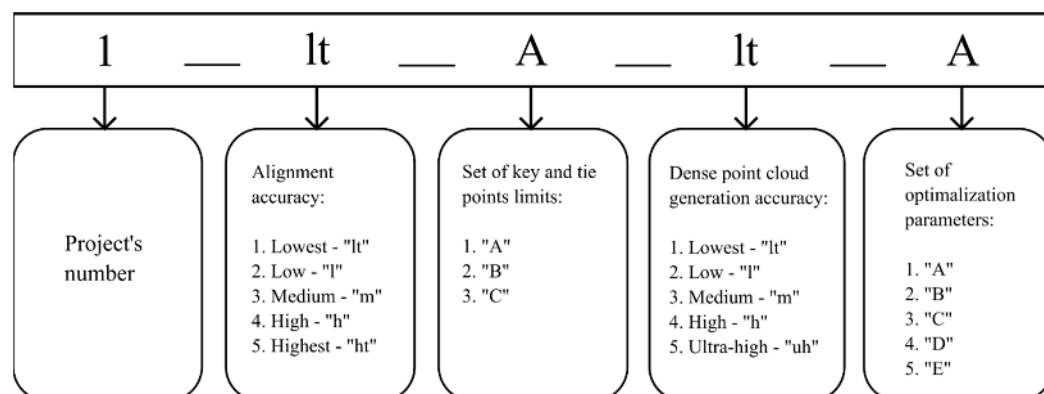


**Figure 3.** Scheme of project's code naming.

The levels of accuracy mentioned above determine the sampling rates at which the software processes the data. When the calculation accuracy is set to high at the image alignment stage, the software works on images with their original resolution. On the other hand, when the medium accuracy is set, the original image is reduced four times, in the low setting 16 times and in the lowest setting 64 times. For detailed photos, the highest level can be used, where the original resolution of the image is upscaled by a factor of 4 to find more key points. The meaning of these levels of settings is the same for the dense point cloud generation. In addition, during the image alignment step, the software calculates the optimization parameters that can be used to optimize the sparse point cloud. The  $f$  parameter is the focal length;  $cx$  and  $cy$  are intercepting axis of the lens optical with sensor plane;  $b1$  and  $b2$  are coefficients of affinity transformation and skew; coefficients  $k1$ ,  $k2$ ,  $k3$  and  $k4$  relate to radial distortion, and coefficients  $p1$  and  $p2$  to tangential distortion [63]. A detailed description of the processing steps, including the characteristics of the accuracy and quality settings, and a description of the optimization parameters process, can be found in the Agisoft Metashape software manual, available on the manufacturer's website (<https://www.agisoft.com/downloads/user-manuals/> accessed on 3 March 2022).

Taking into account all possible values of the above-mentioned parameters, 375 ( $5 \times 3 \times 5 \times 5 = 375$ ) different workflows were formulated and processed. In the first stage, an "initial" project was created in Agisoft Metashape to which the images and

GCPs were imported in the UTM zone 28N coordinate system (EPSG: 25828). DNG photos were not modified or converted in any way before importing them into the software. Subsequently, GCPs were marked into all images. Prepared in this way, the project was duplicated 375 times in order to start processing in the next step in accordance with the adopted workflow for a given project. As part of the calculations, each sparse point cloud was filtered with the Gradual Selection tool, using the same parameters for all models (reprojection error = 0.5, reconstruction uncertainty = 10, image count = 2, projection accuracy = 20). The end result of the processing was a report, a DEM, and an orthomosaic (Figure 4).

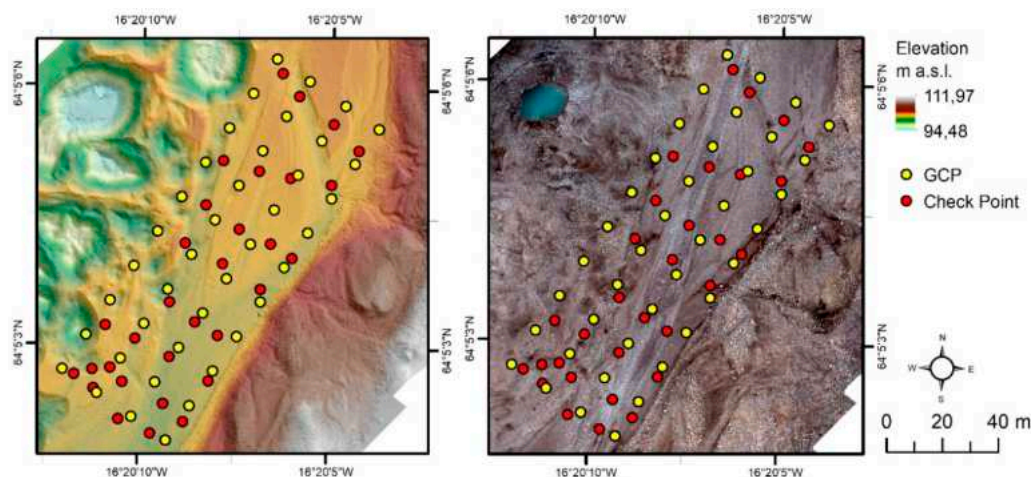


**Figure 4.** Example of end results of the processing: a DEM and an orthomosaic, with locations of GCPs and CPs.

In the next stage, DEMs were checked for height accuracy in the ArcMap software, using 30 CPs not participating in georeferencing. By selecting the Extract Values to Points tool, the differences in height between the CPs and the DEMs were obtained, and then the standard deviation and the root mean square error (RMSE) were calculated for the CPs of each model. We tested the accuracy of DEMs, not raw point clouds, as in most previous geomorphological works, DEMs were the most commonly used as final products for landform interpretation, mapping and change detection analysis [37]. In addition, we also visually checked raw point clouds in CloudCompare. For projects where RMSE values were low, the locations of control points were near to point cloud. For projects where RMSE values were high, control points were noticeably above or under the cloud. Additionally, based on the data from the report, the calculation time for each processing step was checked and the total calculation time for each project was summarized. Detailed information on each workflow is included in the Supplementary Materials (S1).

### 3. Results

Out of 375 projects, 195 did not generate a dense point cloud nor produced a DEM and orthomosaic. The step of aligning images at the lowest accuracy is responsible for the first 75 unsuccessful projects—the number of points remaining after filtration of sparse point clouds at this level (~600 points for all 75 chunks) was insufficient. Hence, the first result of the analysis is the statement that the level of accuracy of alignment set to lowest and subsequently filtered is insufficient to generate photogrammetric products. The sets of the “A” and “B” optimization parameters and alignment of images at low, medium, high, and highest accuracy are responsible for the remaining 120 projects, for which it was not possible to generate dense clouds. In these workflows, the sparse point clouds were not optimized with the k1 and k2 parameters, which were characterized by a high RMSE for GCPs of ~48.23 cm and a high reprojection error in the range of 2.74–5.80 pixels. Parameters k1 and k2 are responsible for the optimization of the sparse point cloud in terms of the

radial distortion of the lens—the conclusion is that images from the DJI FC6310 camera are burdened with high radial distortion. Due to the absence of dense point clouds and DEMs in these projects, they were not included in any further work, and so only reports were generated.

In the remaining 180 projects, DEMs, orthomosaics and calculation reports were generated, in line with the planned workflows. The spatial resolution of the photogrammetric products depended on the level of accuracy set for dense point cloud generation—at the lowest level the resolution was ~28 cm, at the low level ~14 cm, at the medium level ~7 cm, at the high level ~3.5 cm, and at the ultra-high level ~1.75 cm. The spatial resolution of all orthomosaics was the same: 1.75 cm. RMSE and standard deviation based on CPs were calculated. From the obtained results, it can be concluded that when the accuracy of alignment of images was set to the high or highest level and then combined with the exclusion of  $k_3$ ,  $k_4$ ,  $p_1$ , and  $p_2$  optimization parameters, the results were characterized by an increase in the RMSE value and standard deviation based on CPs. RMSE/SD for the high level reached the values of 14–15 cm, and for highest level 43–44 cm. The increase in the RMSE value and standard deviation based on CPs occurs with an increase in the number of points in the sparse cloud. Only when the optimization of the sparse point cloud was conducted using the set “E” (optimization of the parameters  $f$ ,  $c_x$ ,  $c_y$ ,  $k_1$ ,  $k_2$ ,  $k_3$ ,  $k_4$ ,  $p_1$ ,  $p_2$ ,  $b_1$ ,  $b_2$ ) were the high values of RMSE and standard deviations based on CPs reduced to values <2.5 cm. Figure 5 shows histograms for the 12 selected models, demonstrating the effect of parameters  $k_3$ ,  $k_4$ ,  $p_1$ , and  $p_2$  on the height difference distribution based on CPs. Histograms of the height difference distribution, calculated based on CPs for each model, are included in S2 as Supplementary Materials. Moreover, a noticeable effect on the RMSE and standard deviation value was noted for the step of dense point cloud generation—with the increase in its quality and optimization of all parameters (set “E”), the values decrease.

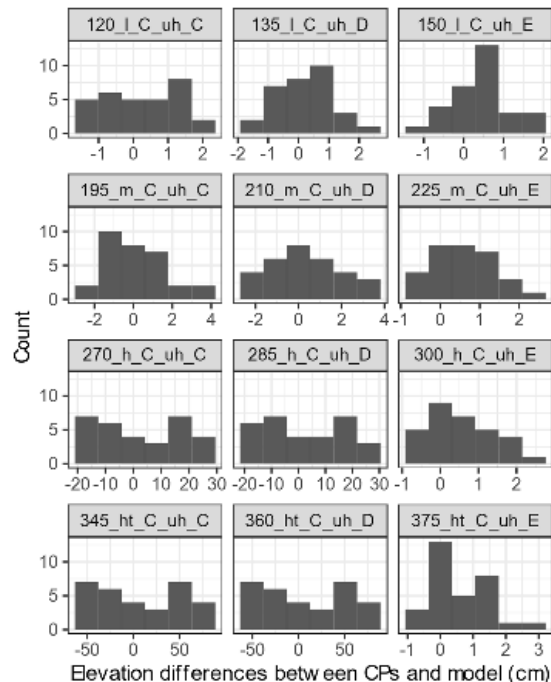


**Figure 5.** Distribution of the difference in elevation between 30 CPs and DEMs for the 12 selected workflows. The histograms are arranged according to the sets of optimization parameters and the level of accuracy of image alignment: in the first column there are four histograms for projects with the “C” set, in the second with the “D” set, and in the third with the “E” set. The level of accuracy for generating the sparse point cloud in the column is set from low (first row) to highest (fourth row).



All histograms are for projects where the quality of dense point cloud generation has been set to ultra-high. The following regularities can be seen: (1) increasing the quality of generating a sparse point cloud increases the differences in elevation for models with optimized parameter sets “C” and “D” (approximately from  $-2$  to  $2$  cm for low, from  $-2$  to  $4$  cm for medium, from  $-20$  to  $30$  cm for high and from  $-50$  to  $50$  cm for ultra-high quality); (2) optimization of the sparse point cloud with all parameters (set “E”) significantly affects the accuracy of the models, resulting in the standard deviation of  $<2.5$  cm.

In addition to analyzing the quality of the models, the calculation time for each step was checked, while calculation time for each project was summarized to compare the workflows in terms of calculation time and test if the increase in accuracy can be achieved with reasonable computing time. The step of generating a dense point cloud turned out to be crucial—the calculation time at the lowest level of accuracy may be shorter than ultra-high even six times, and between high and ultra-high three times (Table 1). The detailed results of the calculations, along with the quantitative and qualitative characteristics of the models, can be found in the Supplementary Materials (S1).

**Table 1.** An example of the calculation time data from Supplementary Materials (S1) for each processing step. The data concern 15 projects which include: accuracy of alignment of images at the medium level, three different sets of tie points and key point limits, accuracy of generating a dense cloud of points at five different levels, and a set “C” of optimization parameters. It is clearly visible that the step of generating a dense point cloud is the most time consuming. It is worth noting that the orthomosaic generation step can account for over 60% of the calculation time (e.g., project 181\_m\_A\_lt\_C).

| Project's Code | Calculation Time (h) |                         |                              |                |                        |          |
|----------------|----------------------|-------------------------|------------------------------|----------------|------------------------|----------|
|                | Alignment of Images  | Optimization Parameters | Dense Point Cloud Generation | DEM Generation | Orthomosaic Generation | SUM      |
| 181_m_A_lt_C   | 00:03:47             | 00:00:00                | 00:07:44                     | 00:00:06       | 00:19:19               | 00:30:56 |
| 182_m_B_lt_C   | 00:04:30             | 00:00:05                | 00:07:09                     | 00:00:05       | 00:20:28               | 00:32:17 |
| 183_m_C_lt_C   | 00:05:13             | 00:00:04                | 00:06:23                     | 00:00:05       | 00:21:22               | 00:33:07 |
| 184_m_A_l_C    | 00:03:45             | 00:00:01                | 00:07:18                     | 00:00:12       | 00:21:12               | 00:32:28 |
| 185_m_B_l_C    | 00:04:49             | 00:00:06                | 00:07:09                     | 00:00:11       | 00:21:02               | 00:33:17 |
| 186_m_C_l_C    | 00:05:03             | 00:00:04                | 00:07:01                     | 00:00:10       | 00:20:56               | 00:33:14 |
| 187_m_A_m_C    | 00:03:53             | 00:00:01                | 00:23:15                     | 00:00:45       | 00:19:33               | 00:47:27 |
| 188_m_B_m_C    | 00:04:53             | 00:00:04                | 00:14:48                     | 00:00:36       | 00:19:48               | 00:40:09 |
| 189_m_C_m_C    | 00:05:04             | 00:00:08                | 00:13:29                     | 00:00:33       | 00:19:52               | 00:39:06 |
| 190_m_A_h_C    | 00:03:49             | 00:00:01                | 00:47:01                     | 00:02:07       | 00:20:00               | 01:12:58 |
| 191_m_B_h_C    | 00:04:54             | 00:00:03                | 00:46:09                     | 00:01:56       | 00:19:33               | 01:12:35 |
| 192_m_C_h_C    | 00:05:04             | 00:00:07                | 00:48:08                     | 00:02:00       | 00:19:05               | 01:14:24 |
| 193_m_A_uh_C   | 00:03:50             | 00:00:01                | 02:51:00                     | 00:06:33       | 00:25:20               | 03:26:44 |
| 194_m_B_uh_C   | 00:05:00             | 00:00:04                | 02:34:00                     | 00:06:11       | 00:24:19               | 03:09:34 |
| 195_m_C_uh_C   | 00:04:38             | 00:00:06                | 02:44:00                     | 00:07:04       | 00:23:00               | 03:18:48 |

## 4. Discussion

In the following subsections, we discuss the impact of subsequent processing steps in SfM software on the accuracy of DEMs and orthomosaics.

### 4.1. Influence of Processing Parameters

#### 4.1.1. Alignment of Images

The level of accuracy in the alignment of images may affect the results of standard deviations and RMSE based on CPs; nevertheless, for each level of accuracy in this step, values below 1 cm are possible to achieve. However, higher values in the order of 9, 15 or 44 cm were recorded where the level of accuracy was set to high or highest, the sparse point cloud was not optimized with the k3, k4, p1, and p2 parameters (“E” optimization parameter set), and no point limits were introduced in the sparse cloud. Such high results

did not occur at the low and medium levels in projects with a similar number of points in a sparse cloud, hence the influence of the size of the sparse point cloud on this issue should be excluded. In addition, this step significantly influenced the calculation time—the use of high or highest level of accuracy, while not applying the key and tie points' limits, only increased the calculation time, but did not increase the accuracy of the photogrammetric products. At the low and medium level of accuracy, the difference in calculation time was visibly lower. It has to be noted that downsampling of the original images (i.e., levels lowest, low, and medium) can mix spectral values of pixels. Therefore, in the case of large spectral differences between control points and surroundings, this aspect can influence the accuracy assessment.

#### 4.1.2. Key and Tie Points' Limits

The limit of key and tie points, with one exception, did not affect the accuracy of DEMs. In the group of projects with the set "A" (i.e., limit 10,000 key points and 1000 tie points), the lowest standard deviation based on CPs was 0.63 cm (which is the best result among all 180 projects). The most accurate project with the "B" set (i.e., limit 100,000 key points and 10,000 tie points) had a standard deviation of 0.65 cm, and with the "C" set (i.e., no limit on key or tie points) the standard deviation was 0.67 cm. Similar results of the sets "A", "B" and "C" were also recorded for the RMSE values (0.76, 0.76, and 0.80 cm, respectively). The exception here is the generation of a sparse point cloud at the high and highest level of accuracy, plus a lack of optimization with parameters k3, k4, p1, and p2, which significantly reduces the accuracy of the models (standard deviation and RMSE based on CPs in the range of 9–44 cm). Such large values for high and highest settings can be potentially related to the general roughness of the surface or false matches related to similar texture of the studied area.

Therefore, increasing the number of points in the sparse cloud by increasing the limit of key and tie points or removing them completely does not always improve the accuracy of the models, and may result in an extension of the calculation time during its generation and subsequent processing steps. This applies, for example, to the three projects with the longest calculation times, of which the longest was almost five hours.

#### 4.1.3. Dense Point Cloud Generation

The process of generating a dense point cloud turned out to be a significant element in terms of the accuracy of the models. High and ultra-high quality in combination with optimization of the parameters from the "E" set produced the best results—the resultant DEMs were characterized by standard deviation and RMSE based on CPs  $\leq 1$  cm. That likely results from the texture of the surface (gravels)—in this case, more characteristic points can be identified in the images and used to construct point cloud. The increase of quality of the dense point cloud generation step, along with the use of the key and tie points' limits from the "A" set, result in a significant decrease in the value of the standard deviation and RMSE based on CPs. It should be underlined that calculating dense cloud with the highest possible quality resulted in the extension of the calculation time: in the case of the ultra-high quality, even several times. This is because the ultra-high settings oversample the original images and, therefore, quadruple memory consumption.

#### 4.1.4. Optimization Alignment

The optimization of the sparse point cloud turned out to be the most important processing step in terms of the accuracy of DEMs. As mentioned in Section 3, projects with parameter sets "A" and "B" did not generate a dense point cloud. Only adding the parameters k1 and k2 to the sets "C", "D", and "E" resulted in the generation of a dense point cloud and photogrammetric products. These parameters relate to radial distortion [64], which characterizes the images from the DJI FC6310 camera [50], hence the lack of these parameters in the optimization could cause the problem with generation of a dense point cloud. The lowest RMSE and SD of CP errors were recorded in the

workflows with the “E” set, in which all possible optimization parameters were applied, i.e., responsible for radial and tangential distortion, affinity and orthogonality. Nearly all the most accurate models in the experiment have been optimized with these parameters, therefore we recommend their use. A comparison of DEM accuracy results in relation to the optimization sets is presented in Figure 6. However, the possibility of overparameterization should be taken into account [65], for it may result in a poorly modeled surface and that is not reflected in its actual shape. It should be emphasized that the option to skip this step completely or partially should be used only when the operator has more reliable calibration parameters than those estimated by the software (for example, when using cameras calibrated in laboratory conditions). The gain in time is negligible compared to the significant loss in accuracy. Before the use of DEMs for further analyses, we recommend checking them first with CPs.

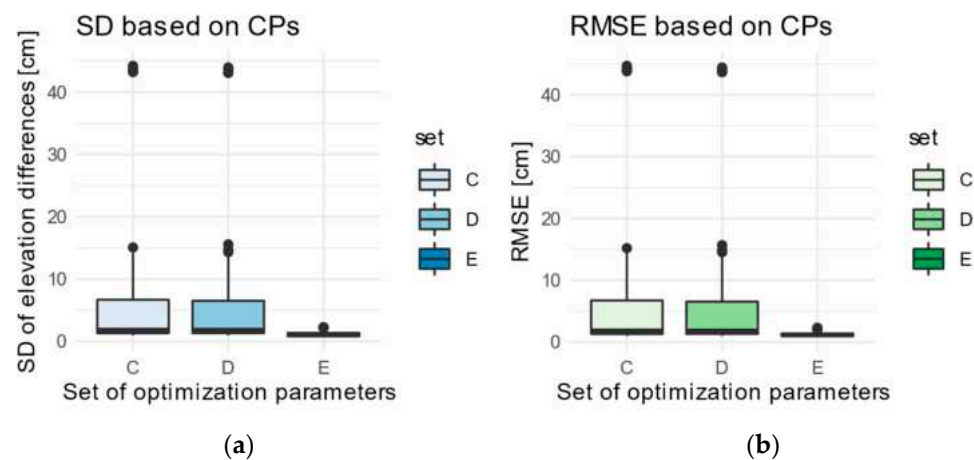


**Figure 6.** Distribution of standard deviation (a) and RMSE (b) values based on CPs. The figure suggests that use of the “E” set would result in lower error values. For the projects with the “E” set, no DEMs with very high errors of ~45 cm were found.

#### 4.2. Best Workflows

Out of 180 completed projects, three workflows were selected, corresponding to the requirements formulated on account of the research aims. The main determinant was the low values of standard deviation and RMSE based on CPs in relation to the processing time of the set of images. On the other hand, when choosing the fastest procedure, it was assumed that the spatial resolution of the obtained DEM was better than 10 cm. The full characteristics of the workflows are presented in Table 2 based on the data contained in Supplementary Materials (S1).

#### 4.3. Workflows in Python Scripts

In order to process many sets of images more efficiently or develop accurate DEMs and orthomosaics, workflows and their settings presented in the previous subsection were prepared in the form of Python scripts for Agisoft Metashape Professional (runs stable in version 1.7.1 build 11,797). The scripts are text files that run in the software with the Run script tool. They are written to make calculations on all chunks in an open project. The scripts should be used for projects with imported images, and to obtain a high-accuracy model, one should put GCPs on the images before running the scripts. Some of the previous studies have paid attention to the reproducibility of algorithms in Agisoft Metashape software, indicating that they may result in different outcomes (elevation variations  $\geq 10$  cm) even while using the same set of images and processed with exactly the same processing workflow [66]. For this reason, the scripts were checked on the same set of images used in the study, in which no significant differences were found based on reports and analysis of the results. Nevertheless, random differences in other larger sets of images cannot be excluded, such that the variance of the point cloud [50] or precision

map [67] should be investigated before proceeding with further analysis of the processed data. The scripts are provided as Supplementary Materials for this article.

**Table 2.** Detailed description of the three workflows that meet the requirements formulated in view of the research aims. The difference in the SD of CP errors between workflows I and II is 0.38 cm, and between II and III only 0.07 cm. However, the workflows differ from each other mainly in terms of the time of calculations, which in the I type was more than seven times faster than the III type. The conclusion is that setting higher levels of accuracy in the software is not always appropriate (remembering that the total calculation time depends mainly on the computing power).

| Type of Workflow  | Project's Code | Processing Parameters  | DEM GSD (cm) | RMSE (cm) | SD of Elevation Differences (cm) | Calculation Time (h) |
|-------------------|----------------|--|--------------|-----------|----------------------------------|----------------------|
| I. The fastest    | 128_I_B_m_D    | 1. Alignment accuracy: low.<br>2. Count of key and tie points: 100,000 (key points), 10,000 (tie points).<br>3. Dense point cloud generation quality: medium.<br>4. Optimization parameters: f, cx, cy, k1, k2, b1, b2.                    | 7.01         | 1.03      | 1.01                             | 00:35:08             |
| II. Optimal       | 147_I_C_h_E    | 1. Alignment accuracy: low.<br>2. Count of key and tie points: no limits.<br>3. Dense point cloud generation quality: high.<br>4. Optimization parameters: f, cx, cy, k1, k2, k3, k4, p1, p2, b1, b2.                                      | 3.50         | 0.81      | 0.70                             | 01:05:14             |
| III. Best quality | 223_m_A_uh_E   | 1. Alignment accuracy: medium<br>2. Count of key and tie points: 10,000 (key points), 1000 (tie points).<br>3. Dense point cloud generation quality: ultra-high.<br>4. Optimization parameters: f, cx, cy, k1, k2, k3, k4, p1, p2, b1, b2. | 1.75         | 0.76      | 0.63                             | 03:47:02             |

#### 4.4. Potential Applications

The scripts can be used in the analysis of many research objects. The set of images analyzed in this study concerned proglacial areas with different terrain heights. Other potential applications may include, for instance, studies of alluvial fans [68], glacial landforms [40,69], glacier lake outburst floods [70,71] or aeolian landforms [72–74]. Furthermore, the scripts can be used for modelling various small objects, e.g., in archaeology [75] or geomorphology [76]. The presented scripts enabled a quick launch and systematic work, thereby making it possible to process more efficiently, e.g., several dozen large sets of images in agriculture [77], where each field can be used as a separate point of interest. The use of scripts, instead of selecting parameters manually, will be particularly helpful when processing many projects simultaneously in a computing cluster, positively influencing usage efficiency. This utility will be of most effective importance for multiannual, cyclical analyses of the same research areas (e.g., glaciers) [44,45], as it provides a constant, comparable workflow, reduces the time spent on calculations and project preparation, and will make comparisons between models more reliable, e.g., in research geomorphological fields such as change detection (e.g., [78]). In addition, field work may require a quick check on a

portable notebook to ensure that the selected flight parameters (altitude, forward and side overlap of images) are sufficient to generate an accurate model. Script #1, with the shortest calculation time, may well be the answer to such needs. To increase the chance of repeating our results, we emphasize the importance of the quality of the input data and recommend the use of RAW images.

## 5. Conclusions

In this study, we delivered the first empirical test of the impact of processing parameters in Agisoft Metashape on the accuracy of the results of SfM processing based on typical application in geomorphological research. To achieve accurate DEM, it is crucial to use correct settings, including parameters optimizing a sparse point cloud. Moreover, needlessly increasing the level of accuracy of calculations does not always result in an increase in the accuracy of photogrammetric products, but may only extend the calculation process and delay the obtainment of results. To address these problems, three different workflows in the form of Python scripts for Agisoft Metashape were prepared, which, depending on the needs and available computing power, allow for the development of accurate models. For many scientists dealing with surface dynamics, scripts in which automating calculation work is performed should be a noticeable facilitation and may turn out to be a new method of improving quality in their research work. Key calculation settings and parameters, applied in the form of editable scripts, will increase the efficiency in processing and comparing large datasets, in addition to significant time savings due to the use of a powerful computing cluster. The high usability of the scripts is seen in the long-term observations, for example, of many glaciers and their forelands, where the automated workflow allows for a better management of numerous projects, not to mention rendering the process of comparing models reliable. Moreover, the authors do not exclude that the developed scripts will find their use in creating other three-dimensional models of various objects, not necessarily those related to glaciers and their forelands. In addition, it is suggested to perform the same experiment in the future for sets of images from several different cameras, and also including ground-based and oblique images.

**Supplementary Materials:** The following supporting information can be downloaded at: <https://www.mdpi.com/article/10.3390/rs14061312/s1>, S1: Detailed information on each workflow (Table S1), S2: Elevation differences between check points and model for each workflow, S3: Python Script #1 (the fastest), S4: Python Script #2 (optimal), S5: Python Script #3 (best quality).

**Author Contributions:** Conceptualization, S.Ś. and M.W.E.; methodology, S.Ś. and M.W.E.; software, S.Ś. and M.W.E.; validation, S.Ś. and M.W.E.; formal analysis, S.Ś.; investigation, S.Ś. and M.W.E.; resources, S.Ś. and M.W.E.; data curation, S.Ś.; writing—original draft preparation, S.Ś.; writing—review and editing, S.Ś. and M.W.E.; visualization, S.Ś.; supervision, M.W.E.; project administration, S.Ś. and M.W.E.; funding acquisition, M.W.E. All authors have read and agreed to the published version of the manuscript.

**Funding:** This research was funded by the National Science Centre, Poland, Grant Number 2019/35/B/ST10/03928.

**Institutional Review Board Statement:** Not applicable.

**Informed Consent Statement:** Not applicable.

**Data Availability Statement:** Data will be available on reasonable request.

**Acknowledgments:** This work would not be possible without the discussions and technical support from Adam Młynarczyk and Sławomir Królewicz.

**Conflicts of Interest:** The authors declare no conflict of interest. The funders had no role in the design of the study; in the collection, analyses, or interpretation of data; in the writing of the manuscript, or in the decision to publish the results.

## References

1. Ayalew, L.; Yamagishi, H. The application of GIS-based logistic regression for landslide susceptibility mapping in the Kakuda-Yahiko Mountains, Central Japan. *Geomorphology* **2005**, *65*, 15–31. [[CrossRef](#)]
2. Stumvoll, M.J.; Schmaltz, E.M.; Glade, T. Dynamic characterization of a slow-moving landslide system—Assessing the challenges of small process scales utilizing multi-temporal TLS data. *Geomorphology* **2021**, *389*, 107803. [[CrossRef](#)]
3. Turner, D.; Lucieer, A.; de Jong, S.M. Time Series Analysis of Landslide Dynamics Using an Unmanned Aerial Vehicle (UAV). *Remote Sens.* **2015**, *7*, 1736–1757. [[CrossRef](#)]
4. Bourova, E.; Maldonado, E.; Leroy, J.-B.; Alouani, R.; Eckert, N.; Bonnefoy-Demongeot, M.; Deschatres, M. A new web-based system to improve the monitoring of snow avalanche hazard in France. *Nat. Hazards Earth Syst. Sci.* **2016**, *16*, 1205–1216. [[CrossRef](#)]
5. Xiang, J.; Chen, J.; Sofia, G.; Tian, Y.; Tarolli, P. Open-pit mine geomorphic changes analysis using multi-temporal UAV survey. *Environ. Earth Sci.* **2018**, *77*, 220. [[CrossRef](#)]
6. Kršák, B.; Blišťan, P.; Paulíková, A.; Puškárová, P.; Kovanič, L.; Palková, J.; Zelizňáková, V. Use of low-cost UAV photogrammetry to analyze the accuracy of a digital elevation model in a case study. *Measurement* **2016**, *91*, 276–287. [[CrossRef](#)]
7. Mohamed, I.N.L.; Verstraeten, G. Analyzing dune dynamics at the dune-field scale based on multi-temporal analysis of Landsat-TM images. *Remote Sens. Environ.* **2012**, *119*, 105–117. [[CrossRef](#)]
8. Kociuba, W. Assessment of sediment sources throughout the proglacial area of a small Arctic catchment based on high-resolution digital elevation models. *Geomorphology* **2017**, *287*, 73–89. [[CrossRef](#)]
9. Kociuba, W.; Kubisz, W.; Zagórski, P. Use of terrestrial laser scanning (TLS) for monitoring and modelling of geomorphic processes and phenomena at a small and medium spatial scale in Polar environment (Scott River—Spitsbergen). *Geomorphology* **2014**, *212*, 84–96. [[CrossRef](#)]
10. Dietrich, J.T. Riverscape mapping with helicopter-based Structure-from-Motion photogrammetry. *Geomorphology* **2016**, *252*, 144–157. [[CrossRef](#)]
11. Tomczyk, A.M.; Ewertowski, M.W.; Carrivick, J.L. Geomorphological impacts of a glacier lake outburst flood in the high arctic Zackenberg River, NE Greenland. *J. Hydrol.* **2020**, *591*, 125300. [[CrossRef](#)]
12. Carrivick, J.L.; Smith, M.W. Fluvial and aquatic applications of Structure from Motion photogrammetry and unmanned aerial vehicle/drone technology. *WIREs Water* **2019**, *6*, e1328. [[CrossRef](#)]
13. Ewertowski, M.W.; Tomczyk, A.M. Quantification of the ice-cored moraines' short-term dynamics in the high-Arctic glaciers Ebbabreen and Ragnarbreen, Petuniabukta, Svalbard. *Geomorphology* **2015**, *234*, 211–227. [[CrossRef](#)]
14. Tonkin, T.N.; Midgley, N.G.; Cook, S.J.; Graham, D.J. Ice-cored moraine degradation mapped and quantified using an unmanned aerial vehicle: A case study from a polythermal glacier in Svalbard. *Geomorphology* **2016**, *258*, 1–10. [[CrossRef](#)]
15. Bernard, E.; Friedt, J.M.; Schiavone, S.; Tolle, F.; Griselin, M. Assessment of periglacial response to increased runoff: An Arctic hydrosystem bears witness. *Land Degrad. Dev.* **2018**, *29*, 3709–3720. [[CrossRef](#)]
16. Sziło, J.; Bialik, R. Recession and Ice Surface Elevation Changes of Baranowski Glacier and Its Impact on Proglacial Relief (King George Island, West Antarctica). *Geosciences* **2018**, *8*, 355. [[CrossRef](#)]
17. Carrivick, J.L.; Heckmann, T. Short-term geomorphological evolution of proglacial systems. *Geomorphology* **2017**, *287*, 3–28. [[CrossRef](#)]
18. Song, X.P.; Hansen, M.C.; Stehman, S.V.; Potapov, P.V.; Tyukavina, A.; Vermote, E.F.; Townshend, J.R. Global land change from 1982 to 2016. *Nature* **2018**, *560*, 639–643. [[CrossRef](#)]
19. Ding, Y.; Mu, C.; Wu, T.; Hu, G.; Zou, D.; Wang, D.; Li, W.; Wu, X. Increasing cryospheric hazards in a warming climate. *Earth-Sci. Rev.* **2021**, *213*, 103500. [[CrossRef](#)]
20. Knight, J.; Harrison, S. Evaluating the impacts of global warming on geomorphological systems. *Ambio* **2012**, *41*, 206–210. [[CrossRef](#)]
21. Hugonnet, R.; McNabb, R.; Berthier, E.; Menounos, B.; Nuth, C.; Girod, L.; Farinotti, D.; Huss, M.; Dussailant, I.; Brun, F.; et al. Accelerated global glacier mass loss in the early twenty-first century. *Nature* **2021**, *592*, 726–731. [[CrossRef](#)] [[PubMed](#)]
22. Dąbski, M.; Zmarz, A.; Rodzewicz, M.; Korczak-Abshire, M.; Karsznia, I.; Lach, K.; Rachlewicz, G.; Chwedorzewska, K. Mapping Glacier Forelands Based on UAV BVLOS Operation in Antarctica. *Remote Sens.* **2020**, *12*, 630. [[CrossRef](#)]
23. Ewertowski, M.W.; Evans, D.J.A.; Roberts, D.H.; Tomczyk, A.M.; Ewertowski, W.; Pleksot, K. Quantification of historical landscape change on the foreland of a receding polythermal glacier, Hørbyebreen, Svalbard. *Geomorphology* **2019**, *325*, 40–54. [[CrossRef](#)]
24. Benn, D.I.; Evans, D.J.A. *Glaciers and Glaciation*; Hodder Education: London, UK, 2010.
25. Knight, J.; Harrison, S. Transience in cascading paraglacial systems. *Land Degrad. Dev.* **2018**, *29*, 1991–2001. [[CrossRef](#)]
26. Knight, J.; Harrison, S. The impacts of climate change on terrestrial Earth surface systems. *Nat. Clim. Chang.* **2013**, *3*, 24–29. [[CrossRef](#)]
27. Benn, D.I.; Bolch, T.; Hands, K.; Gulley, J.; Luckman, A.; Nicholson, L.I.; Quincey, D.; Thompson, S.; Toumi, R.; Wiseman, S. Response of debris-covered glaciers in the Mount Everest region to recent warming, and implications for outburst flood hazards. *Earth-Sci. Rev.* **2012**, *114*, 156–174. [[CrossRef](#)]
28. Ewertowski, M.W.; Tomczyk, A.M. Reactivation of temporarily stabilized ice-cored moraines in front of polythermal glaciers: Gravitational mass movements as the most important geomorphological agents for the redistribution of sediments (a case study from Ebbabreen and Ragnarbreen, Svalbard). *Geomorphology* **2020**, *350*. [[CrossRef](#)]

29. Carrivick, J.L.; Tweed, F.S. A review of glacier outburst floods in Iceland and Greenland with a megafloods perspective. *Earth-Sci. Rev.* **2019**, *196*, 102876. [[CrossRef](#)]
30. Carrivick, J.L.; Tweed, F.S. A global assessment of the societal impacts of glacier outburst floods. *Glob. Planet Chang.* **2016**, *144*, 1–16. [[CrossRef](#)]
31. Russell, A.J.; Carrivick, J.L.; Ingeman-Nielsen, T.; Yde, J.C.; Williams, M. A new cycle of jökulhlaups at Russell Glacier, Kangerlussuaq, West Greenland. *J. Glaciol.* **2011**, *57*, 238–246. [[CrossRef](#)]
32. Colomina, I.; Molina, P. Unmanned aerial systems for photogrammetry and remote sensing: A review. *ISPRS J. Photogramm. Remote Sens.* **2014**, *92*, 79–97. [[CrossRef](#)]
33. Smith, M.W.; Carrivick, J.L.; Quincey, D.J. Structure from motion photogrammetry in physical geography. *Prog. Phys. Geogr. Earth Environ.* **2016**, *40*, 247–275. [[CrossRef](#)]
34. Carrivick, J.L.; Smith, M.W.; Quincey, D.J. *Structure from Motion in the Geosciences*; Wiley-Blackwell: Oxford, UK, 2016; p. 208.
35. Anderson, K.; Gaston, K.J. Lightweight unmanned aerial vehicles will revolutionize spatial ecology. *Front. Ecol. Environ.* **2013**, *11*, 138–146. [[CrossRef](#)]
36. Bhardwaj, A.; Sam, L.; Akanksha; Martín-Torres, F.J.; Kumar, R. UAVs as remote sensing platform in glaciology: Present applications and future prospects. *Remote Sens. Environ.* **2016**, *175*, 196–204. [[CrossRef](#)]
37. Śledź, S.; Ewertowski, M.W.; Piekarczyk, J. Applications of unmanned aerial vehicle (UAV) surveys and Structure from Motion photogrammetry in glacial and periglacial geomorphology. *Geomorphology* **2021**, *378*, 107620. [[CrossRef](#)]
38. Fugazza, D.; Scaioni, M.; Corti, M.; D'Agata, C.; Azzoni, R.S.; Cernuschi, M.; Smiraglia, C.; Diolaiuti, G.A. Combination of UAV and terrestrial photogrammetry to assess rapid glacier evolution and map glacier hazards. *Nat. Hazards Earth Syst. Sci.* **2018**, *18*, 1055–1071. [[CrossRef](#)]
39. Westoby, M.J.; Brasington, J.; Glasser, N.F.; Hambrey, M.J.; Reynolds, J.M. 'Structure-from-Motion' photogrammetry: A low-cost, effective tool for geoscience applications. *Geomorphology* **2012**, *179*, 300–314. [[CrossRef](#)]
40. Allaart, L.; Friis, N.; Ingólfsson, Ó.; Håkansson, L.; Noormets, R.; Farnsworth, W.R.; Mertes, J.; Schomacker, A. Drumlins in the Nordenskiöldbreen forefield, Svalbard. *Gff* **2018**, *140*, 170–188. [[CrossRef](#)]
41. Storrar, R.D.; Ewertowski, M.; Tomczyk, A.M.; Barr, I.D.; Livingstone, S.J.; Ruffell, A.; Stoker, B.J.; Evans, D.J.A. Equifinality and preservation potential of complex eskers. *Boreas* **2019**, *49*, 211–231. [[CrossRef](#)]
42. Tomczyk, A.M.; Ewertowski, M.W. UAV-based remote sensing of immediate changes in geomorphology following a glacial lake outburst flood at the Zackenberg river, northeast Greenland. *J. Maps* **2020**, *16*, 86–100. [[CrossRef](#)]
43. Whitehead, K.; Moorman, B.J.; Hugenholtz, C.H. Brief Communication: Low-cost, on-demand aerial photogrammetry for glaciological measurement. *Cryosphere* **2013**, *7*, 1879–1884. [[CrossRef](#)]
44. Chandler, B.M.P.; Evans, D.J.A.; Chandler, S.J.P.; Ewertowski, M.W.; Lovell, H.; Roberts, D.H.; Schaefer, M.; Tomczyk, A.M. The glacial landsystem of Fjallsjökull, Iceland: Spatial and temporal evolution of process-form regimes at an active temperate glacier. *Geomorphology* **2020**, *361*, 107192. [[CrossRef](#)]
45. Westoby, M.J.; Rounce, D.R.; Shaw, T.E.; Fyffe, C.L.; Moore, P.L.; Stewart, R.L.; Brock, B.W. Geomorphological evolution of a debris-covered glacier surface. *Earth Surf. Process. Landf.* **2020**, *45*, 3431–3448. [[CrossRef](#)]
46. Chandler, B.M.P.; Chandler, S.J.P.; Evans, D.J.A.; Ewertowski, M.W.; Lovell, H.; Roberts, D.H.; Schaefer, M.; Tomczyk, A.M. Sub-annual moraine formation at an active temperate Icelandic glacier. *Earth Surf. Process. Landf.* **2020**, *45*, 1622–1643. [[CrossRef](#)]
47. Westoby, M.J.; Dunning, S.A.; Woodward, J.; Hein, A.S.; Marrero, S.M.; Winter, K.; Sugden, D.E. Sedimentological characterization of Antarctic moraines using UAVs and Structure-from-Motion photogrammetry. *J. Glaciol.* **2015**, *61*, 1088–1102. [[CrossRef](#)]
48. Ewertowski, M.W.; Tomczyk, A.M.; Evans, D.J.A.; Roberts, D.H.; Ewertowski, W. Operational Framework for Rapid, Very-high Resolution Mapping of Glacial Geomorphology Using Low-cost Unmanned Aerial Vehicles and Structure-from-Motion Approach. *Remote Sens.* **2019**, *11*, 65. [[CrossRef](#)]
49. James, M.R.; Chandler, J.H.; Eltner, A.; Fraser, C.; Miller, P.E.; Mills, J.P.; Noble, T.; Robson, S.; Lane, S.N. Guidelines on the use of structure-from-motion photogrammetry in geomorphic research. *Earth Surf. Process. Landf.* **2019**, *44*, 2081–2084. [[CrossRef](#)]
50. James, M.R.; Antoniazza, G.; Robson, S.; Lane, S.N. Mitigating systematic error in topographic models for geomorphic change detection: Accuracy, precision and considerations beyond off-nadir imagery. *Earth Surf. Process. Landf.* **2020**, *45*, 2251–2271. [[CrossRef](#)]
51. Gindraux, S.; Boesch, R.; Farinotti, D. Accuracy Assessment of Digital Surface Models from Unmanned Aerial Vehicles' Imagery on Glaciers. *Remote Sens.* **2017**, *9*, 186. [[CrossRef](#)]
52. Mesas-Carrascosa, F.-J.; Torres-Sánchez, J.; Clavero-Rumbao, I.; García-Ferrer, A.; Peña, J.-M.; Borra-Serrano, I.; López-Granados, F. Assessing Optimal Flight Parameters for Generating Accurate Multispectral Orthomosaics by UAV to Support Site-Specific Crop Management. *Remote Sens.* **2015**, *7*, 12793–12814. [[CrossRef](#)]
53. Sanz-Ablanedo, E.; Chandler, J.H.; Ballesteros-Pérez, P.; Rodríguez-Pérez, J.R. Reducing systematic dome errors in digital elevation models through better UAV flight design. *Earth Surf. Processes Landf.* **2020**, *45*, 2134–2147. [[CrossRef](#)]
54. Sanz-Ablanedo, E.; Chandler, J.H.; Rodríguez-Pérez, J.R.; Ordóñez, C. Accuracy of Unmanned Aerial Vehicle (UAV) and SfM Photogrammetry Survey as a Function of the Number and Location of Ground Control Points Used. *Remote Sens.* **2018**, *10*, 1606. [[CrossRef](#)]
55. Tonkin, T.; Midgley, N. Ground-Control Networks for Image Based Surface Reconstruction: An Investigation of Optimum Survey Designs Using UAV Derived Imagery and Structure-from-Motion Photogrammetry. *Remote Sens.* **2016**, *8*, 786. [[CrossRef](#)]

56. Rangel, J.M.G.; Gonçalves, G.R.; Pérez, J.A. The impact of number and spatial distribution of GCPs on the positional accuracy of geospatial products derived from low-cost UAVs. *Int. J. Remote Sens.* **2018**, *39*, 7154–7171. [[CrossRef](#)]
57. Martínez-Carricondo, P.; Agüera-Vega, F.; Carvajal-Ramírez, F.; Mesas-Carrascosa, F.-J.; García-Ferrer, A.; Pérez-Porrás, F.-J. Assessment of UAV-photogrammetric mapping accuracy based on variation of ground control points. *Int. J. Appl. Earth Obs. Geoinf.* **2018**, *72*, 1–10. [[CrossRef](#)]
58. Cook, K.L.; Dietze, M. Short communication: A simple workflow for robust low-cost UAV-derived change detection without ground control points. *Earth Surf. Dyn.* **2019**, *7*, 1009–1017. [[CrossRef](#)]
59. De Haas, T.; Nijland, W.; McArdeell, B.W.; Kalthof, M.W.M.L. Case Report: Optimization of Topographic Change Detection with UAV Structure-From-Motion Photogrammetry Through Survey Co-Alignment. *Front. Remote Sens.* **2021**, *2*. [[CrossRef](#)]
60. Forsmo, J.; Anderson, K.; Macleod, C.J.A.; Wilkinson, M.E.; DeBell, L.; Brazier, R.E. Structure from motion photogrammetry in ecology: Does the choice of software matter? *Ecol. Evol.* **2019**, *9*, 12964–12979. [[CrossRef](#)]
61. Nesbit, P.; Hugenholtz, C. Enhancing UAV-SfM 3D Model Accuracy in High-Relief Landscapes by Incorporating Oblique Images. *Remote Sens.* **2019**, *11*, 239. [[CrossRef](#)]
62. Peppas, M.V.; Hall, J.; Goodyear, J.; Mills, J.P. Photogrammetric Assessment and Comparison of Dji Phantom 4 Pro and Phantom 4 Rtk Small Unmanned Aircraft Systems. *Int. Arch. Photogramm. Remote Sens. Spat. Inf. Sci.* **2019**, *XLII-2/W13*, 503–509. [[CrossRef](#)]
63. Agisoft. *Agisoft Metashape User Manual Professional Edition, Version 1.8*; Agisoft LLC: St. Petersburg, Russia, 2022; p. 195.
64. Carbonneau, P.E.; Dietrich, J.T. Cost-effective non-metric photogrammetry from consumer-grade sUAS: Implications for direct georeferencing of structure from motion photogrammetry. *Earth Surf. Process. Landf.* **2017**, *42*, 473–486. [[CrossRef](#)]
65. James, M.R.; Robson, S.; d’Oleire-Oltmanns, S.; Niethammer, U. Optimising UAV topographic surveys processed with structure-from-motion: Ground control quality, quantity and bundle adjustment. *Geomorphology* **2017**, *280*, 51–66. [[CrossRef](#)]
66. Hendrickx, H.; Vivero, S.; De Cock, L.; De Wit, B.; De Maeyer, P.; Lambiel, C.; Delaloye, R.; Nyssen, J.; Frankl, A. The reproducibility of SfM algorithms to produce detailed Digital Surface Models: The example of PhotoScan applied to a high-alpine rock glacier. *Remote Sens. Lett.* **2018**, *10*, 11–20. [[CrossRef](#)]
67. James, M.R.; Robson, S.; Smith, M.W. 3-D uncertainty-based topographic change detection with structure-from-motion photogrammetry: Precision maps for ground control and directly georeferenced surveys. *Earth Surf. Process. Landf.* **2017**, *42*, 1769–1788. [[CrossRef](#)]
68. Tomczyk, A.M.; Ewertowski, M.W.; Stawska, M.; Rachlewicz, G. Detailed alluvial fan geomorphology in a high-arctic periglacial environment, Svalbard: Application of unmanned aerial vehicle (UAV) surveys. *J. Maps* **2019**, *15*, 460–473. [[CrossRef](#)]
69. Ely, J.C.; Graham, C.; Barr, I.D.; Rea, B.R.; Spagnolo, M.; Evans, J. Using UAV acquired photography and structure from motion techniques for studying glacier landforms: Application to the glacial flutes at Isfallsglaciären. *Earth Surf. Process. Landf.* **2017**, *42*, 877–888. [[CrossRef](#)]
70. Wilson, R.; Harrison, S.; Reynolds, J.; Hubbard, A.; Glasser, N.F.; Wünderlich, O.; Iribarren Anaconda, P.; Mao, L.; Shannon, S. The 2015 Chileno Valley glacial lake outburst flood, Patagonia. *Geomorphology* **2019**, *332*, 51–65. [[CrossRef](#)]
71. Tomczyk, A.M.; Ewertowski, M.W. Baseline data for monitoring geomorphological effects of glacier lake outburst flood: A very-high-resolution image and GIS datasets of the distal part of the Zackenberg River, northeast Greenland. *Earth Syst. Sci. Data* **2021**, *13*, 5293–5309. [[CrossRef](#)]
72. Mancini, F.; Dubbini, M.; Gattelli, M.; Stecchi, F.; Fabbri, S.; Gabbianelli, G. Using Unmanned Aerial Vehicles (UAV) for High-Resolution Reconstruction of Topography: The Structure from Motion Approach on Coastal Environments. *Remote Sens.* **2013**, *5*, 6880–6898. [[CrossRef](#)]
73. Van Puijenbroek, M.E.B.; Nolet, C.; de Groot, A.V.; Suomalainen, J.M.; Riksen, M.J.P.M.; Berendse, F.; Limpens, J. Exploring the contributions of vegetation and dune size to early dune development using unmanned aerial vehicle (UAV) imaging. *Biogeosciences* **2017**, *14*, 5533–5549. [[CrossRef](#)]
74. Solazzo, D.; Sankey, J.B.; Sankey, T.T.; Munson, S.M. Mapping and measuring aeolian sand dunes with photogrammetry and LiDAR from unmanned aerial vehicles (UAV) and multispectral satellite imagery on the Paria Plateau, AZ, USA. *Geomorphology* **2018**, *319*, 174–185. [[CrossRef](#)]
75. Lauria, G.; Sineo, L.; Ficarra, S. A detailed method for creating digital 3D models of human crania: An example of close-range photogrammetry based on the use of Structure-from-Motion (SfM) in virtual anthropology. *Archaeol. Anthropol. Sci.* **2022**, *14*. [[CrossRef](#)]
76. Eichel, J.; Draebing, D.; Kattenborn, T.; Senn, J.A.; Klingbeil, L.; Wieland, M.; Heinz, E. Unmanned aerial vehicle-based mapping of turf-banked solifluction lobe movement and its relation to material, geomorphometric, thermal and vegetation properties. *Permafrost. Periglacial Processes* **2020**, *31*, 97–109. [[CrossRef](#)]
77. Zhang, C.; Kovacs, J.M. The application of small unmanned aerial systems for precision agriculture: A review. *Precis. Agric.* **2012**, *13*, 693–712. [[CrossRef](#)]
78. Midgley, N.G.; Tonkin, T.N.; Graham, D.J.; Cook, S.J. Evolution of high-Arctic glacial landforms during deglaciation. *Geomorphology* **2018**, *311*, 63–75. [[CrossRef](#)]



Appendix S1: Detailed information on each workflow.

| Number | Code         | Reprojection error [pix] | RMSE (GCP) [cm] | RMSE (CPs) [cm] | Standard deviation (CPs) [cm] | Point density [points/cm <sup>2</sup> ] | Point cloud (after gradual selection) [points] | Dense point cloud [points] | Resolution [cm] |            | Calculation time [h] |                        |                              |     |            |          |
|--------|--------------|--------------------------|-----------------|-----------------|-------------------------------|---|--|----------------------------|-----------------|------------|----------------------|------------------------|------------------------------|-----|------------|----------|
|        |              |                          |                 |                 |                               |   |  |                            | DEM             | Ortomosaic | Alignment            | Optimization alignment | Dense point cloud generation | DEM | Ortomosaic | SUM      |
| 1      | 1_lt_A_lt_A  | 5.76                     | 48.23           |                 |                               |   | 642  |                            |                 |            | 00:03:37             | 00:00:00               |                              |     |            | 00:03:37 |
| 2      | 2_lt_B_lt_A  | 5.78                     | 48.23           |                 |                               |   | 641  |                            |                 |            | 00:03:33             | 00:00:00               |                              |     |            | 00:03:33 |
| 3      | 3_lt_C_lt_A  | 5.72                     | 48.23           |                 |                               |   | 658  |                            |                 |            | 00:03:27             | 00:00:00               |                              |     |            | 00:03:27 |
| 4      | 4_lt_A_l_A   | 5.78                     | 48.23           |                 |                               |   | 655  |                            |                 |            | 00:03:28             | 00:00:00               |                              |     |            | 00:03:28 |
| 5      | 5_lt_B_l_A   | 5.76                     | 48.23           |                 |                               |   | 649  |                            |                 |            | 00:03:04             | 00:00:00               |                              |     |            | 00:03:04 |
| 6      | 6_lt_C_l_A   | 5.76                     | 48.23           |                 |                               |   | 636  |                            |                 |            | 00:03:23             | 00:00:00               |                              |     |            | 00:03:23 |
| 7      | 7_lt_A_m_A   | 5.79                     | 48.23           |                 |                               |   | 658  |                            |                 |            | 00:03:28             | 00:00:00               |                              |     |            | 00:03:28 |
| 8      | 8_lt_B_m_A   | 5.75                     | 48.23           |                 |                               |   | 650  |                            |                 |            | 00:03:11             | 00:00:00               |                              |     |            | 00:03:11 |
| 9      | 9_lt_C_m_A   | 5.77                     | 48.23           |                 |                               |   | 643  |                            |                 |            | 00:03:10             | 00:00:00               |                              |     |            | 00:03:10 |
| 10     | 10_lt_A_h_A  | 5.76                     | 48.23           |                 |                               |   | 648  |                            |                 |            | 00:03:34             | 00:00:00               |                              |     |            | 00:03:34 |
| 11     | 11_lt_B_h_A  | 5.78                     | 48.23           |                 |                               |   | 637  |                            |                 |            | 00:03:43             | 00:00:00               |                              |     |            | 00:03:43 |
| 12     | 12_lt_C_h_A  | 5.80                     | 48.23           |                 |                               |   | 632  |                            |                 |            | 00:03:30             | 00:00:00               |                              |     |            | 00:03:30 |
| 13     | 13_lt_A_uh_A | 5.79                     | 48.23           |                 |                               |   | 646  |                            |                 |            | 00:03:09             | 00:00:00               |                              |     |            | 00:03:09 |
| 14     | 14_lt_B_uh_A | 5.76                     | 48.23           |                 |                               |   | 656  |                            |                 |            | 00:03:01             | 00:00:00               |                              |     |            | 00:03:01 |
| 15     | 15_lt_C_uh_A | 5.76                     | 48.23           |                 |                               |   | 642  |                            |                 |            | 00:03:06             | 00:00:00               |                              |     |            | 00:03:06 |
| 16     | 16_lt_A_lt_B | 5.60                     | 48.23           |                 |                               |   | 638  |                            |                 |            | 00:03:23             | 00:00:00               |                              |     |            | 00:03:23 |
| 17     | 17_lt_B_lt_B | 5.56                     | 48.23           |                 |                               |   | 643  |                            |                 |            | 00:03:32             | 00:00:00               |                              |     |            | 00:03:32 |
| 18     | 18_lt_C_lt_B | 5.57                     | 48.23           |                 |                               |   | 665  |                            |                 |            | 00:03:40             | 00:00:00               |                              |     |            | 00:03:40 |
| 19     | 19_lt_A_l_B  | 5.54                     | 48.23           |                 |                               |   | 648  |                            |                 |            | 00:03:30             | 00:00:00               |                              |     |            | 00:03:30 |
| 20     | 20_lt_B_l_B  | 5.60                     | 48.23           |                 |                               |   | 644  |                            |                 |            | 00:03:30             | 00:00:00               |                              |     |            | 00:03:30 |
| 21     | 21_lt_C_l_B  | 5.59                     | 48.23           |                 |                               |   | 645  |                            |                 |            | 00:03:26             | 00:00:00               |                              |     |            | 00:03:26 |
| 22     | 22_lt_A_m_B  | 5.62                     | 48.23           |                 |                               |   | 646  |                            |                 |            | 00:03:26             | 00:00:00               |                              |     |            | 00:03:26 |
| 23     | 23_lt_B_m_B  | 5.56                     | 48.23           |                 |                               |   | 655  |                            |                 |            | 00:03:28             | 00:00:00               |                              |     |            | 00:03:28 |
| 24     | 24_lt_C_m_B  | 5.58                     | 48.23           |                 |                               |   | 658  |                            |                 |            | 00:03:28             | 00:00:00               |                              |     |            | 00:03:28 |
| 25     | 25_lt_A_h_B  | 5.55                     | 48.23           |                 |                               |   | 646  |                            |                 |            | 00:03:37             | 00:00:00               |                              |     |            | 00:03:37 |
| 26     | 26_lt_B_h_B  | 5.57                     | 48.23           |                 |                               |   | 643  |                            |                 |            | 00:03:29             | 00:00:00               |                              |     |            | 00:03:29 |
| 27     | 27_lt_C_h_B  | 5.61                     | 48.23           |                 |                               |   | 635  |                            |                 |            | 00:03:38             | 00:00:00               |                              |     |            | 00:03:38 |
| 28     | 28_lt_A_uh_B | 5.60                     | 48.23           |                 |                               |   | 644  |                            |                 |            | 00:04:01             | 00:00:00               |                              |     |            | 00:04:01 |
| 29     | 29_lt_B_uh_B | 5.54                     | 48.23           |                 |                               |   | 654  |                            |                 |            | 00:03:48             | 00:00:00               |                              |     |            | 00:03:48 |
| 30     | 30_lt_C_uh_B | 5.58                     | 48.23           |                 |                               |   | 643  |                            |                 |            | 00:03:24             | 00:00:00               |                              |     |            | 00:03:24 |
| 31     | 31_lt_A_lt_C | 3.93                     | 1.47            |                 |                               |   | 642  |                            |                 |            | 00:02:52             | 00:00:00               |                              |     |            | 00:02:52 |
| 32     | 32_lt_B_lt_C | 3.95                     | 1.47            |                 |                               |   | 650  |                            |                 |            | 00:03:26             | 00:00:00               |                              |     |            | 00:03:26 |
| 33     | 33_lt_C_lt_C | 3.94                     | 1.40            |                 |                               |   | 643  |                            |                 |            | 00:03:04             | 00:00:00               |                              |     |            | 00:03:04 |
| 34     | 34_lt_A_l_C  | 3.93                     | 1.47            |                 |                               |   | 643  |                            |                 |            | 00:03:32             | 00:00:00               |                              |     |            | 00:03:32 |
| 35     | 35_lt_B_l_C  | 3.96                     | 1.47            |                 |                               |   | 645  |                            |                 |            | 00:03:33             | 00:00:00               |                              |     |            | 00:03:33 |
| 36     | 36_lt_C_l_C  | 3.97                     | 1.47            |                 |                               |   | 631  |                            |                 |            | 00:03:34             | 00:00:00               |                              |     |            | 00:03:34 |
| 37     | 37_lt_A_m_C  | 3.93                     | 1.47            |                 |                               |   | 641  |                            |                 |            | 00:03:29             | 00:00:00               |                              |     |            | 00:03:29 |
| 38     | 38_lt_B_m_C  | 3.94                     | 1.47            |                 |                               |   | 644  |                            |                 |            | 00:03:28             | 00:00:00               |                              |     |            | 00:03:28 |
| 39     | 39_lt_C_m_C  | 3.94                     | 1.47            |                 |                               |   | 643  |                            |                 |            | 00:02:51             | 00:00:00               |                              |     |            | 00:02:51 |
| 40     | 40_lt_A_h_C  | 3.94                     | 1.47            |                 |                               |   | 643  |                            |                 |            | 00:02:50             | 00:00:00               |                              |     |            | 00:02:50 |
| 41     | 41_lt_B_h_C  | 3.95                     | 1.40            |                 |                               |   | 641  |                            |                 |            | 00:02:50             | 00:00:00               |                              |     |            | 00:02:50 |
| 42     | 42_lt_C_h_C  | 3.94                     | 1.40            |                 |                               |   | 643  |                            |                 |            | 00:02:49             | 00:00:00               |                              |     |            | 00:02:49 |
| 43     | 43_lt_A_uh_C | 3.97                     | 1.47            |                 |                               |   | 653  |                            |                 |            | 00:02:55             | 00:00:00               |                              |     |            | 00:02:55 |
| 44     | 44_lt_B_uh_C | 3.94                     | 1.47            |                 |                               |   | 643  |                            |                 |            | 00:02:52             | 00:00:00               |                              |     |            | 00:02:52 |
| 45     | 45_lt_C_uh_C | 3.96                     | 1.47            |                 |                               |   | 639  |                            |                 |            | 00:03:30             | 00:00:00               |                              |     |            | 00:03:30 |
| 46     | 46_lt_A_lt_D | 3.99                     | 1.44            |                 |                               |   | 642  |                            |                 |            | 00:03:38             | 00:00:00               |                              |     |            | 00:03:38 |
| 47     | 47_lt_B_lt_D | 3.96                     | 1.44            |                 |                               |   | 651  |                            |                 |            | 00:03:46             | 00:00:00               |                              |     |            | 00:03:46 |
| 48     | 48_lt_C_lt_D | 3.98                     | 1.44            |                 |                               |   | 651  |                            |                 |            | 00:04:07             | 00:00:00               |                              |     |            | 00:04:07 |
| 49     | 49_lt_A_l_D  | 3.97                     | 1.44            |                 |                               |   | 657  |                            |                 |            | 00:04:44             | 00:00:00               |                              |     |            | 00:04:44 |
| 50     | 50_lt_B_l_D  | 3.96                     | 1.44            |                 |                               |   | 634  |                            |                 |            | 00:04:57             | 00:00:00               |                              |     |            | 00:04:57 |
| 51     | 51_lt_C_l_D  | 3.97                     | 1.44            |                 |                               |   | 666  |                            |                 |            | 00:04:31             | 00:00:00               |                              |     |            | 00:04:31 |
| 52     | 52_lt_A_m_D  | 3.97                     | 1.44            |                 |                               |   | 654  |                            |                 |            | 00:03:54             | 00:00:00               |                              |     |            | 00:03:54 |
| 53     | 53_lt_B_m_D  | 3.95                     | 1.44            |                 |                               |   | 636  |                            |                 |            | 00:03:31             | 00:00:00               |                              |     |            | 00:03:31 |
| 54     | 54_lt_C_m_D  | 3.97                     | 1.44            |                 |                               |   | 654  |                            |                 |            | 00:03:27             | 00:00:00               |                              |     |            | 00:03:27 |
| 55     | 55_lt_A_h_D  | 3.94                     | 1.44            |                 |                               |   | 646  |                            |                 |            | 00:03:04             | 00:00:00               |                              |     |            | 00:03:04 |
| 56     | 56_lt_B_h_D  | 3.94                     | 1.44            |                 |                               |   | 643  |                            |                 |            | 00:02:46             | 00:00:00               |                              |     |            | 00:02:46 |
| 57     | 57_lt_C_h_D  | 3.94                     | 1.44            |                 |                               |   | 645  |                            |                 |            | 00:02:50             | 00:00:00               |                              |     |            | 00:02:50 |
| 58     | 58_lt_A_uh_D | 3.94                     | 1.44            |                 |                               |   | 643  |                            |                 |            | 00:02:52             | 00:00:00               |                              |     |            | 00:02:52 |





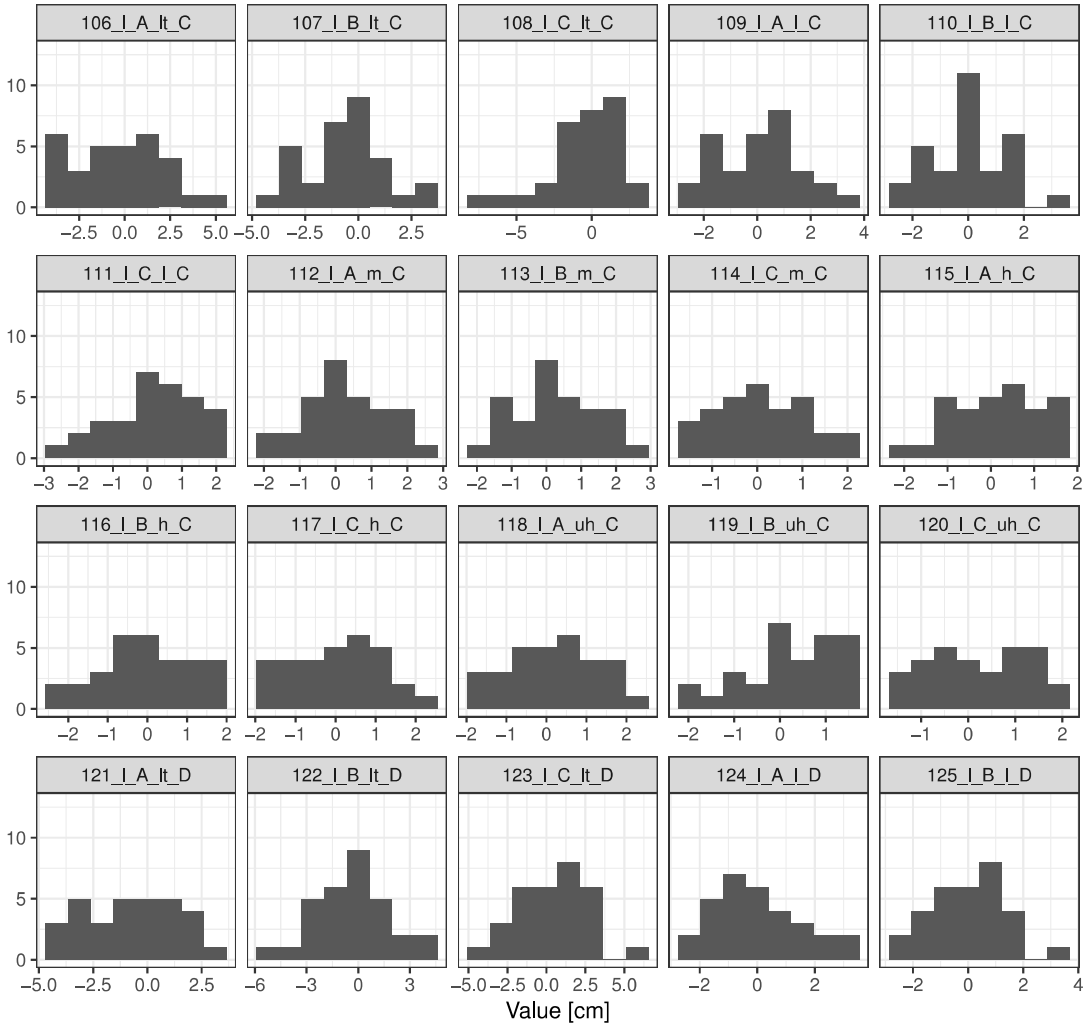




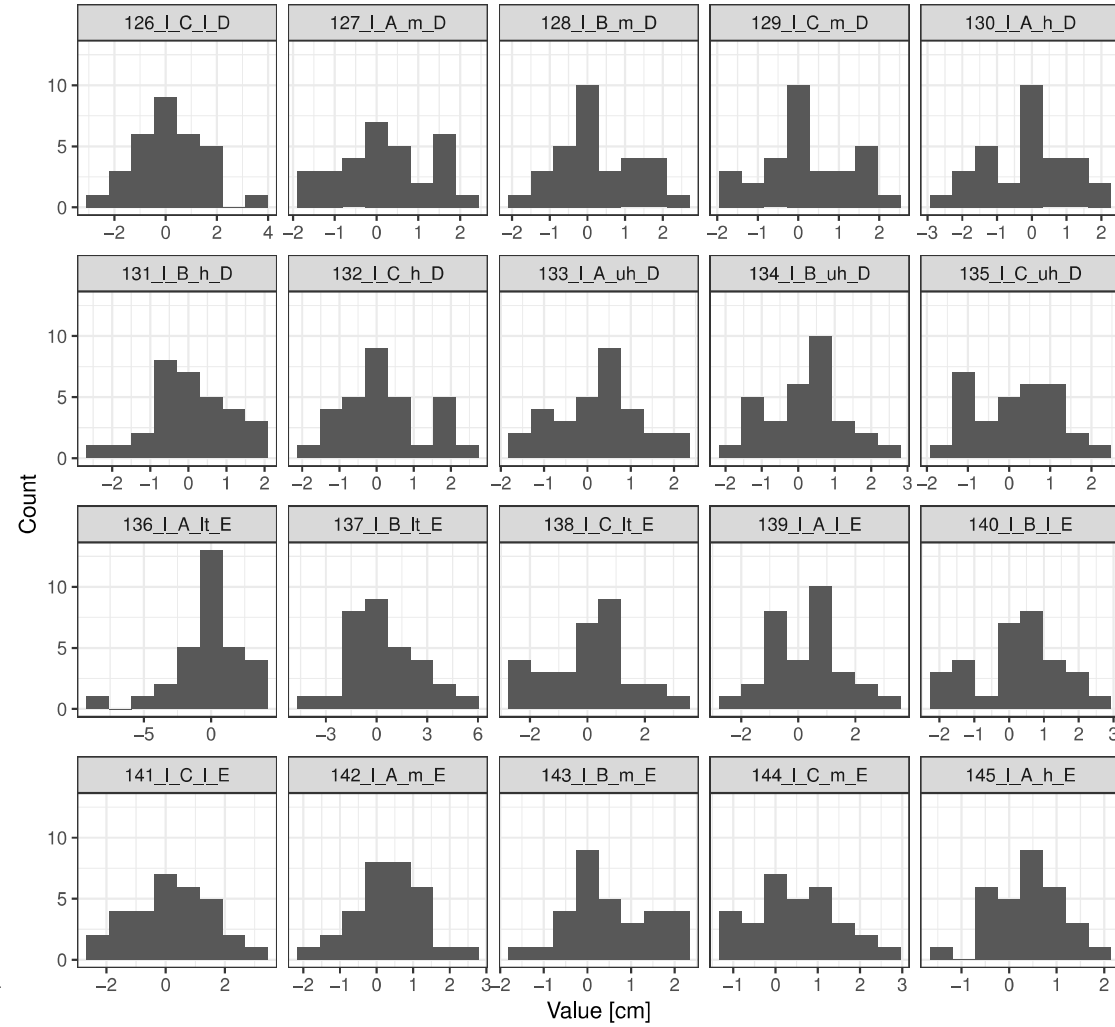


o "U ^XU ` } ` IJU DXtX ~ X o }}v }( Z ]v(o v } ( } ]vP u ]v ^ r ( }urD) }}v } ( ` }v Z o] ` } ( ]P] o o }}  
Z u} ^ v ]vPU ~ X Z Wll }}X} Pl X i l  
v ] ^ W o }}v ](( v ` v Z l }}v v u} o ( } Z ` } l(o)`X

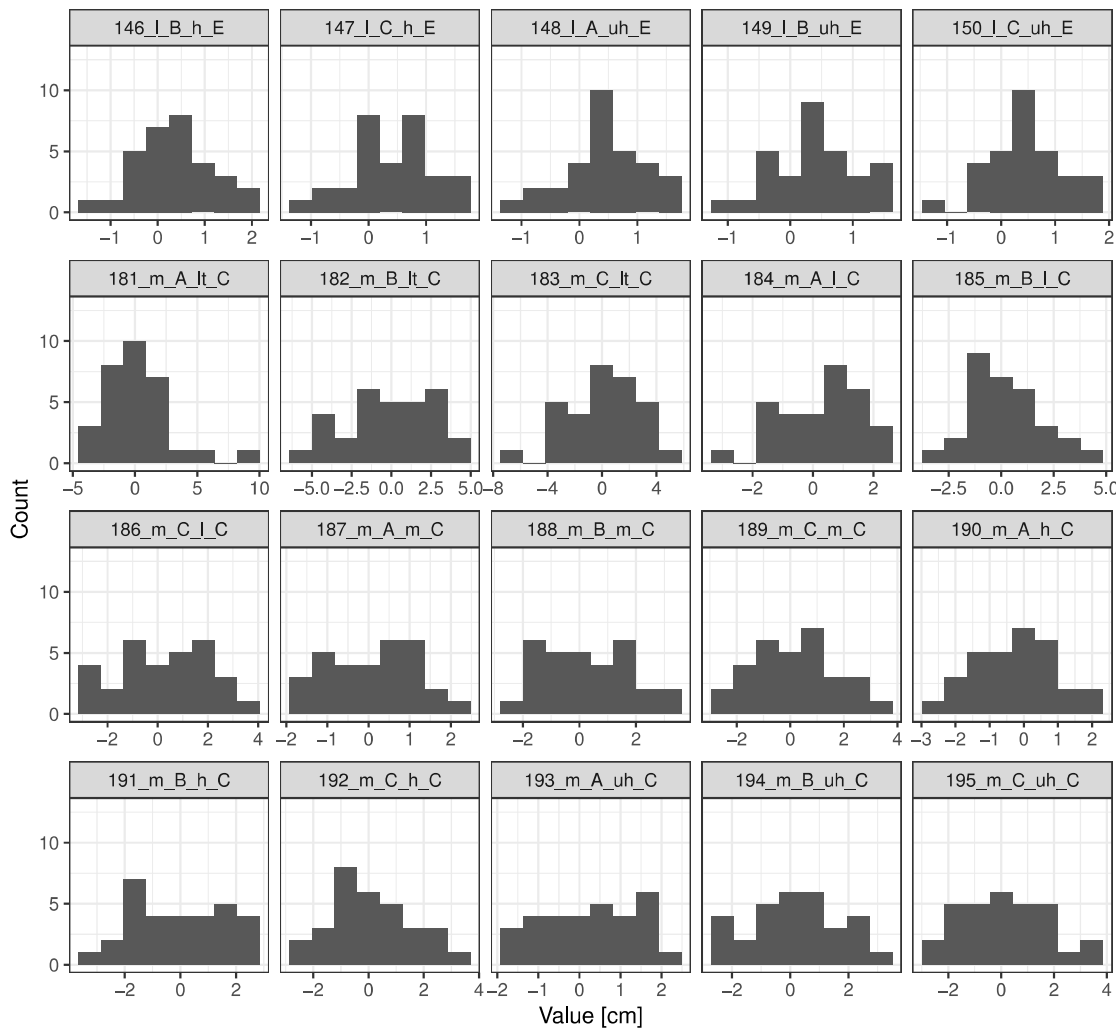
Elevation differences between check points and model



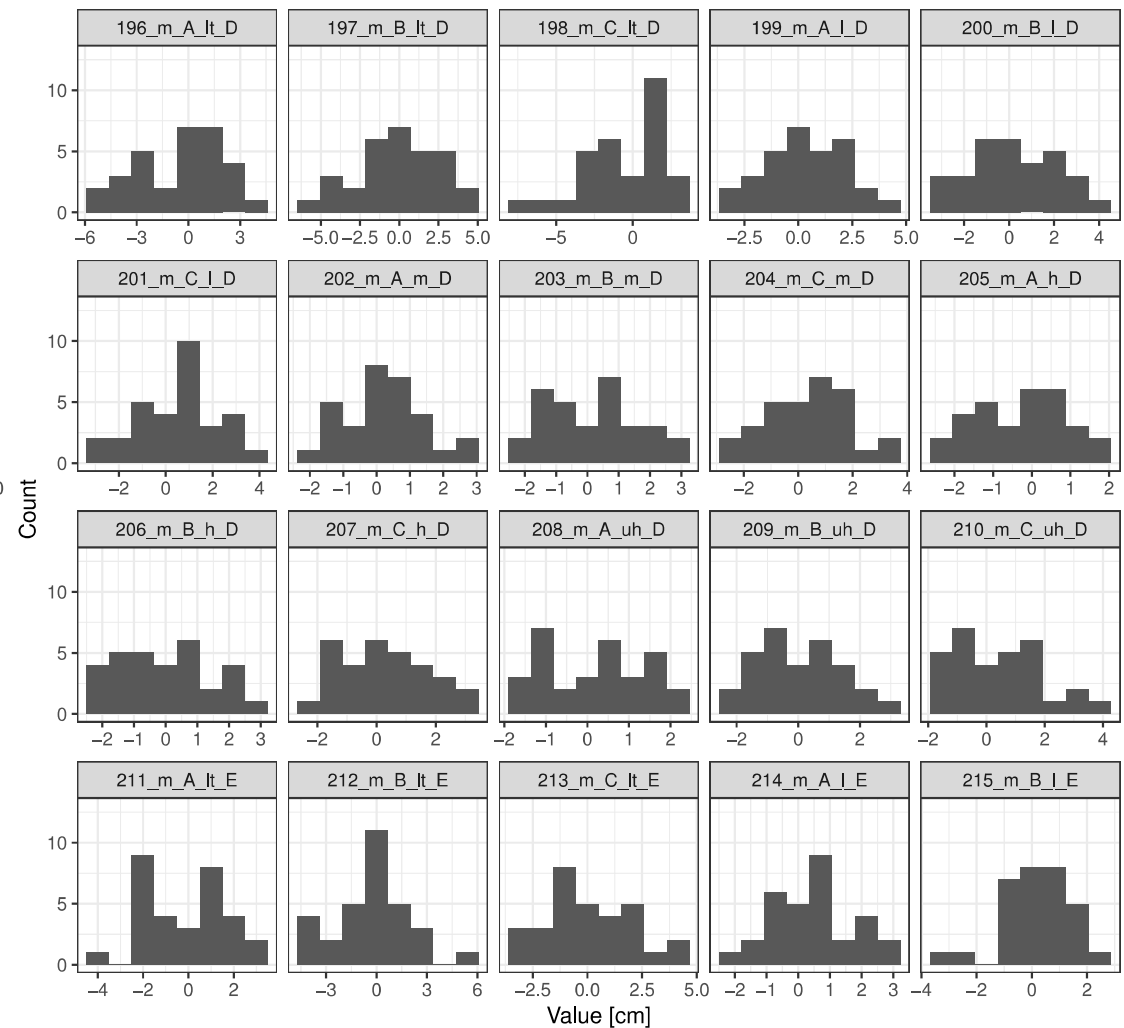
Elevation differences between check points and model



Elevation differences between check points and model

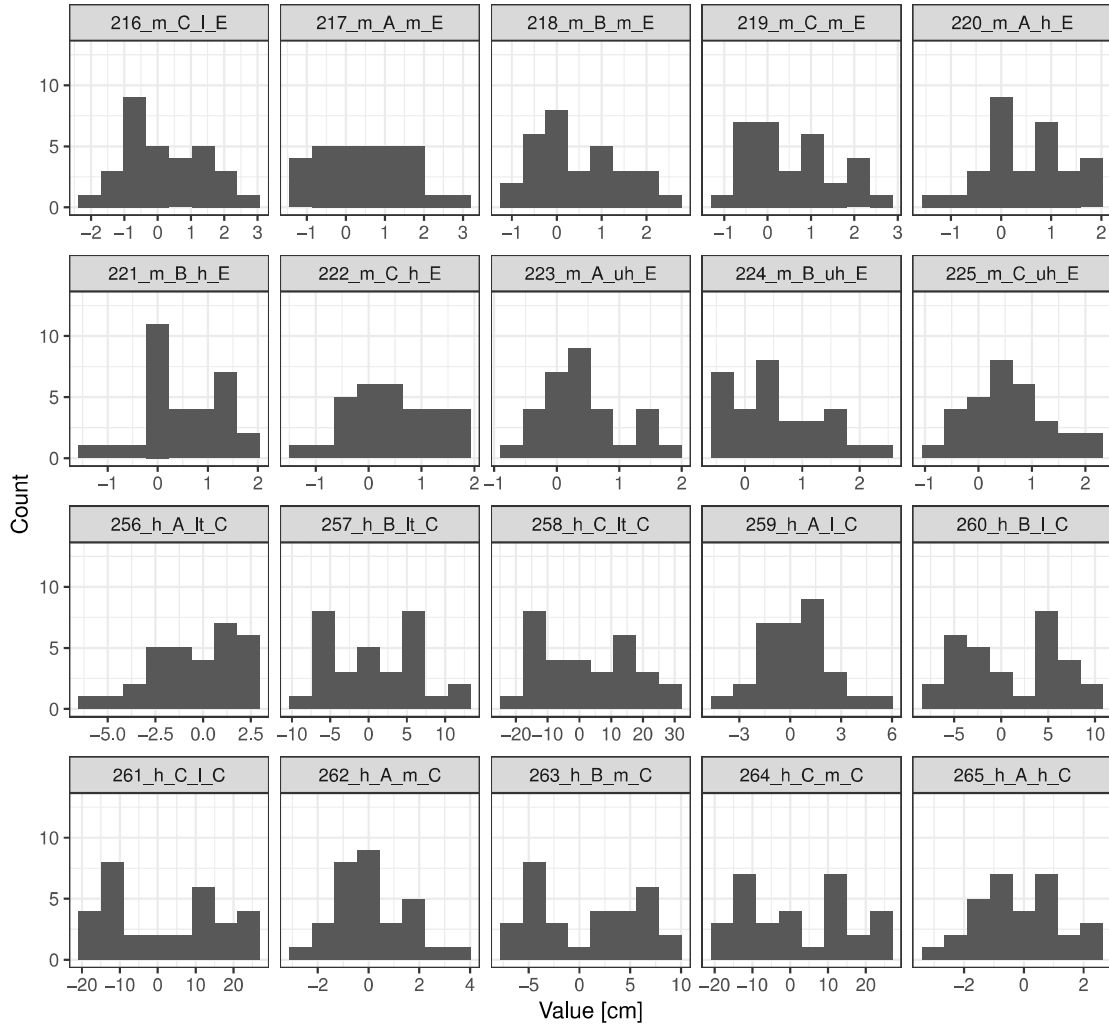


Elevation differences between check points and model

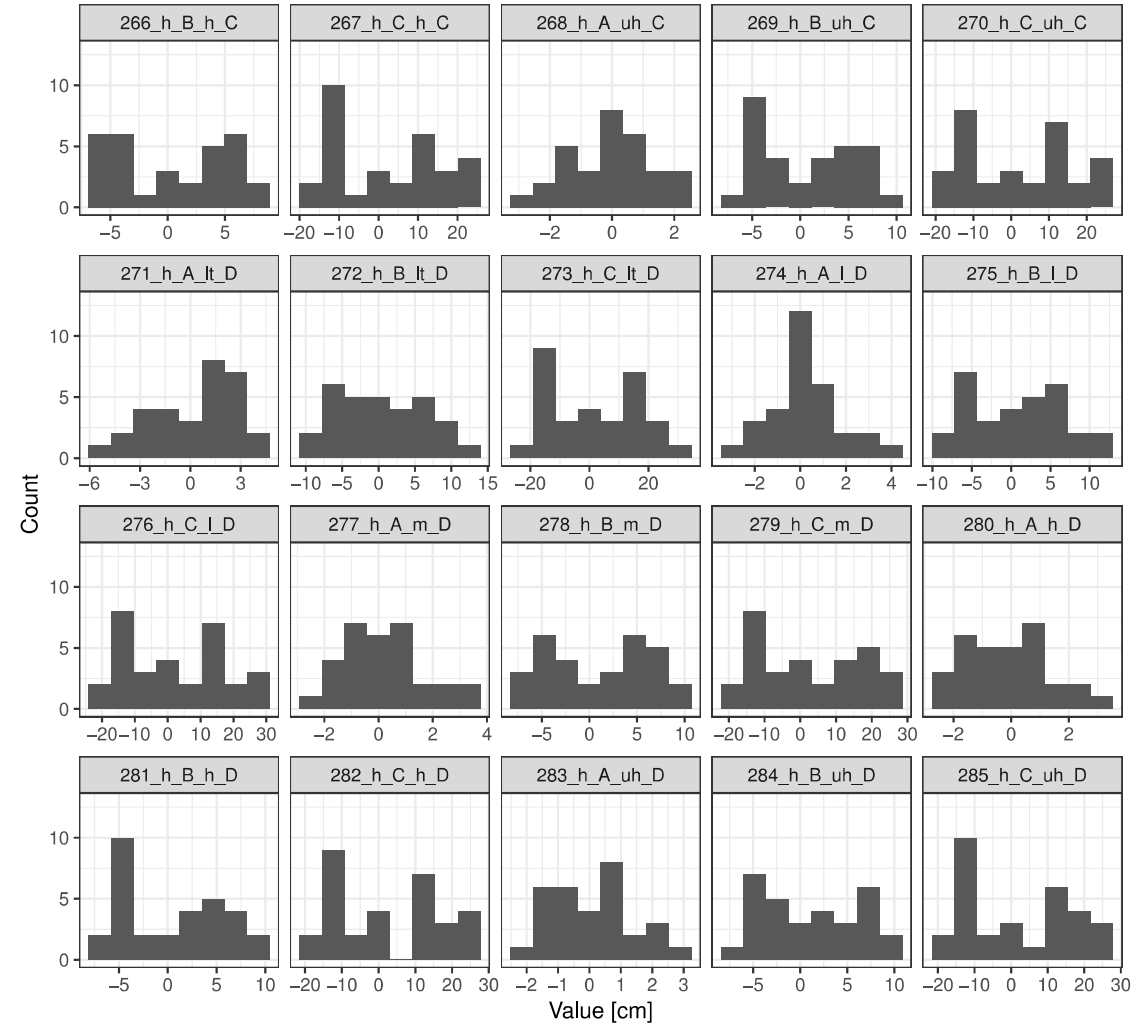




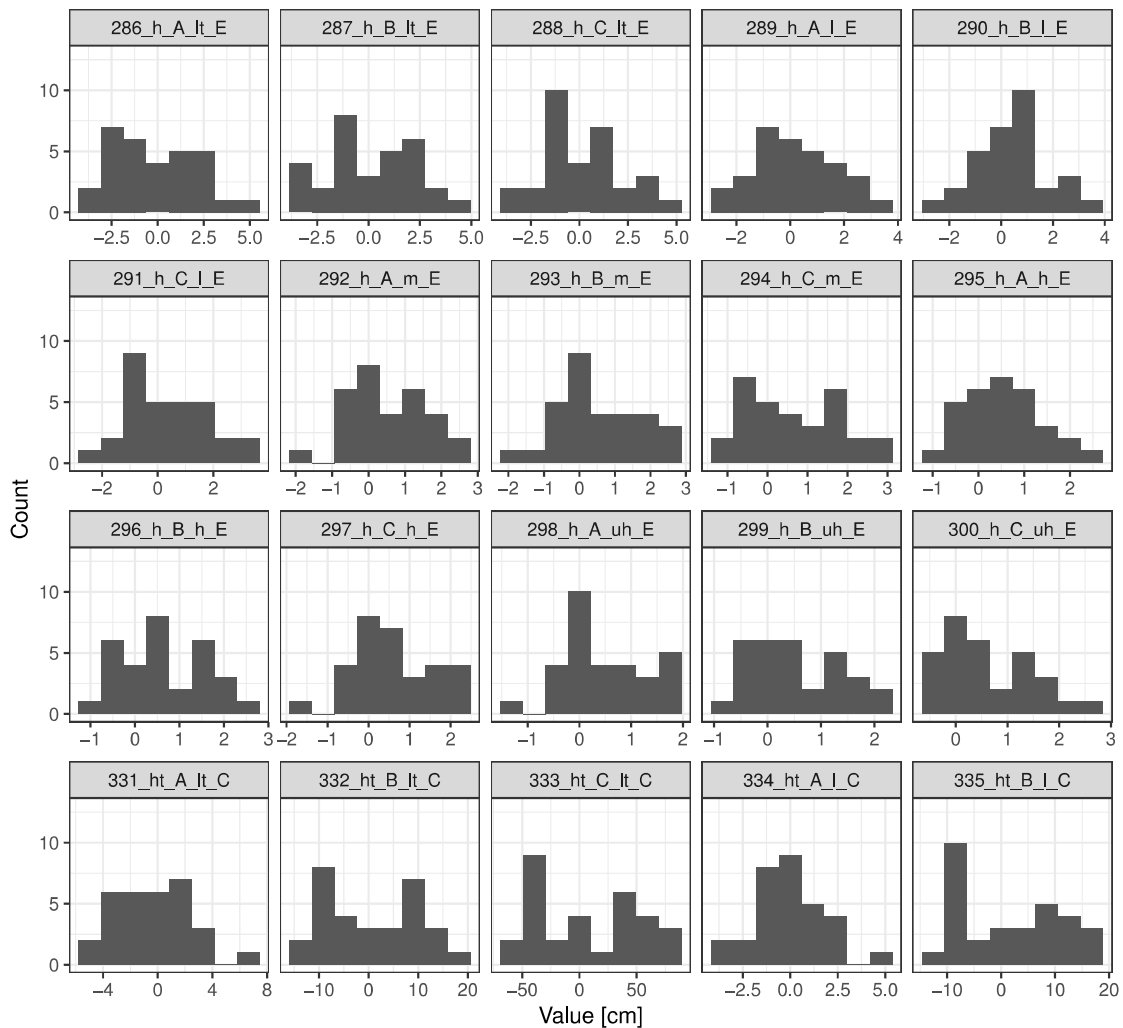
Elevation differences between check points and model



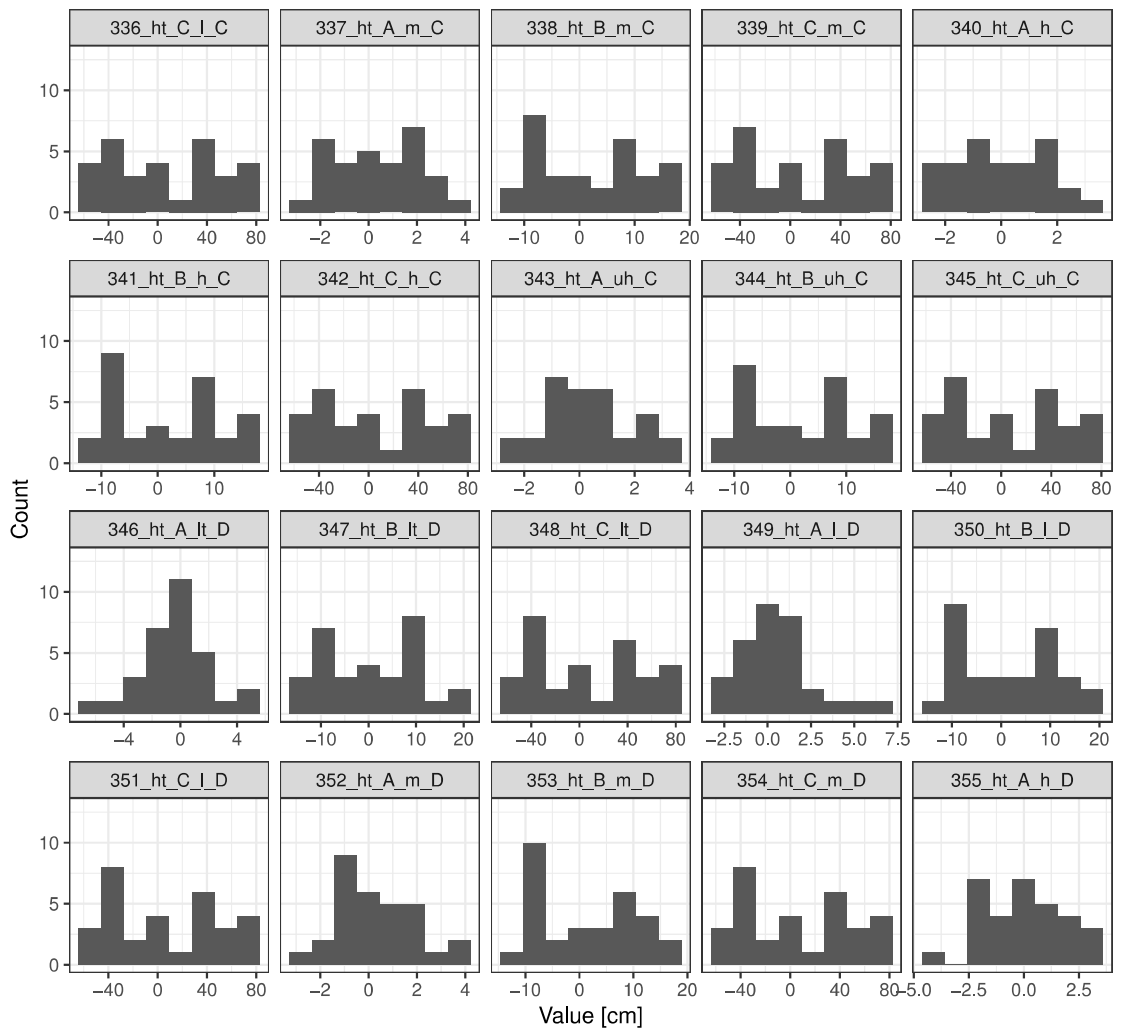
Elevation differences between check points and model



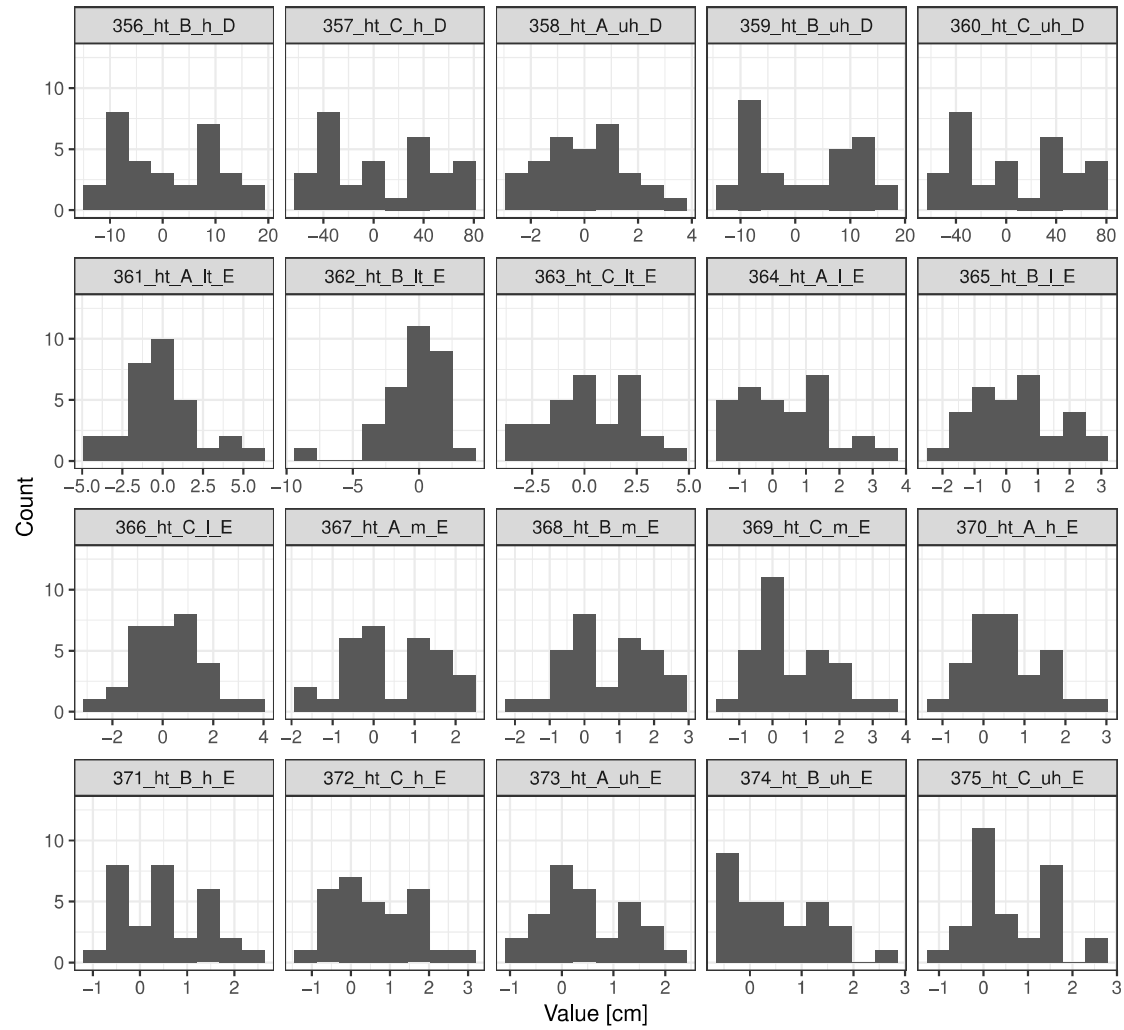
Elevation differences between check points and model



Elevation differences between check points and model



### Elevation differences between check points and model



Appendix S3: Python Script #1 (the fastest).

```
1 #First scheme: the fastest
2
3 import Metashape
4
5 doc = Metashape.app.document
6
7 for chunk in doc.chunks:
8
9 #alignment
10 chunk.matchPhotos(
11     downscale = 4,
12     keypoint_limit = 100000,
13     tiepoint_limit = 10000,
14     mask_tiepoints = False,
15     reset_matches = True,
16     generic_preselection = True,
17     reference_preselection = True)
18 chunk.alignCameras(reset_alignment = True)
19 doc.save()
20
21 #cloud filter
22 f = Metashape.PointCloud.Filter()
23
24 reprojection_error_threshold = 0.5
25 reconstruction_uncertainty_threshold = 10
26 image_count_threshold = 2
27 projection_accuracy_threshold = 20
28
29 f.init(chunk, criterion = Metashape.PointCloud.Filter.ReprojectionError)
30 f.removePoints(reprojection_error_threshold)
31
32 f.init(chunk, criterion = Metashape.PointCloud.Filter.ReconstructionUncertainty)
33 f.removePoints(reconstruction_uncertainty_threshold)
34
35 f.init(chunk, criterion = Metashape.PointCloud.Filter.ImageCount)
36 f.removePoints(image_count_threshold)
37
38 f.init(chunk, criterion = Metashape.PointCloud.Filter.ProjectionAccuracy)
39 f.removePoints(projection_accuracy_threshold)
40 doc.save()
41
42 #optimization of point cloud
43 chunk.optimizeCameras(
44     fit_f = True,
45     fit_cx = True,
46     fit_cy = True,
47     fit_b1 = True,
48     fit_b2 = True,
49     fit_k1 = True,
50     fit_k2 = True,
51     fit_k3 = False,
52     fit_k4 = False,
53     fit_p1 = False,
54     fit_p2 = False,
55     tiepoint_covariance = True)
56 doc.save()
57
58 #build dense cloud
59 chunk.buildDepthMaps(filter_mode = Metashape.AggressiveFiltering, reuse_depth = True)
60 chunk.buildDenseCloud(point_colors = True)
61 doc.save()
62
63 #build DEM
64 chunk.buildDem(source_data = Metashape.DenseCloudData)
65 doc.save()
66
67 #build orthomosaic
68 chunk.buildOrthomosaic(surface_data = Metashape.ElevationData)
69 doc.save()
70
71 #remove orthophotos
72 ortho = chunk.orthomosaic
73 ortho.removeOrthophotos()
74 doc.save()
75
76 Metashape.app.messageBox("Well done!")
77 #Metashape.app.quit()
```

Appendix S4: Python Script #2 (optimal).

```
1 #Second scheme: optimal
2
3 import Metashape
4
5 doc = Metashape.app.document
6
7 for chunk in doc.chunks:
8
9 #alignment
10 chunk.matchPhotos(
11     downscale = 4,
12     keypoint_limit = 0,
13     tiepoint_limit = 0,
14     mask_tiepoints = False,
15     reset_matches = True,
16     generic_preselection = True,
17     reference_preselection = True)
18 chunk.alignCameras(reset_alignment = True)
19 doc.save()
20
21 #cloud filter
22 f = Metashape.PointCloud.Filter()
23
24 reprojection_error_threshold = 0.5
25 reconstruction_uncertainty_threshold = 10
26 image_count_threshold = 2
27 projection_accuracy_threshold = 20
28
29 f.init(chunk, criterion = Metashape.PointCloud.Filter.ReprojectionError)
30 f.removePoints(reprojection_error_threshold)
31
32 f.init(chunk, criterion = Metashape.PointCloud.Filter.ReconstructionUncertainty)
33 f.removePoints(reconstruction_uncertainty_threshold)
34
35 f.init(chunk, criterion = Metashape.PointCloud.Filter.ImageCount)
36 f.removePoints(image_count_threshold)
37
38 f.init(chunk, criterion = Metashape.PointCloud.Filter.ProjectionAccuracy)
39 f.removePoints(projection_accuracy_threshold)
40 doc.save()
41
42 #optimization of point cloud
43 chunk.optimizeCameras(
44     fit_f = True,
45     fit_cx = True,
46     fit_cy = True,
47     fit_b1 = True,
48     fit_b2 = True,
49     fit_k1 = True,
50     fit_k2 = True,
51     fit_k3 = True,
52     fit_k4 = True,
53     fit_p1 = True,
54     fit_p2 = True,
55     tiepoint_covariance = True)
56 doc.save()
57
58 #build dense cloud
59 chunk.buildDepthMaps(downscale = 2, filter_mode = Metashape.AggressiveFiltering,
60 reuse_depth = True)
61 chunk.buildDenseCloud(point_colors = True)
62 doc.save()
63
64 #build DEM
65 chunk.buildDem(source_data = Metashape.DenseCloudData)
66 doc.save()
67
68 #build orthomosaic
69 chunk.buildOrthomosaic(surface_data = Metashape.ElevationData)
70 doc.save()
71
72 #remove orthophotos
73 ortho = chunk.orthomosaic
74 ortho.removeOrthophotos()
75 doc.save()
76
77 Metashape.app.messageBox("Well done!")
78 #Metashape.app.quit()
```

Appendix S5: Python Script #3 (best quality).

```
1 #Third scheme: best quality
2
3 import Metashape
4
5 doc = Metashape.app.document
6
7 for chunk in doc.chunks:
8
9 #alignment
10 chunk.matchPhotos(
11     downscale = 2,
12     keypoint_limit = 10000,
13     tiepoint_limit = 1000,
14     mask_tiepoints = False,
15     reset_matches = True,
16     generic_preselection = True,
17     reference_preselection = True)
18 chunk.alignCameras(reset_alignment = True)
19 doc.save()
20
21 #cloud filter
22 f = Metashape.PointCloud.Filter()
23
24 reprojection_error_threshold = 0.5
25 reconstruction_uncertainty_threshold = 10
26 image_count_threshold = 2
27 projection_accuracy_threshold = 20
28
29 f.init(chunk, criterion = Metashape.PointCloud.Filter.ReprojectionError)
30 f.removePoints(reprojection_error_threshold)
31
32 f.init(chunk, criterion = Metashape.PointCloud.Filter.ReconstructionUncertainty)
33 f.removePoints(reconstruction_uncertainty_threshold)
34
35 f.init(chunk, criterion = Metashape.PointCloud.Filter.ImageCount)
36 f.removePoints(image_count_threshold)
37
38 f.init(chunk, criterion = Metashape.PointCloud.Filter.ProjectionAccuracy)
39 f.removePoints(projection_accuracy_threshold)
40 doc.save()
41
42 #optimization of point cloud
43 chunk.optimizeCameras(
44     fit_f = True,
45     fit_cx = True,
46     fit_cy = True,
47     fit_b1 = True,
48     fit_b2 = True,
49     fit_k1 = True,
50     fit_k2 = True,
51     fit_k3 = True,
52     fit_k4 = True,
53     fit_p1 = True,
54     fit_p2 = True,
55     tiepoint_covariance = True)
56 doc.save()
57
58 #build dense cloud
59 chunk.buildDepthMaps(downscale = 1, filter_mode = Metashape.AggressiveFiltering,
60 reuse_depth = True)
61 chunk.buildDenseCloud(point_colors = True)
62 doc.save()
63
64 #build DEM
65 chunk.buildDem(source_data = Metashape.DenseCloudData)
66 doc.save()
67
68 #build orthomosaic
69 chunk.buildOrthomosaic(surface_data = Metashape.ElevationData)
70 doc.save()
71
72 #remove orthophotos
73 ortho = chunk.orthomosaic
74 ortho.removeOrthophotos()
75 doc.save()
76
77 Metashape.app.messageBox("Well done!")
78 #Metashape.app.quit()
```

### **Publikacja nr III**

Śledź, S., Ewertowski, M. W., & Evans, D. J. A. (2023). Quantification of short-term transformations of proglacial landforms in a temperate, debris-charged glacial landsystem, Kvíárjökull, Iceland. *Land Degradation & Development*, 34(17), 5566-5590.  
<https://doi.org/10.1002/ldr.4865>

## RESEARCH ARTICLE

WILEY

# Quantification of short-term transformations of proglacial landforms in a temperate, debris-charged glacial landsystem, Kvíárjökull, Iceland

Szymon Śledź<sup>1</sup>  | Marek W. Ewertowski<sup>1,2</sup>  | David J. A. Evans<sup>3</sup>

<sup>1</sup>Faculty of Geographical and Geological Sciences, Adam Mickiewicz University, Poznań, Poland

<sup>2</sup>School of Earth and Environment, University of Canterbury, Christchurch, New Zealand

<sup>3</sup>Department of Geography, Durham University, Durham, UK

## Correspondence

Szymon Śledź, Faculty of Geographical and Geological Sciences, Adam Mickiewicz University, Krygowskiego 10, 61-680 Poznań, Poland.

Email: [szysle@amu.edu.pl](mailto:szysle@amu.edu.pl)

## Funding information

Narodowe Centrum Nauki, Grant/Award Number: 2019/35/B/ST10/03928

## Abstract

Proglacial areas are dynamic landscapes and important indicators of geomorphic changes related to climate warming. Systematic and repeat surveys of landforms presently evolving on glacier forelands facilitate the quantification of rates of change and an improved understanding of the processes generating those changes. We report short-term (2014–2022) transformations of the proglacial landscape in front of Kvíárjökull, SE Iceland, and place them in a longer-term context of glacial landsystem evolution using aerial image archives since 1945. Short-term quantification uses a time series of uncrewed aerial vehicle (UAV) surveys, processed utilizing a structure-from-motion (SfM) workflow, to produce digital elevation models (DEMs) and orthophoto mosaics. The land elements surveyed include a kame terrace staircase, an outwash plain, an ice-cored hummocky moraine complex and ice-cored hummocky terrain with discontinuous sinuous ridges, for which elevation and volumetric changes are quantified. The kame terraces between 2014 and 2022 and the outwash plain between 2016 and 2022 were mainly stable with, respectively, 87% and 85% of their surfaces showing no change. The ice-cored hummocky terrain with discontinuous sinuous ridges underwent a volume loss of 64,632 m<sup>3</sup> in 2016–2022, with a maximum surface lowering of ≤9 m. The most dynamic land element was the ice-cored hummocky moraine complex, with transformations recorded for more than 87% of its area in 2014–2022; the surface was lowered by ≤23 m in some places, with a total volume loss of 365,773 m<sup>3</sup>. Our results confirm the ongoing degradation of ice-cored moraine and outwash complexes at variable rates related to buried ice volume and age of deglaciation. The evolution of chaotic hummocky terrain from debris-covered glacier ice, glacitectonic thrust masses, outwash fans/heads and complex englacial esker networks is an important modern analogue for informing palaeoglaciological reconstructions.

## KEYWORDS

change detection, debris-charged glacial landsystem, glacial geomorphology, proglacial landforms, UAV, uncrewed aerial vehicle

This is an open access article under the terms of the [Creative Commons Attribution](https://creativecommons.org/licenses/by/4.0/) License, which permits use, distribution and reproduction in any medium, provided the original work is properly cited.

© 2023 The Authors. *Land Degradation & Development* published by John Wiley & Sons Ltd.



## 1 | INTRODUCTION

Global climate warming has contributed to landform transformation for decades (Song et al., 2018) and increasing average air temperatures have resulted in significant changes in regional climates and local ecosystems, thereby increasing the risks of fires, droughts, floods and landslides (Allen et al., 2010; Flannigan et al., 2009; Gariano & Guzzetti, 2016; Hirabayashi et al., 2013; Młynarczyk et al., 2022). In cold climate settings, the impact has been manifested as dynamic responses in glacial systems (Benn et al., 2012; Benn & Evans, 2010). The recent fluctuations in volume and extent of glaciers have been widely analysed (e.g., Bash et al., 2018; Bash & Moorman, 2020; Carrivick et al., 2019; Hugonnet et al., 2021; Jouvét et al., 2019; Kienholz et al., 2020; Matecki, 2016; Matecki, 2022; Rossini et al., 2018; Sziłto & Bialik, 2018) but less attention has been paid to geomorphological transformations taking place in proglacial areas and their possible links to climate warming (Bennett et al., 2010; Bennett & Evans, 2012; Carrivick & Heckmann, 2017; Chandler, Chandler, et al., 2020; Evans et al., 2023; Ewertowski et al., 2019; Ewertowski & Tomczyk, 2020; Hedding et al., 2020; Schomacker, 2008; Seier et al., 2017; Staines et al., 2015; Strzelecki et al., 2018).

Observations on landscape change in proglacial areas are important because such terrains contain a large amount of often unstable, non-consolidated sediments as well as water stored in the form of lakes and ice-cored landforms. The combination of potentially large volumes of meltwater and highly mobile sediments means that rapid, climate-driven transformations in proglacial areas can release substantial, possibly catastrophic, floods and/or debris flows, which in turn can rapidly transform landscapes located downstream (Carrivick & Tweed, 2019; Knight & Harrison, 2012a, 2012b; Knight & Harrison, 2018; Tomczyk et al., 2020; Tonkin et al., 2016). In inhabited parts of mountain and polar regions, the dynamics and scale of landform transformations on glacial forelands may have serious implications for infrastructure and human populations located in the same catchment (Cook et al., 2016, 2018; Harrison et al., 2018). Therefore, there is a strong justification for the monitoring of proglacial areas in such settings in order to understand the temporal aspects of landscape change during deglaciation, especially the de-icing of buried glacier ice masses (Bennett & Evans, 2012; Blauvelt et al., 2020; Evans et al., 2023; Ewertowski & Tomczyk, 2015; Kjær & Krüger, 2001; Krüger & Kjær, 2000; Schomacker, 2008; Schomacker & Kjær, 2007, 2008), as they pertain to applied glacial and paraglacial geomorphology (Carrivick & Heckmann, 2017). Not unrelated to this is the need to better quantify glacial process–form regimes as they pertain to spatio-temporal change in modern glacial landsystems (e.g., Bennett et al., 2010; Bennett & Evans, 2012; Chandler, Chandler, et al., 2020; Evans et al., 2009, 2019, 2022; Evans & Twigg, 2002; Ewertowski et al., 2019; Eyles, 1983a, 1983b; Midgley et al., 2018; Price, 1980).

Most of the previous research on proglacial landscape transformations has focused on the analysis of changes in the glacier forelands on a decadal temporal scale (e.g., Bennett & Evans, 2012; Carrivick & Heckmann, 2017; Etzelmüller, 2000; Ewertowski, 2014,

2019; Staines & Carrivick, 2015). Recently, a number of studies have begun the quantification of changes that take place on shorter temporal scales, from years to days (e.g., Bernard et al., 2016; Bühler et al., 2016; Chandler, Evans, et al., 2020; Evans et al., 2023; Ewertowski & Tomczyk, 2015; 2020; Fey & Krainer, 2020; Groos et al., 2019; Jouvét et al., 2018; Kraaijenbrink et al., 2016; Rossini et al., 2018; Ryan et al., 2015; van der Sluijs et al., 2018; van Woerkom et al., 2019; Westoby et al., 2020), typically using mobile platforms and sensors to collect data (e.g., LIDAR or uncrewed aerial vehicle [UAV]; Śledź et al., 2021 for detailed review). Because of their more detailed temporal and spatial scale, these studies do not cover whole glacial forelands but instead only individual landforms or single landform assemblages.

The aim of this study is to illustrate and quantify the short-term evolution of several different glacial landform assemblages on the foreland of the temperate, debris-charged glacier Kviárjökull in Iceland based on time series of UAV images. This foreland is an exceptional example of a landscape produced by the process of incremental stagnation (*sensu* Bennett & Evans, 2012; Eyles, 1979), whereby belts of debris-charged ice, representative of periodic influxes of debris to the glacier system, arrive occasionally at the receding glacier snout and give rise to the production of inset sequences of ice-cored hummocky moraine arcs over time. Each hummocky moraine arc therefore records the detachment of a debris-charged portion of the snout that is covered with supraglacial debris, retarding normal ablation rates. During progressive but slow de-icing, the hummocky moraine is subject to proglacial pushing or bulldozing by the actively receding glacier margin (Bennett et al., 2010; Bennett & Evans, 2012). Also important on the foreland of Kviárjökull are landform assemblages representative of sedimentation and landform construction in a high debris turnover piedmont glacier terminating in an erosional overdeepening. This has given rise to the development of unusually large latero-frontal terminal moraines, inset with extensive ice-contact glacifluvial landform–sediment associations. These include kame terraces, englacial eskers and pitted outwash, all reflective of the large sediment loads of meltwater networks that have developed over the overdeepening and which have been confined proglacially by the enclosing latero-frontal moraine amphitheatre (Bennett et al., 2010; Bennett & Evans, 2012; Phillips et al., 2017; Spedding & Evans, 2002).

Previous quantification studies at Kviárjökull by Bennett and Evans (2012) provided details on landform change relating to the melt-out of buried glacier ice and concomitant collapse of the ice-cored hummocky moraine arcs. They also documented the impact of the 1990s readvance (*sensu* Bradwell et al., 2006; Evans & Chandler, 2018; Evans & Hiemstra, 2005; Sigurdsson, 2005; Sigurdsson et al., 2007) of the glacier snout into the innermost moraine arc, which resulted in a phase of landform surface uplift by an average of 6.5 m following on from decades of collapse due to de-icing. This study aims to provide a continuation of the quantification of Bennett and Evans (2012) in order to evaluate the rate and extent of landscape degradation representative of modern-day glacierized settings characterized by debris-charged snouts with strong topographical constraints and subject to rapid melting in a warming

climate. An additional aim here is to facilitate the development of glacial process–form models constrained by real-time quantification, thereby strengthening, and indeed improving, those traditionally developed largely by ergodic principles (i.e., location for time reasoning, whereby a spatio-temporal continuum of landform genesis is reconstructed using examples of the landform at various stages of its development regardless of location; cf. Brunsden & Thornes, 1979; Evans, 2013; Evans & Twigg, 2002; Paine, 1985; Price, 1969).

## 2 | MATERIALS AND METHODS

This study is focussed on landform assemblages located on the northern part of the foreland of Kvíárjökull, a temperate, debris-charged outlet glacier of the Öræfajökull ice cap in SE Iceland (Figure 1a), and records their transformation based on time series of aerial photograph archives (Figure 1) and UAV data. Longer timescale change (decadal) was mapped using the digital scans of aerial photographs (0.5–0.9 m ground sampling distance [GSD], that is, ground distance between centres of two pixels) from National Land Survey of Iceland captured in 1945, 1964, 1980 and 1998 by Landmaelingar Islands and in 2003 by Loftmyndir ehf (see Bennett et al., 2010, for details) as well as pan-sharpened (0.5 m GSD) WorldView-2 satellite imagery from Maxar (formerly Digital Globe) for 2012 and 2014. For shorter timescales, we used the popular structure-from-motion (SfM) method (see Westoby et al., 2012) to produce digital elevation models (DEMs) and orthomosaics based on four sets of images obtained from different types of UAVs: fixed-winged (produced by SmartPlane) and several generations of Phantom series quadcopters (produced by DJI) (Table 1). Autonomous flights were carried out in 2021 (Phantom 4 Pro) and 2022 (Phantom 4 RTK), and partly in 2014 (Smartplane), while flights with Phantom 2 in 2014 and Phantom 3 in 2016 were conducted manually. PlanetScope satellite images (3 m GSD) (Planet, 2022), combined with our UAV orthomosaics, were used to map changes in the glacier front during our observation period of 2014–2022.

During the 2022 flying, the UAV was connected to a local GNSS base station in order to increase the accuracy of the coordinates of the images, facilitated by the use of a high-precision RTK survey. The Topcon Link and RTKLIB software were used for post-processing and the application of PPP corrections (Precise Point Positioning) for the 2022 set of images and Ground Control Points (GCPs), along with an estimation of the influence of ocean tides on the measurement (source: <http://holt.oso.chalmers.se/loading/>). The image sets were used to create DEMs and orthomosaics in the Agisoft Metashape 1.7.1 photogrammetry software. Due to the fact that the UAV was equipped with an RTK receiver in 2022, we used one of the image processing schemes proposed by Nota et al. (2022), whereby we co-aligned all sets of images with seven GCPs marked on the 2022 images. We did not use the coordinates of the images from the other sets (2014, 2016 and 2021) as references. The result of this procedure was one, co-aligned, large, sparse point cloud, which was then divided into four separate projects according to the year of survey (2014,

2016, 2021 and 2022), in which only the right images for a given year were processed further to generate dense point clouds. Then, we proceeded to the next steps of processing using the Metashape software, and their detailed description is contained in Śledź and Ewertowski (2022), from which we chose the settings and parameters according to the procedure in script no. 2 ‘Optimal’. The only modification in the script was the higher accuracy of generating a sparse point cloud (from low to high) due to the partial use of JPG images and unsatisfactory results at the low level. Śledź and Ewertowski (2022) also describe and illustrate the method for establishing GCPs in the field, in the form of stone circles and the technique for measuring them with a GNSS receiver, which was identical in this study. The results of the photogrammetric processing were four DEMs, with the GSD ranging from 5.35 to 7.36 cm. Additionally, four high-resolution orthomosaics with GSD of ~3 cm were also exported.

Based on the DEMs and orthomosaics, we defined four case study areas on the glacier foreland which represent land elements (the fundamental level of the glacial landsystems hierarchy; sensu Eyles, 1983a, 2003; Fookes et al., 1978) within the debris-charged, active temperate glacial landsystem at Kvíárjökull (Bennett et al., 2010) (Figure 2). These areas differ from each other in terms of their genesis, material properties and morphology, as well as the rate and scale of surface changes. To estimate changes on the foreland in a quantitative way, we used DEMs of differences (DoDs; Wheaton et al., 2010), which are models showing elevation changes between two surveys. DoDs were calculated in ArcMap 10.8.1 using a Geomorphic Change Detection (GCD) add-in dedicated to this software (Source: <http://gcd.riverscapes.xyz>). Before importing the DEMs to the GCD, we resampled them down to 6 cm per pixel. We also performed an error analysis, whereby variations in elevation differences for the stable areas on each pair of DEMs were calculated to determine the minimum level of detection (minLoD) equalled to 0.2 m. The mapping of the studied area was based on orthomosaics, field surveys and photographic documentation.

## 3 | RESULTS

### 3.1 | Characteristics of land elements of the debris-charged, active temperate foreland at Kvíárjökull

Four land elements characteristic of the foreland were selected to investigate recent surface change or transformations (Figure 3), including case study areas: (1) a kame terrace staircase; (2) an outwash plain; (3) an ice-cored hummocky moraine complex and (4) ice-cored hummocky terrain with discontinuous sinuous ridges. These are representative of the broader proglacial area/foreland as previously mapped by Bennett et al. (2010) and are characterized by different topographies and buried glacier ice content, in addition to their distinctive genetic origins based on observations since the earliest aerial photographs captured in 1945 (Bennett et al., 2010; Bennett & Evans, 2012; Eyles, 1979, 1983b; Spedding & Evans, 2002).

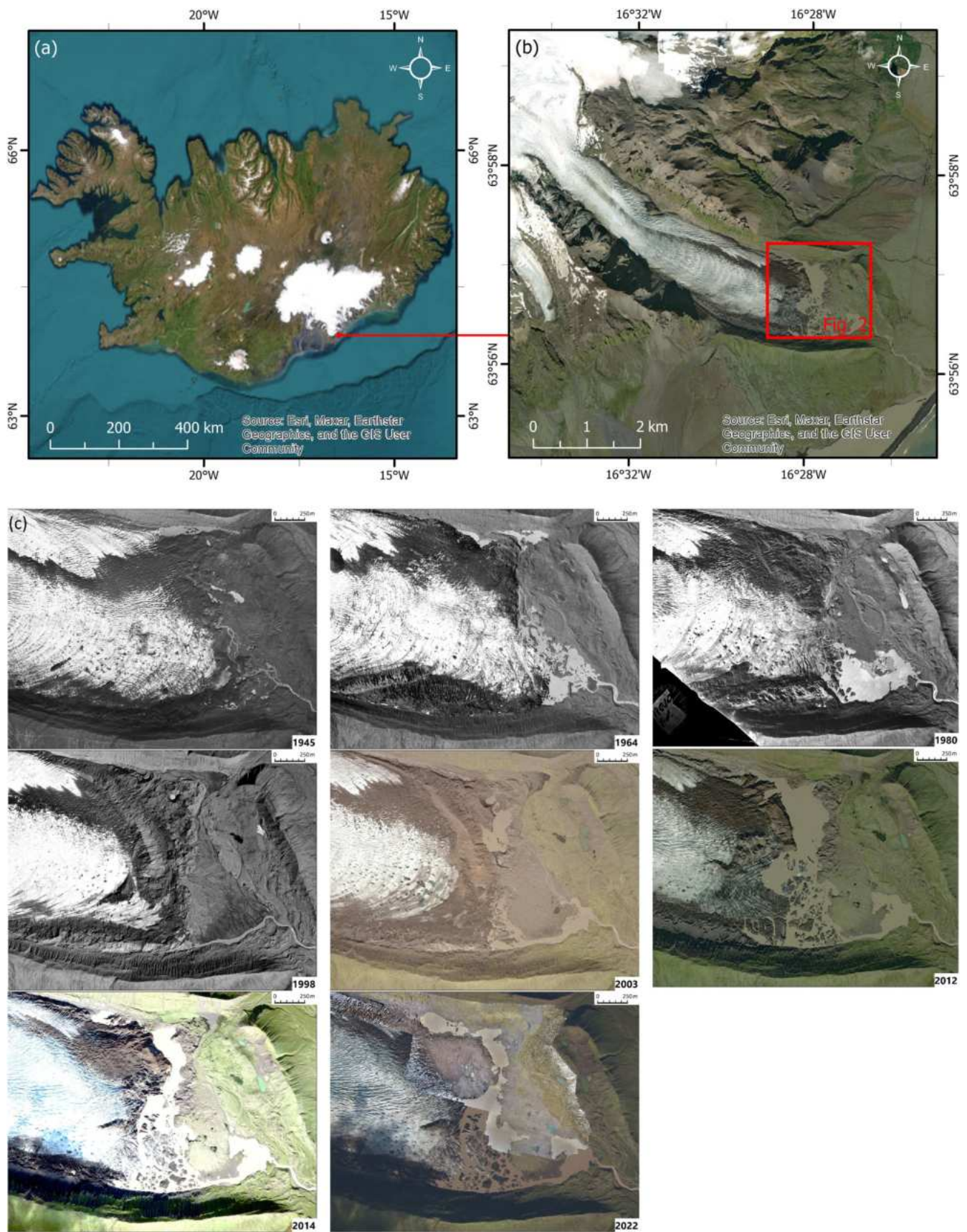


**FIGURE 1** Kviárjökull, SE Vatnajökull, Iceland: (a, b) location of the study area; (c) aerial photograph (1945–2003) and satellite image (2012–2022) extracts from various times since 1945, showing the changes to the glacier snout and foreland. *Source:* 1945–2003—aerial photographs, National Land Survey of Iceland; 2012 and 2014—WorldView-2 images, Maxar (formerly Digital Globe); 2022—PlanetScope, Planet (2022). [Colour figure can be viewed at [wileyonlinelibrary.com](https://onlinelibrary.wiley.com)]

**TABLE 1** Platforms used for quantifying recent, short timescale landscape change and the characteristics of the images.

| Date            | Drone                  | Total number of images | Images format | Type of sensor            |
|-----------------|------------------------|------------------------|---------------|---------------------------|
| 2014, September | DJI Phantom 2 Vision+  | 38                     | DNG           | Build-in, RGB             |
|                 | Smartplane             | 347                    | JPG           | Canon PowerShot S100, RGB |
| 2016, September | DJI Phantom 3 Advanced | 488                    | DNG           | Build-in, RGB             |
| 2021, September | DJI Phantom 4 Pro      | 717                    | DNG           | Build-in, RGB             |
| 2022, May       | DJI Phantom 4 RTK      | 880                    | JPG           | Build-in, RGB             |

Note: In 2014, two types of UAVs were used: a multi-rotor (DJI) and a fixed wing (Smartplane). Images from the fixed-wing and the DJI Phantom 4 RTK were saved in JPG format because these models do not allow saving in RAW format.

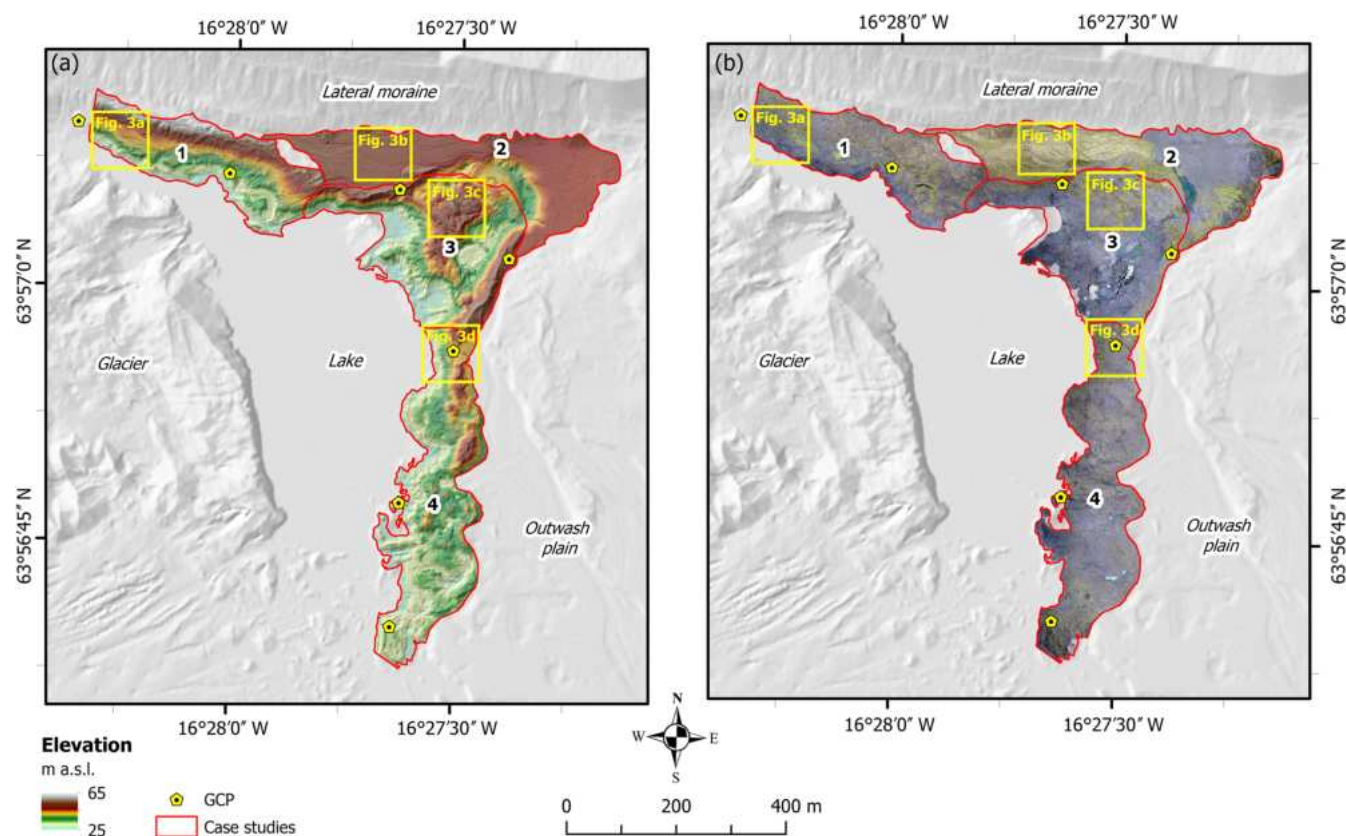


**FIGURE 2** The extent of the four case study areas on the foreland of Kvíárjökull (1: a kame terrace staircase; 2: an outwash plain; 3: an ice-cored hummocky moraine complex; and 4: ice-cored hummocky terrain with discontinuous sinuous ridges), with locations of Ground Control Points (GCPs) marked on the digital elevation model with hillshade (a) and orthomosaic (b) from September 2021. The figure also shows the location of the examples of the land elements in Figure 3. Source of background: IslandsDEM v1.0. Source: <https://www.lmi.is/>. [Colour figure can be viewed at [wileyonlinelibrary.com](https://onlinelibrary.wiley.com)]

The kame terrace staircase (case study area 1; Figures 2 and 3a) was developed between the ice margin and the steep proximal slope of the 100-m-high left lateral moraine (Kumbsmýrarkambur) on the foreland. Five to six distinct terrace levels were visible and characterized by tread widths of 8–25 m and riser heights of 4–13 m, the latter likely representing different period lengths of ice surface stabilization. Kame terraces are formed by meltwater flowing between the ice margin and any constraining slope, in this case the Kumbsmýrarkambur lateral moraine, so that each tread represents a former river bed that became abandoned once the glacier margin receded from the ice-

contact slope/riser. Ground observations at the glacier margin since 1992 record the localized plunging of the meltwater streams beneath the glacier margin to form margin-parallel englacial tunnels whose glaci-fluvial infill are gradually buried by the aggradation of the terrace deposits (Figure 4); this results in the localized burying of remnant ice masses within the terraces (Bennett & Evans, 2012). The gradual melt-out of such buried ice masses gives rise to collapse pits, usually forming a hummocky/pitted appearance to the ice-contact slopes/risers. Additionally, the edges of some of the terrace treads are characterized by the superimposition of small (1–2 m high) push moraines,

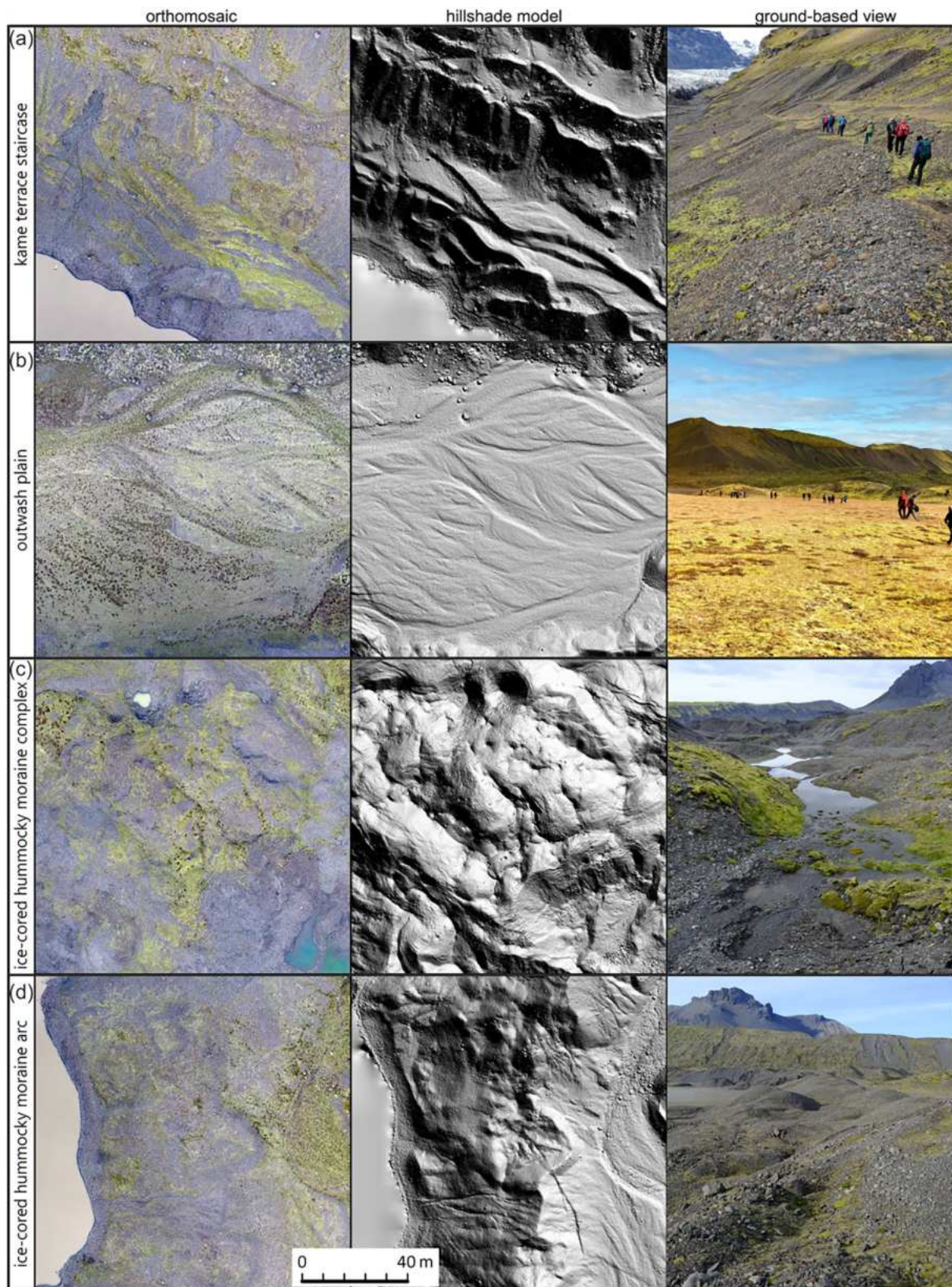


**FIGURE 3** Examples of the landsystem elements on the foreland at Kviárjökull viewed using remotely sensing data and ground photographs: (a) kame terrace staircase; (b) outwash plain; (c) ice-cored hummocky moraine complex and (d) ice-cored hummocky terrain with discontinuous sinuous ridges—see Figure 2 for location. Note that all images in the columns ‘orthomosaic’ and ‘hillshade model’ are presented at the same spatial scale. [Colour figure can be viewed at [wileyonlinelibrary.com](https://onlinelibrary.wiley.com/doi/10.1002/ldr.4865)]

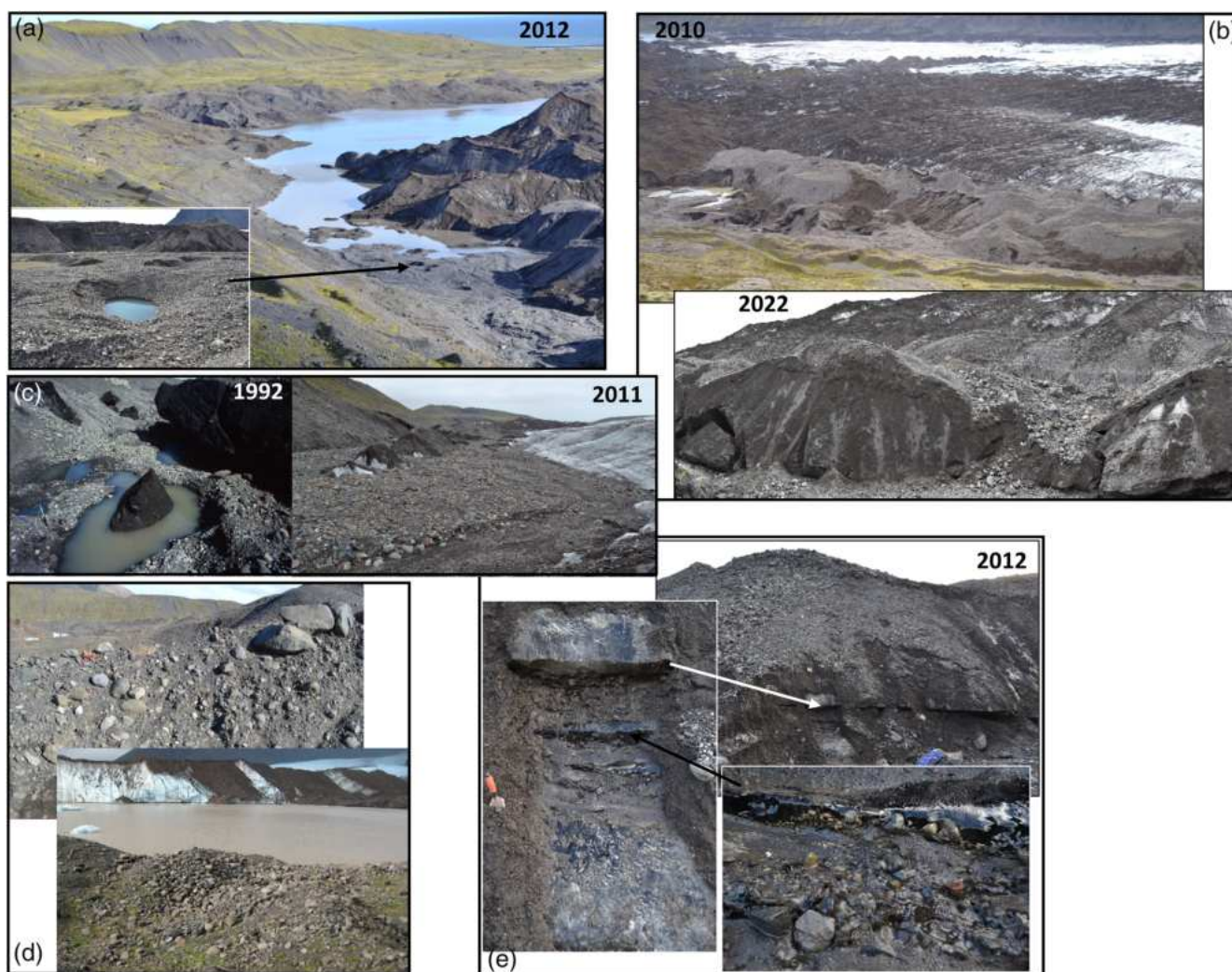


**FIGURE 4** Field photographs of examples of the development of ice-marginal drainage and landform development along the northern margin of the snout captured at various times since 1992: (a) freshly abandoned pitted kame terrace in 2012, with active channel emerging from the ice below an englacial esker; (b) the englacial esker emerging in 2010 (grey-coloured gravel) and overlying ice with active tunnels, depicted in 2022 at a more advanced stage of collapse when the sub-marginal stream had abandoned the adjacent kame terrace; (c) remnant ice in the 1992 and 2011 kame terraces, emerging through marginal outwash gravel and representing collapsed and buried tunnels originally cut by sub-marginal streams; (d) mounds of water-worn gravels forming parts of the sinuous ridges emerging within the ice-cored hummocky moraine during downwasting due to melt-out in 2008 and (e) cross-sections through sub-marginal/englacial tunnel fills exposed after stream downcutting in 2012. [Colour figure can be viewed at [wileyonlinelibrary.com](http://wileyonlinelibrary.com)]

some of which have been observed during formation (Phillips et al., 2017; Figure 3a). Continuous paraglacial reworking of the lateral moraine and the kame terraces has resulted in widespread dissection by debris flow and fluvial channels as well as the deposition of small debris flow-fed lobes and fans.

The outwash plain (case study area 2; Figures 2 and 3b) is a continuation of the highest of the kame terraces and forms a down-valley widening fan that was deposited around and over the outer downwasting glacier snout in the 1980s–1990s, infilling a proglacial/supraglacial lake that occupied the area in the 1960s–1980s (Bennett et al., 2010; Figure 1c). The meltwater deposited a large (~32,800 m<sup>2</sup>), flat area of glaci-fluvial sediments, overlying lake deposits and located between the ice-cored hummocky moraine complex and the former position of the 1990s ice margin to the south and

the Kumbsmýrarkambur lateral moraine to the north. The 1990s readvance moraine (sensu Bradwell et al., 2006; Evans & Chandler, 2018; Evans & Hiemstra, 2005; Sigurðsson, 2005; Sigurdsson et al., 2007) was constructed on the ice-contact face of the fan and now forms a prominent ridge along part of its southern edge. A network of braided stream channels is clearly visible on the outwash plain surface (Figure 3b) and small alluvial and debris flow-fed fans and isolated boulders have been deposited on its northern edge by paraglacial processes operating on the steep slopes of the Kumbsmýrarkambur lateral moraine.

The ice-cored hummocky moraine complex (case study area 3; Figures 2 and 3c) is a triangular-shaped area approximately 300 m long and up to 350 m wide, characterized by a chaotic hummocky topography with numerous, continuously expanding and contracting

areas of exposed glacier ice as a result of rapid and widespread topographic reversal (moraine belt A of Bennett & Evans, 2012). The outermost ridges of the complex are the product of pushing of the buried, stagnant ice mass into the outwash plain to the north and east as a result of the 1990s readvance, during which the surface of the ice-cored hummocky moraine belt increased in elevation by an average of 6.5 m (Bennett et al., 2010; Bennett & Evans, 2012). As a result, the easternmost edge of the moraine complex is very steep and separated from another, older hummocky moraine belt (hummocky moraine complex B of Bennett & Evans, 2012) by a narrow linear sandur that became constricted by the encroachment of the outer moraine edge and was then abandoned by meltwater drainage in the late 1990s (Figure 1c). These inset hummocky belts are the landform signature of incremental stagnation, with the overprinting of push ridges and/or development of glaciectonic structures that document readvance events such as the 1990s readvance (Bennett & Evans, 2012). Since around 2000, a proglacial and partially supraglacial lake (Figure 2) has developed at the western margin of the hummocky moraine complex as a result of more rapid ablation of the sparsely debris-covered glacier snout located up-ice. Lake development is a consequence of the gradual uncovering of the  $\leq 100$ -m-deep overdeepening beneath the snout in this area (Spedding & Evans, 2002). In 2014, the highest hummocks reached 25 m above the water level, but as the degradation intensified, the maximum elevation above the lake was only 15 m in 2022. Sediments that have been visible in the outcrops created by topographic inversion over the last 20 years have ranged from poorly sorted boulder to cobble gravels, gravelly diamictons and localized pockets of well-sorted stratified gravels and sands, the latter representing the melt-out of englacial tunnels/eskers (Bennett et al., 2010; Bennett & Evans, 2012; Spedding & Evans, 2002). Numerous tension cracks, freshly developed collapse pits/sink holes, damp surface sediment and debris flows are visible on the hummocky moraine surface and indicate the presence and ongoing degradation of buried glacier ice (Figure 3c).

Case study area 4 (Figures 2 and 3d) is a 650-m-long arc of ice-cored hummocky terrain with discontinuous sinuous ridges that extends southwards from the ice-cored hummocky moraine of case study area 3. It forms the hummocky ice-proximal face of the large pitted outwash plain previously interpreted by Bennett and Evans (2012) as an emerging outwash head occupying the adverse slope of the underlying bedrock overdeepening. The width of the moraine belt varies from 70 to 200 m with elevations reaching 10–15 m above the proglacial/supraglacial lake level in 2016. Like the hummocky moraine to the north, the hummocks and ridges in case study area 4 comprise a range of poorly sorted boulder to cobble gravels, gravelly diamictons and well-sorted stratified gravels and sands, with the latter clearly relating to west–east trending sinuous ridges that have developed since the 1990s due to the melt-out of englacial eskers linked to the apex of the outwash head (Bennett et al., 2010; Bennett & Evans, 2012; Spedding & Evans, 2002). The outermost ridges of the ice-cored hummocky terrain are arcuate to slightly sinuous in plan form but orientated ice-margin parallel and are push moraines constructed in ice-proximal outwash during the 1990s readvance.

### 3.2 | Glacier snout changes

Between 2011 and 2022, the ice margin was highly dynamic and oscillatory and additionally there was a significant difference in the behaviour between the northern and southern parts of the snout (Figure 5). The margin in the southern part of the snout underwent an almost continuous and gradual retreat (except for 2018, when it advanced by  $\sim 120$  m) as the glacier downwasted and disintegrated through the formation of widening crevasses and their flooding to produce tabular icebergs on the expanding proglacial/supraglacial lake. The northern part of the snout advanced by  $\sim 200$  m in the period 2013–2018 and then remained stable from 2019 to 2022. Likely influential in this varied response is the fact that the southern and northern margins of the snout are fed by different ice-flow units, which flow down either side of a nunatak in the accumulation zone and are nourished in source basins of different sizes. Additionally, ablation rates and hence the extent of glacier surface downwasting will vary significantly between the two ice-flow units in the snout zone (Figure 1c). The southern part of the glacier is characterized by large areas of debris-poor ice and, with the exception of the supraglacial lateral moraines and arcuate debris bands on the extreme southern margin, lacks a supraglacial debris cover. In contrast, the northern part of the glacier has always been characterized by an extensive debris cover delivered to the snout by the pulsed delivery of englacial and supraglacial debris which results in the retardation of ablation (incremental stagnation; Bennett & Evans, 2012). Moreover, the two ice-flow units have different dynamics, whereby the north ice-flow unit has exhibited some significant readvances in addition to that of the 1990s (Phillips et al., 2017). Also, likely important is the apparent glacier karst network, manifested as numerous moulins, which has remained a stable characteristic of the southern ice-flow unit over time and indicates that a complex englacial-to-subglacial tunnel network exists and results in substantial ice surface collapse during downwasting. All of these characteristics are exacerbated by the continuously rapid growth of the proglacial/supraglacial lake since 2011.

### 3.3 | Recent transformations of the land elements

Using the DoDs, land surface and volume change are now presented for the four case study areas (land elements) over the last 8 years or less. Due to differences in the temporal coverage of aerial imagery, the first year of analysis is either 2014 or 2016. Areal, volumetric and vertical averages calculated from DoDs for each land element are summarized in Table 2.

#### 3.3.1 | Case study area 1 (kame terraces)

Between 2014 and 2022, most of the kame terrace staircase was stable (Figure 6a) and detectable changes occurred in only 14% of the area, with a total net volume difference of  $-6402 \pm 1118 \text{ m}^3$ , reaching an average net thickness change of  $-0.99 \pm 0.17 \text{ m}$  (Table 2). A

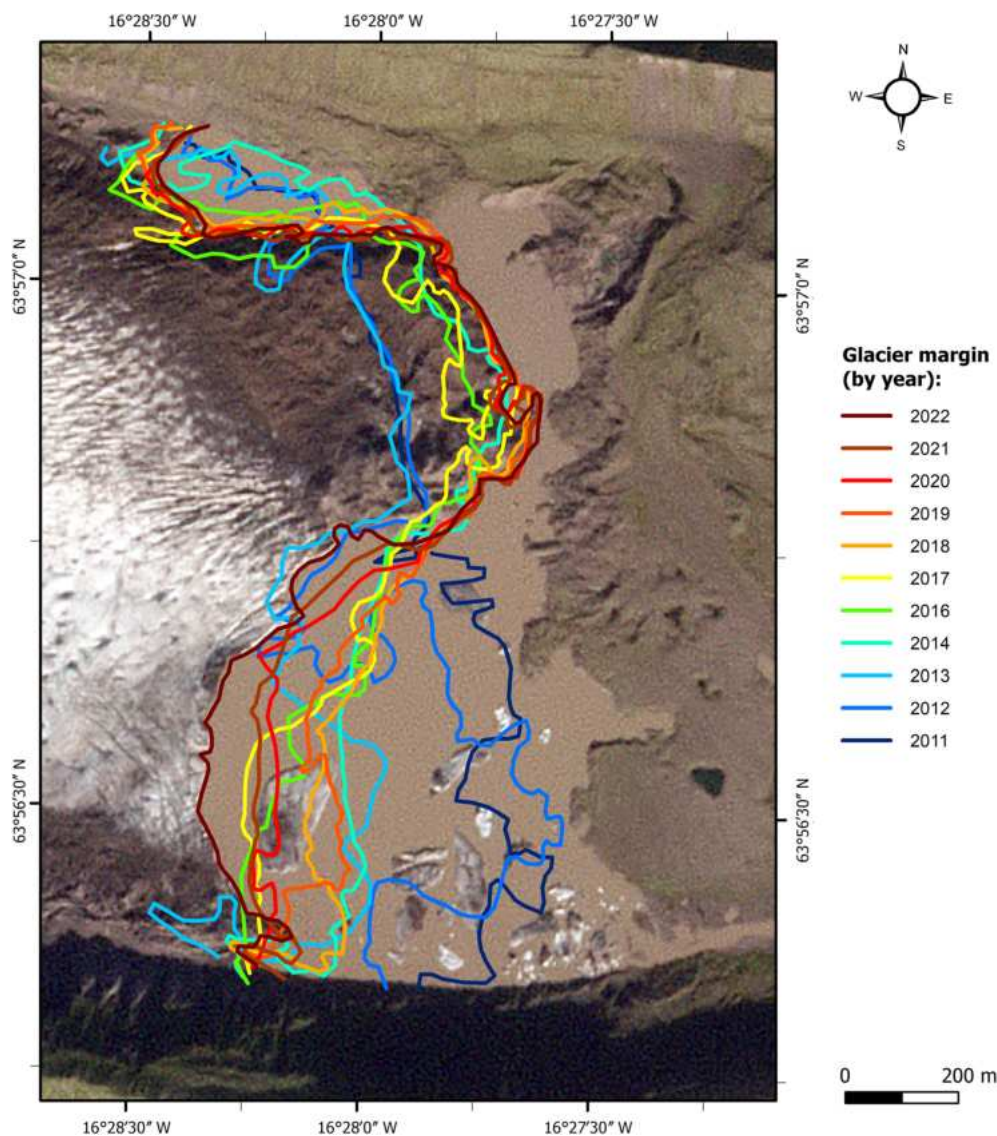


**FIGURE 5** Changes in the margin of the glacier snout in the period 2011–2022 based on the PlanetScope satellite imagery (Planet, 2022). Note that in 2015, scenes from PlanetScope were not available for this location. Date of the background image is 2022. [Colour figure can be viewed at [wileyonlinelibrary.com](https://onlinelibrary.wiley.com/doi/10.1002/ldr.4865)]

decrease in elevation of up to 10 m was recorded for the southern fringe (Figure 6a) or the most recent kame terraces, which was related to melting of the residual buried glacier ice that was created where marginal streams plunged into the lateral margin of the glacier and continued over short distances in englacial tunnels (Figure 4). An increase in elevation of up to 1 m was observed in the upper parts of the terrace sequence, which is likely associated with transfer of sediments from the adjacent lateral moraine slopes by mass movements. A further small area of positive change ( $\leq 3$  m) occurred in the south-east tip of the most recent terraces and is associated with push moraine construction on their former ice-contact slopes during the 2014 snout readvance (Phillips et al., 2017).

### 3.3.2 | Case study area 2 (outwash plain)

Large areas of the outwash plain (Figures 2 and 7) also remained partly stable over the last 6 years. The changes in the period 2016–

2022 took place on only  $\sim 15\%$  of the surface, with a total net volume difference of  $15,440 \pm 1764 \text{ m}^3$  (Figure 7c, Table 2). Two significantly active areas occur in the eastern half of the outwash plain. Firstly, an arcuate, lake-filled collapse pit occurs at the boundary of the ice-cored hummocky moraine complex (see case study area 3; Figure 7c), where the highest values of elevation loss of  $>3$  m are recorded. The degradation of buried ice here started with the development of small, dry sink holes, which enlarged until the buried ice became visible and the expansion of sink holes led to the development of chains of depressions and, finally, to the formation of a single, large elongate depression. This depression has gradually extended northwards to the foot of the Kumbsmýrarkambur lateral moraine slope and is surrounded by arcuate concentric tension fault scarps. The western edge of the depression is dissected by a 25-m-long,  $\leq 3$ -m-deep erosion gully (Figure 7e), which started developing after 2014. The increase in elevation between 2021 and 2022 (Figure 7b) is related to fluctuations in water level, which filled up the depression created between 2014 and 2021. Second, at the eastern, distal extremity of the



**TABLE 2** Areal, volumetric and vertical change averages derived from DEMs of differences for each case study.

| DoD  | Total area of surface lowering (m <sup>2</sup> ) | Total area of surface raising (m <sup>2</sup> ) | Total area of detectable change (m <sup>2</sup> ) | Pre cent of area of interest with detectable change (%) | Total volume of surface lowering (m <sup>3</sup> ) | Total volume of surface raising (m <sup>3</sup> ) | Total net volume change (m <sup>3</sup> ) | Average depth of surface lowering (m) | Average depth of surface raising (m) | Average net thickness of difference (m) for area with detectable change |
|--|--|---|---|---|--|---|---|---------------------------------------|--------------------------------------|---|
| Case study 1 (kame terrace staircase)                                      |  |   |   |   |  |   |   |                                       |                                      |   |
| September 2014–September 2021  | 5676.20  | 1121.85   | 6798.05   | 14.15   | 7550.45 ± 1135.24                                  | 1019.99 ± 224.37                                  | −6530.46 ± 1157.20                        | 1.33 ± 0.20                           | 0.91 ± 0.20                          | −0.96 ± 0.17  |
| September 2021–May 2022  | 323.02   | 396.49  | 719.52  | 1.50  | 122.22 ± 64.61                                     | 92.58 ± 79.30                                     | −29.64 ± 102.28                           | 0.38 ± 0.20                           | 0.23 ± 0.20                          | −0.04 ± 0.14  |
| September 2014–May 2022  | 5502.00  | 982.57  | 6484.57   | 13.49   | 7344.58 ± 1100.40                                  | 942.95 ± 196.51                                   | −6401.62 ± 1117.81                        | 1.33 ± 0.20                           | 0.96 ± 0.20                          | −0.99 ± 0.17  |
| Case study 2 (outwash plain)   |  |   |   |   |  |   |   |                                       |                                      |   |
| September 2016–September 2021  | 9074.76  | 412.60  | 9487.36   | 15.36   | 15,792.40 ± 1814.95                                | 141.78 ± 82.52                                    | −15,650.61 ± 1816.83                      | 1.74 ± 0.20                           | 0.34 ± 0.20                          | −1.65 ± 0.19  |
| September 2021–May 2022  | 210.33   | 865.61  | 1075.94   | 1.74  | 75.18 ± 42.07                                      | 267.95 ± 173.12                                   | 192.76 ± 178.16                           | 0.36 ± 0.20                           | 0.31 ± 0.20                          | 0.18 ± 0.17   |
| September 2016–May 2022  | 8811.90  | 409.10  | 9221.00   | 14.94   | 15,582.33 ± 1762.38                                | 142.13 ± 81.82                                    | −15,440.21 ± 1764.28                      | 1.77 ± 0.20                           | 0.35 ± 0.20                          | −1.67 ± 0.19  |
| Case study 3 (ice-cored hummocky moraine complex)                          |  |   |   |   |  |   |   |                                       |                                      |   |
| September 2014–September 2016  | 54,685.07  | 748.31  | 55,433.38   | 83.49   | 90,448.73 ± 10937.01                               | 265.07 ± 149.66                                   | −90,183.66 ± 10938.04                     | 1.65 ± 0.20                           | 0.35 ± 0.20                          | −1.63 ± 0.20  |
| September 2016–September 2021  | 55,483.78  | 425.78  | 55,909.56   | 84.21   | 256,699.33 ± 11096.76                              | 203.27 ± 85.16                                    | −256,496.07 ± 11097.08                    | 4.63 ± 0.20                           | 0.48 ± 0.20                          | −4.59 ± 0.20  |
| September 2021–May 2022  | 17,276.40  | 1440.67   | 18,717.06   | 28.20   | 17,720.79 ± 3455.28                                | 513.23 ± 288.13                                   | −17,207.55 ± 3467.27                      | 1.03 ± 0.20                           | 0.36 ± 0.20                          | −0.92 ± 0.19  |
| September 2014–May 2022  | 57,304.12  | 753.32  | 58,057.43   | 87.41   | 366,080.27 ± 11460.82                              | 307.27 ± 150.66                                   | −365,773.00 ± 11461.81                    | 6.39 ± 0.20                           | 0.41 ± 0.20                          | −6.30 ± 0.20  |
| Case study 4 (ice-cored hummocky terrain with discontinuous sinuous ridge) |  |   |   |   |  |   |   |                                       |                                      |   |
| September 2016–September 2021  | 42,688.40  | 266.32  | 42,954.72   | 60.14   | 60,392.62 ± 8537.68                                | 64.32 ± 53.26                                     | −60,328.30 ± 8537.85                      | 1.41 ± 0.20                           | 0.24 ± 0.20                          | −1.40 ± 0.20  |
| September 2021–May 2022  | 5828.46  | 170.91  | 5999.38   | 8.40  | 1908.44 ± 1165.69                                  | 56.66 ± 34.18                                     | −1851.78 ± 1166.19                        | 0.33 ± 0.20                           | 0.33 ± 0.20                          | −0.31 ± 0.19  |
| September 2016–May 2022  | 43,336.43  | 427.42  | 43,763.85   | 61.26   | 64,733.01 ± 8667.29                                | 101.43 ± 85.48                                    | −64,631.58 ± 8667.71                      | 1.49 ± 0.20                           | 0.24 ± 0.20                          | −1.48 ± 0.20  |

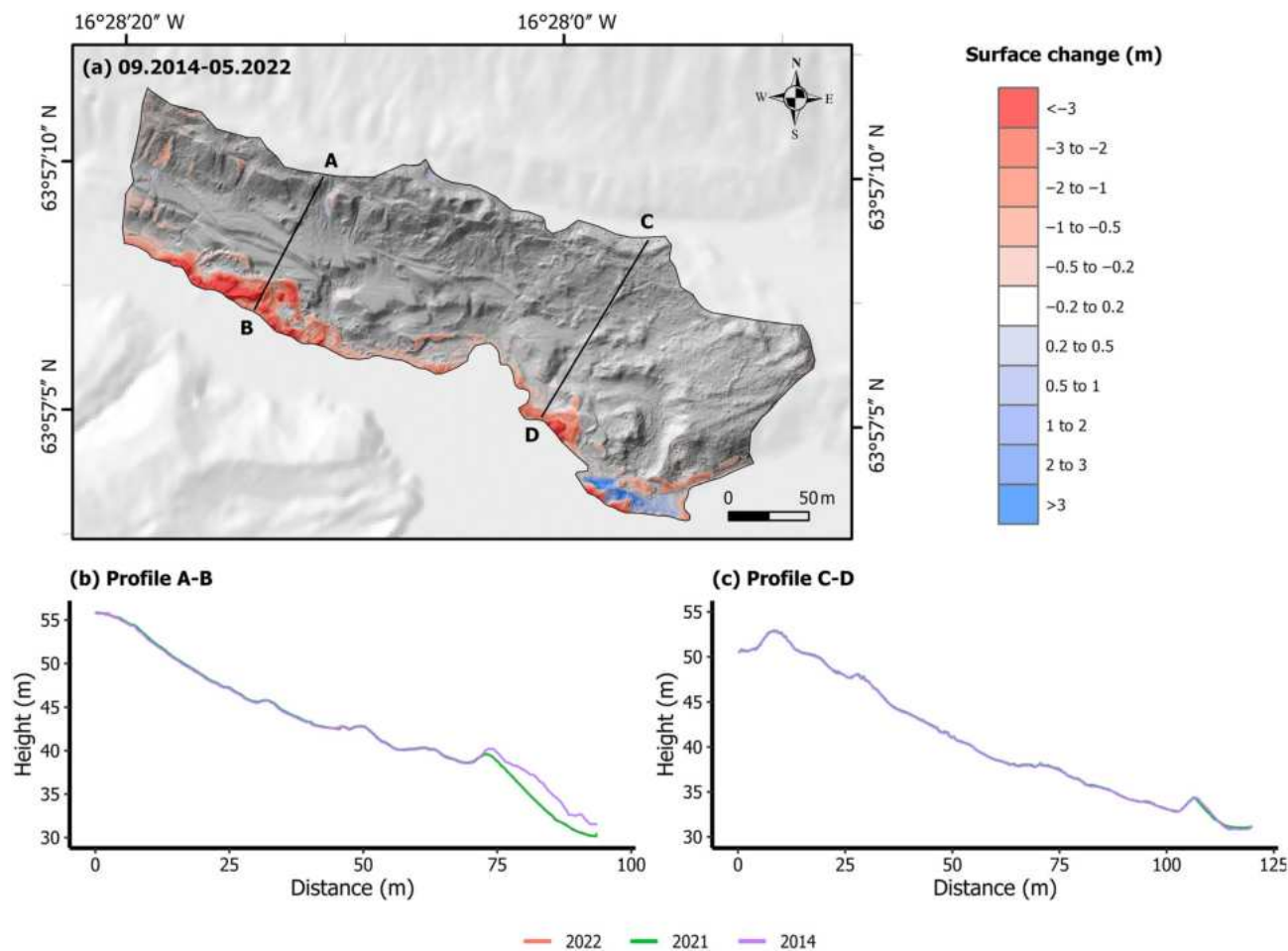


**FIGURE 6** Elevation changes for the kame terrace staircase (case study area 1—see Figure 2 for location) between 2014 and 2022. The minLoD was set at 0.20 m. Source of background: ÍslandsDEM v1.0. [Colour figure can be viewed at [wileyonlinelibrary.com](https://onlinelibrary.wiley.com/doi/10.1002/ldr.4865)]

outwash plain, a large, shallow collapse pit records the sinking of the outwash surface by up to 0.5 m. Other minor recorded changes include deposition in the north-eastern corner of the outwash plain where alluvial fans, debris flow-fed fans and boulders have accumulated as a result of paraglacial reworking of the steep slope of the Kumsmyrkambur lateral moraine.

### 3.3.3 | Case study area 3 (ice-cored hummocky moraine complex)

Case study area 3 is the area that underwent the most changes and maximum activity. Comparing 2014 with 2022 (Figure 8d), changes occurred in 87% of the case study area, reducing its volume by  $-365,773 \pm 11,462 \text{ m}^3$  (Table 2). Maximum elevation changes during this 8-year period reached  $>20 \text{ m}$  (Figure 8f). Importantly, the ice-cored moraine complex also shows significant changes in surface morphology within 1 year (Figure 8c—DoD 2021–2022), where the maximum recorded decrease in elevation was 8 m. The average net thickness of difference for DoD 2014–2022 was  $-6.30 \pm 0.20 \text{ m}$ , which demonstrates the dynamism of the degrading ice-cored complex, suggesting that further degradation should be expected. This

high level of transformation was related to the melting and degradation of ice cores. The surface collapsed in several places, while indicators of downwasting, such as tension cracks and holes, are widespread. There is a fairly visible trend in the spatial distribution of highly active parts of the ice-cored moraine complex, with the highest rates of terrain collapse along the SW–NE axis, where a line of irregular, water-filled depressions was formed after 2016 (Figure 9). Another type of transformation was recorded along the lake shore, where the water edge enhanced debris sliding along the exposed ice cliffs, thereby facilitating ice melting. The inner part of the moraine complex was less dynamic, the transformations manifesting themselves through tension cracks and uneven lowering of different parts of the moraine.

### 3.3.4 | Case study area 4 (ice-cored hummocky terrain with discontinuous sinuous ridges)

The ice-cored hummocky terrain with discontinuous sinuous ridges also turned out to be active (Figure 10) as 61% of its area changed (Figure 10c—DoD 2016–2022) and its volume decreased by  $64,632 \pm 8668 \text{ m}^3$  (Table 2) over the course of 6 years. The average net

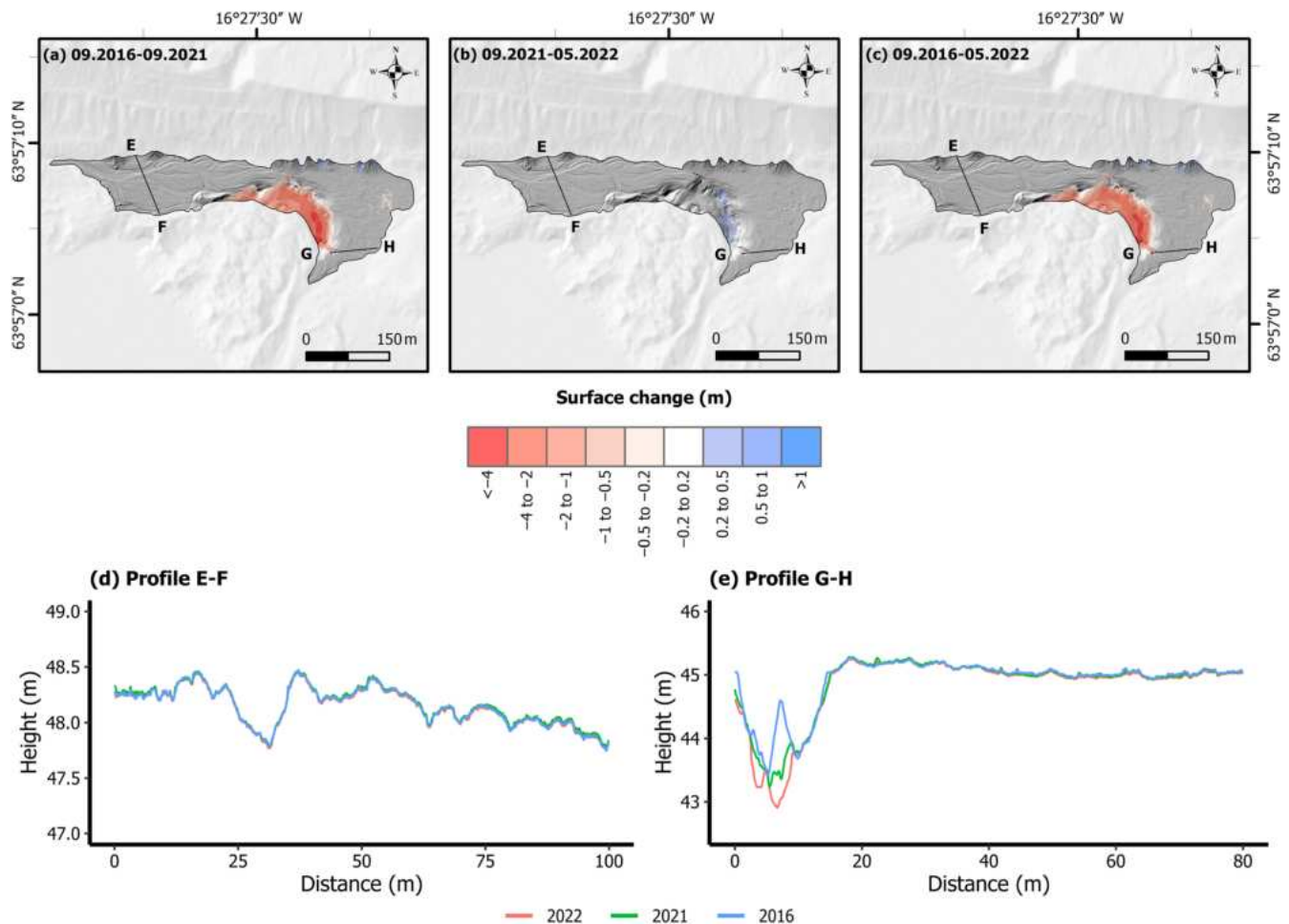


**FIGURE 7** Elevation changes between 2016 and 2022 for the outwash plain (case study area 2—see Figure 2 for location). The minLoD was set at 0.20 m. Source of background: ÍslandsDEM v1.0. [Colour figure can be viewed at [wileyonlinelibrary.com](https://onlinelibrary.wiley.com/doi/10.1002/ldr.4885)]

thickness of difference for the same DoD was  $-1.48 \pm 0.20$  m, but the highest decrease in elevation was  $>9$  m. In the southern part of the area, minor surface accumulation was recorded, but no indicators of deposition were found during the field verification and so we treated this as an artefact due to an erroneous surface reconstruction for 2016. In the calculations for 2021–2022 (Figure 10b), a change in volume of  $-1852 \pm 1166$  m<sup>3</sup> was noted. Reflecting this, the M–N and O–P cross profiles (Figure 10d,e) in the central, most active part of the moraine clearly show that the changes in morphology are concentrated near the lake and along the central axis of the ridge, whereas the rest of the area is more stable.

## 4 | DISCUSSION

### 4.1 | Spatial and temporal distribution of surface changes

During the observation period (2014–2022), the study areas underwent various scales of change (Figures 6–10). Very little activity took

place in case study areas 1 and 2, the kame terraces and outwash plain, where  $\sim 85\%$  of the total surface had not changed in the period 2014–2022. In contrast, case study areas 3 and 4 underwent more dynamic activity, especially the ice-cored moraine of case study area 3, where only 13% of the surface remained stable over the same period (Table 2). Such a diverse response is directly related to the presence of dead ice and its melting. The average annual rate of change for 2021–2022 in all case study areas was lower than in other periods, likely because the survey period comprised mostly the winter season (September 2021–May 2022), before the beginning of the summer ablation peak.

### 4.2 | Processes responsible for surface changes

The degradation of buried dead ice blocks and associated mass movements, including ground surface collapse and widespread debris flows, were the most critical processes responsible for transformation of the ice-cored moraine complexes of study areas 3 and 4 over the period 2014–2022. This was evidenced by the

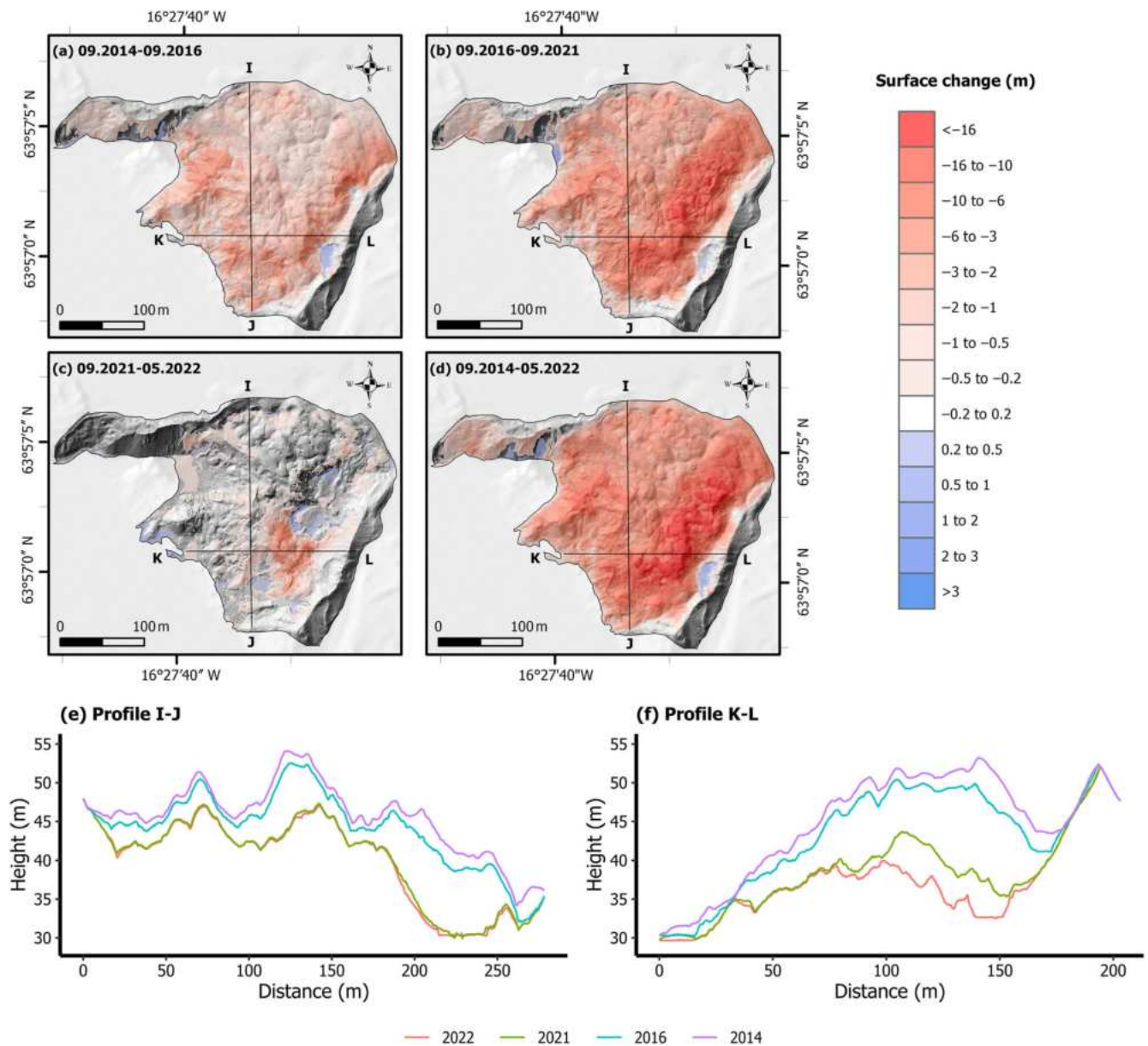


**FIGURE 8** Elevation changes between 2014 and 2022 for the ice-cored hummocky moraine complex (case study 3—see Figure 2 for location). The minLoD was set at 0.20 m. Source of background: ÍslandsDEM v1.0. [Colour figure can be viewed at [wileyonlinelibrary.com](https://onlinelibrary.wiley.com/doi/10.1002/ldr.4865)] [wileyonlinelibrary.com](https://onlinelibrary.wiley.com/doi/10.1002/ldr.4865)]

appearance and changing shape of numerous sinkholes and tension fractures on the moraine surfaces. Another process that impacted significantly on volume change was fluctuations in water levels and concomitant shore erosion around the margins of the proglacial/supraglacial lake and the ponds that developed in enlarging sink holes/kettles. Although surface collapse due to ice melt-out dominated as a process over the surveyed areas, some minor impacts and surface elevation increases were due to paraglacial activity in the historically developed and largely unstable lateral moraine topography, including the development of small debris flows, rockfalls, small rock avalanches and alluvial fans, which added debris to the tops of kame terraces and outwash margins.

### 4.3 | Comparison with short-term rates of surface change at other locations

To compare the land surface dynamics between case studies of varying areal extent, we standardized the volumetric measurements by dividing them according to area and period of observation, thereby ensuring that the average change in annual volume was calculated (Figure 11). The results confirm the low volumetric change of case study area 1 (average elevation changes of  $-0.13 \text{ m a}^{-1}$ ), the intermediate volumetric change of case study areas 2 and 4 ( $-0.29$  and  $-0.26 \text{ m a}^{-1}$ , respectively, for the period 2016–2022) and the high-volume loss of case study area 3 ( $-0.82 \text{ m a}^{-1}$  for the period 2014–2022). Additionally, Table 3 shows the maximum annual

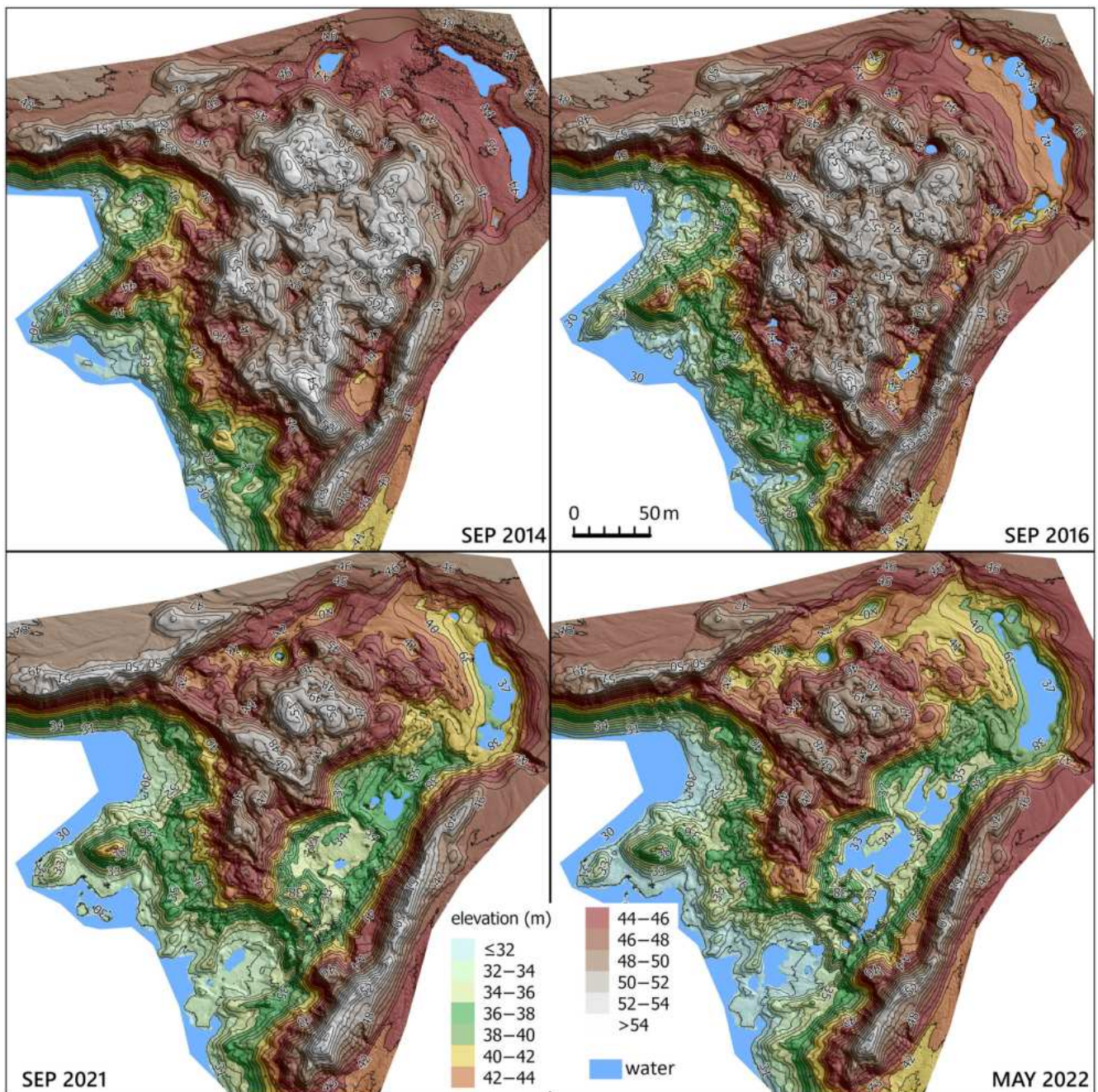


**FIGURE 9** Evolution of ice-cored moraine complex at Kviárjökull between 2014 and 2022—see Figure 2 for location. [Colour figure can be viewed at [wileyonlinelibrary.com](https://onlinelibrary.wiley.com/doi/10.1002/ldr.4885)]

thickness difference for each DoD calculation, ranging from  $-2$  to  $-3 \text{ m a}^{-1}$  for case study areas 1, 2 and 4 up to  $-12.21 \text{ m a}^{-1}$  and for case study area 3 for 2021–2022.

This range of values for volumetric change due to de-icing on the contemporary foreland of a rapidly receding glacier can be compared with those in other settings (Table 4). For example, on the forelands of Ebbabreen and Ragnarbreen, Svalbard, the average annual changes in thickness (i.e., sum of elevation changes divided by the area and period of observation) for an ice-cored moraine complex from 2012 to 2014 ranged from  $-0.14$  to  $-1.83 \text{ m a}^{-1}$  and the average annual

maximum thickness change (i.e., maximal values of elevation changes divided by the period of observations) ranged from  $-1.0$  to  $-7.9 \text{ m a}^{-1}$  (Ewertowski & Tomczyk, 2015). For the ice-cored moraine in the foreland of Midtre Lovénbreen, Svalbard, an average annual thickness change of  $-0.65 \text{ m a}^{-1}$  was measured over the period 2003–2005 (Irvine-Fynn et al., 2011). For the same glacier, but a longer period (2003–2014), Midgley et al. (2018) reported changes ranged from  $-0.02 \text{ m a}^{-1}$  for outwash plain (without buried ice) to  $-0.40 \text{ m a}^{-1}$  for ice-cored medial moraine. In contrast, the ice-cored moraine on the neighbouring foreland of Austre Lovénbreen, Svalbard, displayed

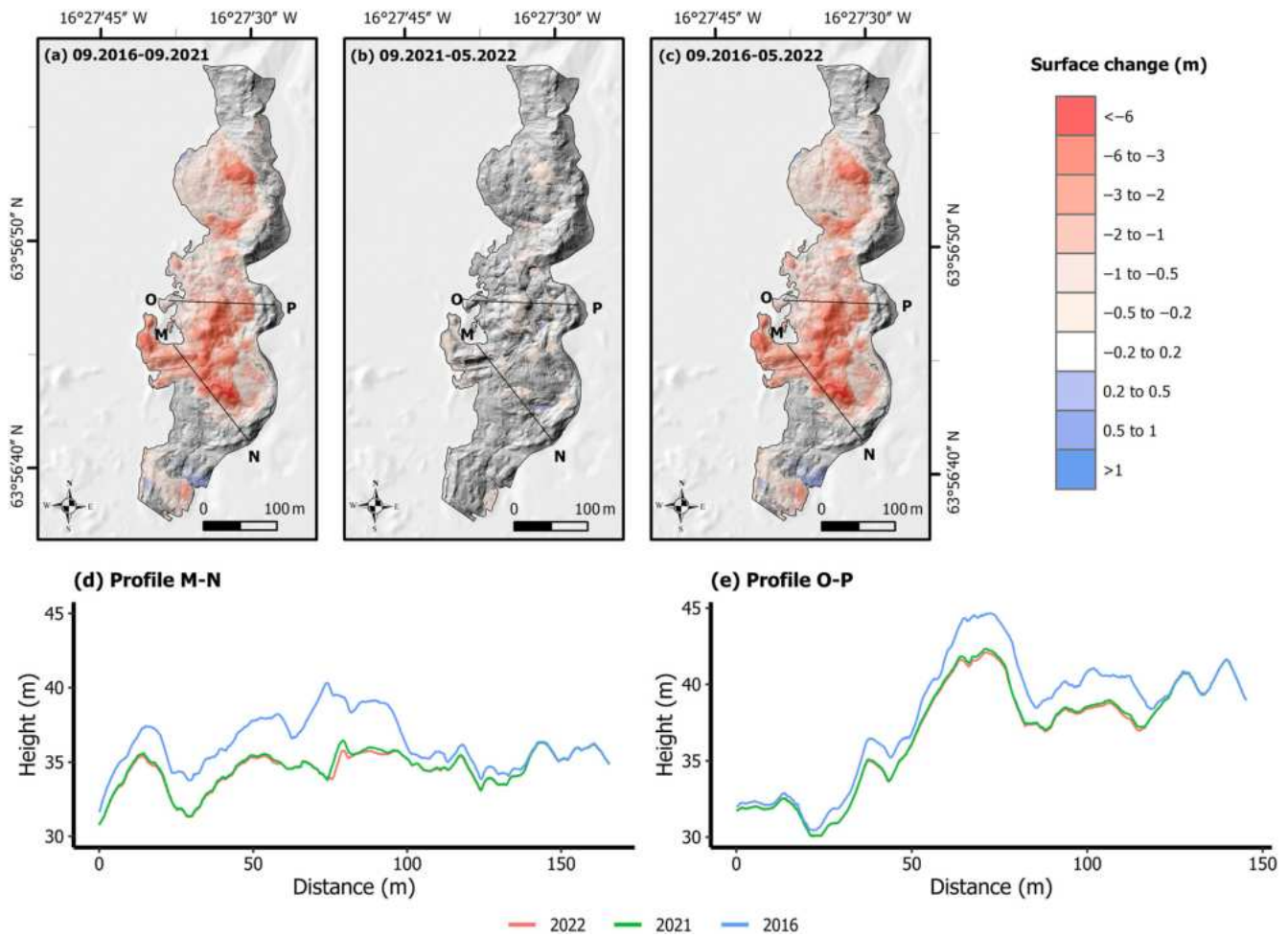


**FIGURE 10** Elevation changes for the thrust ice-cored moraine arc (case study 4—see Figure 2 for location) for the years 2016–2022. The minLoD was set at 0.20 m. Source of background: ÍslandsDEM v1.0. [Colour figure can be viewed at [wileyonlinelibrary.com](https://onlinelibrary.wiley.com/doi/10.1002/ldr.4865)] See the Terms and Conditions (<https://onlinelibrary.wiley.com/terms-and-conditions>) on Wiley Online Library for rules of use; OA articles are governed by the applicable Creative Commons License

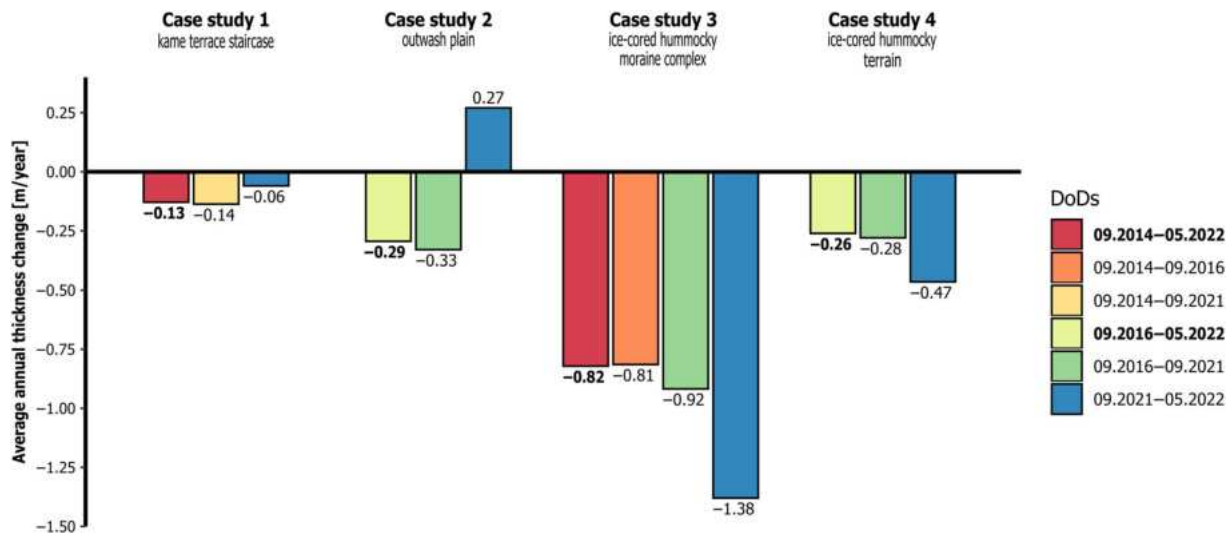


**FIGURE 11** Average annual thickness change for different case study areas on the Kviárjökull foreland. Changes calculated from the summary DoDs (i.e., differences between first and last surveys) for each case study area are indicated by bold fonts. [Colour figure can be viewed at [wileyonlinelibrary.com](https://onlinelibrary.wiley.com/doi/10.1002/ldr.4865)] See the Terms and Conditions (<https://onlinelibrary.wiley.com/terms-and-conditions>) on Wiley Online Library for rules of use; OA articles are governed by the applicable Creative Commons License

**TABLE 3** Average annual maximum thickness change for each case study area.

| DoD                           | Average annual maximum thickness change (m) |
|-------------------------------|---|
| Case study area 1             |   |
| September 2014–September 2021 | −1.53                                       |
| September 2021–May 2022       | −2.70                                       |
| September 2014–May 2022       | −1.43                                       |
| Case study area 2             |   |
| September 2016–September 2021 | −1.26                                       |
| September 2021–May 2022       | −2.06                                       |
| September 2016–May 2022       | −1.02                                       |
| Case study area 3             |   |
| September 2014–September 2016 | −4.83                                       |
| September 2016–September 2021 | −3.81                                       |
| September 2021–May 2022       | −12.21                                      |
| September 2014–May 2022       | −2.96                                       |
| Case study area 4             |   |
| September 2016–September 2021 | −1.76                                       |
| September 2021–May 2022       | −2.69                                       |
| September 2016–May 2022       | −1.60                                       |

Note: Due to fact that the DoDs for September 2021–May 2022 are for a shorter period than 1 year, we calculate the mean with an accuracy of 1 month.

an average elevation change of only  $-1.42$  m in the 11-year period 2003–2014 ( $\sim 0.13$  m  $a^{-1}$ ), with the maximum change exceeding  $-4$  m (Tonkin et al., 2016). Much greater change has been observed on the foreland of Fjallsjökull, Iceland, where calculations have been made on an annual basis between 2016 and 2019; from 2016 to 2017 in particular, the highest rate of average maximum elevation change of  $-0.5$  m per month ( $6$  m  $a^{-1}$ ) was recorded (Chandler, Evans, et al., 2020). Other land elements in the foreland of Fjallsjökull and Hrutárjökull (Iceland) were characterized by average annual elevation changes between  $-0.08$  and  $-1.33$  m  $a^{-1}$  (Table 4) (Evans et al., 2023).

#### 4.4 | Short-term versus long-term changes in proglacial areas

Bennett and Evans (2012) assessed the dynamics of the Kvíárjökull foreland on a decadal temporal scale based on DEMs generated from aerial images taken in the period 1945–2003, generating four DoDs for the periods: 1945–1964, 1964–1980, 1980–1998 and 1998–2003. They identified the fact that elevation changes in the ice-cored moraine complex did not proceed at the same rate. Changes in the average annual thickness decreased during the first three periods ( $-0.8$  m  $a^{-1}$  in 1945–1964,  $-0.3$  m  $a^{-1}$  in 1964–1980 and  $0.015$  m  $a^{-1}$  in 1980–1998) and then started to slightly increase in the fourth period ( $0.044$  m  $a^{-1}$  in 1998–2003). Positive values in the period

1980–1998 were a result of snout readvance into ice-cored terrain as a response to the 1990s readvance event in southern Iceland (sensu Evans & Hiemstra, 2005; Sigurðsson, 2005; Bradwell et al., 2006; Sigurðsson et al., 2007; Evans & Chandler, 2018). The results of our more recent, short-term calculations reveal that the trend of increasing rates of change for the period 1998–2003 have been sustained, with all the case study areas exceeding the average change in annual thickness of  $0.044$  m  $a^{-1}$  recorded by Bennett and Evans (2012) for the period 1998–2003 (Figure 11). These results are similar to those from other long-term analyses. For example, on the foreland of Ragnarbreen, Svalbard, the average annual change in elevation in the period 1961–2009 was  $-0.033$  m  $a^{-1}$  (Ewertowski, 2014). Additionally, on the Hørbyebreen foreland, Svalbard, ground surface elevation changed annually on average by  $-0.15$  m  $a^{-1}$  throughout the period 1960–2009, with an average maximum volume change of  $-1.3$  m  $a^{-1}$  (Ewertowski et al., 2019). On the foreland of Brúarjökull, Iceland, there was an average ground surface change from  $-0.10$  to  $-0.18$  m  $a^{-1}$  over the period 1945–2005 (Schomacker & Kjaer, 2007) and on the Kötlujökull foreland, Iceland, ice-cored moraine surfaces dropped on average annually from  $-0.3$  to  $-1.4$  m  $a^{-1}$  in 1995–1998 (Krüger & Kjær, 2000). A similarly high level of activity has been reported for the ice-cored moraine on the foreland of Holmströmbreen, Svalbard, by Schomacker and Kjaer (2008), with a mean annual surface change of  $-0.9$  m  $a^{-1}$  for the period 1984–2004 (similar to our case study area 3 at  $-0.82$  m  $a^{-1}$  for the period 2014–2022).

#### 4.5 | Degradation of an ice-cored moraine complex—implications for the interpretation of Pleistocene landforms and sediments

The four case study areas analysed here constitute land elements within the debris-charged, active temperate glacial landsystem at Kvíárjökull (Bennett et al., 2010), the evolution of which are presented in Figures 1c and 12. This provides an overview of landsystem development over the longer timescale of 1945–2014 (Figure 12), during which the kame terrace staircase (area 1), the outwash plain (area 2), the ice-cored hummocky moraine complex (area 3) and the ice-cored hummocky terrain with discontinuous sinuous ridges (area 4) have emerged and evolved on the northern half of the glacier foreland. In the wider context of the foreland, these land elements constitute the landform–sediment assemblages of an outwash head that has developed over the adverse slope of an overdeepening (Bennett & Evans, 2012; Spedding & Evans, 2002). This is a landsystem signature that is becoming more widely recognized on the rapidly evolving forelands of the southern Iceland temperate outlet glaciers, where high ice mass turnover and concomitant high meltwater discharges have given rise to substantial accumulations of glacial sediments widely deposited over downwasting but active snouts (Bennett & Evans, 2012; Chandler, Evans, et al., 2020; Evans et al., 2018, 2019, 2023; Evans & Orton, 2015). Long-term meltwater drainage towards the outwash head can be reconstructed based on the repeat aerial imagery since 1945 and this has facilitated a much improved

**TABLE 4** Comparison of glacial landform degradation rates in different sites in Iceland and Svalbard.

| Location                            | Landform                                     | Observation period                         | Annual average elevation change (m a <sup>-1</sup> ) | Average maximum elevation change (m a <sup>-1</sup> ) | Source                         |                     |
|-------------------------------------|--|--|--|---|--------------------------------|---------------------|
| Short-term surveys (days to annual) |  |  |  |   |                                |                     |
| Midtre Lovénbreen, Svalbard         | Ice-cored moraine                            | 2003–2005                                  | –0.65  | N/A   | Irvine-Fynn et al. (2011)      |                     |
| Ragnarbreen, Svalbard               | Ice-cored moraine                            | 2012–2014                                  | –0.14  | –1.0  | Ewertowski and Tomczyk (2015)  |                     |
| Ebbabreen, Svalbard                 | Ice-cored moraine                            | 2012–2014                                  | –1.83  | –7.9  | Ewertowski and Tomczyk (2015)  |                     |
| Fjallsjökull, Iceland               | Ice-cored moraine                            | 2016–2019                                  | N/A  | –6.0  | Chandler, Evans, et al. (2020) |                     |
| Fjallsjökull, Iceland               | South overdeepening, including               | (a) Large esker network                    | 2014–2022  | –0.15   | –1.94                          | Evans et al. (2023) |
|                                     |  | (b) Inner overdeepening (hummocky terrain) | 2014–2022  | –0.08   | –1.19                          |                     |
|                                     |  | (c) Adverse slope                          | 2014–2022  | –0.63   | –1.94                          |                     |
|                                     |  | (d) Outer overdeepening                    | 2014–2022  | –0.25   | –1.13                          |                     |
| Hrútarjökull, Iceland               | 1990s thrust moraine                         | 2014–2022                                  | –0.96  | –1.94   | Evans et al. (2023)            |                     |
| Hrútarjökull, Iceland               | Overdeepening                                | 2014–2022                                  | –0.79  | –3.69   | Evans et al. (2023)            |                     |
| Hrútarjökull, Iceland               | Hummocky terrain/medial moraine              | 2014–2022                                  | –0.51  | N/A   | Evans et al. (2023)            |                     |
| Hrútarjökull, Iceland               | Collapsed sandur                             | 2014–2022                                  | –0.46  | –1.87   | Evans et al. (2023)            |                     |
| Hrútarjökull, Iceland               | Debris-covered snout                         | 2019–2022                                  | –1.33  | –8.5  | Evans et al. (2023)            |                     |
| Kvíárjökull, Iceland                | Kame terrace staircase                       | 2014–2022                                  | –0.13  | –1.43   | This study                     |                     |
| Kvíárjökull, Iceland                | Outwash plain                                | 2016–2022                                  | –0.29  | –1.02   | This study                     |                     |
| Kvíárjökull, Iceland                | Ice-cored hummocky moraine complex           | 2014–2022                                  | –0.82  | –2.96   | This study                     |                     |
| Kvíárjökull, Iceland                | Ice-cored hummocky terrain                   | 2016–2022                                  | –0.26  | –1.60   | This study                     |                     |
| Long-term surveys (decadal)         |  |  |  |   |                                |                     |
| Austre Lovénbreen, Svalbard         | Ice-cored moraine                            | 2003–2014                                  | –0.13  | –0.36   | Tonkin et al. (2016)           |                     |
| Midtre Lovénbreen, Svalbard         | Frontal moraine (limited buried ice content) | 2003–2014                                  | –0.09  | N/A   | Midgley et al. (2018)          |                     |
| Midtre Lovénbreen, Svalbard         | Lateral moraine (ice-proximal slope)         | 2003–2014                                  | –0.06  | N/A   | Midgley et al. (2018)          |                     |
| Midtre Lovénbreen, Svalbard         | Medial moraine (ice-cored)                   | 2003–2014                                  | –0.40  | N/A   | Midgley et al. (2018)          |                     |
| Midtre Lovénbreen, Svalbard         | Outwash plain                                | 2003–2014                                  | –0.02  | N/A   | Midgley et al. (2018)          |                     |
| Midtre Lovénbreen, Svalbard         | Hummocky moraine                             | 2003–2014                                  | –0.03  | N/A   | Midgley et al. (2018)          |                     |
| Holmströmbreen, Svalbard            | Ice-cored moraine                            | 1984–2004                                  | –0.9   | N/A   | Schomacker and Kjaer (2008)    |                     |
| Ragnarbreen, Svalbard               | Ice-cored moraine                            | 1961–2009                                  | –0.033   | –0.24   | Ewertowski (2014)              |                     |
| Hørbyebreen, Svalbard               | Ice-cored moraine                            | 1960–2009                                  | –0.15  | –1.30   | Ewertowski et al. (2019)       |                     |
| Brúarjökull, Iceland                | Ice-cored moraine                            | 1945–2005                                  | –0.10 to –0.18                                       | N/A   | Schomacker and Kjaer (2007)    |                     |
| Kötlujökull, Iceland                | Ice-cored moraine                            | 1995–1998                                  | –0.3 to –1.4   | N/A   | Krüger and Kjaer (2000)        |                     |
| Kvíárjökull, Iceland                | Ice-cored moraine complex                    | 1945–1964                                  | –0.8   | N/A   | Bennett and Evans (2012)       |                     |
|                                     |  | 1964–1980                                  | –0.3   | N/A   |                                |                     |
|                                     |  | 1980–1998                                  | –0.015   | N/A   |                                |                     |
|                                     |  | 1998–2003                                  | –0.044   | N/A   |                                |                     |



understanding of englacial drainage pathways through snouts overlying overdeepenings (Figure 12).

Meltwater drainage towards the apex of the outwash head was clearly fed by a portal in the centre of the glacier snout but it was not obvious until the capture of 1964 imagery where the lake water centred over study area 2 in 1945 was draining away. This becomes apparent in the emergence of englacial eskers in the debris covered snout on the 1964 and 1980 imagery (Figure 12). An esker origin for these ridges is verified by their field characteristics of well-sorted stratified gravels and sands (Bennett & Evans, 2012; Spedding & Evans, 2002). After lake drainage, meltwater streams flowing over the kame terraces (area 1) to form the outwash plain (area 2) disappeared under the snout margin, emerging again on the northern part of the outwash head apex in 1964 (Figure 12). By 1980, this meltwater pathway through the snout becomes more obvious where an N-S trending stream draining through ice-cored terrain is clearly feeding the active apex of the outwash head at the centre of the snout. The emergence of englacial eskers is manifested in the imagery of the ice-cored moraine complex (area 3) by the appearance of sinuous ridges. These ridges document drainage through the ice in a NW-SE direction prior to 1980, constituting 'engorged eskers' (sensu Mannerfelt, 1945, 1949; Evans et al., 2018). However, later imagery from 2012 shows W-E-orientated ridges, likely documenting the drainage through the glacitectonic thrust mass constructed in the 1990s, towards the meltwater stream that was established around the front of the thrust mass at that time and visible on the 1998 imagery (Figure 12). By 2022, our UAV imagery reveals the emergence of a further set of englacial eskers in the lower part of the collapsing ice-cored moraine complex and aligned ENE-WSW (Figure 13). Drainage towards the higher topography in the ENE seems unlikely, especially as these eskers would have accumulated in tunnels cut through lower elevation ice after thrust mass construction. Consequently, we envisage their production by meltwater drainage away from the extensive collapsed terrain that has developed beneath the eastern end of the outwash plain and towards the contemporary proglacial lake. If correct, this interpretation highlights the development of 'engorged eskers', but of a type that is driven by a groundwater hydrology scenario in which water pressures are not glacier induced. Moreover, drainage directions are the reverse of those that would be reconstructed based solely on landform evidence in a fully deglaciated landscape. Additionally, eskers have developed at different levels within a downwasting glacier mass as a result of two entirely different 'engorged' drainage scenarios.

In addition to the unusually complex esker development, the ice-cored moraine complex (case study area 3) is an excellent example of a terrain produced by incremental stagnation of a debris-covered snout that was subsequently glacitectonically pushed by glacier readvance during the 1990s (Figures 1b, 12 and 13; Bennett and Evans (2012)). Arcuate ridges were constructed at the eastern end of the moraine complex, comprising compressed and thrust stacked ice-cored ridges and eskers, which were gradually emerging through the debris-covered snout prior to the readvance. This is an ice-cored version of a composite glacitectonic thrust moraine (sensu Aber

et al., 1989). The inclusion of buried glacier ice in the thrust mass has significant implications for glacial geomorphology in that de-icing will result in the gradual destruction of linearity and a final landform that resembles hummocky terrain rather than a recognizable glacitectonic thrust mass. In 2014 and 2016 imagery, the arcuate ridges diagnostic of thrust mass construction was still visible despite the significant mass lost through de-icing (Figure 13). Since 2014, however, downwasting due to de-icing has gradually fragmented the linearity and this has been replaced by increasing amounts of chaotic hummocky and pitted terrain as well as the ESE-WNW engorged eskers.

The historical development of the ice-cored hummocky terrain with discontinuous sinuous ridges (area 4) not only serves as an excellent genetic model for outwash heads but also provides insight into the operation of glacial meltwater pathways over overdeepenings. Like study area 3, this area appeared as ice-cored, pitted terrain at the elongate apex of the main proglacial outwash fan in 1980, but was glacitectonically compressed to form an ice-cored composite thrust mass fronted by push ridges in glaci-fluvial deposits during the 1990s readvance (Figures 1c and 12). As it then downwasted into hummocky terrain, it was also incised and reworked in several places by glacial meltwater streams existing from portals on the glacier snout. Associated with the portal positions have been sinuous ridges composed of well-sorted and stratified gravels and sands emerging from the downwasting ice-cored terrain over time. These ridges are interpreted as englacial eskers due to their continuation onto the glacier surface and their clear emergence from englacial positions (Bennett et al., 2010; Bennett & Evans, 2012; Spedding & Evans, 2002). The association of the eskers with an ice-cored proglacial outwash fan clearly demonstrates that the majority of the meltwater draining through the glacier snout has bypassed the floor of the overdeepening, explaining the very restricted occurrence of supercooled ice (Larson et al., 2010; Roberts et al., 2002; Spedding & Evans, 2002; Swift et al., 2006).

#### 4.6 | Problems and limitations in using data collected with optical sensors on UAVs

While the use of UAVs in glacial geomorphology increased rapidly after 2015 (see Śledź et al., 2021), data processing results are not free of artefacts and can exhibit problems, which require careful investigations in order to avoid erroneous interpretation. The most common issues associated with SfM reconstruction are related to water surfaces, which are particularly important in rapidly changing glacier forelands prone to high levels of de-icing and concomitant pond and lake development, growth and decay. For example, SfM can reconstruct points located underwater in shallow, transparent ponds (Carrivick & Smith, 2019); however, the algorithm struggles in cases with high water turbidity or suspended sediments (see Tomczyk & Ewertowski, 2021). In our case studies, this was clearly the case in relation to the large proglacial/supraglacial lake, which was characterized by high suspended sediment concentrations combined with small wind-generated ripples, resulting in the erroneous reconstruction of the water surface. To avoid the impact of these errors on DoD

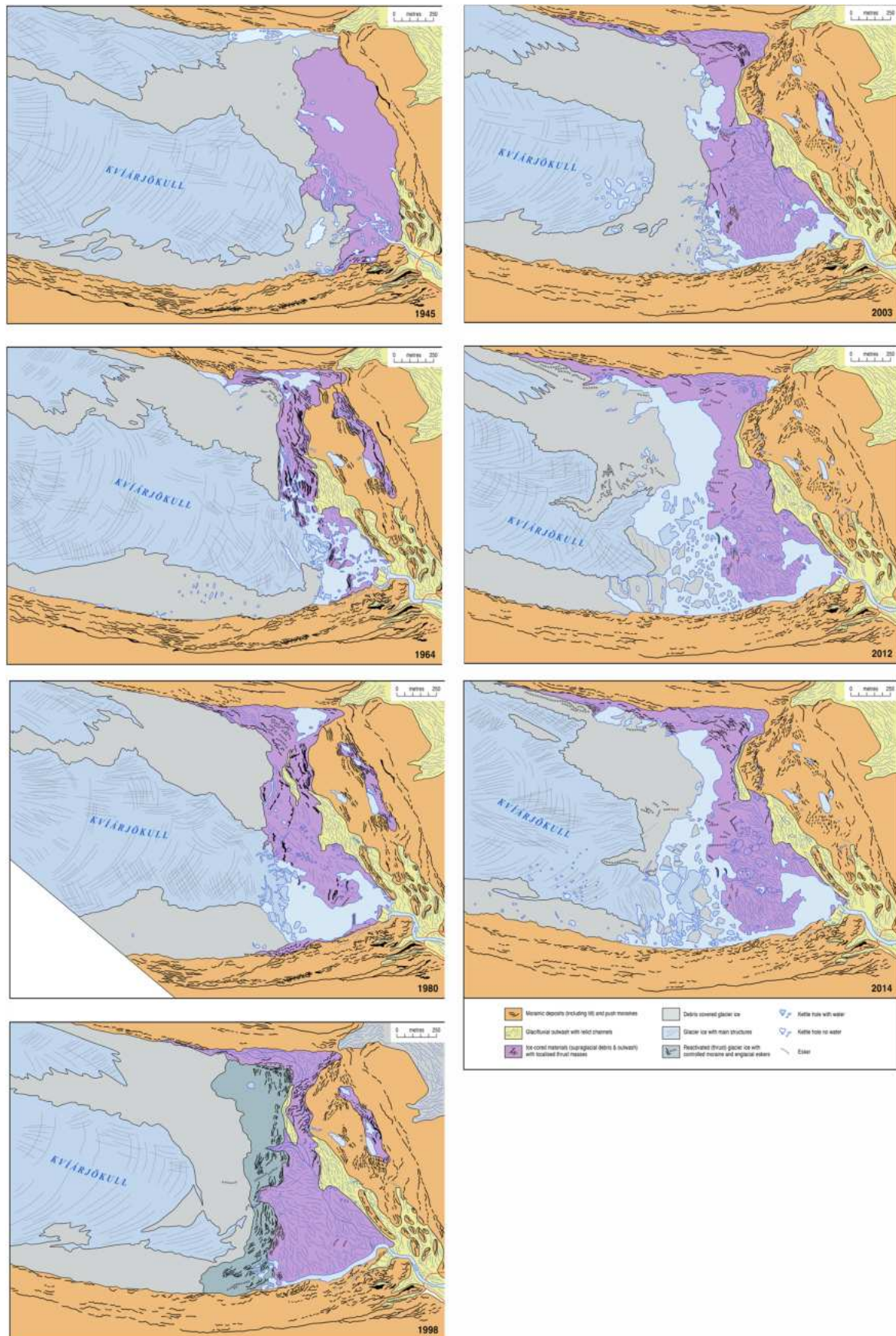
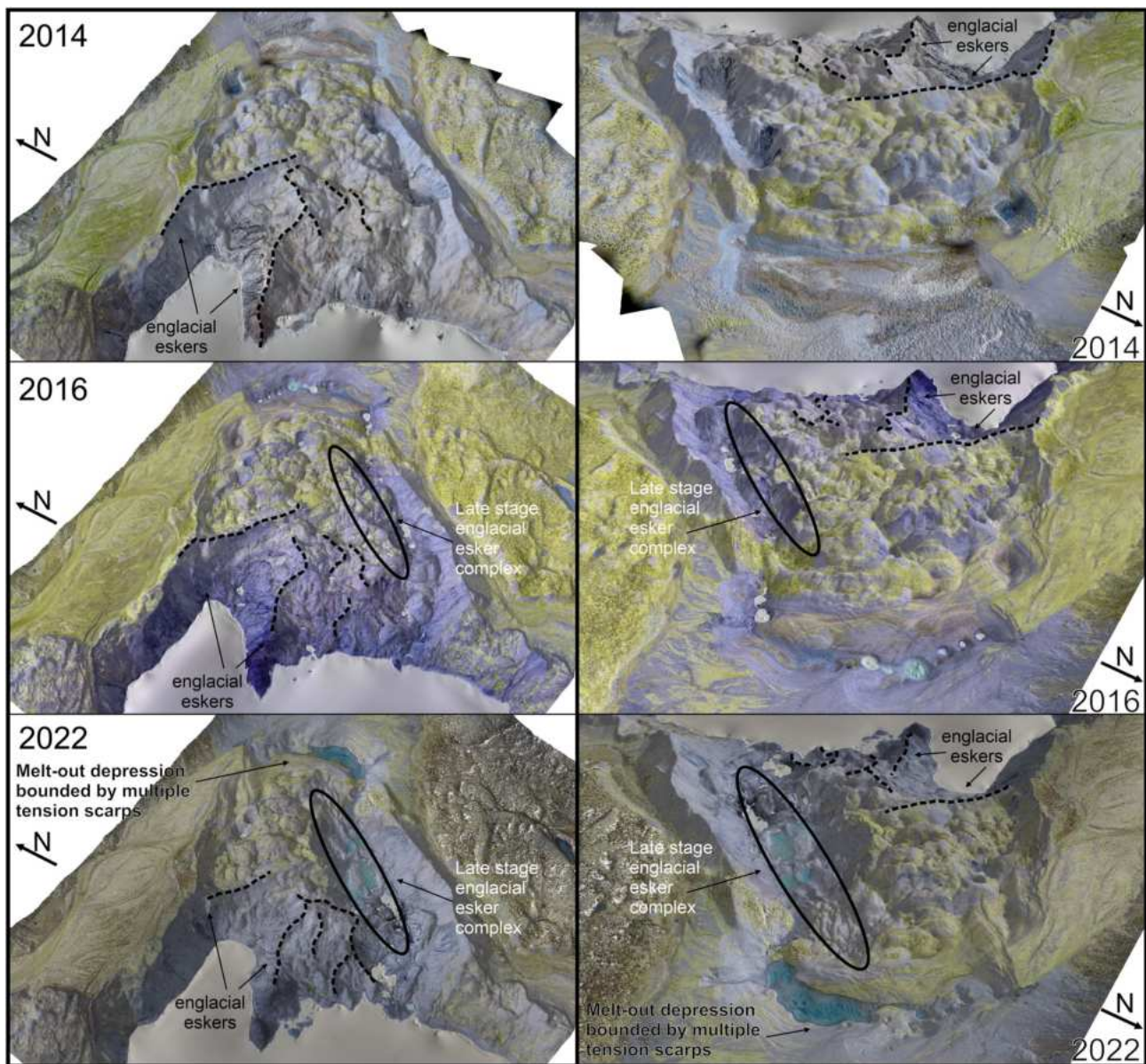


FIGURE 12 Legend on next page.



**FIGURE 13** 3D visualizations of the ice-cored moraine complex (see Figure 2 for location) between 2014 and 2022 illustrating different stages of degradation and the emergence of englacial eskers. [Colour figure can be viewed at [wileyonlinelibrary.com](https://onlinelibrary.wiley.com/doi/10.1111/1365-3113.12023)]

calculations, points characterized by high uncertainty (e.g., located only on two images) were removed from the dense point cloud and a smooth water surface was thereby created (Figure 14a). Moreover, borders of case studies were delineated to avoid the lake area (Figure 2). In the case of minor, transparent waterbodies, depending on the water depth, underwater terrain was reconstructed to some extent, but in some cases erroneous points were generated and this impacted on elevation and shading models (Figure 14b). In such cases,

the careful examination of not only DEMs but also orthomosaics is required.

Indeed, the investigation of different products of SfM (point clouds, DEMs and orthomosaics), in combination with field verification, is crucial for accurate interpretations of geomorphological process–form regimes. For example, in our case study area 2 (outwash plain), a 192 m<sup>3</sup> increase in the volume was recorded for the 2021–2022 period (Figures 7b and 11, Tables 2, 4 and 5) but the analysis of

**FIGURE 12** Palaeogeographic reconstructions of glacier change and landform development for the debris-charged, active temperate foreland at Kviárjökull based on aerial imagery (1945–2003) and high-resolution satellite imagery (2012–2014). [Colour figure can be viewed at [wileyonlinelibrary.com](https://onlinelibrary.wiley.com/doi/10.1111/1365-3113.12023)]

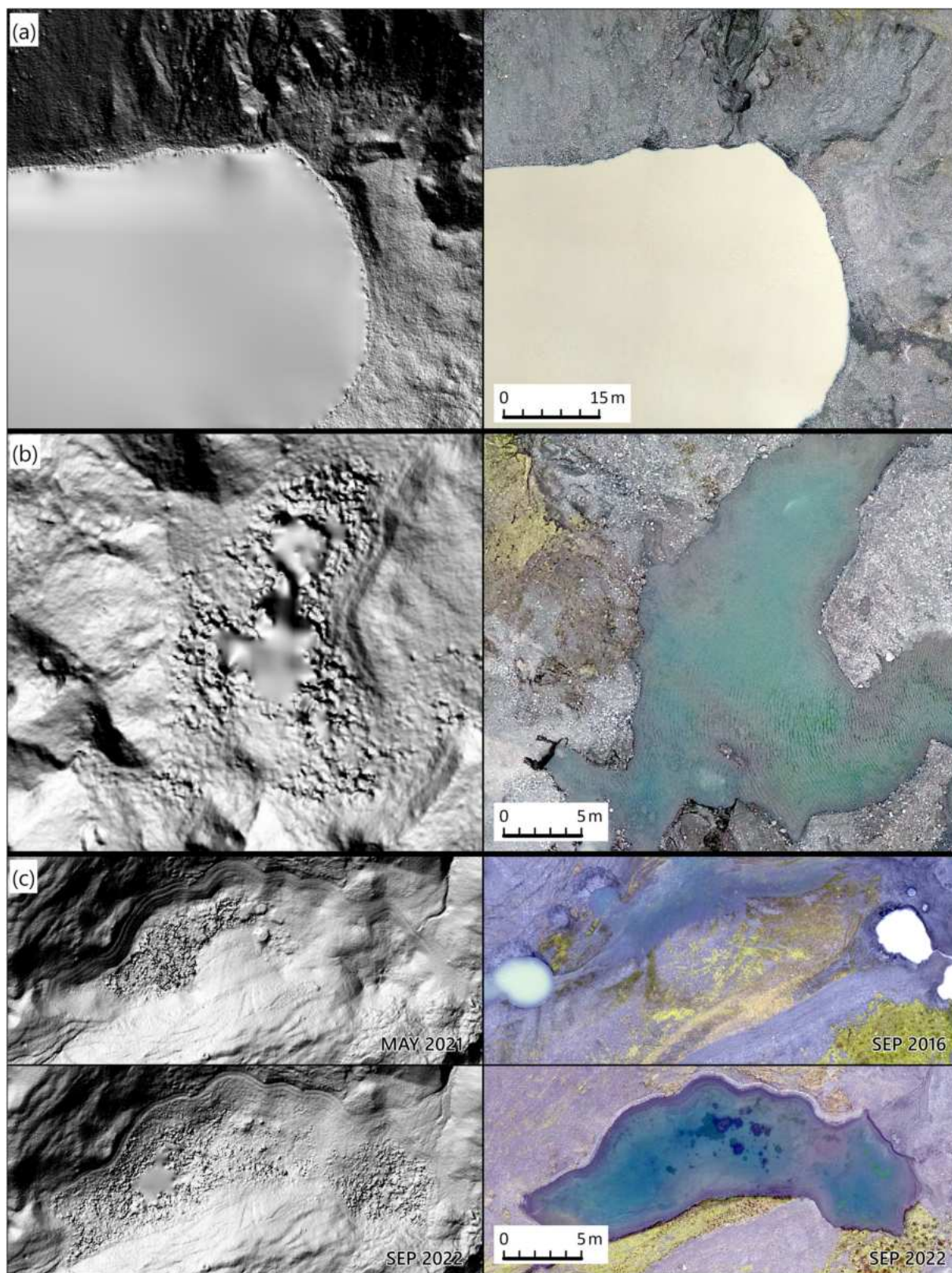


**FIGURE 14** Examples of problems with data processing encountered in the study area: (a) lake with a high concentration of suspended sediments which required filtration of the point cloud; (b) small transparent waterbodies, which generated erroneous surfaces and (c) depression filled with water, which was responsible for an increase in volume recorded by DoD. [Colour figure can be viewed at [wileyonlinelibrary.com](https://onlinelibrary.wiley.com/doi/10.1002/ldr.4865)]

**TABLE 5** Average annual volume change for each case study.

| DoD                             | Average annual volume change (m <sup>3</sup> ) |
|---------------------------------|--|
| Case study 1                    |  |
| September 2014–September 2021   | −932.92  |
| September 2021–May 2022         | −44.46   |
| Total (September 2014–May 2022) | −834.99  |
| Case study 2                    |  |
| September 2016–September 2021   | −3130.12                                       |
| September 2021–May 2022         | 289.14   |
| Total (September 2016–May 2022) | −2724.74                                       |
| Case study 3                    |  |
| September 2014–September 2016   | −45,091.83                                     |
| September 2016–September 2021   | −51,299.21                                     |
| September 2021–May 2022         | −25,811.33                                     |
| Total (September 2014–May 2022) | −47,709.52                                     |
| Case study 4                    |  |
| September 2016–September 2021   | −12,065.66                                     |
| September 2021–May 2022         | −2777.67                                       |
| Total (September 2016–May 2022) | −11,405.57                                     |

Note: DEMs of differences (DoDs) for 09.2021–05.2022 mainly cover winter period, so average values are much lower than in other periods.

orthomosaics indicated that the elevation increase was not related to landform change, but instead to the water that filled the depression over time (Figure 14c).

## 5 | CONCLUSIONS

This study investigated landform transformation in relation to the development of the debris-charged temperate glacial landsystem on the foreland of Kviárjökull, SE Iceland, for the period 1945–2022, with high-resolution quantification of surface change resulting from de-icing over the period 2014–2022. Observations were based on aerial photograph archives, high-resolution satellite imagery and a time series of UAV-gathered data. UAV images were processed using the SfM approach to generate DEMs, which were then used to develop the DoDs and perform the change detection. We selected four case study areas representative of specific landform elements, including a kame terrace staircase, an outwash plain, an ice-cored hummocky moraine complex and an ice-cored hummocky terrain with discontinuous sinuous ridges (englacial eskers). The recorded short-term dynamics of the landform changes at Kviárjökull are consistent with those reported at other rapidly deglaciating forelands in the northern polar region. The average annual change in volume as derived from land surface lowering ranged from  $-0.06 \text{ m a}^{-1}$  in a relatively stable area of kame terrace staircase to  $-0.82 \text{ m a}^{-1}$  for the ice-cored hummocky moraine complex. Compared with long-term research in this foreland since 1945, our results confirm the

ongoing degradation of ice-cored moraine and outwash complexes, visible and quantifiable by using land surface collapse, at variable rates related to buried ice volume and age of deglaciation. The gradual evolution of largely chaotic hummocky terrain from not only debris-covered glacier ice but also from glaciectonic thrust masses, outwash fans/heads and complex englacial esker networks is an important modern landsystem analogue for informing palaeoglaciological reconstructions in areas characterized by hummocky 'moraine' and/or kame and kettle topography.

## ACKNOWLEDGMENTS

This research was funded by the National Science Centre, Poland, grant number 2019/35/B/ST10/03928. Scientific research permits for the fieldwork were kindly provided by the Vatnajökull National Park and the Icelandic Research Council (RANNIS).

## CONFLICT OF INTEREST STATEMENT

The authors declare that they have no conflict of interest.

## DATA AVAILABILITY STATEMENT

The data that support the findings of this study are available from the corresponding author upon reasonable request.

## ORCID

Szymon Śledź  <https://orcid.org/0000-0002-4822-7568>

Marek W. Ewertowski  <https://orcid.org/0000-0002-0422-2327>

## REFERENCES

- Aber, J. S., Croot, D. G., & Fenton, M. M. (1989). *Glaciectonic landforms and structures*. Springer Science+Business Media.
- Allen, C. D., Macalady, A. K., Chenchouni, H., Bachelet, D., McDowell, N., Vennetier, M., Kitzberger, T., Rigling, A., Breshears, D. D., Hogg, E. H., Gonzalez, P., Fensham, R., Zhang, Z., Castro, J., Demidova, N., Lim, J.-H., Allard, G., Running, S. W., Semerci, A., & Cobb, N. (2010). A global overview of drought and heat-induced tree mortality reveals emerging climate change risks for forests. *Forest Ecology and Management*, 259(4), 660–684. <https://doi.org/10.1016/j.foreco.2009.09.001>
- Bash, E., Moorman, B., & Gunther, A. (2018). Detecting short-term surface melt on an Arctic glacier using UAV surveys. *Remote Sensing*, 10(10), 1547. <https://doi.org/10.3390/rs10101547>
- Bash, E. A., & Moorman, B. J. (2020). Surface melt and the importance of water flow – An analysis based on high-resolution unmanned aerial vehicle (UAV) data for an Arctic glacier. *The Cryosphere*, 14(2), 549–563. <https://doi.org/10.5194/tc-14-549-2020>
- Benn, D. I., Bolch, T., Hands, K., Gulley, J., Luckman, A., Nicholson, L. I., Quincey, D., Thompson, S., Toumi, R., & Wiseman, S. (2012). Response of debris-covered glaciers in the Mount Everest region to recent warming, and implications for outburst flood hazards. *Earth-Science Reviews*, 114(1–2), 156–174. <https://doi.org/10.1016/j.earscirev.2012.03.008>
- Benn, D. I., & Evans, D. J. A. (2010). *Glaciers and glaciation*. Hodder Education.
- Bennett, G. L., & Evans, D. J. A. (2012). Glacier retreat and landform production on an overdeepened glacier foreland: The debris-charged glacial landsystem at Kviárjökull, Iceland. *Earth Surface Processes and Landforms*, 37(15), 1584–1602. <https://doi.org/10.1002/esp.3259>
- Bennett, G. L., Evans, D. J. A., Carbonneau, P., & Twigg, D. R. (2010). Evolution of a debris-charged glacier landsystem, Kviárjökull, Iceland. *Journal of Maps*, 6(1), 40–67. <https://doi.org/10.4113/jom.2010.1114>

- Bernard, É., Friedt, J. M., Tolle, F., Marlin, C., & Griselin, M. (2016). Using a small COTS UAV to quantify moraine dynamics induced by climate shift in Arctic environments. *International Journal of Remote Sensing*, 38(8–10), 2480–2494. <https://doi.org/10.1080/01431161.2016.1249310>
- Blauvelt, D. J., Russell, A. J., Large, A. R. G., Tweed, F. S., Hiemstra, J. F., Kulesa, B., Evans, D. J. A., & Waller, R. I. (2020). Controls on jökulhlaup-transported buried ice melt-out at Skeiðarársandur, Iceland: Implications for the evolution of ice-marginal environments. *Geomorphology*, 360, 107164. <https://doi.org/10.1016/j.geomorph.2020.107164>
- Bradwell, T., Dugmore, A. J., & Sugden, D. E. (2006). The little ice age glacier maximum in Iceland and the North Atlantic oscillation: Evidence from Lambatungnajökull, Southeast Iceland. *Boreas*, 35(1), 61–80. <https://doi.org/10.1111/j.1502-3885.2006.tb01113.x>
- Brunsdon, D., & Thornes, J. B. (1979). Landscape sensitivity and change. *Transactions of the Institute of British Geographers NS*, 4, 485–515.
- Bühler, Y., Adams, M. S., Bösch, R., & Stoffel, A. (2016). Mapping snow depth in alpine terrain with unmanned aerial systems (UASs): Potential and limitations. *The Cryosphere*, 10(3), 1075–1088. <https://doi.org/10.5194/tc-10-1075-2016>
- Carrivick, J. L., Boston, C. M., King, O., James, W. H. M., Quincey, D. J., Smith, M. W., Grimes, M., & Evans, J. (2019). Accelerated volume loss in glacier ablation zones of NE Greenland, little ice age to present. *Geophysical Research Letters*, 46(3), 1476–1484. <https://doi.org/10.1029/2018GL081383>
- Carrivick, J. L., & Heckmann, T. (2017). Short-term geomorphological evolution of proglacial systems. *Geomorphology*, 287, 3–28. <https://doi.org/10.1016/j.geomorph.2017.01.037>
- Carrivick, J. L., & Smith, M. W. (2019). Fluvial and aquatic applications of structure from motion photogrammetry and unmanned aerial vehicle/drone technology. *WIREs Water*, 6(1), e1328. <https://doi.org/10.1002/wat2.1328>
- Carrivick, J. L., & Tweed, F. S. (2019). A review of glacier outburst floods in Iceland and Greenland with a megafloods perspective. *Earth-Science Reviews*, 196, 102876. <https://doi.org/10.1016/j.earscirev.2019.102876>
- Chandler, B. M. P., Chandler, S. J. P., Evans, D. J. A., Ewertowski, M. W., Lovell, H., Roberts, D. H., Schaefer, M., & Tomczyk, A. M. (2020). Sub-annual moraine formation at an active temperate Icelandic glacier. *Earth Surface Processes and Landforms*, 45(7), 1622–1643. <https://doi.org/10.1002/esp.4835>
- Chandler, B. M. P., Evans, D. J. A., Chandler, S. J. P., Ewertowski, M. W., Lovell, H., Roberts, D. H., Schaefer, M., & Tomczyk, A. M. (2020). The glacial landsystem of Fjallsjökull, Iceland: Spatial and temporal evolution of process-form regimes at an active temperate glacier. *Geomorphology*, 361, 107192. <https://doi.org/10.1016/j.geomorph.2020.107192>
- Cook, K. L., Andermann, C., Gimbert, F., Adhikari, B. R., & Hovius, N. (2018). Glacial lake outburst floods as drivers of fluvial erosion in the Himalaya. *Science*, 362(6410), 53–57. <https://doi.org/10.1126/science.aat4981>
- Cook, S. J., Kougkoulos, I., Edwards, L. A., Dortch, J., & Hoffmann, D. (2016). Glacier change and glacial lake outburst flood risk in the Bolivian Andes. *The Cryosphere*, 10(5), 2399–2413. <https://doi.org/10.5194/tc-10-2399-2016>
- Etzelmüller, B. (2000). Quantification of thermo-erosion in pro-glacial areas – examples from Svalbard. *Zeitschrift Fur Geomorphologie*, 44(3), 343–361.
- Evans, D. J. A. (Ed.). (2003). *Glacial Landsystems*. Arnold.
- Evans, D. J. A. (2013). The glacial and periglacial research – Geomorphology and retreating glaciers. In J. Schroder, R. Giardino, & J. Harbor (Eds.), *Glacial and periglacial geomorphology* (Vol. 8, pp. 460–478). Academic Press.
- Evans, D. J. A., & Chandler, B. M. P. (2018). Geology, physiography and glaciology of SE Iceland. In D. J. A. Evans (Ed.), *Glacial landsystems of Southeast Iceland: Quaternary applications–field guide* (pp. 1–19). Quaternary Research Association.
- Evans, D. J. A., Ewertowski, M. W., & Orton, C. (2019). The glacial landsystem of Hoffellsjökull, SE Iceland: Contrasting geomorphological signatures of active temperate glacier recession driven by ice lobe and bed morphology. *Geografiska Annaler: Series A, Physical Geography*, 101(3), 249–276. <https://doi.org/10.1080/04353676.2019.1631608>
- Evans, D. J. A., Ewertowski, M. W., Orton, C., & Graham, D. J. (2018). The glacial geomorphology of the ice cap piedmont lobe landsystem of east Mýrdalsjökull, Iceland. *Geosciences*, 8(6), 194.
- Evans, D. J. A., Ewertowski, M. W., Roberts, D. H., & Tomczyk, A. M. (2022). The historical emergence of a geometric and sinuous ridge network at the Hørbyebreen polythermal glacier snout, Svalbard and its use in the interpretation of ancient glacial landforms. *Geomorphology*, 406, 108213. <https://doi.org/10.1016/j.geomorph.2022.108213>
- Evans, D. J. A., Ewertowski, M. W., Tomczyk, A. M., & Chandler, B. M. P. (2023). Active temperate glacial landsystem evolution in association with outwash head/depositional overdeepenings. *Earth Surface Processes and Landforms*, 48, 1573–1598. <https://doi.org/10.1002/esp.5569>
- Evans, D. J. A., & Hiemstra, J. F. (2005). Till deposition by glacier submarginal, incremental thickening. *Earth Surface Processes and Landforms*, 30(13), 1633–1662. <https://doi.org/10.1002/Esp.1224>
- Evans, D. J. A., & Orton, C. (2015). Heinabergsjökull and Skalafellsjökull, Iceland: Active temperate piedmont lobe and outwash head glacial landsystem. *Journal of Maps*, 11(3), 415–431. <https://doi.org/10.1080/17445647.2014.919617>
- Evans, D. J. A., Shand, M., & Petrie, G. (2009). Maps of the snout and proglacial landforms of Fjallsjökull, Iceland (1945, 1965, 1998). *Scottish Geographical Journal*, 125, 304–320.
- Evans, D. J. A., & Twigg, D. R. (2002). The active temperate glacial landsystem: A model based on Breioamerkurjökull and Fjallsjökull, Iceland. *Quaternary Science Reviews*, 21(20–22), 2143–2177.
- Ewertowski, M. (2014). Recent transformations in the high-arctic glacier landsystem, ragnarbreen, svalbard. *Geografiska Annaler: Series A, Physical Geography*, 96(3), 265–285. <https://doi.org/10.1111/geoa.12049>
- Ewertowski, M. W., Evans, D. J. A., Roberts, D. H., Tomczyk, A. M., Ewertowski, M. W., & Pleksot, K. (2019). Quantification of historical landscape change on the foreland of a receding polythermal glacier, Hørbyebreen, Svalbard. *Geomorphology*, 325, 40–54. <https://doi.org/10.1016/j.geomorph.2018.09.027>
- Ewertowski, M. W., & Tomczyk, A. M. (2015). Quantification of the ice-cored moraines' short-term dynamics in the high-Arctic glaciers Ebbabreen and Ragnarbreen, Petuniabukta, Svalbard. *Geomorphology*, 234, 211–227. <https://doi.org/10.1016/j.geomorph.2015.01.023>
- Ewertowski, M. W., & Tomczyk, A. M. (2020). Reactivation of temporarily stabilized ice-cored moraines in front of polythermal glaciers: Gravitational mass movements as the most important geomorphological agents for the redistribution of sediments (a case study from Ebbabreen and Ragnarbreen, Svalbard). *Geomorphology*, 350, 106952. <https://doi.org/10.1016/j.geomorph.2019.106952>
- Eyles, N. (1979). Facies of supraglacial sedimentation on Icelandic and Alpine temperate glaciers. *Canadian Journal of Earth Sciences*, 16(7), 1341–1361. <https://doi.org/10.1139/e79-121>
- Eyles, N. (1983a). Glacial geology: A Landsystems approach. In N. Eyles (Ed.), *Glacial Geology* (pp. 1–18). Pergamon.
- Eyles, N. (1983b). Modern Icelandic glaciers as depositional models for «hummocky moraine» in the Scottish highlands. In E. B. Evenson, C. Schluchter, & J. Rabassa (Eds.), *Tills and related deposits* (pp. 47–59). Balkema.
- Fey, C., & Krainer, K. (2020). Analyses of UAV and GNSS based flow velocity variations of the rock glacier Lazaun (Ötztal Alps, South Tyrol, Italy). *Geomorphology*, 365, 107261. <https://doi.org/10.1016/j.geomorph.2020.107261>

- Flannigan, M. D., Krawchuk, M. A., de Groot, W. J., Wotton, B. M., & Gowman, L. M. (2009). Implications of changing climate for global wildland fire. *International Journal of Wildland Fire*, 18(5), 483–507. <https://doi.org/10.1071/WF08187>
- Fookes, P. G., Gordon, D. L., & Higginbottom, I. E. (1978). Glacial landforms, their deposits and engineering characteristics. In *The engineering behaviour of glacial materials* (pp. 18–51). University of Birmingham.
- Gariano, S. L., & Guzzetti, F. (2016). Landslides in a changing climate. *Earth-Science Reviews*, 162, 227–252. <https://doi.org/10.1016/j.earscirev.2016.08.011>
- Groos, A. R., Bertschinger, T. J., Kummer, C. M., Erlwein, S., Munz, L., & Philipp, A. (2019). The potential of low-cost UAVs and open-source photogrammetry software for high-resolution monitoring of alpine glaciers: A case study from the Kanderfirn (Swiss Alps). *Geosciences*, 9(8), 356. <https://doi.org/10.3390/geosciences9080356>
- Harrison, S., Kargel, J. S., Huggel, C., Reynolds, J., Shugar, D. H., Betts, R. A., Emmer, A., Glasser, N., Haritashya, U. K., Klimeš, J., Reinhardt, L., Schaub, Y., Wiltshire, A., Regmi, D., & Vilimek, V. (2018). Climate change and the global pattern of moraine-dammed glacial lake outburst floods. *The Cryosphere*, 12(4), 1195–1209. <https://doi.org/10.5194/tc-12-1195-2018>
- Hedding, D. W., Erofeev, A. A., Hansen, C. D., Khon, A. V., & Abbasov, Z. R. (2020). Geomorphological processes and landforms of glacier forelands in the upper Aktru River basin (Gorniy Altai), Russia: Evidence for rapid recent retreat and paraglacial adjustment. *Journal of Mountain Science*, 17(4), 824–837. <https://doi.org/10.1007/s11629-019-5845-5>
- Hirabayashi, Y., Mahendran, R., Koirala, S., Konoshima, L., Yamazaki, D., Watanabe, S., Kim, H., & Kanae, S. (2013). Global flood risk under climate change. *Nature Climate Change*, 3(9), 816–821. <https://doi.org/10.1038/nclimate1911>
- Hugonnet, R., McNabb, R., Berthier, E., Menounos, B., Nuth, C., Girod, L., Farinotti, D., Huss, M., Dussaillant, I., Brun, F., & Kaab, A. (2021). Accelerated global glacier mass loss in the early twenty-first century. *Nature*, 592(7856), 726–731. <https://doi.org/10.1038/s41586-021-03436-z>
- Irvine-Fynn, T. D. L., Barrand, N. E., Porter, P. R., Hodson, A. J., & Murray, T. (2011). Recent high-Arctic glacial sediment redistribution: A process perspective using airborne lidar. *Geomorphology*, 125(1), 27–39. <https://doi.org/10.1016/j.geomorph.2010.08.012>
- Jouvet, G., Weidmann, Y., Kneib, M., Detert, M., Seguinot, J., Sakakibara, D., & Sugiyama, S. (2018). Short-lived ice speed-up and plume water flow captured by a VTOL UAV give insights into subglacial hydrological system of Bowdoin Glacier. *Remote Sensing of Environment*, 217, 389–399. <https://doi.org/10.1016/j.rse.2018.08.027>
- Jouvet, G., Weidmann, Y., van Dongen, E., Lüthi, M. P., Vieli, A., & Ryan, J. C. (2019). High-endurance UAV for monitoring calving glaciers: Application to the Inglefield Bredning and Equip Sermia, Greenland. *Frontiers in Earth Science*, 7, 206. <https://doi.org/10.3389/feart.2019.00206>
- Kienholz, C., Pierce, J., Hood, E., Amundson, J. M., Wolken, G. J., Jacobs, A., Hart, S., Wikstrom Jones, K., Abdel-Fattah, D., Johnson, C., & Conaway, J. S. (2020). Deglaciation of a marginal basin and implications for outburst floods, Mendenhall glacier, Alaska. *Frontiers in Earth Science*, 8, 137. <https://doi.org/10.3389/feart.2020.00137>
- Kjær, K. H., & Krüger, J. (2001). The final phase of dead-ice moraine development: Processes and sediment architecture, Kotlujökull, Iceland. *Sedimentology*, 48(5), 935–952. <https://doi.org/10.1046/j.1365-3091.2001.00402.x>
- Knight, J., & Harrison, S. (2012a). The impacts of climate change on terrestrial Earth surface systems. *Nature Climate Change*, 3(1), 24–29. <https://doi.org/10.1038/nclimate1660>
- Knight, J., & Harrison, S. (2012b). Evaluating the impacts of global warming on geomorphological systems. *Ambio*, 41(2), 206–210. <https://doi.org/10.1007/s13280-011-0178-9>
- Knight, J., & Harrison, S. (2018). Transience in cascading paraglacial systems. *Land Degradation & Development*, 29(6), 1991–2001. <https://doi.org/10.1002/ldr.2994>
- Kraaijenbrink, P., Meijer, S. W., Shea, J. M., Pellicciotti, F., De Jong, S. M., & Immerzeel, W. W. (2016). Seasonal surface velocities of a Himalayan glacier derived by automated correlation of unmanned aerial vehicle imagery. *Annals of Glaciology*, 57(71), 103–113. <https://doi.org/10.3189/2016AoG71A072>
- Krüger, J., & Kjær, K. H. (2000). De-icing progression of ice-cored moraines in a humid, subpolar climate, Kötluökull, Iceland. *The Holocene*, 10(6), 737–747. <https://doi.org/10.1191/09596830094980>
- Larson, G. J., Lawson, D. E., Evenson, E. B., Knudsen, Ó., Alley, R. B., & Phanikumar, M. S. (2010). Origin of stratified basal ice in outlet glaciers of Vatnajökull and Örfajökull, Iceland. *Boreas*, 39(3), 457–470. <https://doi.org/10.1111/j.1502-3885.2009.00134.x>
- Matecki, J. (2016). Accelerating retreat and high-elevation thinning of glaciers in Central Spitsbergen. *The Cryosphere*, 10(3), 1317–1329. <https://doi.org/10.5194/tc-10-1317-2016>
- Matecki, J. (2022). Recent contrasting behaviour of mountain glaciers across the European High Arctic revealed by ArcticDEM data. *The Cryosphere*, 16(5), 2067–2082. <https://doi.org/10.5194/tc-16-2067-2022>
- Mannerfelt, C. M. (1945). Några Glacialmorfologiska Fornelement. *Geografiska Annaler*, 27(1–2), 3–5. <https://doi.org/10.1080/20014422.1945.11880732>
- Mannerfelt, C. M. (1949). Marginal drainage channels as indicators of the gradients of quaternary ice caps. *Geografiska Annaler*, 31(1–4), 194–199. <https://doi.org/10.1080/20014422.1949.11880803>
- Midgley, N. G., Tonkin, T. N., Graham, D. J., & Cook, S. J. (2018). Evolution of high-Arctic glacial landforms during deglaciation. *Geomorphology*, 311, 63–75. <https://doi.org/10.1016/j.geomorph.2018.03.027>
- Młynarczyk, A., Konatowska, M., Królewicz, S., Rutkowski, P., Piekarczyk, J., & Kowalewski, W. (2022). Spectral indices as a tool to assess the moisture status of forest habitats. *Remote Sensing*, 14(17), 4267. <https://doi.org/10.3390/rs14174267>
- Nota, E. W., Nijland, W., & de Haas, T. (2022). Improving UAV-SfM time-series accuracy by co-alignment and contributions of ground control or RTK positioning. *International Journal of Applied Earth Observation and Geoinformation*, 109, 102772. <https://doi.org/10.1016/j.jag.2022.102772>
- Paine, A. D. M. (1985). “Ergodic” reasoning in geomorphology: Time for a review of the term? *Progress in Physical Geography*, 9, 1–15.
- Phillips, E., Everest, J., Evans, D. J. A., Finlayson, A., Ewertowski, M., Guild, A., & Jones, L. (2017). Concentrated, ‘pulsed’ axial glacier flow: Structural glaciological evidence from Kviárjökull in SE Iceland. *Earth Surface Processes and Landforms*, 42(13), 1901–1922. <https://doi.org/10.1002/esp.4145>
- Planet. (2022). Planet Application Program Interface: In Space for Life on Earth. <https://api.planet.com>
- Price, R. J. (1969). Moraines, Sandar, Kames and Eskers near Breidamerkurjökull, Iceland. *Transactions of the Institute of British Geographers*, (46), 17–43. <https://doi.org/10.2307/621406>
- Price, R. J. (1980). Rates of geomorphological changes in proglacial areas. In R. A. Cullingford, D. A. Davidson, & J. Lewin (Eds.), *Timescales in geomorphology* (pp. 79–93). Wiley.
- Roberts, M. J., Tweed, F. S., Russell, A. J., Knudsen, O. S., Lawson, D. E., Larson, G. J., Evenson, E. B., & Björnsson, H. (2002). Glaciohydraulic supercooling in Iceland. *Geology*, 30(5), 439–442. [https://doi.org/10.1130/0091-7613\(2002\)030<0439:Gsi>2.0.Co;2](https://doi.org/10.1130/0091-7613(2002)030<0439:Gsi>2.0.Co;2)
- Rossini, M., Di Mauro, B., Garzonio, R., Baccolo, G., Cavallini, G., Mattavelli, M., De Amicis, M., & Colombo, R. (2018). Rapid melting dynamics of an alpine glacier with repeated UAV photogrammetry. *Geomorphology*, 304, 159–172. <https://doi.org/10.1016/j.geomorph.2017.12.039>
- Ryan, J. C., Hubbard, A. L., Box, J. E., Todd, J., Christoffersen, P., Carr, J. R., Holt, T. O., & Snooke, N. (2015). UAV photogrammetry and structure

- from motion to assess calving dynamics at Store Glacier, a large outlet draining the Greenland ice sheet. *The Cryosphere*, 9(1), 1–11. <https://doi.org/10.5194/tc-9-1-2015>
- Schomacker, A. (2008). What controls dead-ice melting under different climate conditions? A discussion. *Earth-Science Reviews*, 90(3–4), 103–113. <https://doi.org/10.1016/j.earscirev.2008.08.003>
- Schomacker, A., & Kjaer, K. H. (2007). Origin and de-icing of multiple generations of ice-cored moraines at Bruarjökull, Iceland. *Boreas*, 36(4), 411–425. <https://doi.org/10.1080/03009480701213554>
- Schomacker, A., & Kjaer, K. H. (2008). Quantification of dead-ice melting in ice-cored moraines at the high-Arctic glacier Holmströmbreen, Svalbard. *Boreas*, 37(2), 211–225. <https://doi.org/10.1111/j.1502-3885.2007.00014.x>
- Seier, G., Kellerer-Pirklbauer, A., Wecht, M., Hirschmann, S., Kaufmann, V., Lieb, G. K., & Sulzer, W. (2017). UAS-based change detection of the glacial and proglacial transition zone at Pasterze glacier, Austria. *Remote Sensing*, 9(6), 549. <https://doi.org/10.3390/rs9060549>
- Sigurðsson, O. (2005). Variations of termini of glaciers in Iceland in recent centuries and their connection with climate. In C. Caseldine, A. Russell, J. Hardardóttir, & Ó. Knudsen (Eds.), *Developments in quaternary sciences* (Vol. 5, pp. 241–255). Elsevier.
- Sigurðsson, O., Jónsson, T., & Jóhannesson, T. (2007). Relation between glacier-termini variations and summer temperature in Iceland since 1930. *Annals of Glaciology*, 46, 170–176. <https://doi.org/10.3189/172756407782871611>
- Śledź, S., & Ewertowski, M. W. (2022). Evaluation of the influence of processing parameters in structure-from-motion software on the quality of digital elevation models and orthomosaics in the context of studies on earth surface dynamics. *Remote Sensing*, 14(6), 1312. <https://doi.org/10.3390/rs14061312>
- Śledź, S., Ewertowski, M. W., & Piekarczyk, J. (2021). Applications of unmanned aerial vehicle (UAV) surveys and structure from motion photogrammetry in glacial and periglacial geomorphology. *Geomorphology*, 378, 107620. <https://doi.org/10.1016/j.geomorph.2021.107620>
- Song, X. P., Hansen, M. C., Stehman, S. V., Potapov, P. V., Tyukavina, A., Vermote, E. F., & Townshend, J. R. (2018). Global land change from 1982 to 2016. *Nature*, 560(7720), 639–643. <https://doi.org/10.1038/s41586-018-0411-9>
- Spedding, N., & Evans, D. J. A. (2002). Sediments and landforms at Kviarjökull, Southeast Iceland: A reappraisal of the glaciated valley landsystem. *Sedimentary Geology*, 149(1–3), 21–42.
- Staines, K. E. H., & Carrivick, J. L. (2015). Geomorphological impact and morphodynamic effects on flow conveyance of the 1999 jökulhlaup at sólheimajökull, Iceland. *Earth Surface Processes and Landforms*, 40(10), 1401–1416. <https://doi.org/10.1002/esp.3750>
- Staines, K. E. H., Carrivick, J. L., Tweed, F. S., Evans, A. J., Russell, A. J., Jóhannesson, T., & Roberts, M. (2015). A multi-dimensional analysis of pro-glacial landscape change at Sólheimajökull, southern Iceland. *Earth Surface Processes and Landforms*, 40(6), 809–822. <https://doi.org/10.1002/esp.3662>
- Strzelecki, M. C., Long, A. J., Lloyd, J. M., Matecki, J., Zagórski, P., Pawłowski, Ł., & Jaskólski, M. W. (2018). The role of rapid glacier retreat and landscape transformation in controlling the post-Little Ice Age evolution of paraglacial coasts in Central Spitsbergen (Billefjorden, Svalbard). *Land Degradation & Development*, 29(6), 1962–1978. <https://doi.org/10.1002/ldr.2923>
- Swift, D. A., Evans, D. J. A., & Fallick, A. E. (2006). Transverse englacial debris-rich ice bands at Kviárjökull, Southeast Iceland. *Quaternary Science Reviews*, 25(13), 1708–1718.
- Szilo, J., & Bialik, R. (2018). Recession and ice surface elevation changes of Baranowski glacier and its impact on proglacial relief (King George Island, West Antarctica). *Geosciences*, 8(10), 355. <https://doi.org/10.3390/geosciences8100355>
- Tomczyk, A. M., & Ewertowski, M. W. (2021). Baseline data for monitoring geomorphological effects of glacier lake outburst flood: A very-high-resolution image and GIS datasets of the distal part of the Zackenberg River, Northeast Greenland. *Earth System Science Data*, 13(11), 5293–5309. <https://doi.org/10.5194/essd-13-5293-2021>
- Tomczyk, A. M., Ewertowski, M. W., & Carrivick, J. L. (2020). Geomorphological impacts of a glacier lake outburst flood in the high arctic Zackenberg River, NE Greenland. *Journal of Hydrology*, 591, 125300. <https://doi.org/10.1016/j.jhydrol.2020.125300>
- Tonkin, T. N., Midgley, N. G., Cook, S. J., & Graham, D. J. (2016). Ice-cored moraine degradation mapped and quantified using an unmanned aerial vehicle: A case study from a polythermal glacier in Svalbard. *Geomorphology*, 258, 1–10. <https://doi.org/10.1016/j.geomorph.2015.12.019>
- van der Sluijs, J., Kokelj, S., Fraser, R., Tunnicliffe, J., & Lacelle, D. (2018). Permafrost terrain dynamics and infrastructure impacts revealed by UAV photogrammetry and thermal imaging. *Remote Sensing*, 10(11), 1734. <https://doi.org/10.3390/rs10111734>
- van Woerkom, T., Steiner, J. F., Kraaijenbrink, P. D. A., Miles, E. S., & Immerzeel, W. W. (2019). Sediment supply from lateral moraines to a debris-covered glacier in the Himalaya. *Earth Surface Dynamics*, 7(2), 411–427. <https://doi.org/10.5194/esurf-7-411-2019>
- Westoby, M. J., Brasington, J., Glasser, N. F., Hambrey, M. J., & Reynolds, J. M. (2012). ‘Structure-from-Motion’ photogrammetry: A low-cost, effective tool for geoscience applications. *Geomorphology*, 179, 300–314. <https://doi.org/10.1016/j.geomorph.2012.08.021>
- Westoby, M. J., Rounce, D. R., Shaw, T. E., Fyffe, C. L., Moore, P. L., Stewart, R. L., & Brock, B. W. (2020). Geomorphological evolution of a debris-covered glacier surface. *Earth Surface Processes and Landforms*, 45(14), 3431–3448. <https://doi.org/10.1002/esp.4973>
- Wheaton, J. M., Brasington, J., Darby, S. E., & Sear, D. A. (2010). Accounting for uncertainty in DEMs from repeat topographic surveys: Improved sediment budgets. *Earth Surface Processes and Landforms*, 35(2), 136–156. <https://doi.org/10.1002/esp.1886>

**How to cite this article:** Śledź, S., Ewertowski, M. W., & Evans, D. J. A. (2023). Quantification of short-term transformations of proglacial landforms in a temperate, debris-charged glacial landsystem, Kviárjökull, Iceland. *Land Degradation & Development*, 34(17), 5566–5590. <https://doi.org/10.1002/ldr.4865>



## **Oświadczenia autorów**

Poznań, 08.02.2024

## OŚWIADCZENIE AUTORÓW

Śledź, S., Ewertowski, M. W., & Piekarczyk, J. (2021). Applications of unmanned aerial vehicle (UAV) surveys and Structure from Motion photogrammetry in glacial and periglacial geomorphology. *Geomorphology*, 378. <https://doi.org/10.1016/j.geomorph.2021.107620>

Autorzy powyższej publikacji deklarują swój udział w jej przygotowaniu następująco:

| Afiliacja   | Autor                  | Udział   |
|---|------------------------|--|
| Uniwersytet im.<br>Adama<br>Mickiewicza w<br>Poznaniu | Szymon Śledź           | Autor był odpowiedzialny za tworzenie koncepcji artykułu, opracowanie metodologii, przeprowadzenie kwerendy literatury, tworzenie bazy danych i jej analizę, opracowanie rycin 1-3, przygotowanie manuskryptu z suplementem, odpowiedzi na recenzje i zarządzanie procesem publikacji. Autor korespondencyjny. |
|   | Marek W.<br>Ewertowski | Autor był odpowiedzialny za tworzenie koncepcji artykułu, nadzór nad poprawnością metodologiczną pracy i przygotowanie odpowiedzi na recenzje.   |
|   | Jan Piekarczyk         | Autor był odpowiedzialny za tworzenie koncepcji artykułu oraz nadzór nad poprawnością metodologiczną pracy.  |

Autor



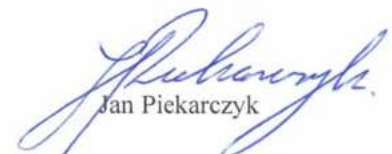
Szymon Śledź

Autor



Marek W. Ewertowski

Autor



Jan Piekarczyk

Poznań, 08.02.2024

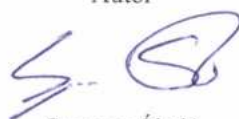
OŚWIADCZENIE  
AUTORÓW

Śledź, S., & Ewertowski, M. W. (2022). Evaluation of the Influence of Processing Parameters in Structure-from-Motion Software on the Quality of Digital Elevation Models and Orthomosaics in the Context of Studies on Earth Surface Dynamics. *Remote Sensing*, 14(6). <https://doi.org/10.3390/rs14061312>

Autorzy powyższej publikacji deklarują swój udział w jej przygotowaniu następująco:

| Afiliacja   | Autor                  | Udział  |
|---|------------------------|---|
| Uniwersytet im.<br>Adama<br>Mickiewicza w<br>Poznaniu | Szymon Śledź           | Autor był odpowiedzialny za tworzenie koncepcji artykułu, opracowanie metodologii, przeprowadzenie kwerendy literatury, wykonanie terenowych pomiarów fotopunktów, przeprowadzenie nalogów bezzałogowych statkiem powietrznym, fotogrametryczne przetworzenie obrazów i opracowanie cyfrowych modeli wysokościowych i ortomozaik, tworzenie i testowanie skryptów, opracowanie wszystkich rycin (Ryc. 1-7 oraz ryciny w załącznikach), przygotowanie manuskryptu z suplementami, odpowiedzi na recenzje, zarządzanie procesem publikacji oraz pozyskanie finansowania publikacji w otwartym dostępie. Autor korespondencyjny. |
|   | Marek W.<br>Ewertowski | Autor był odpowiedzialny za tworzenie koncepcji artykułu, opracowanie metodologii, przeprowadzenie nalogów bezzałogowych statkiem powietrznym, nadzór nad poprawnością metodologiczną pracy i przygotowanie odpowiedzi na recenzje.   |

Autor



Szymon Śledź

Autor



Marek W. Ewertowski

08.02.2024

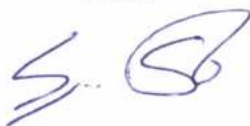
DECLARATION  
OF AUTHORS

Śledź, S., Ewertowski, M.W., & Evans, D.J.A. (2023). Quantification of short-term transformations of proglacial landforms in a temperate, debris-charged glacial landsystem, Kvíárjökull, Iceland. *Land Degradation & Development*, 34(17), 5566-5590. <https://doi.org/10.1002/ldr.4865>

The authors of the above publication declare their participation in its preparation as follows:

| Affiliation   | Author              | Contribution  |
|---|---------------------|---|
| Faculty of Geographical and Geological Sciences, Adam Mickiewicz University, Poznań, Poland | Szymon Śledź        | The author was responsible for conceptualization of the research, literature review, development of the methodology, conducting part of the UAV surveys, surveys of ground control points, photogrammetric processing of the images and generation of time series of digital elevation models and orthomosaics, quantification of landform changes, analysis of satellite images, data interpretation, preparation of the figures 1a,b, 2, 5-8, 10,11; preparation of the manuscript, responses to the reviews, obtaining funding for the publication in open access. Corresponding author. |
|   | Marek W. Ewertowski | The author was responsible for the conceptualization of the research, development of the methodology, conducting part of the UAV surveys, processing of historical aerial photographs, data interpretation, preparation of figures 3,9,13,14, preparation of the manuscript, supervising the methodological correctness of the work, and preparation of the responses to the reviews.   |
| Department of Geography, Durham University, Durham, UK                                      | David J. A. Evans   | The author was responsible for the conceptualization of the research, literature review, development of the methodology, conducting fieldwork, geomorphological mapping, data interpretation, preparation of figures 1c, 4, 12, preparation of the manuscript, supervising the methodological correctness of the work; preparation of the responses to the reviews.   |

Author



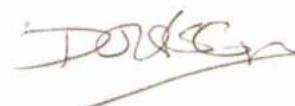
Szymon Śledź

Author



Marek W. Ewertowski

Author



David J. A. Evans